

Document Version

Final published version

Citation (APA)

Zhang, S. (2025). *Correlating Ion Dynamics with Structure: From Liquid to Hybrid Solid Electrolytes*. [Dissertation (TU Delft), Delft University of Technology]. <https://doi.org/10.4233/uuid:460d8fd5-d9c9-4156-8e1c-6b64439c98b2>

Important note

To cite this publication, please use the final published version (if applicable).
Please check the document version above.

Copyright

In case the licence states "Dutch Copyright Act (Article 25fa)", this publication was made available Green Open Access via the TU Delft Institutional Repository pursuant to Dutch Copyright Act (Article 25fa, the Taverne amendment). This provision does not affect copyright ownership.
Unless copyright is transferred by contract or statute, it remains with the copyright holder.

Sharing and reuse

Other than for strictly personal use, it is not permitted to download, forward or distribute the text or part of it, without the consent of the author(s) and/or copyright holder(s), unless the work is under an open content license such as Creative Commons.

Takedown policy

Please contact us and provide details if you believe this document breaches copyrights.
We will remove access to the work immediately and investigate your claim.

**Correlating Ion Dynamics with Structure:
From Liquid to Hybrid Solid Electrolytes**

Shengnan ZHANG

Correlating Ion Dynamics with Structure: From Liquid to Hybrid Solid electrolytes

Dissertation

for the purpose of obtaining the degree of doctor
at Delft University of Technology
by the authority of the Rector Magnificus, Prof.dr.ir. T.H.J.J. van der Hagen,
chair of the Board for Doctorates
to be defended publicly on
Monday 17 March 2025 at 12:30 o'clock

by

Shengnan ZHANG

Master of Engineering in Materials Physics and Chemistry
Sun Yat-sen University, China

This dissertation has been approved by the promotor.

Composition of the doctoral committee:

Rector Magnificus	Chairperson
Prof. dr. ir. M. Wagemaker	Delft University of Technology, promotor
Dr. S. Ganapathy	Delft University of Technology, copromotor

Independent members:

Prof. dr. J. Janek	Justus Liebig University Giessen, Germany
Prof. dr. M. Tromp	University of Groningen, the Netherlands
Prof. dr. F. M. Mulder	Delft University of Technology, the Netherlands
Dr. M. Liu	Tsinghua University, China
Dr. ir. L. J. Bannenberg	Delft University of Technology, the Netherlands
Prof. dr. E. H. Brück	Delft University of Technology (reserve member)



The work described in this thesis was carried out in the group of Storage of Electrochemical Energy (SEE), Faculty of Applied Sciences, Delft University of Technology. This work was partially supported by China Scholarship Council (CSC).

Keywords: Lithium-metal anode; solid electrolyte interphase; hybrid solid electrolytes; lithium-ion dynamics; interface.

Cover design: Luna & Sol. Inspired by a 2D exchange NMR spectrum and Delft's autumn sky; some geographical details are omitted for technical reasons.

ISBN 978-94-6384-717-9

Copyright © 2025 by Shengnan Zhang

All rights reserved.

Printed by ProefschriftMaken || www.proefschriftmaken.nl

An electronic version of this dissertation is available at <https://repository.tudelft.nl/>

To my grandma

Contents

1. Introduction	1
1.1 The choice of Li-metal batteries.....	2
1.2 The journey towards solid-state Li-metal batteries	4
1.2.1 Hybrid solid electrolytes: Components and classifications.....	4
1.2.2 Ion conduction mechanisms in hybrid solid electrolytes	7
1.3 Interfaces in hybrid solid electrolytes for Li-metal batteries.....	11
1.4 NMR spectroscopy for Li-ion dynamics.....	14
1.4.1 Interfacial Li-ion transport dynamics.....	15
1.4.2 Local Li-ion dynamics	16
1.5 Thesis outline and goals.....	18
1.5.1 Connecting Li exchange with SEI properties.....	18
1.5.2 Structure-ion dynamics relationship in hybrid solid electrolytes	19
References.....	21
2. Solid-state Nuclear Magnetic Resonance Spectroscopy	27
2.1 The principle of NMR.....	28
2.2 NMR signal detection via one-pulse measurement	29
2.3 Interactions in NMR.....	31
2.4 NMR techniques used in this thesis	35
2.4.1 Relaxation time measurements	35
2.4.2 Line-width analysis.....	37
2.4.3 Cross polarization	38
2.4.4 Two-dimensional NMR.....	41
2.4.5 One-dimensional exchange spectroscopy	44
2.4.6 Operando NMR.....	45
References.....	48
3. The Lasting Impact of Formation Cycling on the Li-ion Kinetics Between SEI and the Li-metal Anode and Its Correlation with Efficiency	49
Abstract.....	50
3.1 Introduction.....	51
3.2 Results.....	54

3.2.1 The impact of electrochemical preconditioning on the LMBs performance	54
3.2.2 Li-ion diffusion between the ED-Li and the SEI.....	57
3.2.3 Quantification of the Li-ion exchange.....	59
3.2.4 Composition of the SEI.....	62
3.2.5 Quantification of the dead Li	65
3.3 Discussion	68
3.4 Conclusions	71
3.5 Methods.....	71
3.6 Supplementary information.....	75
References	88
4. Revealing Local Diffusive Dynamics in Hybrid Solid Electrolytes	95
Abstract	96
4.1 Introduction	97
4.2 Results	99
4.2.1 Li-ion conduction.....	99
4.2.2 Local Li-ion dynamics	101
4.2.3 Polymer structure and dynamics	108
4.2.4 Compatibility towards the Li-metal anode.....	110
4.3 Conclusions	112
4.4 Methods.....	113
4.5 Supplementary information.....	116
References	128
5. Improving Li-ion Interfacial Transport in Hybrid Solid Electrolytes	133
Abstract	134
5.1 Introduction	135
5.2 Results	136
5.2.1 Interface structure and Li-ion diffusion in the hybrid LiTFSI-PEO-Li ₆ PS ₅ Cl solid electrolyte.....	136
5.2.2 Addition of ionic liquids to enhance the conductivity of the PEO-Li ₆ PS ₅ Cl hybrid solid electrolyte.....	139
5.2.3 Impact of the ionic liquid on the bulk PEO and PEO-Li ₆ PS ₅ Cl interface structure.....	141
5.2.4 Impact of the ionic liquid on the interfacial diffusion between PEO-LiTFSI and Li ₆ PS ₅ Cl	145
5.2.5 Electrochemical evaluation of the hybrid solid electrolyte upon introduction of ionic liquids.....	148
5.3 Conclusions	150
5.4 Methods.....	150
5.5 Supplementary information.....	152
References	160

6. Elucidating the Impact of Functional Additives on the Structure and Ion Dynamics of Hybrid Solid Electrolytes	165
Abstract	166
6.1 Introduction	167
6.2 Results	169
6.2.1 Improving Li-ion diffusion between PEO-LiTFSI and Li ₆ PS ₅ Cl with a LiI additive	169
6.2.2 Impact of LiI on bulk and local structures of the HSE.....	171
6.2.3 Evaluation of ionic conductivity and electrochemical performance of the HSEs	178
6.2.4 Interfacial stability of HSE-LiI with Li-metal.....	181
6.2.5 Impact of local and bulk structures in HSEs	183
6.3 Conclusions	185
6.4 Methods.....	186
6.5 Supplementary information.....	189
References.....	202
Summary.....	209
Samenvatting.....	214
Acknowledgements.....	219
List of publications.....	227
Curriculum vitae.....	229

1

Introduction

“欲穷千里目，更上一层楼”

“To see a thousand miles ahead, one must ascend another story.”

王之涣《登鹳雀楼》(Climbing the Stork Tower)

1.1 The choice of Li-metal batteries

Advanced energy storage is an intrinsic requirement in modern life, which posts an ever-growing demand for high-energy-density battery systems. However, current commercial lithium (Li)-ion batteries (LIBs) are nearing the theoretical limits of their electrode materials, particularly with respect to the graphite anode (372 mAh g^{-1})¹. As a “beyond Li-ion” battery chemistry, the Li-metal anode, which is lightweight (0.534 g cm^{-3}), has the lowest electrochemical redox potential ($-3.04 \text{ V vs. standard hydrogen electrode}$), and an ultrahigh theoretical capacity (3860 mAh g^{-1}), holds the potential to enable batteries with the highest specific energy^{2,3}. Nonetheless, practical lithium-metal batteries (LMBs) are still not viable, primarily due to two major challenges: the unstable Li-metal/electrolyte interfaces and dendrite propagation during repeated plating and stripping. The parasitic reactions between the intrinsically reactive Li-metal and the electrolyte components typically lead to the formation of a solid electrolyte interphase (SEI) layer, which is composed of the insoluble reaction products, with its composition and structure being decisive for the cycling performance⁴⁻⁶. To minimize Li losses, an ideal SEI should feature proper thickness and morphology to enable reversible ion transport and electrodeposition while blocking electron permeability⁷. However, the SEI is inherently dynamic, with both its morphology and composition evolving spatially and temporally⁶. The lateral heterogeneity induced by the dynamic evolution of the SEI during cycling can cause uneven distribution of ions and electrons, which renders heterogeneous surface nucleation and uncontrollable dendrite growth^{8,9}. The high-surface-area Li dendrites can grow locally and produce electrochemically inactive Li (“dead” Li), leading to rapid performance degradation and even cell short circuits^{10,11}.

To intelligently handle the above issues, both fundamental and practical insights and strategies are imperative. The fundamental perspective involves studying Li-ion kinetics and correlating it with dynamic conditions (e.g., current densities, ion concentration). As a result, the Li-metal cycling efficiency has been associated with properties such as charge-transfer kinetics¹²⁻¹⁵, Li electrode potential^{15,16}, and Li-ion exchange¹⁷⁻¹⁹. It is well established that charge transfer processes, including Li-ion desolvation and migration within the SEI, are critical rate-determining steps for Li-ion transfer kinetics. Typically, electroplating occurs

through two positions: at the buried Li-SEI interfaces and at the fresh Li-electrolyte interfaces, each with distinct kinetics^{13,15}. The favored position is closely related to the characteristics of the formed SEI, which plays a critical role in regulating Li-ion exchange between the electrolyte and the electrode. For instance, the cycling efficiency and its retention at high rates are positively correlated with the rate of Li-ion exchange within the SEI¹⁷. Additionally, its evolution provides insights into the effectiveness of the initial plating step during the formation cycle^{12,20,21}. Therefore, regulating SEI properties is a widely used strategy for optimizing Li-ion kinetics.

However, accurately correlating the aforementioned features with the reversibility of Li-metal remains ambiguous, given the strong electrolyte-dependent picture of the SEI evolution (e.g., both positive correlation^{15,19,22}, and negative correlation^{23,24} are linked to interfacial electroplating kinetics and Li efficiency). Therefore, considerable research effort has been dedicated to electrolyte engineering, which is typically divided into two branches: liquid and solid-state electrolytes (SSEs). For liquid electrolytes, strategies have focused on tuning the electrolyte components, including the use of fluorinated electrolytes²⁵⁻²⁷, localized high-concentration electrolytes²⁸⁻³⁰, and various additives^{31,32}. It is widely recognized that a robust SEI layer, enriched with inorganic compounds in the inner layer (e.g., LiF, Li₂O, and Li₂CO₃), is more conducive to efficient interfacial charge transfer⁵. Nonetheless, organic liquid electrolytes inherently pose safety risks due to their highly volatile and flammable solvents, which presents even greater challenges for high-energy-density power batteries³³. Consequently, SSEs have seen increased development due to their potential to reduce safety concerns and improve electrochemical and thermal stability. In addition, the good mechanical strength of SSEs helps reduce Li dendrite propagation, which reduces the risk of short circuits and thermal runaway while extending battery lifespan, enhancing performance, and ensuring more reliable operation of LMBs^{33,34}. Despite this, achieving practical implementation of solid-state LMBs (SSLMBs) remains challenging due to the complex interplay of interior interfaces, pronounced mechanical deformation, and the necessity to balance ionic conductivity, stability, mechanical strength and scalability³⁵. This thesis is dedicated to developing SSLMBs based on the hybrid solid electrolytes (HSEs) system. A more detailed introduction to this system is presented in the next section.

1.2 The journey towards solid-state Li-metal batteries

1.2.1 Hybrid solid electrolytes: Components and classifications

Replacing the liquid electrolyte, SSEs lie at the heart of realizing the concept of SSLMBs, motivating intensive research dedicated to the development of a diverse range of solid ionic conductors. Each of these materials possess unique physicochemical characteristics and complex dynamic properties. Driven by the advancements in characterization techniques and nanotechnology, numerous research efforts have been committed to the fundamental understanding and property enhancements of SSEs. This thesis focuses on a hybrid system that combines a polyethylene oxide (PEO) polymer matrix with argyrodite-type inorganic electrolytes. Therefore, a general overview of the polymer and inorganic components is presented before delving into the details of the hybrid systems.

Solid polymer electrolytes

Solid polymer electrolytes (SPEs) are complexes created when Li salts interact with the polar groups in polymer hosts. Thus, the ability to dissolve salts and dissociate Li-ions is crucial for forming homogeneous polymer electrolyte complexes. To ensure effective salt dissolution and ion dissociation, the solvation energy of the salt in the polymer matrix must be sufficient to exceed the inherent lattice energy of the added salt³⁶. Polymers with functional polar groups like carbonyls (C=O), ethers (R-O-R'), and nitriles (C≡N) are inherently advantageous as they facilitate dissolving Li salt and forming complexes through solvation with the polar groups. Meanwhile, Li salts with large anion sizes and low lattice energies are more easily ionized, which aids in increasing the concentration of the free Li-ions. In comparison to ceramic solid electrolytes, SPEs offer advantages such as high flexibility, light in weight, and effective electrode wettability, which are vital for commercial application in batteries. However, they usually face challenges including low ionic conductivity at room temperature, poor thermal stability, and insufficient mechanical strength. In addition, their narrow electrochemical stability window limits their compatibility with high-voltage cathodes.

PEO-based electrolytes are among the most widely studied SPEs as the $-\text{CH}_2\text{CH}_2\text{O}-$ groups in the PEO backbone have a high donor number, which effectively dissolves the Li salts without creating interactions strong enough to hinder ion movement. Additionally, they

offer good electrode compatibility, high membrane-forming capability, and are cost-effective. Ion conduction through PEO chains is driven by segmental motion above its glass transition temperature (T_g) and is dominated by the amorphous regions. Thus, an ideal PEO matrix should be highly amorphous with a low T_g . While reducing the molecular weight of PEO can enhance these properties, it often comes at the cost of mechanical strength. At the same time, the solubility of Li salt within the PEO matrix is crucial for increasing the concentration of free Li-ions. Therefore, strategies like copolymerization, Li salt optimization, additive engineering and morphological adjustments have been developed to achieve the ideal scenario³⁷.

Inorganic solid electrolytes

To date, the most extensively studied inorganic solid electrolytes (ISEs) are oxide- and sulfide-based ceramics, with halide materials beginning to attract more attention. Oxide electrolytes typically include LISICON-like (lithium superionic conductor), NASICON-like (sodium superionic conductor), perovskite- and garnet- types³⁸. Among them, the garnet-type electrolyte is the most widely investigated, with $\text{Li}_7\text{La}_3\text{Zr}_2\text{O}_{12}$ (LLZO) and its derivatives representing this class of electrolytes. The cubic phase LLZO exhibits an ionic conductivity $\sim 10^{-4}$ S cm^{-1} at room temperature, with excellent stability against Li-metal and wide electrochemical stability window^{39,40}. Nonetheless, LLZO suffers from poor chemical stability in moist conditions, leading to the formation of decomposition products that accumulate at the surface and impede ion transfer⁴¹. Perovskite-type SSEs, such as $\text{La}_{3-x}\text{Li}_{2/3-x}\text{TiO}_3$, are known for their high oxidation potential and mechanical strength but are plagued by significant grain boundary resistances, often much higher than the bulk resistance. Furthermore, they are unstable in contact with Li-metal⁴². NASICON-like materials (e.g., $\text{Li}_{1.3}\text{Al}_{0.3}\text{Ti}_{1.7}(\text{PO}_4)_3$, LATP), exhibit high oxidation voltages and ionic conductivity and are stable in the atmosphere, yet they are brittle and unstable towards Li-metal. In contrast, traditional LISICON-like electrolytes (e.g., Li_3PS_4) while also highly stable under ambient conditions, have relatively low ionic conductivity and are unstable with Li-metal as well^{42,43}. Sulfide-based SSEs show superior ionic conductivity among ISEs, comparable to that of conventional organic liquid electrolytes. Their ductile nature helps maintain good interfacial contact with electrode materials, reduces grain boundary resistance, and contributes to desirable mechanical properties and processability⁴⁴. Argyrodite-structured sulfides, such as

$\text{Li}_6\text{PS}_5\text{X}$ (where $\text{X} = \text{Cl}, \text{Br}, \text{or I}$), are representative materials in this category and are predominantly utilized in fabricating solid-state batteries. Their attractiveness stems from high Li-ion conductivities (up to 24 mS cm^{-1}) and scalable synthesis methods, both of which are crucial for commercial viability.⁴⁵ However, the main challenges in their practical application originates from their chemical and electrochemical instabilities, including high sensitivity to moisture and decomposition upon contact with active materials, which leads to increased interfacial resistance.

Classifications

The term “hybrid solid electrolytes” cover a broad range of material combinations. The development of HSEs initially involved dispersing inert (non-conductive) fillers like Al_2O_3 , SiO_2 and TiO_2 within a polymer-Li salt matrix. While these fillers do not directly conduct Li-ions, they function as plasticizers, disrupting the regularity of polymer chains and thereby reducing crystallinity. Furthermore, the Lewis acid-base model has been proposed to explain the interactions between filler surfaces and salt anions, which enhances the dissociation of Li salts⁴⁰.

Recently, there has been growing interest in incorporating active (ion-conductive) fillers into SPEs matrices, driven by the advancements in highly conductive ISEs. Combining these two types of ion conductors holds promise for leveraging their strengths while overcoming their individual limitations. The goal is to introduce additional Li-ion conduction pathways while preserving the general functions of the inert fillers. To achieve this, it is essential to establish an interface that is active in Li-ion conduction.

Following this, depending on which phase constitutes the main structural component of the electrolyte, HSEs can be classified into two categories: ceramic-in-polymer and polymer-in-ceramic. Sun et al. investigated the effectiveness of suppressing Li dendrite using HSEs from ceramic-in-polymer to polymer-in-ceramic types⁴⁶. The HSEs were fabricated by blending PEO with varying concentrations of $\text{Li}_{6.4}\text{La}_3\text{Zr}_{1.4}\text{Ta}_{0.6}\text{O}_{12}$ (LLZTO) (20, 50, and 80 vol%). Their study revealed that ceramic-in-polymer offered higher ionic conductivity, while polymer-in-ceramic provided enhanced mechanical strength. This indicates that optimizing HSEs design requires balancing conductivity with mechanical properties. Moreover, factors such as particle size, shape, and the hybridization strategy play crucial roles in influencing these characteristics.

1.2.2 Ion conduction mechanisms in hybrid solid electrolytes

Ionic conduction in HSEs is inherently complex, as these materials typically feature multiphase structures at both macroscopic and microscopic levels (**Fig. 1.1**). The coexistence of different phases provides various Li-ion transport pathways, making the distribution and structure of these phases, especially the polymer phases, and their interphase interactions crucial factors. Therefore, before delving into the ion conduction mechanisms in HSEs, it is important to first understand the conduction mechanisms of their individual organic and inorganic components.

Ion conduction in solid polymer electrolytes

Dissolving salt in a polymer matrix can result in the coexistence of various phases: amorphous and crystalline polymer phases, amorphous and crystalline polymer-salt complexes (with different concentrations), and pure salt phase. This makes the ion transport mechanism in the SPEs more complex, and requires careful deconstruction of the observed mixed behavior.

Due to the complexity of the system and the highly temperature-dependent phase transition behavior, several models have been developed to describe the ion diffusion mechanism in the SPEs. The most widely recognized one is the segment migration model, which considers ion dynamics in the rigid crystalline phase to be sluggish, with ion transport primarily occurring in the amorphous phase. This model has also been utilized in this thesis. Specifically, the polymer molecules in the amorphous region participate in ion transport by local segmental motion. Ions migrate by continuous coordination-discoordination along the polymer chains or between different chains (**Fig. 1.1b**). Therefore, the mobility of the polymer chains and the number of free Li-ions are decisive for the ionic conductivity of the SPEs. Reducing the crystallinity of the polymer phase and increasing salt dissociation are key to enhancing the concentration and mobility of the charge carriers. It is worth noting that while strong coordination between the polymer's polar groups and the cations can promote the dissolution and dissociation of the salt, it can also impede cation movement. Thus, a rational design of the polymer structure and salt concentration is essential.

The segmental-related mobility is dependent on the T_g as the amorphous phase dominates the ion movement in the SPEs. Therefore, the empirical Vogel-Tamman-Flucher

(VTF) equation⁴⁷ is commonly used to describe the ion conduction in the SPEs above T_g :

$$\sigma(T) = \sigma_0 e^{-\frac{B}{k_B(T-T_0)}} \quad (1.3)$$

where $\sigma(T)$ is the temperature-dependent ionic conductivity, σ_0 is the pre-exponential factor, B is the pseudo-activation energy, T_0 is the Vogel temperature equal to T_g in ideal glass state. The VTF equation assumes that the chain mobility is influenced by free volume, which follows an exponential relationship and approaches zero at T_0 , the temperature at which polymer chain motion ceases.

Another diffusion model in SPEs is based on ion hopping, which pertains to the crystalline regions of the SPEs and resembles transport mechanisms in ISEs. This type of diffusion can occur below the T_g and is expected to follow the Arrhenius behavior. Bruce et al. proposed that Li-ion diffusion takes place through cylindrical channels formed by the PEO chains when the EO:Li ratio is 6:1 (EO:Li refers to the ratio of ether oxygen units to Li-ions)⁴⁸. This diffusion behavior is independent of segmental motion, with a more ordered crystal structure results in higher ionic conductivity.

Given the multiphase interactions in SPEs, various modes of ion diffusion can coexist within the system, making it challenging to unravel the conduction behavior without a clearly defined structure. Despite this complexity, Li-ion movement in the crystalline region is still much slower than in the amorphous region due to the effects of the channel structure and inter-ion Coulomb forces. Therefore, the main strategy to improve ionic conductivity should focus on increasing the fraction of the amorphous phase at ambient and sub-ambient temperatures.

Ion conduction in inorganic solid electrolytes

Typically, ionic diffusion in crystalline ISEs can be described by a hopping mechanism, where ions move from one lattice site to an adjacent vacant site. This diffusion process is highly dependent on the material's structure, including factors such as the number of vacancies, interstitials, lattice site occupancy, and the dimensionality of the diffusion pathway.

There are three main mechanisms governing ion conduction: vacancy diffusion, direct interstitial migration, and interstitial knock-off migration⁴⁹ (**Fig. 1.1c**). In vacancy diffusion, an ion moves to a vacancy, an empty lattice site, or a defect within the crystal structure,

creating a new vacancy that allows another ion to move and thus facilitates ion movement across the lattice. Direct interstitial migration refers to an ion moving directly from one interstitial site to another. Lastly, the interstitial knock-off mechanism involves an interstitial ion displacing a lattice ion to an adjacent interstitial site, thus enhancing ion migration within the lattice⁵⁰.

Grasping these diffusion mechanisms necessitates an understanding of ion mobility (μ), which is related to the ion diffusion coefficient (D) through the Nernst-Einstein equation:

$$\mu = \frac{D}{k_B T} \quad (1.1)$$

where k_B is the Boltzmann constant, and T is the absolute temperature. Therefore, the ionic conductivity exhibits a temperature-dependent mechanism. Ion diffusion typically occurs along the path of minimum resistance, where an energy barrier for ion migration is defined, with lower migration energy corresponding to higher ionic conductivity. It can be expressed by Arrhenius equation:

$$\sigma(T) = \frac{\sigma_0}{T} e^{-\frac{E_a}{k_B T}} \quad (1.2)$$

where $\sigma(T)$ is the temperature-dependent ionic conductivity, σ_0 is the pre-exponential factor, and E_a is the activation energy. Factors like the charge of the mobile ions, the hopping distance, the dimensionality of the diffusion pathway, and the system entropy are all related to the prefactor, σ_0 .

Ion conduction in hybrid system

In a hybrid system that combines a polymer electrolyte with ISE fillers, it is well-recognized that three distinct phases are present: the polymer-salt phase, the filler particles, and the polymer-filler interfaces (i.e., the particle surfaces). Ideally, a percolating ion-conducting network between these phases is present, making use of the high conductivity of the ISE (**Fig. 1.1**). However, practically the Li-ion diffusion can be preferentially along the polymer phase (in the case of ceramic-in-polymer), in the filler phase (in the case of polymer-in-ceramic), or at the polymer-filler interfaces. This is affected by a multitude of factors, including the polymer's structure and degree of crystallinity, the salt concentration and the efficiency of

ion dissociation, the filler properties (such as particle size and shape, conductivity, stability, surface chemistry), the polymer/filler interfacial compatibility, the presence of additives, the filler loading and fabrication methods.

Given the presence of coupled conduction mechanisms and multiple interfaces in the HSE, percolation theory is applied to assess the efficiency of ion transport within these complex systems⁴⁰. Traditionally, percolation theory is used to describe the connectivity of random composites, with the percolation threshold representing the critical concentration beyond which a continuous, long-range conductive phase exists⁵¹. In the context of HSEs, the percolation threshold is often correlated with the filler concentration. However, the role of the interface cannot be overlooked. The formation of an interfacial phase transforms the system into a three-phase composite, where the interfacial properties critically influence the percolation threshold and, consequently, the contribution of both ion-conducting phases to the overall ionic conductivity.

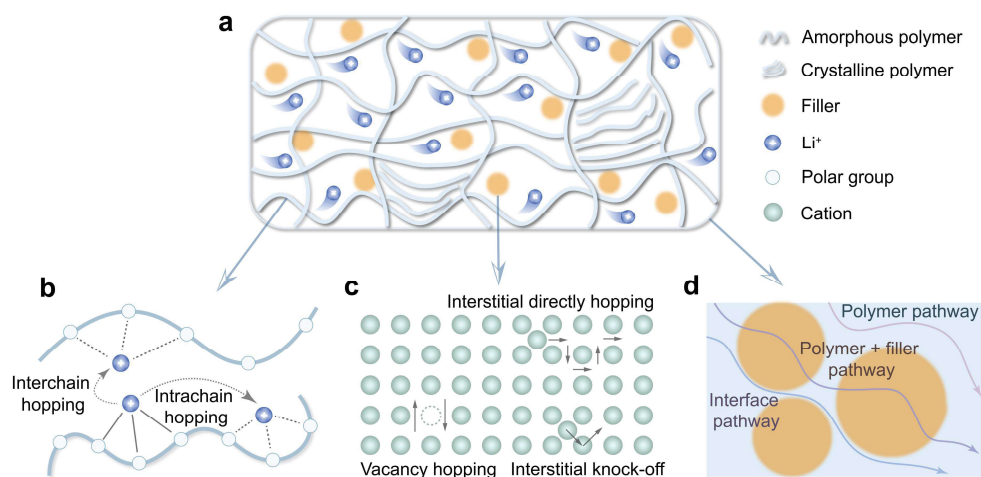


Fig. 1.1. Schematic representation of the Li-ion conduction mechanisms and pathways. (a) Illustration of a typical HSE. Representative Li-ion conduction mechanisms in (b) solid polymer electrolytes (SPEs), and (c) inorganic solid electrolytes (ISEs). (d) Schematic depiction of the possible Li-ion diffusion pathways through the HSEs.

Beyond that, research has also identified fast ion diffusion pathways along the polymer-filler interfaces³⁶. The Lewis acid-base theory has been applied to explain interfacial ion transport, clarifying how overall ionic conductivity, coupled with polymer mobility, ion

dynamics, and free ion density, are all influenced by these interfaces. Therefore, in practice, macroscopic percolation is often depends on microscopic interfacial interactions, which will be explained in more detail in the next section. Collectively, it is evident that the ion conduction in HSEs is highly composition-dependent, with the interface playing a crucial role.

1.3 Interfaces in hybrid solid electrolytes for Li-metal batteries

As previously mentioned, incorporating fillers into the polymer electrolyte matrix boosts the ionic conductivity of the HSEs by decreasing the polymer crystallinity, as well as creating fast ion channels via the active filler phase and/or the polymer-filler interfaces. In this scenario, the efficient interfacial ion conduction between the distinct components of the HSEs is crucial for forming a percolated ion-conducting network. Currently, two interfacial interaction mechanisms in the HSEs systems are of major interest: (i) the Lewis acid-base interaction between the polymer matrix and the inorganic fillers; (ii) the space charge layer formation at the polymer-inorganic interfaces. Aside from the internal interfaces, evaluating the external interfacial stability of HSEs with both the anode and cathode materials is essential for their viability in SSLMBs. This thesis specifically focuses on the interfaces between the Li-metal anode and HSEs.

Lewis acid-base interactions

For inorganic fillers that feature Lewis acid-base characteristics, a competitive environment develops between polymer segments and filler particles for coordinating with Li-ions, which aids in dissociating the Li salts and increasing the concentration of mobile Li-ions (**Fig. 1.2a**). The effectiveness of the Lewis acid-base interactions varies depending on the properties of the added fillers. Croce et al, investigated the Lewis acid-base interactions in a PEO-LiCF₃SO₃ system using three different types of Al₂O₃ fillers: acidic, basic, and neutral⁵². Introducing acidic Al₂O₃ nanoparticles leads to stronger attraction between the salt anions and the acidic group on the Al₂O₃ surface compared to with the cations, and the protons in the acidic groups result in a more polarizable environment of the Li when compared to the polymer. These effects together contributed to the dissociation of the Li salt and increased Li-ion mobility. When Al₂O₃ with Lewis basic surface groups was added, the interaction

between the polar O atoms on its surface and Li-ions promoted the dissociation of both the Li salt ion pairs and the polymer-Li-ion bonds. Although this leads to a lower Li-ion transference number as the concentration of free anions increases, more charge carriers migrate in the vicinity of the fillers. Upon adding neutral Al₂O₃ particles, both of the aforementioned interactions still took place. However, the anions re-coordinated with the Li-ions to form new ion pairs, which offset the promotion of ion migration.

1 Creating concentrated defects (e.g., oxygen vacancies) is a common strategy for strengthening Lewis acid-base interactions. For instance, Y₂O₃-doped ZrO₂ nanowires have been shown to enhance LiClO₄ dissociation by generating additional oxygen vacancies, which act as strong Lewis acid sites⁵³. Similarly, using active fillers like LLZO enhances Lewis acid-base interactions through substitution, with these fillers serving as strong Lewis acid centres⁵⁴. Zhang et al. demonstrated that the synergistic coupling between La atoms in LLZTO and poly(vinylidene fluoride) (PVDF) promotes the dissociation of Li salt, thereby improving ionic conductivity⁵⁵. It should be noted that the application of Lewis acid-base theory to HSEs provides only a qualitative explanation often leaving many questions, owing to the challenges in selectively characterizing interface properties and quantitatively describing Li-ion dynamics.

Space-charge effect

In the polymer-active filler hybrid system, the improvement of ionic conductivity is also related to the formation of space-charge regions at the interfaces (**Fig. 1.2b**). When a secondary ion-conducting phase is introduced into the polymer matrix, the original conduction pathway is altered due to disrupted thermodynamic equilibrium. The differing conduction properties of the phases can induce misaligned charge carrier densities, leading to discontinuities at the interface and deviations from local electroneutrality. In the space-charge region, ion or electron migration is promoted to equalize the electrochemical potential difference between different phases.

The space-charge effect impacts ionic conduction in two ways: it creates an additional kinetic pathway, and/or affects ionic conductivity by altering the concentration of the conducting sites in nearby boundary regions. In the PEO-Ga-LLZO system, Guo et al. found that the enhanced ionic conductivity is attributed to the ion conduction in the space-charge region at the PEO-Ga-LLZO interfaces⁵⁶. When Ga-LLZO particles interact with PEO chains,

Li-ions within the Ga-LLZO lattice sites migrate to the surface sites, causing an accumulation of positive charges on the Ga-LLZO surfaces. This process establishes an equilibrium state with a high concentration of Li-ions in the interfacial space-charge region.

The space-charge effect can also be strategically utilized to improve ionic conductivity by optimizing the filler geometry. In principle, a well-aligned nanostructured filler is ideal for forming a continuous space-charge region at the polymer-filler interfaces. As a result, ion conduction occurs not only in the bulk phase but also within the more continuous space-charge regions. Additionally, a uniform mixture with a well-aligned filler aids in creating more continuous and shorter ion transport pathways. This strategy has been validated in various HSE systems. Wang et al. developed a hybrid electrolyte using vertically aligned $\text{Li}_{1.5}\text{Al}_{0.5}\text{Ge}_{1.5}(\text{PO}_4)_3$ (LAGP) fillers and PEO, while Liu et al. integrated well-oriented $\text{Li}_{0.33}\text{La}_{0.56}\text{TiO}_3$ (LLTO) nanowires into a PAN-based electrolyte^{57,58}. Other geometries, such as three-dimensional (3D) nanofibers and 3D textile ceramic fillers, have also proven effective in establishing an interconnected ion conduction network within the polymer matrix^{59,60}.

Interface between HSEs and Li-metal anode

Due to the high electropositivity and chemical reactivity of metallic Li, developing highly conductive and intimate SSE/Li-metal interfaces present three main challenges: (i) (electro)chemical reactions; (ii) Li dendrite formation; and (iii) poor contact.

Similar to liquid electrolytes, many SSEs are (electro)chemically unstable in contact with Li-metal. SPEs with polar groups (such as -OH and $\text{C}\equiv\text{N}$) in their polymer backbones are prone to reactions with Li, while ISEs may exhibit poor (electro)chemical stability due to the presence of easily reduced elements. However, hybridizing these two types of electrolytes has proven effective in mitigating their chemical reactions with Li-metal. For instance, HSEs incorporating a LATP-PAN fiber network into the PEO-LiTFSI matrix demonstrate considerably improved electrochemical stability towards Li-metal compared to pure PEO-LiTFSI, by preventing direct contact between Li and LATP⁶¹. The inorganic particles in the HSEs can also exhibit scavenging abilities that reduce the interfacial resistance between HSEs and Li-metal⁶². In addition, HSEs typically show enhanced electrochemical stability compared to their SPE components. This enhancement in anodic stability is attributed to the superior oxidative stability of the inorganic component, as well as the polymer-filler

interactions, which can modify the decomposition potential of the Li salts⁶³.

Addressing Li dendrite formation requires careful consideration of interfacial contacts. SPEs offer excellent electrode wettability but are limited by inadequate mechanical strength. ISEs provide high mechanical strength but suffer from poor adhesion to Li-metal. HSEs present a promising solution by providing an optimal balance between high mechanical strength and effective surface contact with Li-metal, thereby effectively suppressing Li dendrite growth. Another strategy is to increase the Li-ion transference number to reduce polarization effects and delay dendrite formation. Zhang et al. developed an anion-immobilized HSE composed of PEO-LiTFSI and Al-doped LLZTO⁶⁴. The TFSI⁻ anions are tethered by a polymer matrix and ceramic fillers, which enables faster Li-ion transport and promotes uniform Li deposition, thus alleviating dendrite growth.

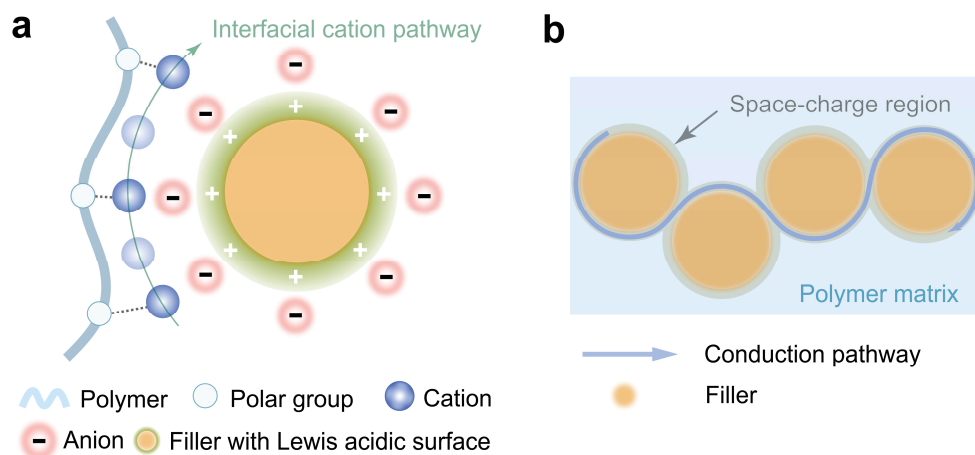


Fig. 1.2. Schematic diagram of the polymer-filler interactions in the HSEs. (a) Lewis acid-base interactions, and (b) space-charge effect between polymer and fillers.

1.4 NMR spectroscopy for Li-ion dynamics

Nuclear magnetic resonance (NMR) spectroscopy stands out in its ability to selectively and non-destructively probe the local chemical environments and ionic dynamics of specific nuclei. This makes it an indispensable technique for analyzing local structure and ionic movement across various time/length scales. Recently, with the growing popularity of LMBs, an array of solid-state NMR (ssNMR) methods have been developed to study critical factors

in the LMB system (e.g., SEI, Li dendrites), and to assess the properties of solid ionic conductors for advancing SSLMBs. This is in line with the central focus of this thesis: using ssNMR to access the structural and dynamic properties of HSEs to enable SSLMBs, starting with an in-depth study of the SEI. The structural properties can be correlated to Li-ion dynamics, providing insight into the practical application of LMBs. This section focuses on the background of Li-ion dynamics studied in this thesis using ssNMR. The theoretical principles of NMR and the relevant techniques employed in this thesis are presented in Chapter 2.

1.4.1 Interfacial Li-ion transport dynamics

Li-metal-SEI interface

It is well-recognized that constructing a favorable and efficient SEI layer is among the most effective ways to inhibit dendrite propagation and thereby improve the cycling efficiency of LMBs. In this context, NMR spectroscopy proves particularly valuable, as it can detect Li exchange at the Li-metal-SEI interfaces while also offering insights into the microscopic properties of the SEI.

To date, the NMR techniques that have been reported for tracing the interfacial Li-ion diffusion between Li and SEI include: (i) ${}^6\text{Li} \rightarrow {}^7\text{Li}$ isotope labelling; (ii) ${}^7\text{Li}$ chemical exchange saturation transfer (CEST) experiment; (iii) one-dimensional and two-dimensional (1D and 2D) exchange spectroscopy (EXSY). In 2018, Jerschow et al. demonstrated Li exchange between the electrolyte and Li-metal under open-circuit voltage conditions by immersing a ${}^6\text{Li}$ -enriched Li-metal strip in a carbonate-based electrolyte⁶⁵. This straightforward method allows for the quantification of both Li exchange and SEI formation rates. Later, in 2021, Marbella et al. employed 1D and 2D ${}^7\text{Li}$ magic angle spinning (MAS) EXSY experiments to identify and quantify chemical exchange between Li-metal and the SEI in ether-based electrolytes¹⁹. Following that, Leskes et al. applied ${}^7\text{Li}$ CEST to detect and quantify the exchange rate and energy barrier between the Li-metal and the in-situ formed SEI⁶⁶.

Combining these techniques, NMR spectroscopy has shown great potential in describing SEI properties and related diffusion processes, which can further be applied during cycling to enable the coupling of interfacial kinetics and electrochemical performance. While current

studies have primarily focused on electrolyte engineering, these techniques can also be extended to study other dynamic conditions such as current density, temperature, and pressure.

Organic/inorganic interface in HSEs

1 Li-ion transport across the organic/inorganic interface is regarded as the rate-determining step in overall Li-ion diffusion in HSEs⁵⁴. Therefore, investigating the interface structure and determining the diffusion barrier over the interfaces are crucial for developing an effective ion-conducting network in HSEs. In this context, the research from Hu's group on the PEO-LLZO hybrid system is noteworthy⁶⁷. High-resolution ⁶Li ssNMR was used to distinguish and quantify Li-ions at the interface. Further, the interfacial components were verified through ¹H→⁶Li cross polarization (CP) MAS NMR, which leverages the spatial proximity between ¹H and ⁶Li. By varying the CP contact time, the CP buildup rate can be obtained for each Li-containing component. The faster buildup observed for the interfacial Li compared to the Li in LLZO suggests that the interfacial Li is closer to the PEO phase. In addition, ⁷Li-⁷Li 2D-EXSY is used to resolve the spatial distribution of Li-ions in PEO, interface, and LLZO. Recently, these methods have also been applied to other HSE systems, such as poly(vinylidene fluoride)-Li₃Zr₂Si₂PO₁₂ (PVDF-LZSP)⁶⁸, poly(ethylene glycol) dimethyl ether-Li_(1+x)Al_xTi_(2-x)(PO₄)₃ (PEGDME-LATP)⁶⁹, and PEO-LAGP⁷⁰, demonstrating the broad applicability of these methods.

2D-EXSY is also applicable for determining the Li-ion diffusion barrier at the interfaces/interphases by performing experiments at various temperatures, as detailed in Chapters 5 and 6 of this thesis. Combining these experiments provides valuable insight into the composition and properties of the organic/inorganic interface in HSEs, which aids in identifying the Li-ion transport pathways and understanding their ion transport mechanisms.

1.4.2 Local Li-ion dynamics

While 2D-EXSY experiments are used to detect ion transfer across interphases, NMR relaxometry and line-width measurements can be specifically employed to assess intra-phase or local ion mobility in HSEs.

⁷Li spin-lattice relaxation time (T_1) measurements are commonly used to access local Li-ion motion in HSEs. Factors such as the addition of fillers or their concentrations have been studied^{71,72}, which indicate that local Li-ion mobility in the polymer phase can be

enhanced or hindered depending on the efficiency of interfacial Li-ion conduction. In addition, comparing T_1 values at different temperatures within the same sample provides further insights into Li-ion dynamics by revealing temperature-dependent dynamic behaviors, such as activation energies for ion motion or phase transitions that affect ion mobility.

Li-ions are present in various chemical environments within HSEs. T_1 relaxation measurements enable the distinct characterization of T_1 values for each environment, allowing for the assessment of the impact of organic-inorganic interactions on each phase. This technique can also be used to evaluate how different fillers, salt concentrations, and preparation methods affect local Li-ion mobility.

Another approach to studying local ion dynamics is the line-width measurement. In contrast to relaxometry, which operates on a nanosecond time scale, line-width analysis probes ion behavior over a longer range on the microsecond time frame (**Fig. 1.3**). In polymer electrolytes, motional narrowing of the peak shape is closely related to the T_g . Jeon et al. studied Li-ion motion in a P(EO-EC)-LiCF₃SO₃ polymer electrolyte by measuring the line-width of the central ⁷Li transition as a function of temperature⁷³. Their results revealed two distinct Arrhenius regions, below and above T_g , each with different slopes. The obtained activation energies are consistent with the ionic conductivity data. This correlation between T_g and line narrowing behavior underscores the utility of line-width measurements in probing phase fractions and transitions within the polymer matrix of HSEs.

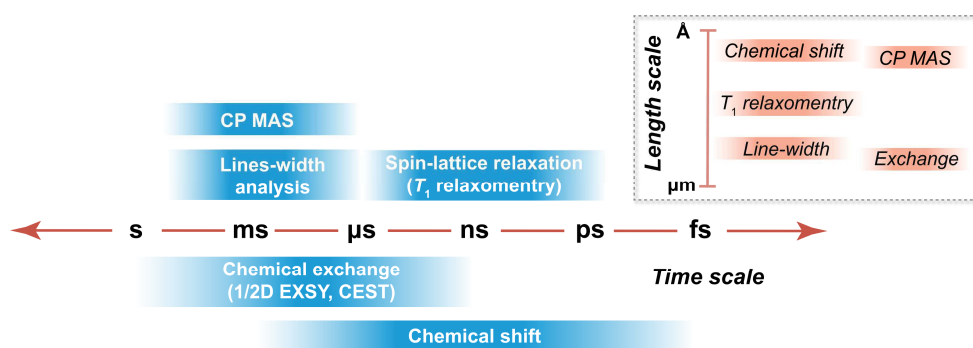


Fig. 1.3. Time and length scales of the ssNMR techniques for studying interfacial and local Li-ion dynamics.

1.5 Thesis outline and goals

The main objective of this thesis is to formulate a microscopic picture of Li-ion diffusion and its correlation with the macroscopic battery performance. Specifically, the research focus begins with an in-depth analysis of Li-ion diffusion across Li-SEI interfaces in a standard liquid electrolyte system. This approach was then extended to the HSEs system with the aim of enabling SSLMBs. The correlation between structure and spontaneous Li-ion diffusion at various length scales in the HSEs was investigated. To achieve this, ssNMR was chosen as the main technique due to its sensitivity to specific nuclei and capability to serve as a local probe across different length and time scales. Therefore, Chapter 2 is added to give a general overview of the NMR technique and a brief introduction to the relevant methods used in this thesis.

1.5.1 Connecting Li exchange with SEI properties

The structure and properties of the SEI are crucial for controlling the morphology of deposited Li and achieving high-efficiency LMBs, with their formation being highly dependent on the electrochemical protocols used during formation cycles. To gain a fundamental understanding of the underlying mechanism, a key aspect is accessing the ionic permeability of the SEI formed under different formation cycling conditions. In **Chapter 3** a systematic study is conducted on electrochemical formation protocols and their impact on subsequent cycling. By correlating Li-metal cyclability with Li-ion kinetics across various Li-SEI interfaces and the as-formed SEI structure and components, a picture of SEI formation protocols and their impact on practical performance metrics in LMBs is presented. When applying an intermediate high current density in the formation process, the energy barrier for Li-ion diffusion across the Li-SEI interface is minimized. The observed faster charge-transfer kinetics are attributed to the formation of a more compact SEI that is richer in inorganic components. By studying the evolution of this dynamic process through further cycling and correlating it with electrochemical rechargeability, the “template effect” of the initially formed SEI is identified. This chapter presents opportunities of improving the stability and cycling efficiency of LMBs by tailoring formation protocols.

1.5.2 Structure-ion dynamics relationship in hybrid solid electrolytes

The ion dynamics within the HSE system, comprising a PEO-LiTFSI polymeric matrix and argyrodite $\text{Li}_6\text{PS}_5\text{Cl}$ fillers, have been studied from local, interfacial, and macroscopic perspectives. The specific structures, including those of the polymer and the organic/inorganic interfaces, have been correlated to these dynamics. These studies are complementary, yet focus on different aspects, collectively they provide a more comprehensive understanding of the structure-ion dynamics relationship in HSEs.

In **Chapter 4**, insight into local Li-ion diffusivity in the PEO-LiTFSI- $\text{Li}_6\text{PS}_5\text{Cl}$ hybrid system, with a specific focus on the polymer phase, are presented based on line-width and spin-lattice relaxation NMR measurements. Compared to the pure (non-filled) polymer electrolyte, incorporating fillers has been shown to enhance local Li-ion diffusion kinetics in the polymer phase, and introduce additional relaxation behavior at low temperatures. This indirectly reflects the polymer-filler interactions, which increase the chain mobility and alter the polymer configuration. Additionally, the second relaxation component indicates potential Li-ion conduction pathways at the polymer-filler interfaces at low temperatures. In comparing the preparation methods (solvent-assisted and dry-mixing), the morphology and heterogeneous nature of the HSEs are also studied. By correlating these local ion dynamics with macroscopic ion conduction and extending the analysis to the Li/HSE interfaces, a clearer picture of how polymer-filler interactions affect the HSEs is obtained, providing valuable insight for optimizing the performance and reliability in practical applications.

While local Li-ion dynamics centers on intra-phase behavior, the study of interfacial Li-ion diffusion focuses on interphase dynamics. A key aspect of building a percolating ion-conduction network in HSEs is to enable ion transport through multiple phases, i.e., the organic matrix, the inorganic filler, and the interface between the organic and inorganic components. To achieve this, effective interfacial Li-ion transport is essential for attaining the desired ionic conductivity necessary for practical battery operation. In **Chapter 5**, the organic/inorganic interface structure and interfacial Li-ion transport in the HSEs are investigated. Using multinuclear ssNMR as a probe, the organic/inorganic interface is found to be inactive or limited in ion-conduction due to the side reactions between the two ion conductors, which leads to the accumulation of by-products. To improve interfacial Li-ion transport, an ionic liquid additive is introduced, which settles at the interface due to its poor

miscibility with the PEO matrix. As a result, the overall ionic conductivity improved significantly, enabling the cycling of LiFePO_4 -Li-metal cells at room temperature with a Coulombic efficiency of 99.9%. This study identifies the bottleneck for Li-ion transport in HSEs and proposes new strategies for interface engineering.

Having established the understanding of local and interfacial Li-ion dynamics in the HSEs, a detailed study of the polymer structure and its relationship with ion dynamics within the above HSE system is presented in **Chapter 6**. Here, using LiI as a functional additive ‘activates’ the aforementioned inert interface between PEO-LiTFSI and $\text{Li}_6\text{PS}_5\text{Cl}$, leading to a noticeable increase in overall ionic conductivity. Diving deep into both the macroscopic and local structures reveals that incorporating LiI results in a more Li-ion conductive environment, characterized by altered carbon configuration of the PEO chains, improved Li salt dissociation, and enhanced proton kinetics. This study disentangles the relationship between bulk and interface structures in the complex hybrid system, offering important insights into how the bulk structure affects the interfaces. In addition, adding LiI improves compatibility with the Li-metal anode, enabling the operation of all-solid-state Li-sulfur batteries. These improvements are a combination of the increased Li-ion conductivity, improved mechanical strength, and higher electrochemical stability of the HSEs. Understanding the structure-ion dynamics relationship is crucial for elucidating these correlations.

References

1. Yu, Y., Liu, Y. & Xie, J. Building better Li metal anodes in liquid electrolyte: challenges and progress. *ACS Applied Materials & Interfaces* **13**, 18–33 (2021).
2. Cheng, X.-B., Zhang, R., Zhao, C.-Z. & Zhang, Q. Toward safe lithium metal anode in rechargeable batteries: A Review. *Chemical Reviews* **117**, 10403–10473 (2017).
3. Xu, W., Wang, J., Ding, F., Chen, X., Nasybulin, E., Zhang, Y. & Zhang, J. G. (2014). Lithium metal anodes for rechargeable batteries. *Energy & Environmental Science* **7**, 513–537 (2014).
4. Cheng, X. B., Zhang, R., Zhao, C. Z., Wei, F., Zhang, J. G. & Zhang, Q. A review of solid electrolyte interphases on lithium metal anode. *Advanced Science* **3**, 1500213 (2016).
5. Jagger, B. & Pasta, M. Solid electrolyte interphases in lithium metal batteries. *Joule* **7**, 1–17 (2023).
6. Wu, H., Jia, H., Wang, C., Zhang, J. & Xu, W. Recent progress in understanding solid electrolyte interphase on lithium metal anodes. *Advanced Energy Materials* **11**, 2003092 (2021).
7. Svirinovsky Arbeli, A., Juelsholt, M., May, R., Kwon, Y. & Marbella, L. E. Using NMR spectroscopy to link structure to function at the Li solid electrolyte interphase. *Joule* **8**, 1919–1935 (2024).
8. Wang, C., Wang, A., Ren, L., Guan, X., Wang, D., Dong, A. & Luo, J. Controlling Li Ion flux through materials innovation for dendrite-free lithium metal anodes. *Advanced Functional Materials* **29**, 1905940 (2019).
9. Lin, D., Liu, Y. & Cui, Y. Reviving the lithium metal anode for high-energy batteries. *Nature nanotechnology* **12**, 194–206 (2017).
10. Wang, H., Yu, Z., Kong, X., Kim, S. C., Boyle, D. T., Qin, J. & Cui, Y. Liquid electrolyte: The nexus of practical lithium metal batteries. *Joule* **6**, 588–616 (2022).
11. Zhang, Y., Zuo, T. T., Popovic, J., Lim, K., Yin, Y. X., Maier, J. & Guo, Y. G. Towards better Li metal anodes: Challenges and strategies. *Materials Today* **33**, 56–74 (2020).
12. Oyakhire, S. T., Zhang, W., Yu, Z., Holmes, S. E., Sayavong, P., Kim, S. C. & Bent, S. F. Correlating the formation protocols of solid electrolyte interphases with practical performance metrics in lithium metal batteries. *ACS Energy Letters* **8**, 869–877 (2023).
13. Boyle, D. T., Kong, X., Pei, A., Rudnicki, P. E., Shi, F., Huang, W. & Cui, Y. Transient voltammetry with ultramicroelectrodes reveals the electron transfer kinetics of lithium metal anodes. *ACS Energy Letters* **5**, 701–709 (2020).
14. Tao, R., Bi, X., Li, S., Yao, Y., Wu, F., Wang, Q. & Lu, J. Kinetics Tuning the electrochemistry of lithium dendrites formation in lithium batteries through electrolytes. *ACS Applied Materials & Interfaces* **9**, 7003–7008 (2017).

15. Boyle, D. T., Kim, S. C., Oyakhire, S. T., Vilá, R. A., Huang, Z., Sayavong, P. & Cui, Y. Correlating kinetics to cyclability reveals thermodynamic origin of lithium anode morphology in liquid electrolytes. *Journal of the American Chemical Society* **144**, 20717–20725 (2022).
16. Ko, S., Obukata, T., Shimada, T., Takenaka, N., Nakayama, M., Yamada, A. & Yamada, Y. Electrode potential influences the reversibility of lithium-metal anodes. *Nature Energy* **7**, 1217–1224 (2022).
17. Hobold, G. M., Kim, K.-H. & Gallant, B. M. Beneficial vs. inhibiting passivation by the native lithium solid electrolyte interphase revealed by electrochemical Li⁺ exchange. *Energy & Environmental Science* **16**, 2247–2261 (2023).
18. Columbus, D., Arunachalam, V., Glang, F., Avram, L., Haber, S., Zohar, A. & Leskes, M. (2022). Direct detection of lithium exchange across the solid electrolyte interphase by ⁷Li chemical exchange saturation transfer. *Journal of the American Chemical Society* **144**, 9836–9844 (2022).
19. May, R., Fritzsche, K. J., Livitz, D., Denny, S. R. & Marbella, L. E. Rapid interfacial exchange of Li ions dictates high coulombic efficiency in Li metal anodes. *ACS Energy Letters* **6**, 1162–1169 (2021).
20. Xu, Y., Wu, H., Jia, H., Zhang, J. G., Xu, W. & Wang, C. Current density regulated atomic to nanoscale process on Li deposition and solid electrolyte interphase revealed by cryogenic transmission electron microscopy. *ACS Nano* **14**, 8766–8775 (2020).
21. Pei, A., Zheng, G., Shi, F., Li, Y. & Cui, Y. Nanoscale nucleation and growth of electrodeposited lithium metal. *Nano Letters* **17**, 1132–1139 (2017).
22. Chen, X. R., Yao, Y. X., Yan, C., Zhang, R., Cheng, X. B. & Zhang, Q. A Diffusion–reaction competition mechanism to tailor lithium deposition for lithium-metal batteries. *Angewandte Chemie International Edition* **59**, 7743–7747 (2020).
23. Liu, Y., Xu, X., Sadd, M., Kapitanova, O. O., Krivchenko, V. A., Ban, J. & Matic, A. Insight into the critical role of exchange current density on electrodeposition behavior of lithium metal. *Advanced Science* **8**, 2003301 (2021).
24. Su, C. C., He, M., Shi, J., Amine, R., Zhang, J. & Amine, K. Solvation rule for solid-electrolyte interphase enabler in lithium-metal batteries. *Angewandte Chemie International Edition* **59**, 18229–18233 (2020).
25. Cao, X., Ren, X., Zou, L., Engelhard, M. H., Huang, W., Wang, H. & Zhang, J. G. Monolithic solid–electrolyte interphases formed in fluorinated orthoformate-based electrolytes minimize Li depletion and pulverization. *Nature Energy* **4**, 796–805 (2019).
26. Huang, W., Wang, H., Boyle, D. T., Li, Y. & Cui, Y. Resolving nanoscopic and mesoscopic heterogeneity of fluorinated species in battery solid-electrolyte interphases by cryogenic electron microscopy. *ACS Energy Letters* **5**, 1128–1135 (2020).
27. Tan, S., Kuai, D., Yu, Z., Perez-Beltran, S., Rahman, M. M., Xia, K. & Hu, E. Evolution and interplay of lithium metal interphase components revealed by experimental and theoretical studies. *Journal of the American Chemical Society* **146**, 11711–11718 (2024).

28. Ren, X., Zou, L., Cao, X., Engelhard, M. H., Liu, W., Burton, S. D. & Xu, W. Enabling high-voltage lithium-metal batteries under practical conditions. *Joule* **3**, 1662–1676 (2019).
29. Zeng, H., Yu, K., Li, J., Yuan, M., Wang, J., Wang, Q. & Chi, S. S. Beyond LiF: tailoring Li_2O -dominated solid electrolyte interphase for stable lithium metal batteries. *ACS nano* **18**, 1969–1981 (2024).
30. Zhao, Y., Zhou, T., Jeurgens, L. P., Kong, X., Choi, J. W. & Coskun, A. Electrolyte engineering for highly inorganic solid electrolyte interphase in high-performance lithium metal batteries. *Chem* **9**, 682–697 (2023).
31. Zheng, G., Xiang, Y., Chen, S., Ganapathy, S., Verhallen, T. W., Liu, M. & Yang, Y. Additives synergy for stable interface formation on rechargeable lithium metal anodes. *Energy Storage Materials* **29**, 377–385 (2020).
32. Zhao, Q., Chen, P., Li, S., Liu, X. & Archer, L. A. Solid-state polymer electrolytes stabilized by task-specific salt additives. *Journal of Materials Chemistry A* **7**, 7823–7830 (2019).
33. Xia, S., Wu, X., Zhang, Z., Cui, Y. & Liu, W. Practical challenges and future perspectives of all-solid-state lithium-metal batteries. *Chem* **5**, 753–785 (2019).
34. Liu, J., Yuan, H., Liu, H., Zhao, C. Z., Lu, Y., Cheng, X. B. & Zhang, Q. Unlocking the failure mechanism of solid state lithium metal batteries. *Advanced Energy Materials* **12**, 2100748 (2022).
35. Zhao, Q., Stalin, S., Zhao, C.-Z. & Archer, L. A. Designing solid-state electrolytes for safe, energy-dense batteries. *Nature Reviews Materials* **5**, 229–252 (2020).
36. Li, Z., Fu, J., Zhou, X., Gui, S., Wei, L., Yang, H. & Guo, X. Ionic conduction in polymer-based solid electrolytes. *Advanced Science* **10**, 2201718 (2023).
37. Zhang, D., Meng, X., Hou, W., Hu, W., Mo, J., Yang, T. & Li, M. Solid polymer electrolytes: Ion conduction mechanisms and enhancement strategies. *Nano Research Energy* **2**, e9120050 (2023).
38. Cheng, Z., Liu, T., Zhao, B., Shen, F., Jin, H. & Han, X. Recent advances in organic-inorganic composite solid electrolytes for all-solid-state lithium batteries. *Energy Storage Materials* **34**, 388–416 (2021).
39. Murugan, R., Thangadurai, V. & Weppner, W. Fast lithium ion conduction in garnet-type $\text{Li}_7\text{La}_3\text{Zr}_2\text{O}_{12}$. *Angewandte Chemie International Edition* **46**, 7778–7781 (2007).
40. Liu, S., Liu, W., Ba, D., Zhao, Y., Ye, Y., Li, Y. & Liu, J. Filler-integrated composite polymer electrolyte for solid-state lithium batteries. *Advanced Materials* **35**, 2110423 (2022).
41. Thangadurai, V., Narayanan, S. & Pinzaru, D. Garnet-type solid-state fast Li ion conductors for Li batteries: critical review. *Chemical Society Reviews* **43**, 4714 (2014).
42. Zhang, B., Tan, R., Yang, L., Zheng, J., Zhang, K., Mo, S. & Pan, F. Mechanisms and properties of ion-transport in inorganic solid electrolytes. *Energy Storage Materials* **10**,

139–159 (2018).

43. Vu, T. T., Cheon, H. J., Shin, S. Y., Jeong, G., Wi, E. & Chang, M. Hybrid electrolytes for solid-state lithium batteries: Challenges, progress, and prospects. *Energy Storage Materials* **61**, 102876 (2023).
44. Zhang, Q., Cao, D., Ma, Y., Natan, A., Aurora, P. & Zhu, H. Sulfide-based solid-state electrolytes: synthesis, stability, and potential for all-solid-state batteries. *Advanced Materials* **31**, 1901131 (2019).
45. Zhou, L., Minafra, N., Zeier, W. G. & Nazar, L. F. Innovative approaches to li-argyrodite solid electrolytes for all-solid-state lithium batteries. *Accounts of Chemical Research* **54**, 2717–2728 (2021).
46. Huo, H., Chen, Y., Luo, J., Yang, X., Guo, X. & Sun, X. Rational design of hierarchical “ceramic-in-polymer” and “polymer-in-ceramic” electrolytes for dendrite-free solid-state batteries. *Advanced Energy Materials* **9**, 1804004 (2019).
47. Quartarone, E. & Mustarelli, P. Electrolytes for solid-state lithium rechargeable batteries: recent advances and perspectives. *Chemical Society Reviews* **40**, 2525 (2011).
48. Stoeva, Z., Martin-Litas, I., Staunton, E., Andreev, Y. G. & Bruce, P. G. Ionic conductivity in the crystalline polymer electrolytes PEO₆:LiXF₆, X = P, As, Sb. *Journal of the American Chemical Society* **125**, 4619–4626 (2003).
49. Famprikis, T., Canepa, P., Dawson, J. A., Islam, M. S. & Masquelier, C. Fundamentals of inorganic solid-state electrolytes for batteries. *Nature Materials* **18**, 1278–1291 (2019).
50. Mehrer, H. Diffusion in solids: fundamentals, methods, materials, diffusion-controlled processes. *Springer*, Berlin New York (2007).
51. Bunde, A. & Dieterich, W. Percolation in composites. *Journal of Electroceramics* **5**, 81–92 (2000).
52. Croce, F., Persi, L., Scrosati, B., Serraino-Fiory, F., Plichta, E. & Hendrickson, M. A. Role of the ceramic fillers in enhancing the transport properties of composite polymer electrolytes. *Electrochimica Acta* **46**, 2457–2461 (2001).
53. Liu, W., Lin, D., Sun, J., Zhou, G. & Cui, Y. Improved lithium ionic conductivity in composite polymer electrolytes with oxide-ion conducting nanowires. *ACS Nano* **10**, 11407–11413 (2016).
54. Keller, M., Varzi, A. & Passerini, S. Hybrid electrolytes for lithium metal batteries. *Journal of Power Sources* **392**, 206–225 (2018).
55. Zhang, X., Liu, T., Zhang, S., Huang, X., Xu, B., Lin, Y. & Shen, Y. Synergistic coupling between Li_{6.75}La₃Zr_{1.75}Ta_{0.25}O₁₂ and poly (vinylidene fluoride) induces high ionic conductivity, mechanical strength, and thermal stability of solid composite electrolytes. *Journal of the American Chemical Society* **139**, 13779–13785 (2017).
56. Li, Z., Huang, H. M., Zhu, J. K., Wu, J. F., Yang, H., Wei, L. & Guo, X. Ionic conduction in composite polymer electrolytes: case of PEO:Ga-LLZO Composites. *ACS Applied Materials & Interfaces* **11**, 784–791 (2019).

57. Liu, W., Lee, S. W., Lin, D., Shi, F., Wang, S., Sendek, A. D. & Cui, Y. Enhancing ionic conductivity in composite polymer electrolytes with well-aligned ceramic nanowires. *Nature Energy* **2**, 17035 (2017).
58. Wang, X., Zhai, H., Qie, B., Cheng, Q., Li, A., Borovilas, J. & Yang, Y. Rechargeable solid-state lithium metal batteries with vertically aligned ceramic nanoparticle/polymer composite electrolyte. *Nano Energy* **60**, 205–212 (2019).
59. Gong, Y., Fu, K., Xu, S., Dai, J., Hamann, T. R., Zhang, L. & Wachsman, E. D. Lithium-ion conductive ceramic textile: A new architecture for flexible solid-state lithium metal batteries. *Materials Today* **21**, 594–601 (2018).
60. Fu, K., Gong, Y., Dai, J., Gong, A., Han, X., Yao, Y. & Hu, L. Flexible, solid-state, ion-conducting membrane with 3D garnet nanofiber networks for lithium batteries. *Proceedings of the National Academy of Sciences* **113**, 7094–7099 (2016).
61. Li, D., Chen, L., Wang, T. & Fan, L.-Z. 3D Fiber-network-reinforced bicontinuous composite solid electrolyte for dendrite-free lithium metal batteries. *ACS Applied Materials & Interfaces* **10**, 7069–7078 (2018).
62. Keller, M., Appetecchi, G. B., Kim, G. T., Sharova, V., Schneider, M., Schuhmacher, J. & Passerini, S. Electrochemical performance of a solvent-free hybrid ceramic-polymer electrolyte based on $\text{Li}_7\text{La}_3\text{Zr}_2\text{O}_{12}$ in $\text{P}(\text{EO})_{15}\text{LiTFSI}$. *Journal of Power Sources* **353**, 287–297 (2017).
63. Zhao, Y., Huang, Z., Chen, S., Chen, B., Yang, J., Zhang, Q. & Xu, X. A promising PEO/LAGP hybrid electrolyte prepared by a simple method for all-solid-state lithium batteries. *Solid State Ionics* **295**, 65–71 (2016).
64. Zhao, C. Z., Zhang, X. Q., Cheng, X. B., Zhang, R., Xu, R., Chen, P. Y. & Zhang, Q. An anion-immobilized composite electrolyte for dendrite-free lithium metal anodes. *Proceedings of the National Academy of Sciences* **114**, 11069–11074 (2017).
65. Ilott, A. J. & Jerschow, A. Probing solid-electrolyte interphase (sei) growth and ion permeability at undriven electrolyte–metal interfaces using ^7Li NMR. *The Journal of Physical Chemistry C* **122**, 12598–12604 (2018).
66. Columbus, D., Arunachalam, V., Glang, F., Avram, L., Haber, S., Zohar, A. & Leskes, M. Direct detection of lithium exchange across the solid electrolyte interphase by ^7Li chemical exchange saturation transfer. *Journal of the American Chemical Society* **144**, 9836–9844 (2022).
67. Zheng, J., Tang, M. & Hu, Y.-Y. Lithium ion pathway within $\text{Li}_7\text{La}_3\text{Zr}_2\text{O}_{12}$ -polyethylene oxide composite electrolytes. *Angewandte Chemie International Edition* **55**, 12538–12542 (2016).
68. Zhu, L., Chen, J., Wang, Y., Feng, W., Zhu, Y., Lambregts, S. F. & Xia, Y. Tunneling interpenetrative lithium ion conduction channels in polymer-in-ceramic composite solid electrolytes. *Journal of the American Chemical Society* **146**, 6591–6603 (2024).
69. Boaretto, N., Ghorbanzade, P., Perez-Furundarena, H., Meabe, L., Lopez del Amo, J. M., Gunathilaka, I. E. & Martinez-Ibañez, M. Transport properties and local ions dynamics

in LATP-based hybrid solid electrolytes. *Small* **20**, 2305769 (2023).

70. Liu, M., Cheng, Z., Ganapathy, S., Wang, C., Haverkate, L. A., Tułodziecki, M. & Wagemaker, M. Tandem interface and bulk li-ion transport in a hybrid solid electrolyte with microsized active filler. *ACS Energy Letters* **4**, 2336–2342 (2019).
71. Wu, N., Chien, P. H., Qian, Y., Li, Y., Xu, H., Grundish, N. S. & Goodenough, J. B. Enhanced surface interactions enable fast Li⁺ conduction in oxide/polymer composite electrolyte. *Angewandte Chemie International Edition* **59**, 4131–4137 (2020).
72. Zheng, J. & Hu, Y.-Y. New Insights into the Compositional Dependence of li-ion transport in polymer–ceramic composite electrolytes. *ACS Applied Materials & Interfaces* **10**, 4113–4120 (2018).
73. Jeon, J.-D. & Kwak, S.-Y. Variable-temperature ⁷Li Solid-state NMR investigation of Li-ion mobility and its correlation with conductivity in pore-filling polymer electrolytes for secondary batteries. *Macromolecules* **39**, 8027–8034 (2006).

2

Solid-state Nuclear Magnetic Resonance Spectroscopy

“工欲善其事，必先利其器”

“To do a good job, one must first sharpen his tools.”

《论语·卫灵公》(The Analects)

Solid-state NMR is a powerful tool for accessing the structure and dynamics of battery materials, as summarized in some recent reviews¹⁻⁴. In this chapter, a brief introduction to the basic theory and signal detection of NMR is provided in sections 2.1, 2.2, and 2.3, followed by an overview of the experimental NMR techniques relevant to this thesis in section 2.4. The goal is to offer foundational information and practical insights into these methods. It is hoped that this chapter will help steepen the learning curve and inspire other battery scientists who are new to these techniques.

2.1 The principle of NMR

Nuclei with a non-zero spin quantum number ($I \neq 0$) inherently possess a magnetic moment, rendering them accessible to NMR spectroscopy. Upon application of an external magnetic field, B_0 , the ground state energy of a nucleus with spin I experiences Zeeman splitting, resulting in the separation into $2I + 1$ equidistant energy levels. For nuclei such as ^1H and ^{13}C with $I = 1/2$, this splitting produces two distinct energy states corresponding to the magnetic quantum numbers $m_I = \pm 1/2$ (**Fig. 2.1**).

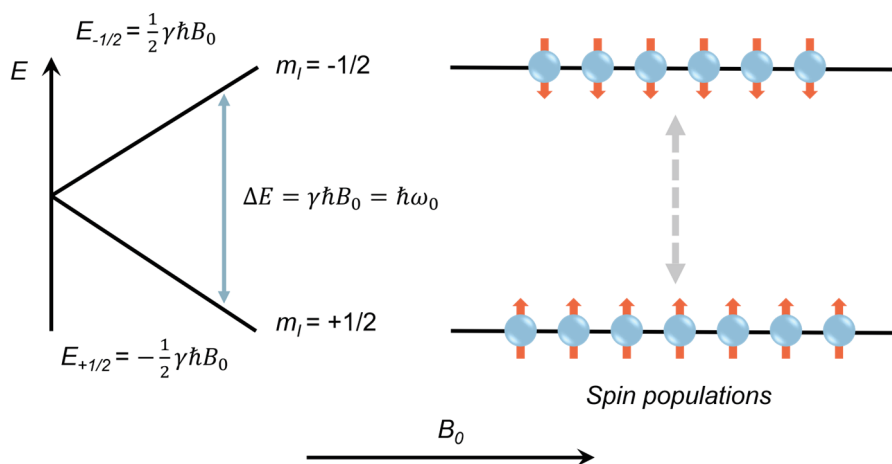


Fig. 2.1 Schematic representations of Zeeman interaction and spin populations. For a half spin nucleus with positive gyromagnetic ratio γ .

In equilibrium, the distribution of energy states follows a Boltzmann distribution, leading to a slight excess of spins in the lower energy state (N_I) compared to the higher energy

state (N_2)⁵. The probability of being in each state is given by:

$$P_i = \frac{\exp\left(-\frac{E_i}{k_B T}\right)}{\exp\left(-\frac{E_1}{k_B T}\right) + \exp\left(-\frac{E_2}{k_B T}\right)} \quad (2.1)$$

where E_i is the energy of state i , k_B is the Boltzmann constant and T is the absolute temperature in Kelvin. As such, when an external magnetic field is applied, the ratio of the populations between two energy levels can be expressed as:

$$\frac{N_2}{N_1} = \frac{P_2}{P_1} = \exp\left(-\frac{\Delta E}{k_B T}\right) = \exp\left(-\frac{\gamma \hbar B_0}{k_B T}\right) \quad (2.2)$$

where ΔE represents the energy difference between the spin states, given by $\Delta E = \gamma \hbar B_0$, with γ being the gyromagnetic ratio that is specific for each nucleus, and \hbar the reduced Planck's constant.

In the presence of applied external magnetic field B_0 , the interaction between the nuclear magnetic moment μ and B_0 induces a torque, resulting in μ to precess around the direction of B_0 . This process is called Larmor precession. The frequency of this precession is associated with the energy transition ΔE , which corresponds to γB_0 , the natural precession frequency of a spin, known as the Larmor frequency, ω_0 (rad s⁻¹). Therefore, it gives:

$$\Delta E = \gamma \hbar B_0 = \hbar \omega_0 \quad (2.3)$$

This implies that every magnetic field can be expressed with a corresponding frequency.

2.2 NMR signal detection via one-pulse measurement

The one-pulse (also known as single-pulse or 90° pulse) NMR experiment is the most basic pulse acquisition technique in NMR. Typically, a radio frequency (RF) pulse is applied to generate a magnetic field (B_1) perpendicular to the applied magnetic field B_0 . When the RF transmitter matches the Larmor frequency, the system reaches resonance, prompting the nuclei to absorb energy and flip their spins to a higher energy state⁶. In principle, the NMR signal arises from the difference between the energy absorbed by spins transitioning from the lower energy state to the higher one, and the energy emitted by spins simultaneously

transitioning from the higher energy state to the lower one. Therefore, the signal is directly proportional to the population difference between these states. Despite the small population differences, NMR can detect these subtle variations due to its high sensitivity stemming from resonance.

When the RF pulse is properly calibrated, it rotates the net magnetization vector from the z -axis (the direction of the external magnetic field) into the transverse plane (xy -plane). Following the pulse, the nuclear spins relax back to equilibrium and precess within the xy -plane (**Fig. 2.2**). This precession of the net magnetization induces an oscillating current in the RF coil, which is recorded by the NMR receiver as a free induction decay (FID) signal. Applying a Fourier transform to convert this time-domain signal into a frequency-domain signal yields the characteristic NMR spectrum (shown in the dotted box in **Fig. 2.2**). From this spectrum, valuable information can be obtained by analyzing peak positions (chemical shifts), which indicate the local chemical environment of the nuclei, peak broadening/splitting, which reveals interactions between nearby nuclei (see Section 2.3), and peak intensities, which reflect the amount of equivalent nuclei.

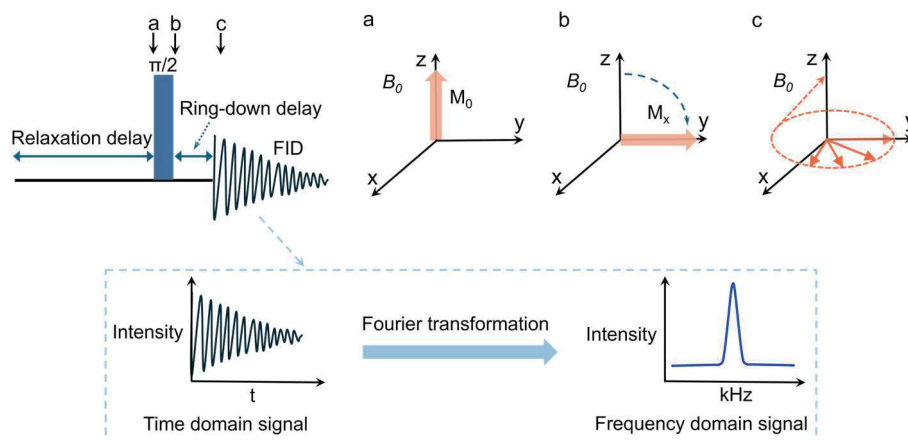


Fig. 2.2. Pulse sequence for the one-pulse measurement. Schematic showing the positions of the magnetization vectors at three time points (a, b and c) in the pulse sequence. The relaxation delay is the time allotted for nuclear spins to fully return to thermal equilibrium between successive scans. The ring-down delay is the time period for the receiver to recover from the strong RF pulse and stabilize to accurately detect the weak NMR signal. FID (free induction decay) is the decaying signal from the excited nuclear spins, which provides the data for generating the NMR spectrum via Fourier transformation, as shown in the dotted box.

Accurate flip angles are crucial in NMR experiments to achieve optimal signal intensity. For instance, a 90° pulse provides the maximum signal strength. Thus, it is imperative that the RF pulse be precisely calibrated and sufficiently strong to flip off-resonant peaks by $\sim 90^\circ$, especially when measuring a broad spectrum. The flip angle β (in radians) is given by $\beta = \omega_1 t_p$, where ω_1 is the RF field strength and t_p is the duration of the applied RF pulse. Once a hard or soft pulse (a “hard pulse” is a strong, non-selective RF pulse that excites all nuclei, while a “soft pulse” is weaker and selectively targets specific nuclei) has been selected, the pulse duration can be finely tuned to ensure that the target peak is on-resonance. It should be noted that in systems with multiple resonances, it is essential to recognize that different chemical environments may necessitate distinct t_p values to reach their optimal signal intensity. In the HSE systems, one-pulse NMR experiments are crucial for elucidating critical aspects such as the chemical environment, ion coordination, solvation degree, phase composition (e.g., crystalline and amorphous regions of PEO), and the local structure and dynamics (via line-shape and line-width analysis).

2.3 Interactions in NMR

Although Equation (2.3) predicts that nuclei of the same isotope should resonate at a single Larmor frequency, NMR spectra typically display multiple resonances at various frequencies. This variation arises because nuclear spins are influenced not just by the external magnetic field but also by other interactions. These include the magnetic fields generated by the movement of surrounding electrons (chemical shielding), interactions with neighboring nuclear spins (dipole coupling via space, and J coupling via chemical bonds), and, for nuclei with $I > 1/2$, interactions with electric field gradients (through quadrupole coupling). These interactions, acting as perturbations to the Zeeman splitting, offer detailed insight into the nuclei’s environment.

Chemical shielding and anisotropy

When an external magnetic field B_0 is applied to a nucleus, it induces the circulation of surrounding electrons. This in turn, generates a local magnetic field that opposes B_0 . As a result, the effective local magnetic field B_{eff} experienced by the nucleus is given by:

$$B_{eff} = (1 - \sigma)B_0 \quad (2.4)$$

where σ is the shielding constant that accounts for the local shielding effects. A complete mathematical description of chemical shielding involves the chemical shielding tensor⁶, which accounts for the anisotropy of the electronic environment around the nucleus.

Differences in the local chemical environments surrounding nuclei lead to variations in their resonance frequencies, due to the differing degrees of shielding experienced by each nucleus. This phenomenon, known as the chemical shift (δ), makes NMR a sensitive probe of molecular structure and chemical environment. The magnitude of the chemical shift is influenced by factors such as the chemical bonding, molecular structure, and the presence of electronegative atoms, which can cause resonant peaks to shift upfield or downfield, indicating variations in the electronic environment around the nucleus. As an example, in this thesis it is seen that adding the LiI additive to the HSE results in a downfield shift of the ${}^7\text{Li}$ ($I = 3/2$) resonance in the polymer phase, signifying a reduction in electron density around the Li nucleus. This shift is attributed to the strong electronegativity of the iodide anions (I^-), which withdraw electron density from the Li nucleus, thereby inducing a de-shielding effect. This shift gives direct insight into the interaction between Li^+ and I^- , as well as the coordination environment of Li within the polymer matrix.

For most molecules, the chemical shift varies with the orientation of the molecule relative to the applied magnetic field, a phenomenon known as chemical shift anisotropy (CSA, **Fig. 2.3a**). In liquid samples, this effect is averaged out due to rapid molecular tumbling, resulting in an isotropic shift. In contrast, powder samples, composed of crystals with varying orientations, typically produce broad spectra with sharp edges. This broadening occurs because the spectrum is a superposition of resonances from each individual crystal, a pattern referred to as the powder pattern.

Dipolar interaction

While chemical shielding results from interactions between nuclei and surrounding electrons, nuclei can also interact directly (via dipole coupling) or indirectly (via J coupling) through bonding electrons. Here, the focus is on dipole coupling, as J coupling is less relevant to solid ion conductors.

Magnetic dipole interactions arise from the coupling between two nuclear spins, typically through space (**Fig. 2.3b**). One nucleus generates a magnetic field, while the other experiences it, with these roles being interchangeable. Therefore, the interaction is inherently a property of the pair of nuclei involved. The magnitude of this through-space dipolar interaction (in rad s^{-1}) between two nuclear spins, I and S , can be expressed as:

$$d_{IS} = -\frac{1}{2} \frac{\mu_0 \gamma_I \gamma_S \hbar}{4\pi r_{IS}^3} (3\cos^2\theta - 1) \quad (2.5)$$

where γ_I and γ_S are the gyromagnetic ratios of the two nuclei, r_{IS} is the distance between them, μ_0 is the magnetic constant, and θ is the angle between the internuclear vector and the applied magnetic field B_0 . Thus, dipole coupling is most intense for spins in close spatial proximity and diminishes rapidly with increasing distance between them. This interaction can be used as a direct spectroscopic tool for probing interatomic and internuclear distances.

The relaxation resulting from dipolar interactions is proportional to the square of the coupling strength ($\gamma_I^2 \gamma_S^2 \frac{1}{r_{IS}^6}$). Therefore, nuclear pairs with high gyromagnetic ratios are the most effective in promoting relaxation⁵. For instance, all other factors being equal, a ^1H - ^1H pair will relax 16 times faster than a ^{13}C - ^1H pair ($\gamma_{\text{H}}/\gamma_{\text{C}} \approx 4$). Dipole couplings can occur between identical (homonuclear) or different (heteronuclear) NMR-active nuclei, which also enables many multidimensional NMR experiments.

Quadrupolar interaction

Nuclei with spin greater than $\frac{1}{2}$ possess a quadrupolar moment, leading to strong interactions with the electric field gradient (EFG) created by the asymmetric charge distribution, which results in distinct central and satellite transitions in the NMR spectra (**Fig. 2.3c**). The quadrupolar coupling is mainly an intramolecular interaction.

In NMR for solids, the local site asymmetry can be interpreted using the quadrupole coupling constant (C_Q), which is defined as follows:

$$C_Q = \frac{e^2 q_{zz} Q}{h} \quad (2.6)$$

where e is the proton charge, Q is the nuclear quadrupole moment, h is the Planck's constant, and eq_{zz} represents the largest principle axis value of the EFG tensor.

Nuclei exhibiting quadrupolar properties each possess a distinct quadrupole moment Q (e.g., for ${}^6\text{Li}$, $Q = -8.08 \times 10^{-26} \text{ m}^2$, and for ${}^7\text{Li}$, $Q = -4.01 \times 10^{-28} \text{ m}^2$). The interaction between these nuclei and the EFG can cause significant peak broadening in NMR spectra, with the magnitudes reaching up to 10^6 Hz. However, the quadrupolar interaction is influenced by both the nuclear properties (the Q value) and the molecular properties (the EFG generated by the surrounding electron distribution). As a result, nuclei with a large Q value may exhibit relatively small quadrupole couplings if their nuclear environment is highly symmetric and thus results in a small EFG, as what can be seen from the ${}^{6/7}\text{Li}$ nuclei in this thesis.

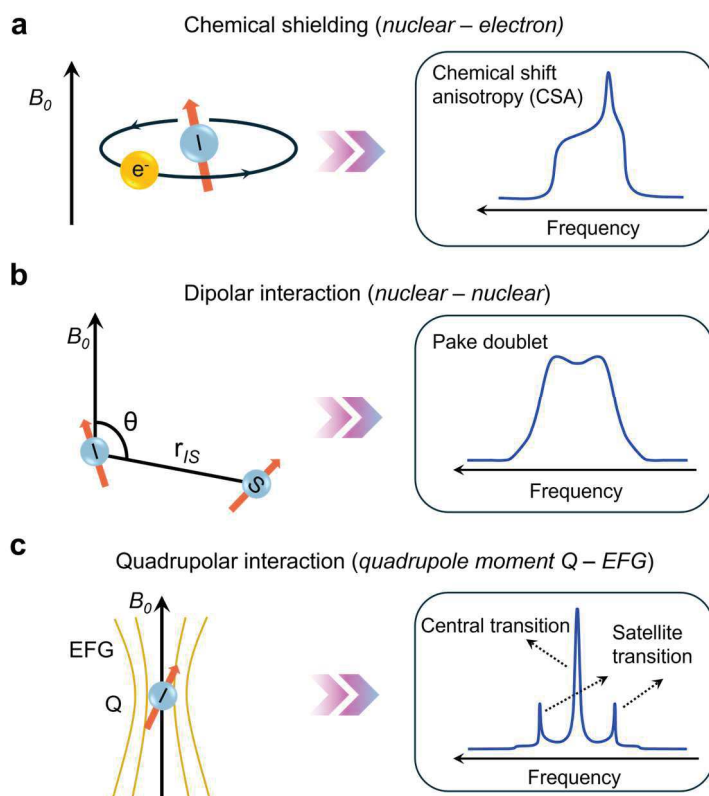


Fig. 2.3. Schematic representations of internal NMR interactions. (a) Chemical shielding, (b) dipolar interaction, and (c) quadrupolar interaction. The corresponding characteristic NMR line-shapes are depicted in the rounded boxes (for powder samples, static measurement).

Magic angle spinning

In solid-state NMR, the aforementioned anisotropic spin interactions (CSA, dipolar and quadrupolar interactions) typically lead to overlapping broad resonances, making it challenging to resolve distinct chemical environments. To improve the spectral resolution, magic angle spinning (MAS) is commonly used in experiments on solids to average out these orientation-dependent interactions. This process involves setting the physical rotation of the sample at $\theta = 54.74^\circ$, where θ is the angle between the nuclear moment and the applied magnetic field B_0 , by which the geometry-dependent term $(3\cos^2\theta - 1)$ vanishes. This simulates the isotropic tumbling seen in solution-state NMR, which averages out the anisotropic components of the chemical shift⁷. For a rotation frequency that is larger than the combined magnitude of these interactions, an isotropic peak shift with a resolution near to that of a liquid sample is observed. Otherwise spinning sidebands emerge at frequencies $\omega_i^{iso} + k\omega_r$, where ω_r is the spinning speed and k is an integer.

2.4 NMR techniques used in this thesis

This section outlines the specific NMR techniques used in this thesis. The goal is to investigate Li-ion dynamics and the underlying structural mechanisms of Li-metal-SEI exchange, as well as the interphase interactions in HSEs. These experiments involve multi-nuclear ($^6/7\text{Li}$, ^1H , ^{13}C , ^{19}F), multi-dimensional, ex-situ and operando NMR. The obtained results are complementary and provide valuable insight into Li-ion diffusion behavior across a range of timescales and temperatures.

2.4.1 Relaxation time measurements

NMR has broader application beyond the analysis of coupling interactions and magnetic shielding. Relaxation in NMR investigates the characteristic timescales required for nuclear spins to return to thermal equilibrium following external perturbation. Equilibrium is the state where (i) the energy level populations follow the Boltzmann distribution, and (ii) no transverse magnetization or, more broadly, no coherences exist in the system⁵. This approach provides valuable insight into the dynamics of atomic nuclei and their interactions with the surrounding molecular environment.

NMR relaxation is characterized by two fundamental processes: spin-lattice (or

longitudinal) relaxation, which describes the return of the z -magnetization to its equilibrium state, and spin-spin (or transverse) relaxation, which accounts for the loss of phase coherence in the xy -plane. These processes are described by the time constants T_1 and T_2 , respectively. In solids, T_2 relaxation is generally more efficient than T_1 relaxation due to the smaller frequency range of diffusion compared to liquids ($T_2 \ll T_1$). The time-dependent precession of the net magnetization vector M , along with its relaxation, is mathematically described by the phenomenological Bloch equations:

$$\frac{dM_x}{dt} = \gamma(M_y B_z - M_z B_y) - \frac{M_x}{T_2} \quad (2.7)$$

$$\frac{dM_y}{dt} = \gamma(M_z B_x - M_x B_z) - \frac{M_y}{T_2} \quad (2.8)$$

$$\frac{dM_z}{dt} = \gamma(M_x B_y - M_y B_x) - \frac{M_z - M_0}{T_1} \quad (2.9)$$

where M_x, M_y, M_z represent the components of the net magnetization vector in their respective directions, with M_0 the equilibrium magnetization along the z -axis. γ is the gyromagnetic ratio, and $B_x, B_y,$ and B_z are the components of the external magnetic field along the $x, y,$ and z axes, respectively.

By means of the RF pulse, an external field is applied to intentionally excite the spins into a higher energy state. Concurrently, intrinsic oscillating fields are present within the sample, causing each spin to experience its local field. This local field fluctuates in magnitude and orientation due to the thermal motion of the molecules. Suppose the local field at a particular spin causes its magnetic moment to align more closely with the z -axis. In that case, the interaction energy with the applied field decreases, making this configuration energetically more favorable. This process is known as spin-lattice relaxation. Furthermore, spin relaxation can also occur through direct interactions between spins due to longer-range motions, leading to the loss of phase coherence, which is described as spin-spin relaxation. Magnetic moments precess around the z -component at the Larmor frequency in the external field, B_0 . However, each spin experiences not only B_0 but also a much smaller local field, causing slight variations in the precession frequency among individual spins.

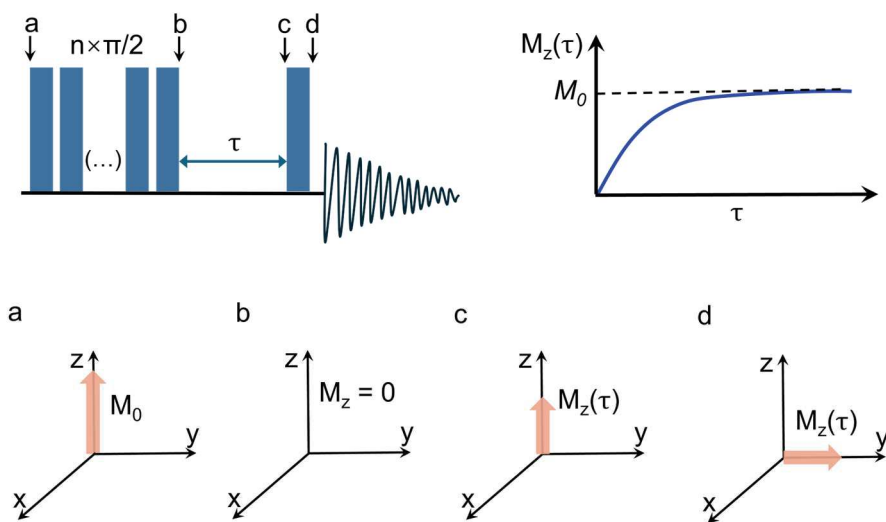


Fig. 2.4. Pulse sequence for saturation recovery to measure T_1 . Schematic showing the magnetization vectors of a single resonance at four time points (a, b, c and d) in the pulse sequence, along with a plot of signal intensity as a function of recovery time τ , corresponding to Equation 2.10.

The two most commonly used methods for measuring T_1 are inversion recovery and saturation recovery. The latter one is used in this thesis and its pulse sequence is illustrated in **Fig. 2.4**. Initially, a series of 90° RF pulses are applied in quick succession to disrupt the equilibrium magnetization. The magnetization then begins to recover towards its equilibrium state during a recovery time, τ . After this period, a single 90° pulse is applied to reorient the recovered magnetization. By increasing the recovery time, the signal is given more time to return to equilibrium. The signal reaches its maximum when τ is sufficiently long, suggesting that the magnetization has fully recovered. **Fig. 2.4** shows multiple saturation pulses over time, revealing a recovery curve of the longitudinal magnetization M_z as a function of τ . The specific shape of this recovery curve is determined by the spin-lattice relaxation processes, which can be described by an exponential function typical of T_1 relaxation:

$$M_z(\tau) = M_0 \left[1 - \exp\left(-\frac{\tau}{T_1}\right) \right] \quad (2.10)$$

2.4.2 Line-width analysis

Spectral line-width as a function of temperature can be used to evaluate the relative mobility

of nuclei within a sample. In solids, line broadening typically occurs in two forms: homogeneous and inhomogeneous broadening.

A homogeneously broadened line, which exhibits a Lorentzian line shape in the absence of other broadening mechanisms, arises from interactions that uniformly affect all spins, such as dipolar interactions or CSA. The line-width $\Delta\nu$ of a homogeneously broadened line is proportional to the inverse of T_2 ($\Delta\nu \propto 1/T_2$). During the transverse relaxation process, the loss of phase coherence leads to destructive interference within the acquired signal, resulting in shorter NMR signal (FID). A shorter FID corresponds to a broader peak on the spectrum.

In contrast, inhomogeneous broadening results from variations in the local magnetic field, often due to crystal imperfections or sample heterogeneity, and typically produces a Gaussian-shaped resonance. This type of broadening is generally considered independent of T_2 . In practice, the observed line-shape is often a combination of both homogeneous and inhomogeneous broadening.

Motional narrowing occurs when the exchange between different environments happens so rapidly that the spin system cannot accumulate a significant phase difference, leading to an averaged precession frequency over the varying magnetic environments. As a result, the nuclei experience a more homogeneous magnetic field on the timescale of their interactions. Therefore, similar to T_2 , variations in spectral line-width can indicate ion mobility within the sample under consistent experimental conditions. The onset of motional narrowing and the temperature at which the lattice becomes rigid can be analyzed. For the study of Li-ion conductors, combining this method with electrochemical impedance spectroscopy makes it possible to correlate local Li-ion dynamics with overall Li-ion conduction.

2.4.3 Cross polarization

Nuclei with small gyromagnetic ratio, low natural abundance, or long T_1 (e.g., ^{13}C or ^{15}N) typically present low NMR sensitivity. Cross polarization (CP) can enhance the signal of these nuclei by providing polarization transfer from the abundant spins (e.g., ^1H or ^{19}F). The CP process of transferring magnetization from abundant nuclei I to rare nuclei S involves three main steps (**Fig. 2.5**):

Initial excitation: A standard 90° pulse is applied to excite the abundant nuclei I . This pulse rotates the magnetization of the I spins from its equilibrium state (along the z -axis in

the rotating frame) into the transverse plane, usually along the x -axis.

Magnetization transfer: Spin-lock pulses are applied simultaneously to both the I and S spins, generally along the same axis (often the y -axis in the rotating frame). These pulses suppress the free precession of the magnetization of the I spins and lock it along the chosen axis in the rotating frame of reference. During the period called *contact time*, the S spins acquire magnetization by draining polarization from the I spins.

Detection: After the CP step, the RF field on the S spin is turned off, and the transverse magnetization on the S spin is detected. Meanwhile, the RF field on the I spin remains on during the acquisition to suppress line broadening effect caused by the heteronuclear dipolar couplings (also known as decoupling).

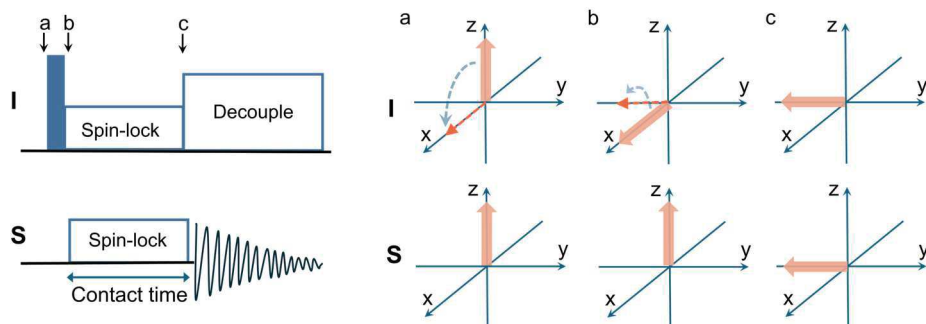


Fig. 2.5. Pulse sequence for CP measurement. Schematic showing the magnetization vectors of at three time points (a, b and c) in the pulse sequence, depicting the magnetization transfer from I spins to S spins.

An effective CP process requires the energy levels of two different nuclei to be matched in the rotating frame, which is described by the Hartmann-Hahn condition⁸:

$$\gamma_I B_1^I = \gamma_S B_1^S \quad (2.11)$$

where γ_I and γ_S are the gyromagnetic ratios of the I and S nuclei, respectively, and B_1^I and B_1^S are the strengths of the RF fields applied to the I and S spins. Under this condition, the magnetization is transferred from the I spins to the S spins through the heteronuclear dipolar coupling mechanism. This results in high spatial sensitivity of the CP experiments, given the $1/r^3$ dependence of the dipolar interaction on the internuclear distance r (Equation 2.5). S spins that are in close proximity to I spins experience stronger dipolar couplings, leading to

more efficient magnetization transfer compared to S spins located further away. In practical applications, aligning the 90° pulses for the I and S spins to the same numerical value ensures that the Hartmann-Hahn condition for effective CP process is (closely) met. Since the flip angle is given by $\beta = \omega_1 t_p$ (Section 2.2, t_p is the pulse length), if the flip angle is identical for both spins when applying the same pulse length, it follows that $\omega_{1I} = \omega_{1S}$. However, due to the averaging effect on the heteronuclear dipolar coupling, under the MAS condition with a spinning speed of ω_r , the Hartmann-Hahn condition needs to be adapted to:

$$\gamma_I B_1^I = \gamma_S B_1^S + n\omega_r \quad (2.12)$$

where n is an integer. That is, when applying CP MAS, polarization transfer is most efficient at a multiple of the sample spinning speed, typically $n = \pm 1, \pm 2, \dots$

In comparison to direct excitation experiments, signal enhancement in CP experiments is achieved not only through polarization transfer but also by enabling faster repetition of scans. Since the CP experiment can be repeated according to the T_1 relaxation time of the abundant spin system, which typically has a much shorter T_1 than the rare spin species, more scans can be acquired within the same timeframe relative to what is obtainable through direct excitation of the rare spin species.

Due to the orientation-dependent nature of the dipolar coupling (Equation 2.5), the CP signal is also indicative of the motional dynamics of the I and S spins. Varying the contact times in CP spectra allows for the quantification of CP kinetics. Specifically, based on the assumption that $T_{IS}/T_{1\rho S} \approx 0$, where T_{IS} is the time constant for the polarization transfer from the I spins to the S spins, and $T_{1\rho S}$ is the spin-lattice relaxation time constant for the S spins in the rotating frame, the magnetization-evolution of the S spins as a function of contact time can be fitted by:

$$M(t) = M_0 \left(1 - \frac{T_{IS}}{T_{1\rho I}}\right)^{-1} \left[\exp\left(-\frac{t}{T_{1\rho I}}\right) - \exp\left(\frac{t}{T_{IS}}\right) \right] \quad (2.13)$$

where M_0 is the constant proportional to the equilibrium magnetization obtained from a typical one-pulse experiment for the species undergoing CP, t is the contact time, and $T_{1\rho I}$ is the rotating frame spin-lattice relaxation time constant for I spins. It is important to note that

if $T_{1\rho I}$ is too short, the I spins will relax back to equilibrium before effective polarization transfer to the S spins can occur, rendering them incapable of being adequately spin-locked. Therefore, low CP efficiency can arise from both rapid and slow nuclear dynamics.

2.4.4 Two-dimensional NMR

In one-dimensional (1D) NMR, the signal is acquired by monitoring the spin system's response to applied RF pulses during a single acquisition period. Upon Fourier transformation, this signal yields a spectrum with signal intensity on the y -axis as a function of frequency f_2 (or chemical shift) on the x -axis. As an alternative to the specialized techniques utilized in 1D NMR, the basic principle of two-dimensional (2D) NMR experiments involves measurements over two distinct time variables, the incremental delay t_1 and the acquisition time t_2 . The signal is recorded during the t_2 period for each discrete value of t_1 . For instance, in the initial experiment, t_1 is set to 0; in the subsequent experiment, t_1 is adjusted to Δ , then 2Δ , 3Δ , and so on for further experiments. As a result, the 2D spectrum displays signal intensity as a function of two frequency dimensions, f_1 and f_2 . The specific representation of these frequency axes are defined by the delay period t_1 and the pulse sequence used. Thus, the immediate benefit of 2D NMR lies in increasing signal dispersion and thus resolving overlapping signals.

The general form for 2D NMR usually includes: preparation of the magnetization by RF pulses and delays to place the nuclei in a nonequilibrium spin state; evolution of the magnetization during t_1 ; mixing of the magnetization with further RF pulses and delays; and finally during the detection period t_2 the signal is recorded. Notably, signal detection occurs only in the t_2 dimension. The 2D NMR techniques used in this thesis are briefly introduced in the next sections.

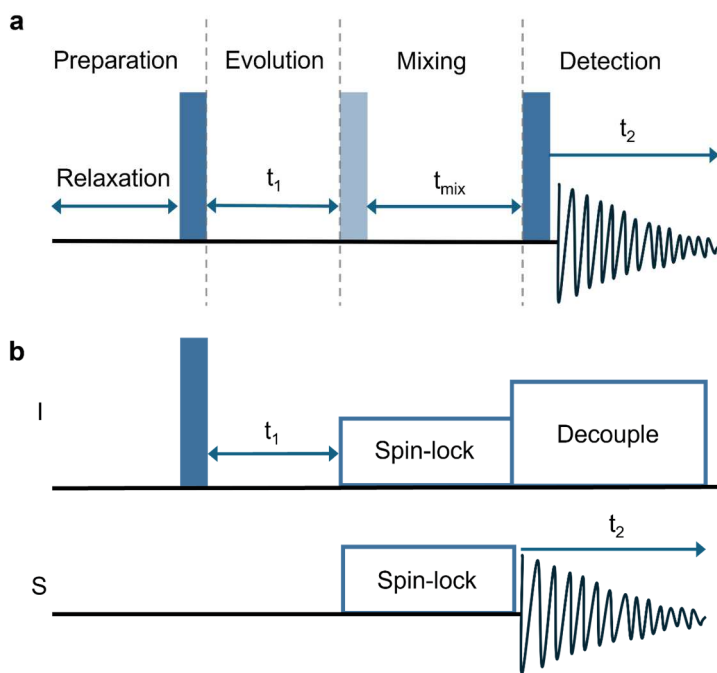


Fig. 2.6. Pulse sequences for the 2D NMR measurements used in this thesis. (a) Pulse sequence for the 2D-EXSY and NOESY experiments, with the middle pulse in light blue representing a -90° pulse. (b) Pulse sequence for the HECTOR experiment in its simplest form.

Two-dimensional exchange spectroscopy

2D-EXSY NMR is used throughout this thesis to study the Li-ion dynamics across various solid-solid interfaces. This technique enables the determination of timescales and energy barriers associated with Li-ion exchange between Li present at distinct chemical environments, operating within the temporal range between T_2 and T_1 . Its pulse sequence comprises several key steps (**Fig. 2.6a**):

- Initiating transverse magnetization with the first 90° pulse, then allowing spins to evolve with their characteristic precession frequencies and being stored with their “frequency label” during t_1 .
- Applying the second -90° pulse to reorient the magnetization along the longitudinal axis, followed by a mixing period (t_{mix}) during which chemical exchange occurs and the spins acquire the precession frequencies of their new environments.

- A final 90° pulse is used to restore the magnetization to the transverse plane, where the frequencies are detected during t_2 .

The initially labelled spins give rise to the diagonal peaks with identical frequencies in the f_1 and f_2 dimensions, corresponding to the nuclear spin that did not experience chemical exchange. In contrast, the cross-peaks with different frequencies in these two dimensions, observed after the mixing period, arise from spin exchange between sites during the mixing time.

Determining the energy barrier for chemical exchange requires measuring temperature-dependent 2D-EXSY experiments with stepped mixing times. At each temperature, the integrated cross-peak intensity as a function of mixing time exhibits exponential growth. By fitting the data to a diffusional model, the corresponding diffusion coefficient can be obtained (see details in Chapters 5 and 6). An Arrhenius analysis of the diffusion coefficients across different temperatures then provides the activation energy for ion diffusion. Quantitative analysis using 2D-EXSY is applicable under two key conditions: a sufficient difference between the two resonances involved in the exchange and a suitably long T_1 relaxation time to allow for the exchange process to occur.

Nuclear Overhauser effect spectroscopy

Nuclear Overhauser effect spectroscopy (NOESY) NMR uses a sequence similar to that of the 2D-EXSY experiment (**Fig. 2.6a**), with the key distinction being that NOESY relies on dipolar cross-relaxation rather than exchange phenomena. NOESY is based on the dipolar coupling between nuclei that are spatially close, even if they are not directly bonded.

In a NOESY spectrum, cross-peaks arise from these dipolar interactions between spatially proximate nuclei. The integrated intensity of these cross-peaks is typically interpreted as an indicator of the distance between the interacting spins. Thus, the presence and intensity of these cross-peaks provide valuable information about the spatial arrangement of atoms within the molecule.

Heteronuclear correlation spectroscopy

Heteronuclear correlation spectroscopy (HETCOR) is a typical 2D NMR technique that capitalizes on heteronuclear interactions to provide detailed information about correlations between different types of nuclei. In its simplest form, HETCOR involves generating

transverse magnetization for one nuclear species, which is then allowed to evolve at its characteristic frequency during the t_1 period. Subsequently, this magnetization is transferred to another nuclear species through a CP step, with the resulting signal being collected during the t_2 period (**Fig. 2.6b**).

The output of a HETCOR experiment is a 2D spectrum where one axis corresponds to the frequency of one nucleus species and the other axis to the frequency of the second. Peaks in this spectrum signify correlations between nuclei of different types that are coupled to each other, reflecting direct or spatially proximal interactions within the molecular framework. Thus, HETCOR is uniquely effective in evaluating the connectivity and interactions between different nuclei, making it a powerful tool for resolving the structures of complex molecules. This becomes particularly useful in cases where conventional CP MAS spectra do not offer sufficient resolution for detailed structural analysis.

2.4.5 One-dimensional exchange spectroscopy

As previously discussed (Section 2.3.5), the applicability of quantitative analysis using 2D-EXSY is limited by the T_1 relaxation times of the resonances. Specifically, a short T_1 restricts the mixing times to regions where there is insufficient buildup of cross-peak intensity, while a long T_1 requires extended spectrometer time to achieve sufficient signal intensity.

As seen in the Li-metal-SEI exchange study in Chapter 3, the SEI exhibits a very long T_1 relaxation time (> 10 s) due to diamagnetic Li-containing species, making 2D-EXSY experiments excessively time-consuming. In such cases, one-dimensional (1D)-EXSY experiment can be utilized to significantly reduce the spectrometer time required for 2D-EXSY experiments. In the 1D measurements, the SEI resonance is initially selectively filtered out using a T_2 filter. The timescale for the depopulation of the Li-metal resonance and the population of the SEI resonance directly reflects the ion diffusion between the two resonances.

The pulse sequence for the 1D-EXSY experiments includes a specific phase cycle to cancel direct magnetization (**Fig. 2.7**). After the initial 90° excitation pulse, a spin-echo-based T_2 filter is applied. This involves a 180° refocusing pulse to correct for dephasing caused by field inhomogeneities, thereby filtering out signals from spins with short T_2 relaxation times and refocusing only those with longer T_2 . Subsequently, a mixing period (t_{mix}) is introduced to allow for magnetization exchange between different nuclear sites, followed by a detection

pulse and signal acquisition.

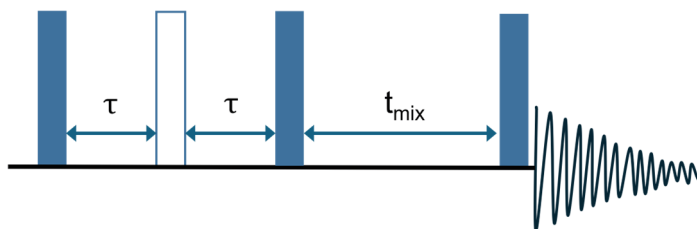


Fig. 2.7. Pulse sequences for the 1D-EXSY experiment. Pulse sequence for the 1D-EXSY experiment, with the unfilled pulse representing a 180° pulse. During the first delay time τ , xy coherences evolve after the transverse magnetization generated by the initial 90° pulse. In the second delay time τ , the phases of all the spins precess to 2π .

2.4.6 Operando NMR

Unlike traditional methods that often require disassembly and risk altering or damaging the battery's internal structure, the non-invasive operando NMR technique enables the collection of real-time data during electrochemical cycling. This approach effectively minimizes the influence of self-relaxation process, allowing for the detection of the short-lived metastable or reactive phases and the acquisition of dynamic information.

In this thesis, operando NMR spectroscopy is used to investigate Li stripping/plating efficiency in cells subjected to various electrochemical formation protocols. The Li resonances observed in these experiments cover a broad range of chemical shifts. Li in diamagnetic environments, such as within the electrolyte or Li-containing SEI species, typically appears at around ± 10 ppm. In contrast, metallic Li exhibits a much higher shift at ~ 242 ppm, due to the interaction of nuclear spins with unpaired electrons at the Fermi level of the conduction band, known as the Knight shift.

The peak shifts and intensity changes of the ^7Li NMR signals are commonly used to infer morphological and structural changes in electrodes during electrochemical processes. Specifically, operando NMR is able to detect the dendrite/dead Li formation and their growth, because the NMR response of metallic Li exhibits orientation dependence. This is attributed to the bulk magnetic susceptibility (BMS) effects that alter the local magnetic field experienced by nuclei. For instance, the ^7Li resonance appears at ~ 242 ppm when the metal strip is aligned horizontally to the NMR coil, but shifts to ~ 272 ppm when oriented vertically⁹. Therefore, dendritic or mossy lithium, which grows perpendicular to the electrode surface,

produces a slight shifted peak from the original metallic Li peak, which is consistent with experimental observations¹⁰.

A key factor influencing the detection of Li microstructures in NMR is skin depth, which refers to the distance within a metallic sample where the electromagnetic field, and thus the NMR signal, penetrates before decaying exponentially. When applying an RF excitation pulse, the generated B_1 field, perpendicular to the static B_0 field, causes the net nuclear magnetization to rotate along the B_1 axis. The resulting flip angle depends on the duration and amplitude of the RF pulse. In metallic samples, the skin depth effect causes the RF field strength to decrease with depth, leading to a variation in flip angle at different distances from the metal surface. The strength of the effective RF field ω_1 inside a metal decreases with the depth x from the surface, as described by¹¹:

$$\omega_1(x) = \omega_1(0) \exp\left(-\frac{x}{d}\right) \quad (2.14)$$

Here, d is the skin depth of the metal when an RF field with frequency ν is applied¹²:

$$d = \sqrt{\frac{\rho}{\pi\mu_0\mu_r\nu}} \quad (2.15)$$

where μ_0 is the permeability of the vacuum ($4\pi \cdot 10^{-7}$ m kg s⁻² A⁻²), μ_r is the relative permeability of the medium (1.4 for Li-metal), and ρ is the resistivity of the metal (94.7 n Ω ·m for Li-metal at 298 K). In Chapter 3 of this thesis, the resonance frequency for ⁷Li is 194.4 MHz, corresponding to a skin depth of 9.4 μ m.

Operando NMR provides a relatively straightforward method for monitoring changes in electrodes, such as the Li-metal anode studied in this thesis (Chapter 3). Practically, resolution is the major concern for applying the operando method to specific battery systems. The operando experiments are operated in static mode, which tends to induce signal broadening due to internal NMR interactions. Especially for many cathode materials, the interaction between the unpaired electrons of the paramagnetic transition metal ions causes considerable broadening of the target nucleus signals (e.g., ⁶⁷Li). Additionally, inhomogeneities in the local magnetic field caused by variations in magnetic susceptibility across the sample, contribute to a range of resonance frequencies for the same type of nucleus,

further exacerbating line broadening. Addressing the sources of the BMS effects and optimizing cell design could mitigate these challenges, and improve the applicability of operando NMR in other battery systems.

References

1. Xiang, Y., Li, X., Cheng, Y., Sun, X. & Yang, Y. Advanced characterization techniques for solid state lithium battery research. *Materials Today* **36**, 139–157 (2020).
2. Liu, M., Ganapathy, S. & Wagemaker, M. A direct view on li-ion transport and li-metal plating in inorganic and hybrid solid-state electrolytes. *Accounts of Chemical Research* **55**, 333–344 (2022).
3. Liu, X., Liang, Z., Xiang, Y., Lin, M., Li, Q., Liu, Z. & Yang, Y. Solid-state NMR and MRI spectroscopy for Li/Na batteries: materials, interface, and in situ characterization. *Advanced Materials* **33**, 2005878 (2021).
4. Svirinovsky-Arbeli, A., Juelsolt, M., May, R., Kwon, Y. & Marbella, L. E. Using NMR spectroscopy to link structure to function at the Li solid electrolyte interphase. *Joule* **8**, 1919–1935 (2024).
5. Keeler, J. J. *Understanding NMR Spectroscopy*. (Wiley, Chichester, West Sussex, 2011).
6. Levitt, M. H. *Spin Dynamics: Basics Of Nuclear Magnetic Resonance*. (John Wiley & Sons, Chichester, England, 2s008).
7. Ashbrook, S. E., Griffin, J. M. & Johnston, K. E. Recent advances in solid-state nuclear magnetic resonance spectroscopy. *Annual Review of Analytical Chemistry* **11**, 485–508 (2013).
8. Apperley, D. C., Harris, R. K. & Hodgkinson, P. *Solid-State NMR: Basic Principles & Practice*. (Momentum Press, LLC, New York, 2012).
9. Trease, N. M., Zhou, L., Chang, H. J., Zhu, B. Y. & Grey, C. P. In situ NMR of lithium ion batteries: Bulk susceptibility effects and practical considerations. *Solid State Nuclear Magnetic Resonance* **42**, 62–70 (2012).
10. Bhattacharyya, R., Key, B., Chen, H., Best, A. S., Hollenkamp, A. F. & Grey, C. P. In situ NMR observation of the formation of metallic lithium microstructures in lithium batteries. *Nature Materials* **9**, 504–510 (2010).
11. Chandrashekar, S., Trease, N. M., Chang, H. J., Du, L. S., Grey, C. P. & Jerschow, A. ^7Li MRI of Li batteries reveals location of microstructural lithium. *Nature Materials* **11**, 311–315 (2012).
12. Gunnarsdóttir, A. B., Amanchukwu, C. V., Menkin, S. & Grey, C. P. Noninvasive in situ NMR study of “dead lithium” formation and lithium corrosion in full-cell lithium metal batteries. *Journal of the American Chemical Society* **142** 20814–20827 (2020).

3

The Lasting Impact of Formation Cycling on the Li-ion Kinetics Between SEI and the Li-metal Anode and Its Correlation with Efficiency

“风起于青萍之末，浪成于微澜之间”

“A breeze starts from the ends of a green leaf, and waves form from the slightest ripple.”

《汉书·枚乘传》(The Book of Han: Biography of Mei Cheng)

This chapter has been published as: **Zhang, S.**, Li, Y., Bannenberg, L. J., Liu, M., Ganapathy, S. & Wagemaker, M. The lasting impact of formation cycling on the Li-ion kinetics between SEI and the Li-metal anode and its correlation with efficiency. *Science Advances* 10, eadj8889 (2024).

Abstract

Formation cycling is a critical process aimed at improving the performance of lithium (Li)-ion batteries during subsequent use. Achieving highly reversible Li-metal anodes, that would boost battery energy density, is a formidable challenge. Herein, formation cycling, and its impact on the subsequent cycling are largely unexplored. Through solid-state nuclear magnetic resonance spectroscopy experiments, we reveal the critical role of the Li-ion diffusion dynamics between the electrodeposited Li-metal (ED-Li) and the as-formed solid electrolyte interphase (SEI). The most stable cycling performance is realized after formation cycling at a relatively high current density, causing an optimum in Li-ion diffusion over the Li-metal-SEI interface. We can relate this to a specific balance in the SEI chemistry, explaining the lasting impact of formation cycling. Thereby, this work highlights the importance and opportunities of regulating initial electrochemical conditions for improving the stability and cycle life of lithium metal batteries.

3.1 Introduction

Following the introduction of the metallic lithium (Li) electrode by Whittingham in the 1970s, it remains to date a topic of great research interest. This is because Li-metal possesses more than ten times the specific capacity (3860 mAh g⁻¹) of current commercial carbonaceous anodes and the lowest potential (-3.040 V versus the standard hydrogen electrode, SHE)^{1,2}. However, its commercialization remains challenging as severe problems persist, such as the inherent high reactivity with the electrolyte and the non-uniform deposition upon plating/stripping, causing poor reversibility and thus a short cycle life^{3,4}. In general, Li-metal reduces the electrolyte on contact forming an interfacial layer, referred to as the solid electrolyte interphase (SEI), with a thickness in the order of nanometers. During SEI formation, the electrolyte is reduced which passivates a fraction of the Li inventory of the cell. Ideally, the SEI forms a mechanically stable interphase that prevents further electrolyte reduction, while not posing a barrier to Li-ion transport⁵⁻⁷. However, the low surface energy of Li-metal easily leads to the formation of high surface area mossy and dendritic Li-metal morphologies. Each time, this leads to fracturing of the SEI which exposes fresh Li-metal to the electrolyte. This induces further SEI formation and thus irreversible capacity loss^{7,8}. Additionally, mossy and dendritic structures lead to electrical disconnected Li-metal upon repeated plating and stripping, inducing further Li losses. This self-amplifying process, the extent of which depends on the choice of electrolyte, current collector, and cycling conditions, is responsible for poor reversibility of the Li-metal electrode. This is expressed by the Coulombic efficiency (CE), i.e., the ratio of the electrons passed on discharge to those passed on charge⁹. Maintaining a uniform and dense Li-metal morphology, preventing uncontrolled SEI formation and contact losses is considered to be a prerequisite for achieving a high CE and cycle life for Li-metal batteries (LMBs).

It has been shown that the electro-kinetics at the surface of Li-metal plays a central role in the evolution of both its morphology and the SEI formation^{4,10,11}. Whether the electroplating process occurs at a buried Li-SEI interface or at a fresh Li-electrolyte interface is closely related to the applied current density^{8,12-14}. When electroplating occurs at a buried Li-SEI interface, the SEI regulates the Li-ion exchange between the electrolyte and Li-metal, where higher exchange rates have been associated with high CE, typically increasing during

cycling for electrolytes that provide high CE^{15,16}. For electroplating at the fresh Li-electrolyte interface, the strength of Li-ion solvation in different electrolytes has been proposed to influence a preference for dendritic or uniform morphologies^{12,17}. In principle, Li-metal growth is sensitive to a range of factors, including electrolyte chemistry, current density, formation cycles, temperature, and internal pressure among others¹⁸⁻²¹. Understanding the role of each of these is essential in realizing an optimal Li-metal anode performance.

The impact of the formation cycling conditions on the initial SEI morphology and its properties is one such factor that can be anticipated to have a long lasting impact on subsequent cycling^{14,22-24}. This phenomenon has been explored using electrochemical approaches such as pulse-current or cyclic voltammetry pre-modulation which have tentatively probed the influence of initial current densities utilized on the SEI and the Li morphologies²⁵⁻²⁷. For instance, the pulse current protocol improves the cycling performance through higher nucleation densities during initial Li deposition and homogenous SEI film formation²⁷. Previous work observed that during initial medium-high cycling rates, more compact Li microstructures formed, suggesting this results in a templated SEI which defines the subsequent Li-metal morphology²⁸. It was also found that for a weakly solvating, high performance electrolyte, small formation current densities (0.5 mA cm^{-2}) lead to a more porous SEI, where it was postulated that the Li-metal, formed during subsequent cycles, nucleated within the SEI, suppressing electrolyte decomposition and explaining the observed improved CE¹⁴. Therefore, in a certain current density range, the SEI formed at higher rates is more compact with a more uniform Li-metal morphology, while at lower rates the SEI is more porous and with less dense Li-metal morphology.

These findings indicate that the initially formed SEI has a large impact on the subsequent cycling performance of Li-metal anodes^{8,14,17,28,29}. Nevertheless, comprehensive understanding of the underlying mechanisms is lacking, especially because of the diversity of electrolyte chemistries that have been studied^{12,17,30}. A central factor in this is the influence of the properties of the initially formed SEI on the Li-metal morphology and Li-ion charge-transfer kinetics, and how these influence subsequent long-term cycling. Several in-depth studies have been performed to evaluate the SEI morphology and composition, typically using cryo-transmission electron microscopy (TEM) in combination with advanced analysis of electrochemical impedance and voltammetry measurements^{22,26,30-34}. Although the role of

the local Li-ion kinetics both in the SEI and between the SEI, Li-metal, and the electrolyte is believed to play an important role, it remains ambiguous to date. This is mainly because it is very challenging to measure the local Li-ion kinetics of the SEI experimentally. Isotope selective solid-state nuclear magnetic resonance (ssNMR) offers opportunities to probe the Li-ion diffusivity between distinguishable Li-environments. Recently, one-dimensional (1D) and two-dimensional (2D) exchange ssNMR have been used to identify the role of the LiNO₃ additive to an ether-based electrolyte and qualitatively probe the growth of Li dendrites^{35,36}. Additionally, the SEI chemistry can be characterized using multinuclear magic angle spinning (MAS) ssNMR (*ex situ*) in conjunction with X-ray photoelectron spectroscopy (XPS), while *operando* NMR allows quantification of the Li microstructure and the SEI capacity^{37,38}.

Here we study the influence of the formation current density on the Li-ion diffusion kinetics between the SEI and the electrodeposited Li-metal (ED-Li), and how altering the electrochemical preconditioning and the formation cycles, affect subsequent cycling. Different formation cycle current densities ranging from 0.2 to 5 mA cm⁻² are studied in terms of CE and cycling stability. The Li-ion kinetics and SEI properties are evaluated by: (i) variable temperature (VT) exchange ssNMR to quantify the kinetics of Li-ion migration between the two solid phases: ED-Li and SEI; (ii) cross-polarization (CP) ssNMR experiments to assign the chemical components in the SEI; and (iii) *operando* NMR, where the influence of electrochemical preconditioning on dead Li formation has been noninvasively and directly monitored. Complemented by scanning electron microscopy (SEM) and XPS, the equilibrium Li-ion flux between ED-Li and SEI is correlated with the SEI composition for different current density formation cycles. A relatively high formation current density (2 mA cm⁻²) facilitates the local Li-ion transport, which is correlated by a specific balance in the inorganic SEI species. This is found to be the origin for the improved reversibility and cycling stability, increasing the CE and minimizing the formation of dead Li-metal. In this manner, the present research uncovers the Li-metal \rightleftharpoons SEI kinetics during formation cycling and how this impacts subsequent cycling performance, providing practical guidelines for formation cycling protocols to be used in LMBs.

3.2 Results

3.2.1 The impact of electrochemical preconditioning on the LMBs performance

To identify the effect of formation cycling, Li||Cu half cells were assembled using a commercial carbonate-based 1 M LiPF₆ (lithium hexafluorophosphate) in ethylene carbonate/dimethyl carbonate [EC/DMC; 1:1 (w/w)] electrolyte. The cells were subjected to different formation conditions by decreasing the current density used during the five formation cycles from 5 to 0.2 mA cm⁻² guided by previous research^{22,28}. In addition, formation cycles at a current density of 0.5 mA cm⁻² were performed as a blank reference (control group). Following the five formation cycles, all the cells were cycled for more than 400 hours at 0.5 mA cm⁻² to an areal plating capacity of 1 mAh cm⁻² for each cycle.

As seen in **Fig. 3.1**, the electrochemical cycling highlights that the formation current density has a pronounced impact on the subsequent cycles. Comparing the four different formation protocols, a formation current density of 0.2 mA cm⁻² (**Fig. 3.1d**) initially displays a gradual increase in overpotential from the start of the working cycles (cycles after formation), which is notably accelerated after 200 hours of cycling, resulting in an overpotential of about 100 mV (**Fig. 3.1d**, insert), similar to that continuously cycled at 0.5 mA cm⁻² (**Fig. 3.1c**, insert). For formation cycles at a relatively high current density of 2 mA cm⁻², a smaller increase in overpotential of ~40 mV is observed after ~205 h (**Fig. 3.1b**, insert). The cell with a formation current density of 5 mA cm⁻² results again in a higher overpotential of ~70 mV at ~206.5 h (**Fig. 3.1a**, insert), suggesting there is an optimal formation current density around 2 mA cm⁻² at which the overpotential is minimal. The magnitude of the overpotential plateau reflects the internal resistance, which could be a reflection of the effective conductivity between the electrolyte and Li-metal, thus related to the SEI properties. This trend agrees with the impedance results reported by Xu et al.²², where the minimum resistance of the deposited Li was also found to be at 2 mA cm⁻². A similar trend is also observed in the comparison of the CE. The cell cycled at a formation current density of 2 mA cm⁻² results in the highest CE during the subsequent cycling (0.5 mA cm⁻²), stabilizing around ~96% for more than 100 cycles, while the cell cycled from 0.2 to 0.5 mA cm⁻² shows an obvious fading of the CE to around 80% (**Fig. 3.1e**). The reference cell, cycled constantly at

0.5 mA cm⁻², maintains a CE of around 88%. A formation cycling density of 5 mA cm⁻² results in fluctuations and a decreasing CE.

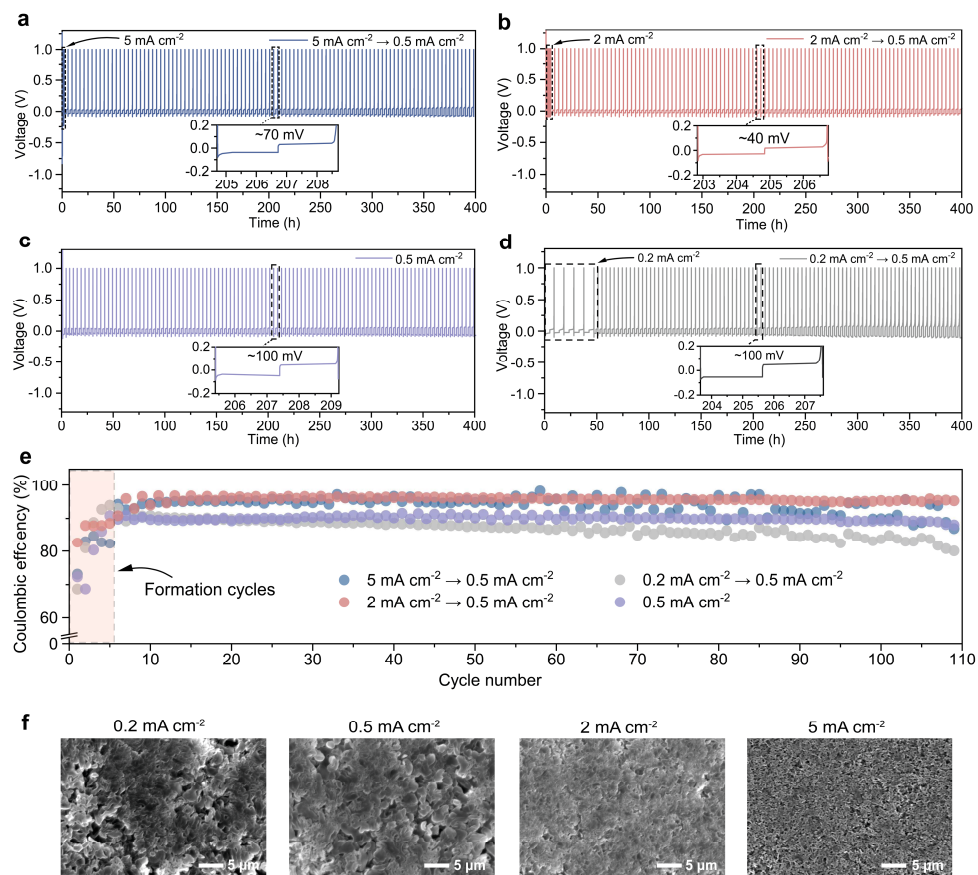


Fig. 3.1. Electrochemical characterization of the LMBs with different formation current densities. Galvanostatic cycling performance and polarization profiles of the Li||Cu cells cycled at: (a) 5 to 0.5 mA cm⁻², (b) 2 to 0.5 mA cm⁻², (c) 0.5 mA cm⁻², and (d) 0.2 to 0.5 mA cm⁻². Five formation cycles were applied in advance, Li was electrodeposited to a capacity of 1 mAh cm⁻² for each plating step, and inserts are the enlarged view of the voltage profiles at 202 to 209 hours, indicating the overpotential values. (e) Comparison of the corresponding CE for the Li||Cu cells cycled at the current densities given in (a) to (d). (f) SEM images showing the morphology of the Li-metal plated on Cu in Li||Cu half cells after a single plating to a total capacity of 1 mAh cm⁻² at current densities of 0.2, 0.5, 2, and 5 mA cm⁻², respectively.

Post-mortem SEM images (Fig. 3.1f) are taken to visualize the differences in Li-metal morphology caused by using different initial current densities. For Li plated on a Cu foil at 0.2 mA cm⁻², porous Li deposits are observed, sparsely distributed over the Cu foil surface

with tangible Li whiskers, forming spongy Li domains with an average particle size of ~ 5 μm . While the morphology of Li-metal plated at 0.5 mA cm^{-2} is similar to that at 0.2 mA cm^{-2} , it shows a denser column-like morphology having smaller Li-metal deposit sizes. In contrast, the Li-metal morphology formed at 2 mA cm^{-2} is much denser and compact with a more uniform microstructure and smaller Li deposits of around $1 \mu\text{m}$. For the ED-Li deposited at 5 mA cm^{-2} , the Li-metal morphology is more porous again. The morphology of the ED-Li has been further studied by TEM as shown in **Fig. S3.1**. The ED-Li has a different size distribution where 2 and 5 mA cm^{-2} show smaller size than the other two (**Fig. S3.1, a to d**), and the observed SEI thicknesses are $\sim 28 \text{ nm}$, $\sim 23 \text{ nm}$, $\sim 14 \text{ nm}$, and $\sim 36 \text{ nm}$ for the deposition current densities of 0.2 , 0.5 , 2 , and 5 mA cm^{-2} , respectively (**Fig. S3.1, e to h**). The thinner SEI formed at 2 mA cm^{-2} is potentially favorable for faster Li-ion transport by reducing the ion conduction path lengths and consequently the ionic resistance.

This trend is consistent with literature: The Li nucleation size decreases with increasing current density, and the distribution of the deposited Li particles changes from densely packed to overlapping stacked multilayers^{22,23,39}. However, the performance of LMBs can vary greatly with the electrolyte composition. To see the impact of the formation current on different electrolyte formulations, we compared three extra representative electrolytes by applying the same electrochemical test protocols: a modified carbonate-based electrolyte with fluoroethylene carbonate (FEC) and vinylene carbonate (VC) additives $\{1 \text{ M LiPF}_6$ in EC/DMC [1:1 (w:w)] with 10 wt% FEC and 1 wt% VC}, an ether-based electrolyte $\{1 \text{ M lithium bis(trifluoromethane sulfonyl)imide (LiTFSI)}$ in 1,2-dimethoxyethane/1,3-dioxolane (DME/DOL) [1:1 (w:w)]} and a modified ether-based electrolyte with a lithium nitrate (LiNO_3) additive $\{1 \text{ M LiTFSI}$ in DME/DOL [1:1 (w:w)] with 5 wt% $\text{LiNO}_3\}$. For the Li||Cu cells cycled with the modified carbonate-based electrolyte (**Fig. S3.2**), similar trends have been found that using 2 and 5 mA cm^{-2} as formation current density improved the cycling stability and efficiency of the subsequent cycles. In the standard ether-based electrolyte (**Fig. S3.3**), 1 M LiTFSI in DOL/DME, a formation current density of 2 mA cm^{-2} does not show as evident an improvement; however, it does result in better stability and lower polarization compared to other cycling protocols. When using the ether-based electrolyte with the functional additive LiNO_3 (**Fig. S3.4**), the impact of the formation current density is similar to what we have observed for the ether-based electrolyte without additive shown in **Fig. S3.3**,

but the cells show smaller polarization and slightly higher CE, which can be attributed to the improved SEI by LiNO_3 reduction products⁴⁰. On the basis of the cycling performance of these electrolytes, it is reasonable to conclude that the current density applied during the formation cycles is instructive for optimizing the LMBs performance.

Nevertheless, the relationship between the initially formed SEI properties and the long-term battery performance is not established. The low overpotential observed on long-term cycling, after formation cycling at 2 mA cm^{-2} , suggests that facile Li-ion transport can be attributed to the presence of a highly conductive and stable SEI. As the SEI is generated during the formation cycles, it is also plausible that it forms a scaffold within which the Li-metal will be plated during subsequent cycles, and thus the morphology and properties of this SEI scaffold will play a large role in the reversibility²². The correlation between the formation current density and SEI conductivity and structure is explored in greater depth in the subsequent sections.

3.2.2 Li-ion diffusion between the ED-Li and the SEI

The direct detection of the spontaneous Li-ion diffusion between the ED-Li and the SEI is feasible by 2D exchange spectroscopy (2D-EXSY) ssNMR experiments under MAS conditions^{41–46}. All the samples were measured *ex situ*, and therefore, the Li-ion exchange represents the equilibrium exchange current density between Li-metal and SEI, which is representative of the Li-ion kinetics between these two phases under equilibrium conditions. Therefore, this includes the charge transfer kinetics at equilibrium (the exchange current density), most likely also Li-ion diffusion through the SEI, but does not include the (de)solvation kinetics between the SEI and liquid electrolyte. Exchange between the detected resonances within the NMR time scale gives rise to off-diagonal (cross) peaks in the 2D contour plots (**Fig. 3.2a**). On incrementing the mixing time T_{mix} , it allows more time for the Li-ions to migrate from one environment to another, resulting either in an increase in cross-peak intensity or the appearance of additional cross peaks between less mobile or spatially distant Li-containing environments (see the pulse sequence in **Fig. 2.6**). Similar observations can be made when performing the experiment at elevated temperatures as Li-ions become more mobile, resulting in faster dynamics (exchange). Therefore, the 2D-EXSY technique allows us to quantify the Li-ion exchange and thus the charge transfer kinetics between the ED-Li and the as-formed SEI phases, similar to that shown for ether-based electrolytes³⁶.

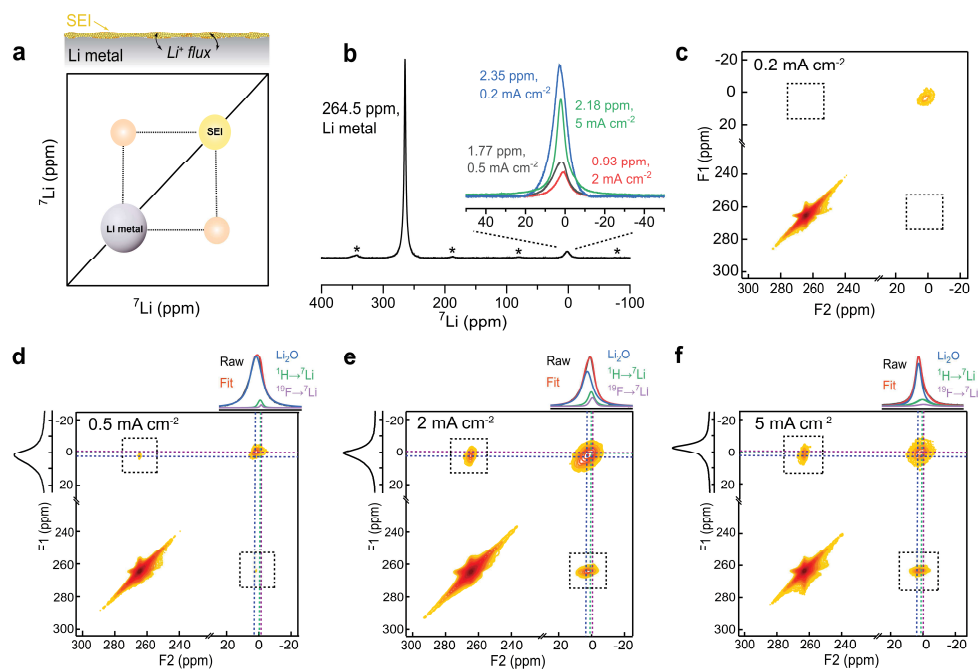


Fig. 3.2. ${}^7\text{Li}$ - ${}^7\text{Li}$ 2D exchange ssNMR experiments measuring Li-ion transport between the initially plated ED-Li and the as-formed SEI. (a) Schematic showing the ${}^7\text{Li}$ - ${}^7\text{Li}$ 2D Li-ion exchange between the ED-Li (grey) and the SEI (yellow). (b) 1D ${}^7\text{Li}$ MAS spectrum of the ED-Li and SEI generated at 5 mA cm^{-2} (green), 2 mA cm^{-2} (red), 0.5 mA cm^{-2} (grey), and 0.2 mA cm^{-2} (blue), respectively (insert). The black spectrum corresponds to the Li-metal peak plated at 2 mA cm^{-2} (see the other three in **Fig. S3.5**). Asterisks denote spinning sidebands. (c to f) 2D ${}^7\text{Li}$ - ${}^7\text{Li}$ exchange spectroscopy (2D-EXSY) of ED-Li and its corresponding SEI formed at: (c) 0.2 mA cm^{-2} , (d) 0.5 mA cm^{-2} , (e) 2 mA cm^{-2} , and (f) 5 mA cm^{-2} at $T_{\text{mix}} = 150$ ms and room temperature (298 K). The projections in F2 and F1 displayed in (d) to (f) correspond to the 1D slices of the SEI and the exchange peaks, aiming at assigning the components that dominate the exchange. The cross-peak at the off-diagonal positions in the dashed boxes represent the diffusion of Li-ions between the ED-Li and the as-formed SEI.

To discriminate the different Li-containing species present in the ED-Li and its SEI after directly plating Li on a Cu substrate at 0.2, 0.5, 2, and 5 mA cm^{-2} , one-pulse ${}^7\text{Li}$ MAS ssNMR spectra were measured, shown in **Fig. 3.2b**. The black spectrum corresponds to 2 mA cm^{-2} (the spectra corresponding to Li-metal plated at 0.2, 0.5, and 5 mA cm^{-2} are provided in the **Fig. S3.5**). Two distinguishable resonances can be observed in the spectrum corresponding to two main kinds of Li environments, one representing metallic Li [~ 264.5 parts per million (ppm)] and the other representing Li-species in the SEI generated (**Fig. 3.2b**, insert). It is worth noting that the chemical shift of the main diamagnetic SEI species depends on the

formation current density. It is observed at 2.18, 0.93, 1.77, and 2.35 ppm for the plating current densities of 5, 2, 0.5, and 0.2 mA cm⁻², respectively. The differences originate from the dominant Li-containing chemical species inside the SEI, which we will discuss in detail in the following sections.

From the 2D exchange spectra measured at $T_{mix} = 150$ ms at room temperature, there are no cross-peaks observed between Li-metal and SEI for the sample electrodeposited at a small current density of 0.2 mA cm⁻² (ED-0.2; **Fig. 3.2c**). When deposited at 0.5 mA cm⁻² (ED-0.5; **Fig. 3.2d**) and 1 mA cm⁻² (ED-1; **Fig. S3.6b**), cross-peaks emerge (indicated by the dashed black box), reflecting equilibrium Li-ion exchange diffusion between Li-metal and the SEI. At the same mixing time, more intense cross-peaks are observed for 2 and 5 mA cm⁻² (ED-2 and ED-5) (**Fig. 3.2, e and f**), indicating more equilibrium exchange between SEI and Li-metal deposited at higher current densities. Results obtained with electrochemical impedance spectroscopy (EIS) after five formation cycles show the same trend (**Fig. S3.10b**), which we have discussed in detail in the next section. The resistance ascribed to the SEI decreases with increasing formation current density ($2 \text{ mA cm}^{-2} < 0.5 \text{ mA cm}^{-2} < 0.2 \text{ mA cm}^{-2}$), which is in agreement with the lack of/lower cross-peak intensities observed at 0.2 and 0.5 mA cm⁻², respectively. When the measurements were performed at an elevated temperature (343 K), cross-peaks were also observed for the ED-0.2 sample (**Fig. S3.6a**), which is a consequence of the thermally enhanced Li-ion exchange.

3.2.3 Quantification of the Li-ion exchange

Given that the exchange experiments only measure the absolute amount of exchanged Li, this will scale with the Li-metal-SEI interface area, which is difficult, if not impossible to assess. The largest amount of Li-ion exchange between SEI and Li-metal is observed after plating at 2 mA cm⁻¹, thus for the most densely plated Li-metal morphologies (**Fig. 3.1f**), which is expected to have the smallest interface area with the SEI. This suggests that the Li-ion kinetics between SEI and Li-metal is much better after formation cycling at this current density (2 mA cm⁻¹). To access the kinetics quantitatively, the activation energy (E_a) for the Li-ion exchange diffusion between SEI and Li-metal is determined by exchange experiments performed at VTs. Since the diamagnetic Li-species in the SEI have a very long spin-lattice relaxation time (T_1) and that of metallic Li is much shorter, 1D ⁷Li exchange spectroscopy

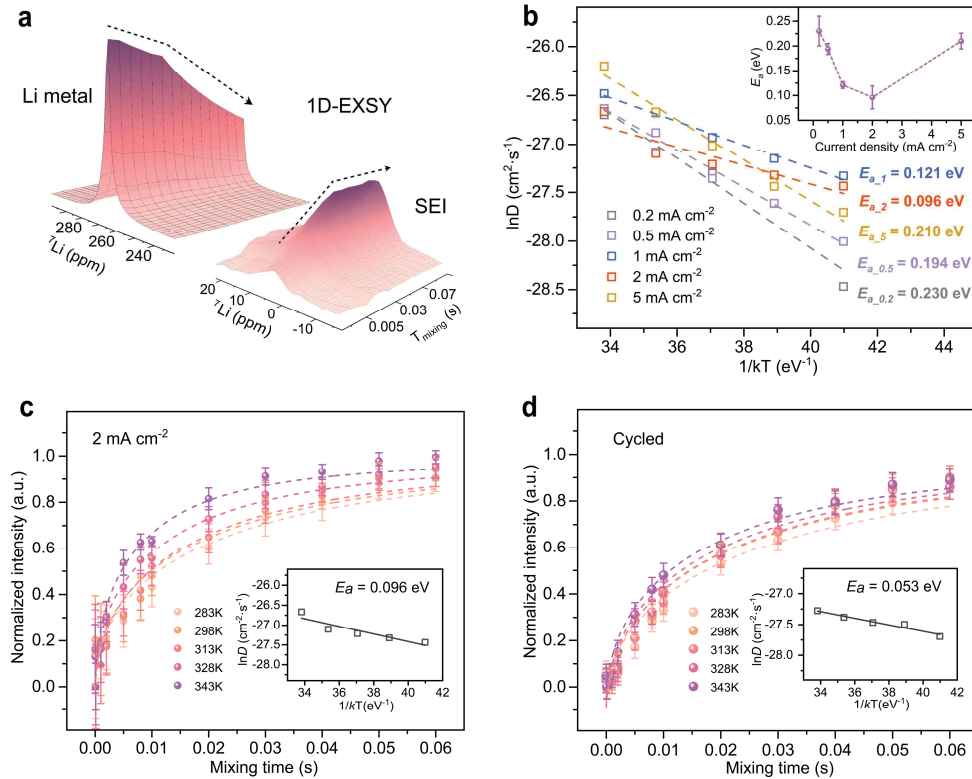


Fig. 3.3. Quantification of Li-ion diffusion between ED-Li and SEI by ^7Li 1D ssNMR exchange experiments. (a) Schematic illustration of the Li-ion transport in the 1D ^7Li exchange spectroscopy measurements (1D-EXSY) by probing the gradual diminishing of ED-Li peak and the increase of SEI peak as a function of mixing time (T_{mix}). (b) Dependence of the diffusion coefficient (D) obtained from fitting the 1D-EXSY data to a diffusion model has been described in detail elsewhere^{47,48}. 1D-EXSY of the initially plated ED-Li and the SEI plated at (c) 2 mA cm^{-2} and the cycled samples of (d) 2 to 0.5 mA cm^{-2} . For the cycled sample, five formation cycles at 2 mA cm^{-2} are first used, followed by ten cycles at 0.5 mA cm^{-2} . One final deposition process at 0.5 mA cm^{-2} is adopted at the end of the cycles to keep the sample amount consistent. Error bars in (b) inset represent the standard error of the fitting, and error bars in (c) and (d) represent the standard deviation of the spectrum noise. a.u., arbitrary units.

(1D-EXSY) ssNMR experiments can be used, a more time efficient method to quantify the Li-ion diffusion compared to the 2D-EXSY measurements. In the 1D-EXSY experiments, the SEI resonance is initially selectively filtered out using a T_2 filter^{44,48}, after which the magnetization transfer from the Li-metal back to the SEI is monitored as a function of mixing time T_{mix} . As depicted in Fig. 3.3a, at very short mixing times $T_{mix} = 0.00001$ s, only a tiny resonance signal was observed for the SEI. Increasing the mixing time, the Li in the metal

phase exchanges with the Li-ion species in the SEI phase, which is responsible for the intensity decrease of the Li-metal resonance and the increase of the SEI resonance. This is evidenced in **Fig. S3.7**, where the 1D spectra corresponding to short and long mixing times are overlaid for the ED-2 sample.

The VT 1D-EXSY reveals evident differences in Li-ion exchange dynamics for the electrodeposited samples depending on the formation current density. The normalized intensities of the evolving ${}^7\text{Li}$ SEI signal as a function of T_{mix} are shown in **Fig. 3.3c** and **Fig. S3.8**. The Li-ion diffusion between the ED-Li and SEI was quantified by fitting the emerging SEI signal as a function of T_{mix} to a diffusion model derived from Fick's law applied to describe the spontaneous equilibrium Li-ion exchange between two solid phases (see **Supplementary Text S3.1**)⁴⁸. The average self-diffusion coefficient (D_{Li}) as a function of temperature obtained from fitting the data to this model pertains to the Li-ion transfer between the ED-Li and the SEI. An Arrhenius law was used to fit D_{Li} obtained for various temperatures from which the E_a for each case was determined (see **Fig. 3.3b**). The inset in **Fig. 3.3b** shows that the lowest energy barrier is observed for ED-2, 0.096 eV, and the highest barrier for ED-0.2, 0.23 eV. This large span of E_a values (more than a factor of 2) shows that Li-ion diffusion between the two solid-state phases (ED-Li and SEI) strongly depends on the current density during formation cycling. For a much higher formation current density of 5 mA cm⁻², E_a increases again, leading to a minimum/optimum current density with respect to achieving a low E_a for Li-ion exchange between SEI and Li-metal. The trend of E_a versus formation current density correlates to the electrochemical performance shown in **Fig. 3.1**, where the CE is inversely related to the E_a for Li-ion exchange between the SEI and the ED-Li. In other words, more facile Li-ion kinetics between SEI and Li-metal correlates to a higher CE.

To evaluate if the charge transfer kinetics set by the formation current density remains upon subsequent cycling, additional ED-Li and SEI samples were measured with 1D-EXSY after five formation cycles at 2 mA cm⁻² followed by ten cycles at 0.5 mA cm⁻² (see **Fig. 3.3d**). Compared to right after plating, the additional cycles reduce the E_a by a factor of 2 (0.053 eV). For comparison, the same experiments were performed for the lower formation current densities, five formation cycles at 0.2 or 0.5 mA cm⁻², followed by ten subsequent cycles at 0.5 mA cm⁻², also resulting in a decrease in E_a from 0.23 to 0.159 eV and from 0.194 eV to

0.093 eV, respectively (**Fig. S3.9**). We can thus conclude that the E_a for Li-ion exchange between SEI and Li-metal, set by the formation cycling, has a lasting impact during subsequent cycling. Moreover, subsequent cycling reduces E_a ; hence, the Li-ion kinetics improve, reflecting better ionic contact between SEI and Li-metal. EIS measurements, performed on the cells after ten subsequent working cycles (**Fig. S3.10**), show a similar trend with resistances decreasing even further after the working cycles, with the biggest decrease seen for cells with a formation cycle current density of 2 mA cm^{-2} . On extended cycling, however, i.e., 50 and 100 working cycles, respectively, the cell resistance increases. This is also unsurprising as it is expected that more Li-metal reacts with the electrolyte during long cycling due to which the as-formed SEI inevitably experiences repetitive breakage/regeneration, resulting in corresponding changes in thickness, composition, and structure of the SEI^{4,5,49}. This indicates that the nature of these interfaces evolve during cycling, although the origin of this cannot be concluded based on these results.

3

3.2.4 Composition of the SEI

To understand the improved Li kinetics, including the charge transfer and Li-ion diffusivity in the SEI, with a formation current density of 2 mA cm^{-2} , the as-formed SEI composition and its distribution are investigated. Because of the strong dipolar interactions and the limited ^7Li chemical shift range of the mainly diamagnetic SEI species, it is difficult to discern the various Li-containing components by a direct $^6,^7\text{Li}$ excitation ssNMR measurement (**Fig. S3.11** shows the SEI spectrum for ^6Li ssNMR). To deconvolute the spectra, CP MAS ssNMR experiments were carried out for $^1\text{H} \rightarrow ^7\text{Li}$ and $^{19}\text{F} \rightarrow ^7\text{Li}$ to resolve the resonances, where Li is in close spatial proximity to ^1H and ^{19}F , respectively (see the pulse sequence in **Fig. 2.5**). In these two cases, ^1H and ^{19}F are considered as the abundant nuclei, and during the CP MAS experiment, transfer of magnetization takes place to any ^7Li environment in the vicinity (few atomic bond lengths) during a specific time duration (contact time). The ^7Li near ^1H is more likely to be assigned to the presence of an organic phase in the SEI, i.e., oligomers/polymers, $(\text{CH}_2\text{OCO}_2\text{Li})_2$ or ROCO_2Li , while the ^7Li close to ^{19}F is assigned to LiF or possible residual Li salt²². Nonetheless, there is still a substantial proportion of other species in the SEI, likely oxygen-containing Li compounds such as Li_2O , LiOH or Li_2CO_3 (**Fig. S3.12** for single-pulse measurements of Li_2O , LiOH , and Li_2CO_3). Apparently, the offset of SEI chemical shift from

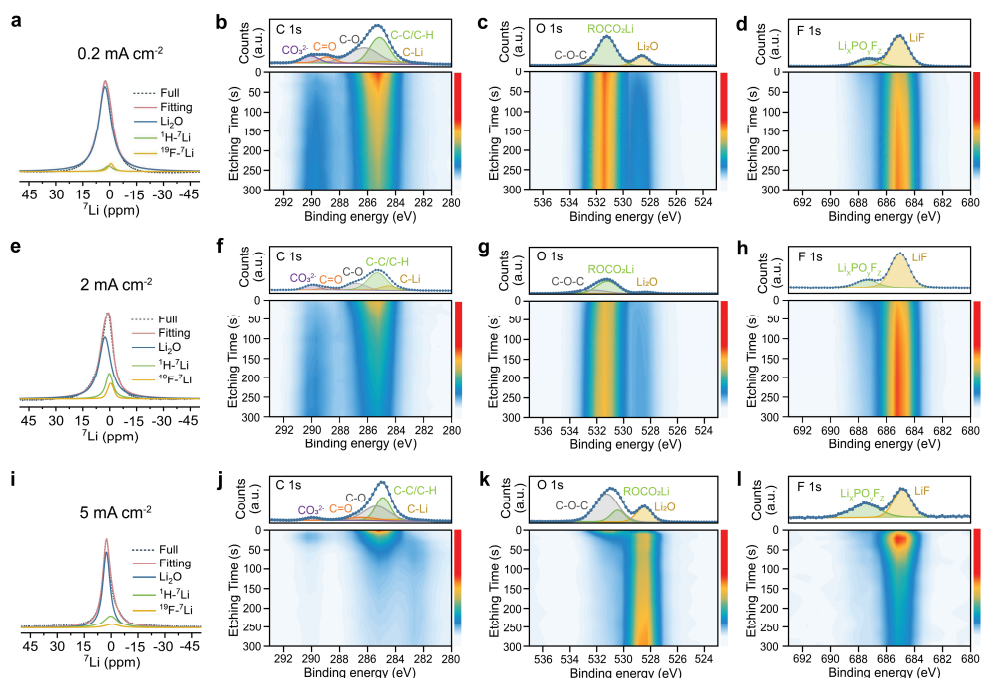


Fig. 3.4. Determining the composition of the SEI on ED-Li initially plated at different current densities using ssNMR and XPS. SEI peak deconvolution for the plating current densities of (a) 0.2 mA cm⁻², (e) 2 mA cm⁻², and (i) 5 mA cm⁻² by combining the fitting of the CP ssNMR spectra of ¹H→⁷Li (Li near H), ¹⁹F→⁷Li (Li near F), and one-pulse measurement of bulk Li₂O. Depth-profiled XPS measurements of C 1s, O 1s, and F 1s for the ED-Li plated on Cu at (b to d) 0.2 mA cm⁻², (f to h) 2 mA cm⁻², and (j to i) 5 mA cm⁻². Each plot comprises of two individual figures, i.e., the point before etching (up) and depth profiling spectrum (down). Color bar indicates the intensity from weak to strong from bottom to top.

0 ppm is mainly caused by the existence of Li₂O; therefore, bulk Li₂O was additionally added to fit the SEI spectra. By resolving the chemical shift and the full width at half-maximum of these three components and keeping these constant while fitting the SEI spectra (see separate spectra of ¹H→⁷Li and ¹⁹F→⁷Li for different current densities in Fig. S3.13), the basic components of the SEI generated at different C-rates on ED-Li can be resolved (Fig. 3.4, a, e, and i, and Fig. S3.14a). The SEI for ED-2 contains considerably more LiF and H-containing Li species among all samples. This is expected as LiF has been regarded to be effective in inhibiting lithium dendrites and the decomposition of the electrolyte, and the H-containing phase has higher affinity to the organic electrolyte solvent, thus facilitating the transport of Li-ions through the SEI^{22,50}. What is worth noting is that the LiF peak for the

ED-5 sample is broader compared to that for the other samples, which could be attributed to a more amorphous LiF phase, generated by a high current density. In addition, ED-2 has the smallest amount of Li₂O (or in this case, the Li₂O with other residual species in the SEI), while ED-0.2, ED-0.5, and ED-5 contain much more Li₂O. The insulating nature of Li₂O present in larger amounts of the SEI can be partially responsible for suppressing the Li-ion conduction inside the SEI^{31,51}. We can additionally use this spectral deconvolution to deduce which species within the SEI exchange Li-ions effectively with Li-metal, which is shown in the F2 projections in **Fig. 3.2, d to f**. The Li correlated to ¹H and ¹⁹F are given in green and purple and Li₂O (plus residual Li-containing components) in blue. Given that Li₂O forms the largest constituent inside the SEI, the exchange is dominated by the Li-ions in the Li₂O phase and Li-metal phase. It is worth noting that the ED-2 sample shows strong cross-peak intensity but with the presence of a smaller amount of Li₂O, indicating that the Li exchange is facilitated by Li species in the vicinity of a H-rich environment and Li near F in the SEI as well.

In addition, depth-profiling XPS was performed on the initially plated ED-Li on Cu foil to further deconstruct the SEI. C 1s (**Fig. 3.4, b, f, and j, and Fig. S3.14b**), O 1s (**Fig. 3.4, c, g, and k, and Fig. S3.14c**) and F 1s (**Fig. 3.4, d, h, and l, and Fig. S3.14d**) spectra are presented for ED-0.2, ED-2, ED-5, and ED-0.5, respectively. Consistent with the CP MAS NMR results (including the ¹H→¹³C CP MAS results in **Fig. S3.15**), the XPS results show that for the sample plated at 2 mA cm⁻², the SEI contains less insulating organics and Li₂O species and larger fraction of LiF as compared to all the other samples. The peak in the F 1s spectrum at ~685 eV, attributed to LiF⁵²⁻⁵⁴, is much higher for the ED-2 sample, which also confirmed in the 1D single-pulse ¹⁹F spectra in **Fig. S3.16**, while the peak at ~529 eV, assigned to Li₂O^{55,56}, is much weaker at this formation current density. For the ED-5 sample, the organic phase and the LiF tend to be more distributed on the surface of the SEI, while the Li₂O intensity is much stronger and slowly increases with the etching level. The origin could be that the high C-rate introduces dense Li nucleation sites and thereby induces highly packed Li-metal deposits, which block the entry of the electrolyte; thus, the decomposition reaction mainly occurs at the surface^{13,23,39}. The higher Li₂O signal is probably ascribed to the large current density, which induces more intense decomposition reactions between the bulk Li and the electrolyte solvent, and introduces a thicker SEI film. Although Li₂O has been

reported in several studies for fostering the Li-ion exchange^{16,57}, our observations indicate that too much Li₂O is detrimental and impedes Li-ion kinetics between SEI and Li-metal; therefore, an optimum amount of Li₂O appears critical, especially near the Li-metal surface. In general, we observe that for the same plating areal capacity (1 mAh cm⁻²), the intensity of the Li-containing SEI species increases with the current density (**Fig. S3.17**), which corroborates that the high current density leads to denser deposition morphology^{23,58}.

The CP MAS ssNMR and XPS results present here reveal how the SEI components and their distribution are affected by current densities. At a reasonably high plating current density (2 mA cm⁻²), an anion-rich, i.e., LiF-rich, SEI is formed. Several studies have reported the relation between applied current densities and the SEI species and structure formed. At high rates, thicker and mosaic SEI structures are more likely to be formed, which implies that current density plays a crucial role in regulating the SEI properties, yet other parameters such as the electrolyte chemistry still need to be taken into account^{8,14,22,56}.

3.2.5 Quantification of the dead Li

With the aim of quantifying dead Li and SEI formation under the influence of varying formation current densities, operando ⁷Li NMR experiments are conducted and compared in four distinct electrochemical protocols, i.e., two formation cycles at 5, 2, 0.5, and 0.2 mA cm⁻², respectively, followed by three working cycles at 0.5 mA cm⁻², reaching a capacity of 1 mAh cm⁻² for each charge step. **Fig. 3.5 (a and d)** and **Fig. S3.20 (a and d)** show the contour plots of the operando ⁷Li NMR spectra together with the corresponding voltage profiles from the galvanostatic cycling. As displayed in these contour plots, all the cells form two co-existing Li-metal phases during the cycling. On the basis of the evolution of these phases, we can infer that phase I is from the Li-metal electrode (~245 ppm), and the emergence and diminishing of the Li signal of phase II directly correspond to the electrochemical plating and stripping of the Li metal (247 to 270 ppm)⁵⁹⁻⁶². The largest Li chemical shift span of phase II is observed in the cell (0.2 to 0.5 mA cm⁻²), which arises from the inhomogeneous Li deposits in the formation cycles (also seen in the uneven Li plating from the SEM image in **Fig. 3.1f**). This subsequently leads to severe accumulation of dead Li-metal in the working cycles. The individual ⁷Li NMR spectra have been extracted at the end of each charge and discharge step, where the Li intensity for each plating (discharging) step is much more constant and

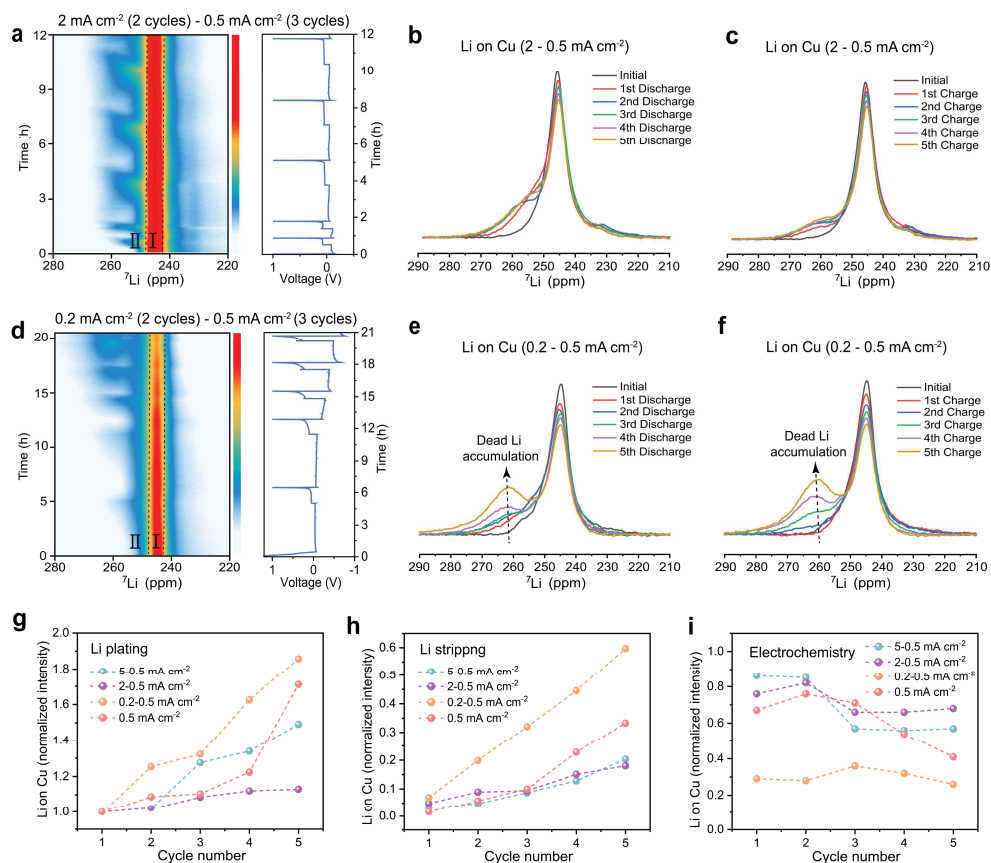


Fig. 3.5. Operando NMR study of the evolution of dead Li for the Li||Cu cells cycled with different formation current densities. (a and d) contour plots of the ${}^7\text{Li}$ NMR spectra acquired during the plating/stripping of Li-metal, along with the electrochemical voltage profile. Each cell was precycled at 2 or 0.2 mA cm^{-2} , respectively, for two cycles and followed by three working cycles at 0.5 mA cm^{-2} . The ${}^7\text{Li}$ NMR signals at the end of discharge (b and e) and charge (c and f) for the five cycles, along with the initial Li peak are plotted separately. Normalized intensities of the Li signal on Cu at the end of (g) plating and (h) stripping (the intensities were normalized to the observed plated-Li signal at the end of the first discharge), and (i) CEs obtained from the electrochemistry for the five cycles of the cells cycled at 5 to 0.5 mA cm^{-2} , 2 to 0.5 mA cm^{-2} , 0.2 to 0.5 mA cm^{-2} , and 0.5 mA cm^{-2} . Color bar indicates the intensity from weak to strong from bottom to top.

reversible for the cell pretreated by 2 mA cm^{-2} than the 0.2 mA cm^{-2} one (Fig. 3.5, b and e), while as comparisons, the cells cycled at 0.5 and 5 mA cm^{-2} experience an obvious buildup of Li metal intensity over the cycles as well (Fig. S3.18, b and e).

Observing that the resonance of the Li source overlaps to some extent with the signal of the plated Li on Cu, we decouple the Li on Cu resonance by fitting the individual components

in each spectrum for the end of charge (stripping) shown in **Fig. S3.19**. As expected, the cell precycled at 2 mA cm^{-2} shows the smallest increase in the Li-metal signal after stripping, indicating the smallest accumulation of dead Li (**Fig. 3.5c** and **Fig. S3.19b**); however, the cell cycled with a small formation current density (0.2 mA cm^{-2}) experiences pronounced dead Li accumulation, especially during the working cycles (**Fig. 3.5f** and **Fig. S3.19c**), while the control group (the cell activated and constantly cycled at 0.5 mA cm^{-2}) shows fast growth of dead Li during cycling (**Fig. S3.20c** and **S3.19d**). By contrast, the cell precycled at 5 mA cm^{-2} has much more dead Li generated in the initial cycles but with slower dead Li growth during following cycles (**Fig. S3.18f** and **S3.19a**).

The normalized integrated area of the ${}^7\text{Li}$ NMR peak of Li on Cu shows that the average plated Li signal detected by NMR (Li_{NMR}) at the end of the fifth discharge (plating) has increased $\sim 13\%$ for the cycled sample of 2 to 0.5 mA cm^{-2} [$(1.13-1) \times 100\% = 13\%$, normalized to the observed plated Li intensity at the end of the first discharge], where the accumulated dead Li accounts for roughly 18% of the initial charge Li signal at the end of the fifth charge (stripping) (**Fig. 3.5, g** and **h**, purple). At this point, the CE of 66 to 82% was realized over these five cycles (**Fig. 3.5i**, purple). In contrast, the cell using the 0.2 to 0.5 mA cm^{-2} displays a rapid linear accumulation of dead Li with each cycle, reaching a dead Li ratio for almost 85% at the end of the fifth discharge, resulting in a low CE around 30% (**Fig. 3.5, g** to **i**, orange). Also, for the cell (5 to 0.5 mA cm^{-2}), 49% dead Li was accumulated at the end of the fifth cycle, which corresponds to the low CE during the working cycles (**Fig. 3.5, g** to **i**, green). The stability of the cell cycled at continuous 0.5 mA cm^{-2} is somewhere in between (**Fig. 3.5, g** to **i**, red).

The efficiency of Li plating (lithium efficiency, LE_{Li}) can be estimated from the inactive Li_{NMR} intensity, combined with the CE measured from electrochemistry (**Table S3.1**), where the capacity loss caused by forming the SEI (SEI efficiency, CE_{SEI}) can also be reckoned (see **Supplementary Text S3.2**)^{37,38}. The LE_{Li} for the cell cycled at 5 to 0.5 mA cm^{-2} protocol is relatively constant but showing a gradual downward trend in the working cycles, which is reflected in the decreasing CE and the accompanying growth in CE_{SEI} (**Fig. S3.20a**). The LE_{Li} is constant and stabilizes at about 90% for the cell cycled at 2 to 0.5 mA cm^{-2} , where in the later three working cycles, the CE is lower due to extra SEI formation (**Fig. S3.20b**). Contrarily, most of the SEI was generated in the first two formation cycles for a formation

current density of 0.2 mA cm^{-2} , where the resulting Li aggregation is assumed to cause a sustained decline of LE_{Li} and consistently low CE over the cycles (**Fig. S3.20c**). Also, the LE_{Li} of the cell cycled at 0.5 mA cm^{-2} are continuously declining with low CE_{SEI} (**Fig. S3.20d**).

3.3 Discussion

The current density during the first formation cycles plays a critical role in controlling the properties of the initial SEI and Li deposition morphology, which strongly impacts subsequent Li plating and stripping. To investigate this, ssNMR was performed to quantify the equilibrium Li-ion exchange between the electrochemically deposited Li-metal (ED-Li) and the as-formed SEI. This includes the charge transfer under equilibrium conditions, the exchange current density, and diffusivity within the SEI. The results demonstrate that the charge transfer kinetics of the initially formed SEI contribute substantially to the efficiency of the subsequent Li-metal plating and stripping cycles. From the range of formation current densities investigated ($0.2, 0.5, 2,$ and 5 mA cm^{-2}), the optimal cell performance was obtained when applying a relative high current density (2 mA cm^{-2}), reflected by a stable CE of $\sim 96\%$ after 100 cycles in the standard 1 M LiPF_6 in EC/DMC electrolyte (**Fig. 3.1**). Visualizing the Li-ion exchange between the ED-Li and the initial as-formed SEI phases with 2D-EXSY ssNMR experiments reveals an increase in the Li-ion exchange with increasing formation current densities (**Fig. 3.2, c to f**). The Li-ion exchange was quantified by 1D-EXSY ssNMR experiments, where the lowest E_a for exchange between SEI and Li-metal was found for 2 mA cm^{-2} (**Fig. 3.3b**), correlating to the highest CE. This is consistent with Xu et al.²² who reported that Li||Cu cells have the lowest impedance at 2 mA cm^{-2} in the carbonate-based electrolyte system. This suggests that the exchange between Li-metal and SEI is a rate-limiting step during plating, dominating the formation of the Li-metal morphology. Moreover, the E_a for exchange reduces remarkably (from 44 up to 70%) upon subsequent cycling, indicating that the Li-ion exchange between Li-metal and SEI evolves, increasing upon subsequent cycling, thus improving ionic contact. This underlines that the SEI grown during the formation cycles has a lasting impact, also proposed by Oyakhire et al. and Lv et al.^{14,28}, where the porous SEI established during formation acts as template for the Li-metal plating upon repeated cycling.

Comparing the ED-Li microstructures visualized from the SEM and TEM images (**Fig.**

3.1f and **Fig. S3.1**), the more compact morphology, smaller particle size and thinner SEI for the sample directly plated at 2 mA cm^{-2} suggests homogenous Li-ion morphology. This is consistent with the results reported by Pei et al. and Zhang et al.^{23,29}, where the authors concluded that more uniform and smaller Li nuclei generated at higher C-rate leads to a more homogeneous and planar Li deposition morphology. Our observation of better Li-ion exchange kinetics between the SEI and Li-metal, suggests better ionic contact at the optimal formation current density. CP MAS ssNMR and XPS (**Fig. 3.4**) indicate that the composition of the SEI is responsible for the different Li exchange kinetics, which is maximum for the lowest amount of Li_2O and the largest amount LiF in the SEI (at 2 mA cm^{-2}). When the current density reaches 5 mA cm^{-2} , LiF is mainly distributed in the outer layer, which is consistent with the findings by Kanamura et al.⁶³. Although the roles of Li_2O and LiF in the SEI are still debateable^{16,64}, the results presented here indicate that a relatively small amount of Li_2O and larger amount of LiF in the SEI are beneficial for the Li-ion diffusion between the SEI and Li-metal, which is responsible for the improved reversibility of the cell. In addition, comparing the dead Li formation of the studied cycling protocols by the operando NMR experiments, the cell cycled at 2 to 0.5 mA cm^{-2} has the least dead Li buildup. The fast dead Li accumulation for the other cycling protocols could result from the impeded reversibility of Li deposition/stripping, caused by the high Li_2O -containing poorly conductive SEI.

As supported by the results above and schematically shown in **Fig. 3.6**, the initially formed SEI not only has a “template effect”, which can have a lasting impact on the subsequent cycles, but it also evolves during cycling, which is closely related to dead Li formation. By quantifying the fraction of dead Li-metal through operando NMR, we are able to correlate the SEI formation and dead Li formation with the different precycling protocols. Particularly, it certifies that the formation cycles contribute markedly to the overall cycling stability and the efficiency of Li-metal anodes. The irreversible capacity is mainly attributed to the as-formed SEI. This is consistent with the work reported by Gunnarsdóttir et al.³⁷. In all cases, there is SEI reformation and growth within each cycle; however, when first cycled with a higher current density (2 mA cm^{-2}), the Li capacity loss towards the SEI formation is minimal, whereas it is nearly four times larger at lower formation current densities (0.2 mA cm^{-2} ; see **Fig. S3.20**). For the subsequent working cycles the CE is apparently higher and more stable. This further verifies the lasting impact of formation cycles at different C-rates.

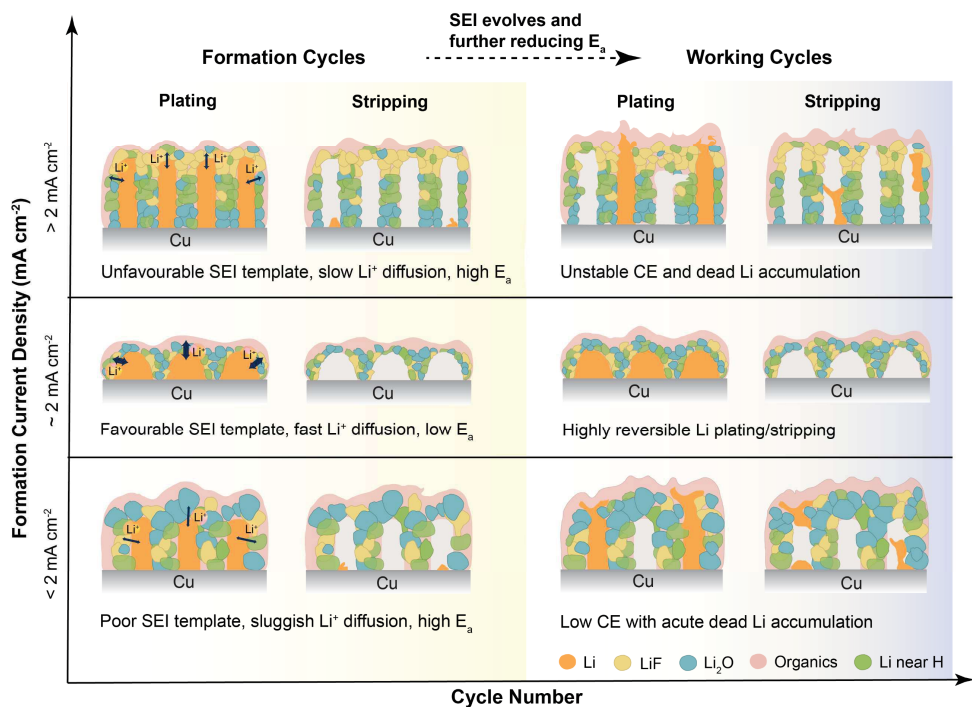


Fig. 3.6. Formation current density-dependent SEI templates and their lasting impact on subsequent cycling.

The different SEI formation rates arise from the distinct morphologies of the Li-metal deposits and the ionic pathways generated under different electrochemical conditions. Therefore, the Li-ion diffusion kinetics highly depend on the degree of passivation and surface area of the ED-Li and the as-formed SEI. During electrochemical preconditioning, the initial SEI forms a template that lasts (**Fig. 3.6**), in which Li nucleation can be assumed to take place on subsequent cycling, affecting the Li plating/stripping efficiency. Although increasing the current density is generally expected to favor a dendritic morphology, within the specific current range studied, an intermediate rate leads to denser Li nuclei distribution and smooth ED-Li surface because of the formation of a favorable SEI at this formation current density, which is beneficial for the long-term stability and reversibility of the LMBs (**Fig. 3.6**). This optimal C-rate can be expected to depend on the electrolyte system. For example, a smaller formation current density (0.5 mA cm^{-2}) leads to the best cycling performance for the weakly solvating electrolyte, 1 M lithium bis(fluorosulfonyl)imide salt

in fluorinated 1,4-dimethoxybutane solvent (1 M LiFSI/FDMB)¹⁴. The Li-ion diffusion kinetics of the SEI and the lasting effect of formation cycles on the subsequent cycling have not been experimentally reported to the best of our knowledge. Combining the cell performance and the local Li-ion diffusion kinetics, the present results provide insight in how electrochemical preconditioning can affect the overall battery performance by influencing the chemical composition and distribution of the SEI.

3.4 Conclusions

In conclusion, a combination of various experimental techniques has been used to provide a dynamic-resolved and quantitative analysis of the lasting influence of the formation current density on Li-metal anodes. Combining ssNMR with SEM, TEM, and XPS, the chemical composition and microstructure of the as-formed SEI are revealed. The spontaneous diffusion of Li-ions between electrochemically deposited Li-metal and the as-formed SEI is disclosed, reflecting a large dependence on the formation current density. Applying an intermediate high formation current density (2 mA cm^{-2}) leads to higher Li-ion mobility between SEI and Li-metal. The denser Li microstructure and favorable chemical SEI composition enable more homogeneous Li deposition and less inactive/dead Li formation. The lasting impact of this initial SEI facilitates Li-ion diffusion between the separate solid phases effectively, which creates ideal conditions for subsequent cycling and gives rise to great improvement of the stability and efficiency of the Li-metal anode. The present work provides in-depth understanding of the formation cycles in LMBs, where the spontaneous Li-ion diffusion dynamics between Li-metal and the SEI can be a potential guide in conjunction with other battery optimization strategies, such as electrolyte design, current collector engineering, and new electrode materials development. Beyond that, the present work could be further extended to solid-state electrolyte systems and other redox chemistries.

3.5 Methods

Batteries assembly and electrochemical testing

The Li||Cu cells were assembled with Li disk (~500 μm thick; Sigma-Aldrich) and Cu foil (~11 μm thick; > 99.99%; MTI Corporation) as electrodes and a polyethylene (PE) (Celgard

2400) separator and a piece of glass fiber (Whatman GF/D) as separators (after being dried in vacuum at 80 °C for more than 24 hours). The electrolytes used were (i) conventional carbonate-based 1 M LiPF₆ in EC/DMC [1:1 (w/w); Sigma-Aldrich], (ii) 1 M LiPF₆ in EC/DMC [1:1 (w/w)] with 10 wt% FEC and 1 wt% VC (Dodochem Co., Ltd.), (iii) 1 M LiTFSI in DOL/DME [1:1 (w/w); Dodochem Co., Ltd.], and (iv) 1 M LiTFSI in DOL/DME [1:1 (w/w)] with 5 wt% LiNO₃ (Dodochem Co., Ltd.). Cell assembly, disassembly, and handling of air sensitive materials were done in an Argon-filled glovebox (O₂ < 1 ppm, H₂O < 0.1 ppm).

Galvanostatic cycling was performed on a Maccor 4000 battery cycler or a Land CT2001A at room temperature by deposition of Li onto the Cu working electrode with different current densities up to a total capacity of 1 mAh cm⁻², followed by Li stripping at different current densities up to 1 V. The EIS measurements were obtained using an Autolab PGSTAT302N in the frequency range 1 MHz to 0.1 Hz with a sinusoidal signal with $V_{rms} = 10$ mV. The EIS spectra were fitted with an Equivalent Circuit (EC) model by RelaxIS 3, where R_{SEI} is the SEI resistance, R_{ct} is the charge-transfer resistance, CPE is constant phase element, the respective CPE describes the capacitance of the corresponding process, and W is Warburg diffusion term.

Solid-state NMR measurements

Individual samples were prepared by plating Li on Cu foil with different current densities (0.2, 0.5, 1, 2, and 5 mA cm⁻²) to a total amount of Li to 10 mAh cm⁻² (electrodeposited samples) or plated to 10 mAh cm⁻² at 0.5 mA cm⁻² after a specific cycling procedure (cycled samples). After plating, the cells were disassembled in the glovebox and the plated electrodes were washed by dipping into DMC solvent for three to five times to remove residual electrolyte, and then the electrodes were dried in a vacuum chamber to evaporate the solvent. The ED-Li and SEI were removed from the Cu foil using a razor blade, and mixed with KBr (dried in vacuum for two weeks at 80 °C before bringing into glovebox) using a mortar and pestle in the glovebox to limit peak broadening caused by the paramagnetic nature of lithium and reduce eddy currents⁶⁵. The mixture was transferred into the 3.2 mm rotor and sealed with a Vespel cap.

All ssNMR measurements were performed on a Bruker Ascend 500 MHz magnet ($B_0 =$

11.7 T) with an NEO console operating at frequencies of 194.37 MHz for ${}^7\text{Li}$, 73.6 MHz for ${}^6\text{Li}$, 500.130 MHz for ${}^1\text{H}$, 470.385 MHz for ${}^{19}\text{F}$, and 125.758 MHz for ${}^{13}\text{C}$. ${}^6,{}^7\text{Li}$ chemical shifts were referenced with respect to a 0.1 M LiCl solution (0 ppm), ${}^1\text{H}$ and ${}^{13}\text{C}$ chemical shifts were referenced in regard to solid adamantane (${}^1\text{H}$ at 1.81 ppm and ${}^{13}\text{C}$ at 38.48 ppm), and ${}^{19}\text{F}$ was referenced to LiF at 204 ppm. A Bruker three-channel MAS 3.2 mm direct variable temperature (DVT) probe was used for all the measurements. The samples were filled into 3.2 mm zirconia rotors, and a MAS frequency of 15 kHz was applied.

One-pulse ${}^7\text{Li}$, ${}^6\text{Li}$, and ${}^{19}\text{F}$ experiments were performed with $\pi/2$ pulse lengths of 4.76, 6, and 3.05 μs , respectively. A recycle delay of about four times T_1 was used for each nuclei, where the T_1 was determined using saturation recovery experiments. ${}^7\text{Li}$ - ${}^7\text{Li}$ 2D-EXSY measurements were performed with a mixing time of 150 ms. All 2D spectra consist of eight scans for each of the 1,950 transients, and each transient was incremented by 6.67 μs .

VT ${}^7\text{Li}$ 1D-EXSY measurements were performed with a recycle delay of 8 s per mixing time (T_{mix}), and T_{mix} was varied between 0.01 ms and 0.1 s with totally 16 time intervals (since the exchange reaches the maximum before $T_{\text{mix}} = 0.06$ s, the normalized intensities of $T_{\text{mix}} > 0.06$ s are reduced in order to obtain better fitting). The pulse sequence with the appropriate phase cycle for cancelation of direct magnetization that may occur after T_1 relaxation has been described in detail elsewhere^{44,48}, which consists of $\pi/2$, τ , π , τ , $-\pi/2$, T_{mix} , $+\pi/2$, and acquisition, with $\pi/2$ pulse length = 5.4 μs . An echo time τ ranging from 200 to 800 μs was used to filter out the SEI resonance with a short T_2 , effectively functioning as a T_2 filter. For each sample, these ${}^7\text{Li}$ 1D-EXSY experiments were performed at five different temperatures (283, 298, 313, 328, and 343 K).

${}^{19}\text{F}$ - ${}^7\text{Li}$ CP MAS experiments were performed with a radio frequency (r.f.) field strengths of 82 kHz and a ramped (90 to 100%) amplitude of ${}^{19}\text{F}$ during CP. A contact time of 200 μs was used, with a recycle delay of 2 s and between 1,024 and 2,048 scans. For ${}^1\text{H}$ - ${}^7\text{Li}$ CP MAS experiments, a radio frequency (r.f.) field strengths of 81 kHz and contact times of 3 ms were utilized, the r.f. field amplitude of ${}^1\text{H}$ during CP experiments was ramped from 70 to 100%, and 10,240 scans were acquired for each sample with a recycle delay of 1 s. The ${}^1\text{H}$ - ${}^{13}\text{C}$ CPMAS experiments were measured with an initial ${}^1\text{H}$ $\pi/2$ pulse of 3.86 μs . During the CP measurements for ${}^{13}\text{C}$, an r.f. field strength of 64 kHz was utilized and 10,240 scans were acquired for each sample with a recycle delay of 10 s.

Operando NMR measurements

Li-metal disk of 0.4×0.7 (cm²) and Cu foil of 0.5×1 (cm²) were used to assemble the operando Li||Cu half-cells. One Celgard 2300 separator and one piece of glass fiber (Whatman GF/D) were used as separators. A 1 M LiPF₆ in EC/DMC [1:1 (w/w)] electrolyte (25 μ L) was added in the cells. Operando NMR experiments were conducted at ambient temperature on a Bruker Avance 500 MHz using a solenoidal Ag-coated Cu coil, which was synchronized with the external electrochemical cyler. The spectra were recorded using an in situ automatic tuning and matching probe (ATM VT X in situ WB NMR probe, NMR Service) that allows for an automatic recalibration of the NMR r.f. circuit during an operando electrochemical measurement. To quantify the operando NMR signal, the automatic retuning of the r.f. circuit is essential because the sample conditions are keep changing during the electrochemical process. The probe is equipped with highly shielded wire connections to the electrochemistry with low-pass filters (5 MHz) attached to the probe, minimizing the interferences between the NMR and the electrochemical test circuit, details are described elsewhere⁶⁶. Single-pulse experiments were used to collect the operando NMR spectra, with a recycle delay of 2 s and 256 transients recorded. This leads to an experimental time of each spectrum for about 4.5 minutes. The shift of ⁷Li was internally referenced to Li-metal at 245 ppm. The acquired series of spectra were processed in the Bruker Topspin software using the phase and baseline correction. Further data processing was done in MestReNova 11.0.

SEM, XPS, and TEM characterizations

For SEM imaging, the samples were transferred into an SEM (JEOL JSM-6010LA) machine under dry Argon conditions by an air-tight Argon-filled sample holder. The images were taken using an accelerating voltage of 10 kV (secondary electron). XPS measurements were performed with a Thermo Fisher K-Alpha spectrometer to investigate the chemical compositions of the plating electrodes. The samples were transferred into the XPS machine under vacuum using an air-tight sample holder. The spectrometer is equipped with a focused monochromatic Al α source (1486.6 eV) anode operating at 36 W (12 kV, 3 mA) and a flood gun operating at 1 V (100 μ A). The base pressure of the analysis chamber was approximately 2×10^{-9} mbar and the spot size was approximately 800×400 (μ m²). Depth profiling was performed with an Ar⁺ ion gun operated at 3kV, corresponding to 0.5 nm s⁻¹ as calibrated on

Ta₂O₅ and a pass energy of 200 eV was used. In the analysis, the binding energy was corrected for the charge shift relative to the primary C 1s hydrocarbon peak at $BE = 284.8$ eV. For each sample, at least three points were measured, which showed similar results. The data were fitted using 70% Gaussian and 30% Lorentzian line shapes (weighted least squares fitting method) and nonlinear Shirley-type background using the Thermo Fisher Avantage software. TEM experiments were performed on transmission electron microscope (TEM) (Tecnai G2, FEI, USA) operated at 60 kV.

For both the SEM and XPS characterizations, the Li-metal-plated electrodes were prepared by charging the Li||Cu half cells to a capacity 1 mAh cm⁻² at variable current densities. The Cu foils with plated Li were rinsed with DMC for three to five times to remove the residual electrolyte in the glove box under a dry argon atmosphere and dried in a vacuum chamber. For the TEM experiments, a lacey carbon TEM grid was put on a Cu foil working electrode and assembled into Li||Cu cells in an Argon-filled glovebox. The cells were charged to 1 mAh cm⁻² capacity at variable current densities, and then the TEM grid was taken out by disassembling the cells for measurement. The TEM grid was carefully transferred into the TEM holder in the glovebox with a specialized shutter to prevent air exposure.

3.6 Supplementary information

Supplementary Texts

Text S3.1: Quantification of interphases exchange

Quantification of exchange between the electrodeposited Li-metal and the as-formed SEI was performed by fitting the growing SEI signal to a diffusion model where in a solution to Fick's law for diffusion is determined $\frac{\partial m(\vec{r}, \vec{t})}{\partial t} = \vec{\nabla} \cdot \{D(\vec{r})m(\vec{r}, \vec{t})\}$, where $m(\vec{r}, \vec{t})$ is the magnetization of Li at position \vec{r} and t , and D is the Li-ion self-diffusion coefficient. By using the mathematical models of Schmidt-Rohr and co-workers for spin diffusion, and by assuming the overall diffusivity to be equal to the effective diffusion coefficient, the rate of demagnetization of Li-ions in the Li-metal can be set equal to the initial magnetization minus the rate of magnetization in the SEI. Assuming a SEI phase embedded in an infinite Li-metal phase, this leads to the following analytical expression for the rate of demagnetization from the Li-metal into SEI as:

$$m(t_{mix}) = 1 - \left\{ \frac{m_0}{2} \sqrt{4Dt_{mix}} \left[\text{ierfc} \left(\frac{d}{\sqrt{4Dt_{mix}}} \right) + \text{ierfc} \left(\frac{-d}{\sqrt{4Dt_{mix}}} \right) - \frac{2}{\sqrt{\pi}} \right] \right\}^3 \quad (3.1)$$

where $\text{ierfc}(x) = 1/\sqrt{\pi} \exp(-x^2) - x[l - \text{erf}(x)]$ and d is the Li diffusion distance from the SEI phase to the Li-metal.

Text S3.2: Calculation of SEI efficiency and Li efficiency

The capacity loss of the electrochemistry originating from the SEI formation and inactive Li accumulation, therefore, the capacity loss caused by forming SEI can be estimated from the NMR detected inactive (dead) Li.

Coulombic efficiency (CE) from the electrochemical process is given by:

$$CE = \frac{C_{stripping}}{C_{plating}} \quad (3.2)$$

where $C_{plating}$ is the capacity obtained by discharging the Li||Cu cell under specific current densities till a total capacity of 1 mAh cm⁻². $C_{stripping}$ is the capacity obtained by charging the cell to a cut-off voltage of 1 V.

Therefore, the loss of CE from the electrochemistry (CE_{loss}) is:

$$CE_{loss} = 1 - CE = CE_{dead Li} + CE_{SEI} \quad (3.3)$$

where $CE_{dead Li}$ is the CE loss resulted from the generation of irreversible Li, CE_{SEI} is the CE loss caused by SEI formation.

Therefore, $CE_{dead Li}$ and CE_{SEI} for cycle n [$n = 1, 2, 3, 4, 5$, DC = discharge (plating), C = charge (stripping)] are:

$$CE_{dead Li, n} = \frac{Li_{end of C, n} - Li_{end of C, n-1}}{Li_{end of DC, n} - Li_{end of C, n-1}} \quad (3.4)$$

$$CE_{SEI, n} = CE_{loss, n} - CE_{dead Li, n} \quad (3.5)$$

where $Li_{end of C, n}$ is the NMR detected Li signal at the end of charge (stripping) of the cycle n , $Li_{end of DC, n}$ is the NMR detected Li signal at the end of discharge (plating) of the cycle n .

The Li efficiency (LE_{Li}) during cycle n is:

$$LE_{Li, n} = 1 - CE_{dead Li, n} \quad (3.6)$$

This Li efficiency is obtained based on the dead Li signal detected by NMR. The difference between the LE_{Li} and the CE is the capacity loss caused by SEI formation^{1,2}, then it leads to:

$$LE_{Li, n} = CE_n + CE_{SEI, n} \quad (3.7)$$

Take the first cycle of the 2 to 0.5 mA cm⁻² cell as an example. Based on the electrochemical test (**Fig. 3.5a**), the CE for the first cycle is:

$$CE = 76\%$$

$$CE_{loss} = 1 - CE = 24\%$$

According to the operando ⁷Li NMR measurement:

$$CE_{dead Li} = \frac{Li_{end\ of\ C}}{Li_{end\ of\ DC}} = \frac{0.049}{0.416} \times 100\% = 11.8\%$$

(0.049 and 0.416 are the normalized intensities of the Li signal on Cu at the end of charge and discharge of the first cycle.)

$$CE_{SEI} = CE_{loss} - CE_{dead Li} = 24\% - 11.8\% = 12.2\%$$

The LE_{Li} of the first cycle is:

$$LE_{Li} = 1 - CE_{dead Li} = 100\% - 11.8\% = 88.2\%$$

Supplementary Figures

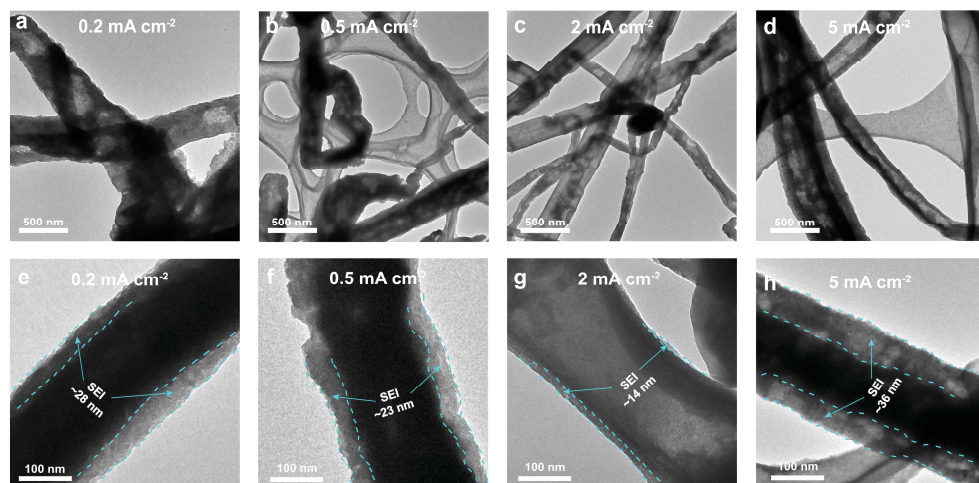


Fig. S3.1. Bright field TEM images of the ED-Li and the SEI plated at different current densities. (a and e) 0.2 mA cm⁻², (b and f) 0.5 mA cm⁻², (c and g) 2 mA cm⁻², and (d and h) 5 mA cm⁻². With dotted lines marking the SEI in (e) to (h).

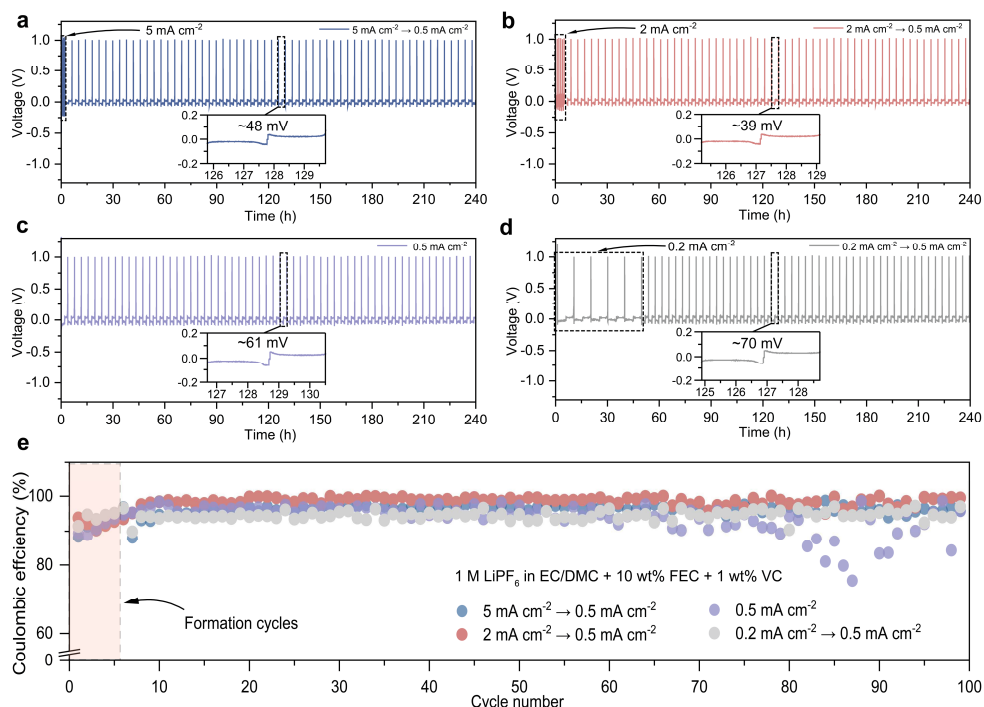


Fig. S3.2. Electrochemical characterization of the LMBs cycled with different formation current densities using 1 M LiPF₆ in EC/DMC + 10 wt% FEC + 1 wt% VC electrolyte. Galvanostatic

cycling performance and polarization profiles of the Li||Cu cells cycled at: (a) 5 to 0.5 mA cm⁻², (b) 2 to 0.5 mA cm⁻², (c) 0.5 mA cm⁻², and (d) 0.2 to 0.5 mA cm⁻². Five formation cycles were applied in advance and Li was electrodeposited to a capacity of 1 mAh cm⁻² for each plating step, inserts are the enlarged view of the voltage profiles at 125 to 131 h, indicating the overpotential values. (e) Comparison of the corresponding CE for the Li||Cu cells cycled at the current densities given in (a) to (d).

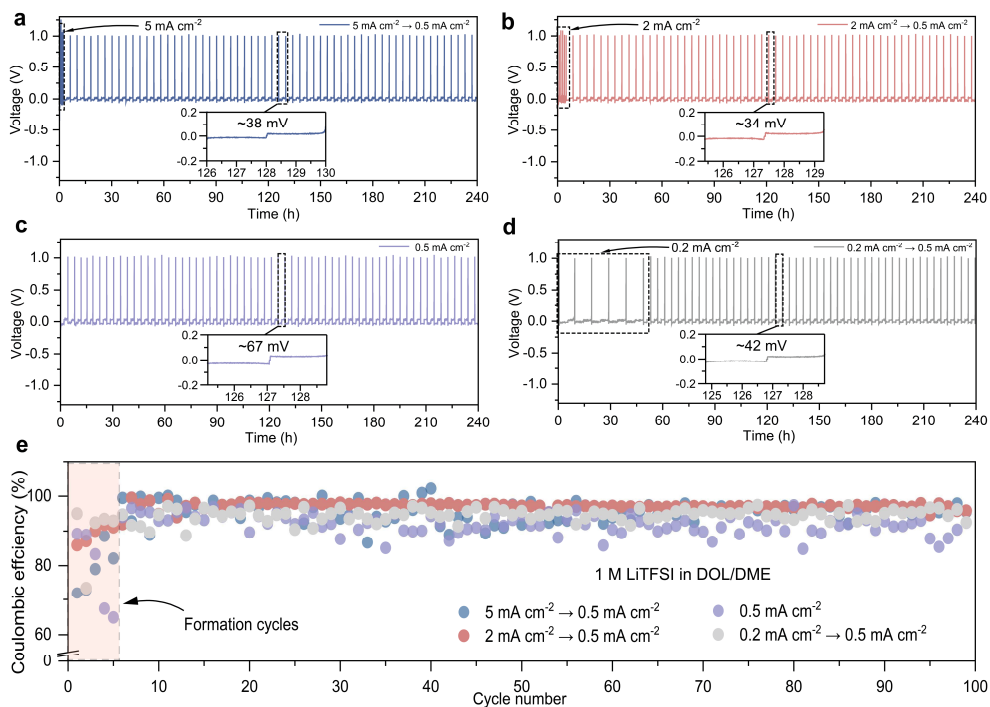


Fig. S3.3. Electrochemical characterization of the LMBs cycled with different formation current densities using 1 M LiTFSI in DOL/DME electrolyte. Galvanostatic cycling performance and polarization profiles of the Li||Cu cells cycled at: (a) 5 to 0.5 mA cm⁻², (b) 2 to 0.5 mA cm⁻², (c) 0.5 mA cm⁻², and (d) 0.2 to 0.5 mA cm⁻². Five formation cycles were applied in advance and Li was electrodeposited to a capacity of 1 mAh cm⁻² for each plating step, inserts are the enlarged view of the voltage profiles at 125 to 130 h, indicating the overpotential values. (e) Comparison of the corresponding CE for the Li||Cu cells cycled at the current densities given in (a) to (d).

3. The Lasting Impact of Formation Cycling on the Li-ion Kinetics Between SEI and the Li-metal Anode and Its Correlation with Efficiency

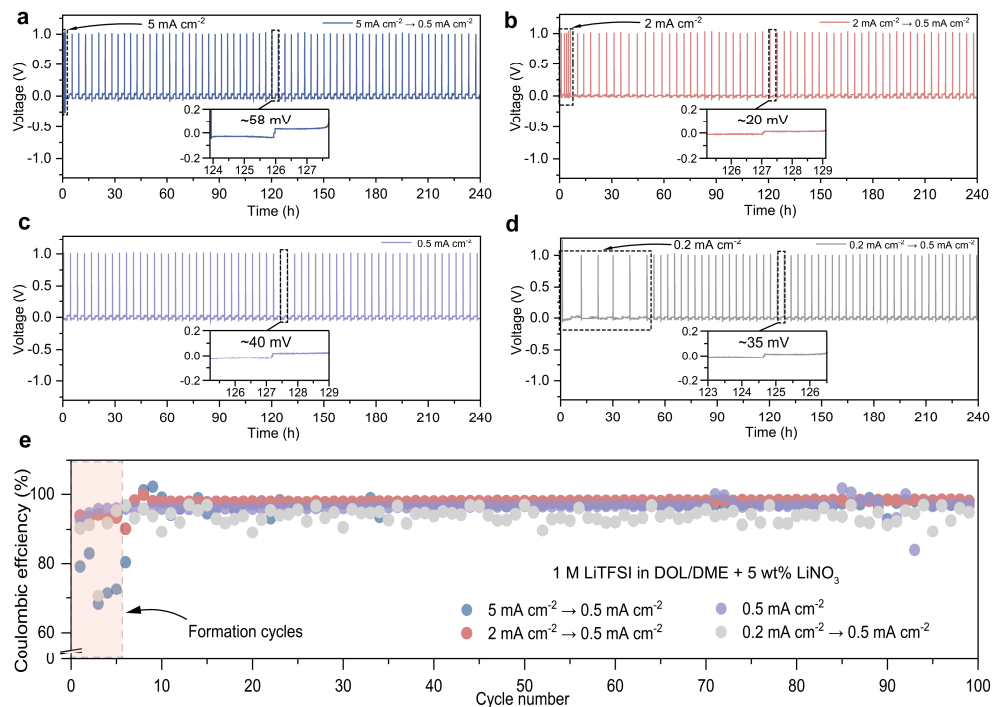


Fig. S3.4. Electrochemical characterization of the LMBs cycled with different formation current densities using 1 M LiTFSI in DOL/DME + 5 wt% LiNO₃ electrolyte. Galvanostatic cycling performance and polarization profiles of the Li||Cu cells cycled at: (a) 5 to 0.5 mA cm⁻², (b) 2 to mA cm⁻², (c) 0.5 mA cm⁻², and (d) 0.2 to 0.5 mA cm⁻². Five formation cycles were applied in advance and Li was electrodeposited to a capacity of 1 mAh cm⁻² for each plating step, inserts are the enlarged view of the voltage profiles at 125 to 130 h, indicating the overpotential values. (e) Comparison of the corresponding CE for the Li||Cu cells cycled at the current densities given in (a) to (d).

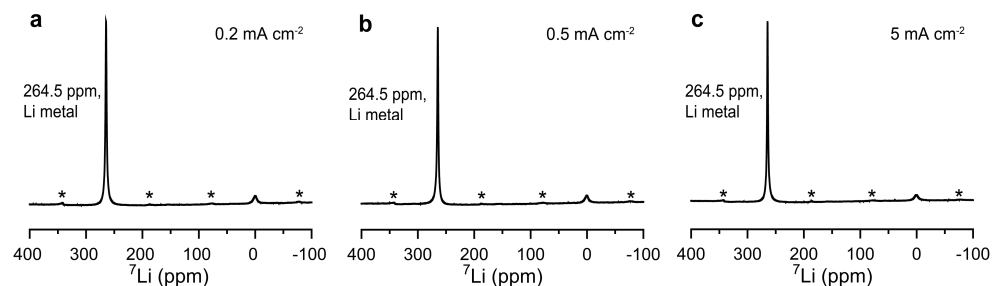


Fig. S3.5. 1D ⁷Li MAS spectra of the ED-Li and the SEI. (a) 0.2 mA cm⁻², (b) 0.5 mA cm⁻², and (c) 5 mA cm⁻². Asterisks denote spinning sidebands.

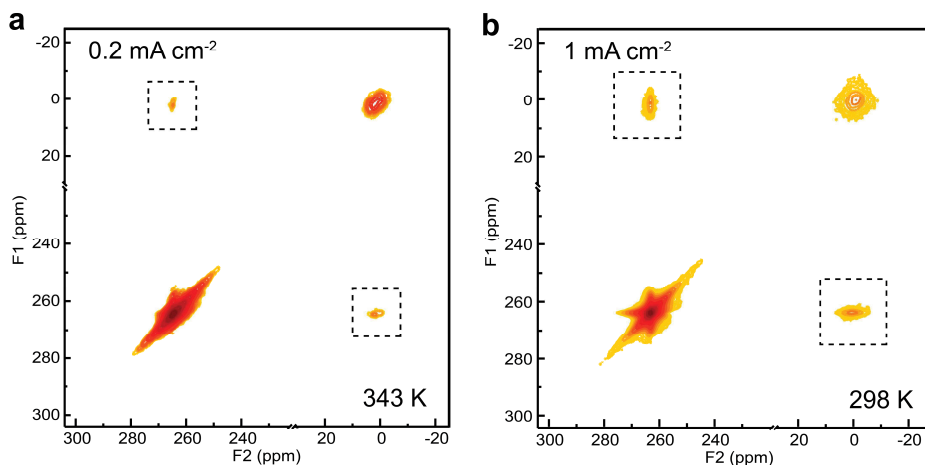


Fig. S3.6. ${}^7\text{Li}$ - ${}^7\text{Li}$ 2D ssNMR exchange experiments measuring Li-ion transport between the electrodeposited Li (ED-Li) and the as-formed SEI. ${}^7\text{Li}$ - ${}^7\text{Li}$ 2D-EXSY of the ED-Li and the SEI formed at: (a) 0.2 mA cm^{-2} (ED-0.2) and (b) 1 mA cm^{-2} (ED-1) at $T_{\text{mix}} = 150 \text{ ms}$, among them the ED-0.2 was measured at 343 K, the ED-1 was measured at 298 K.

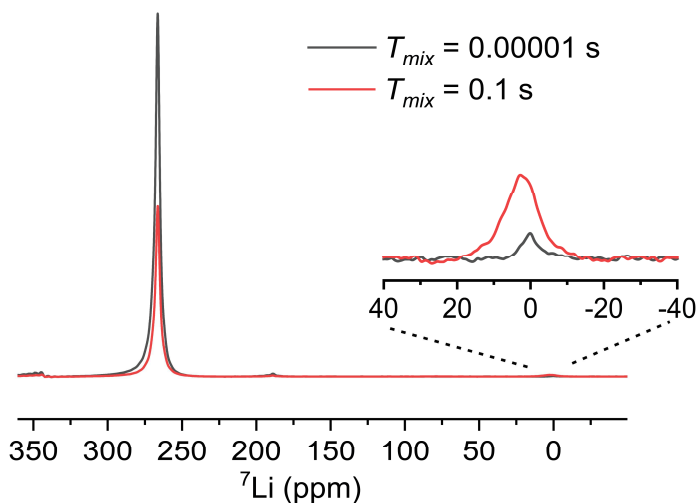


Fig. S3.7. 1D spectra of the first ($T_{\text{mix}} = 0.00001\text{s}$) and last ($T_{\text{mix}} = 0.1\text{s}$) slices of the ${}^7\text{Li}$ 1D-EXSY experiment. Sample shown here is ED-2 at 298 K.

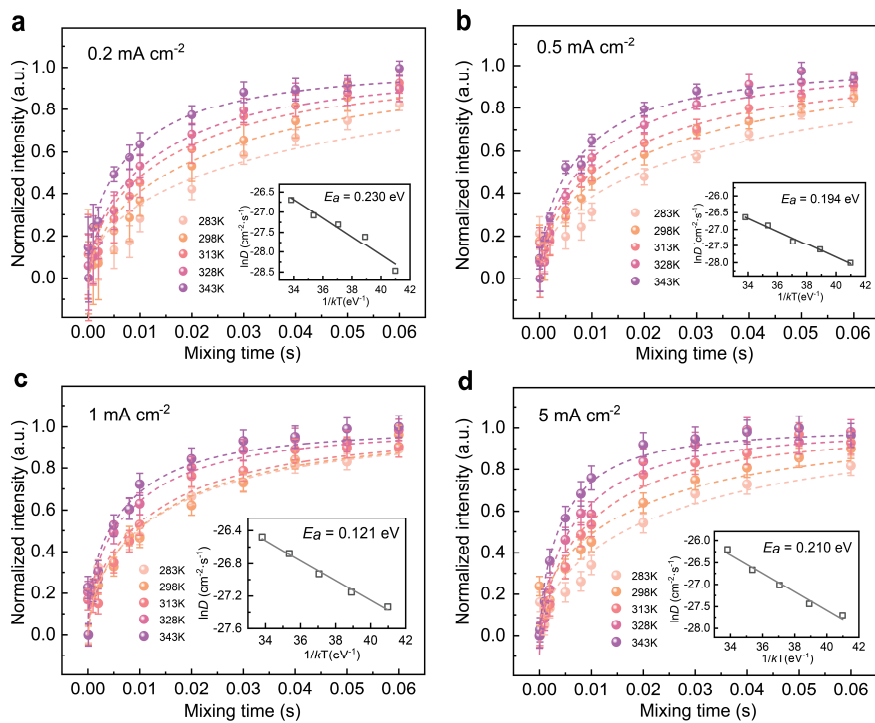


Fig. S3.8. ^7Li 1D-EXSY measurements of the ED-Li and the SEI. (a) 0.2 mA cm^{-2} , (b) 0.5 mA cm^{-2} , (c) 1 mA cm^{-2} , and (d) 5 mA cm^{-2} . Error bars represent the standard deviation of the spectrum noise.

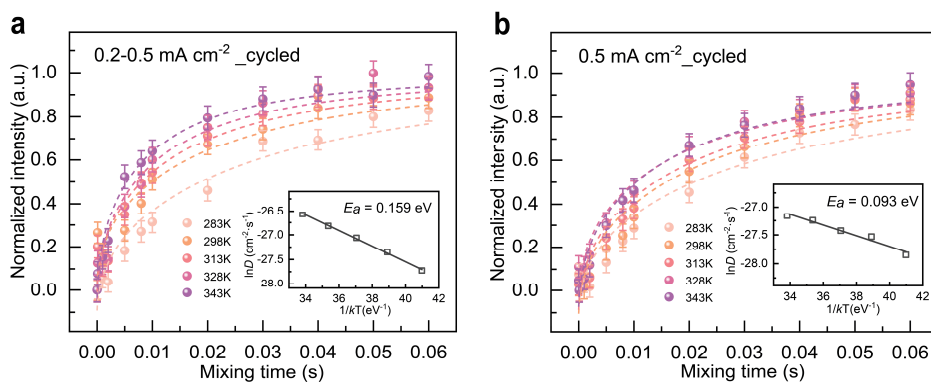


Fig. S3.9. ^7Li 1D-EXSY measurements of the ED-Li and the SEI from the cycled samples. (a) $0.2\text{-}0.5 \text{ mA cm}^{-2}$, (b) 0.5 mA cm^{-2} . Five formation cycles at 0.2 mA cm^{-2} are first employed, followed by ten cycles at 0.5 mA cm^{-2} . One final deposition process at 0.5 mA cm^{-2} is adopted at the end of the cycles to keep the sample amount consistent. Error bars represent the standard deviation of the spectrum noise.

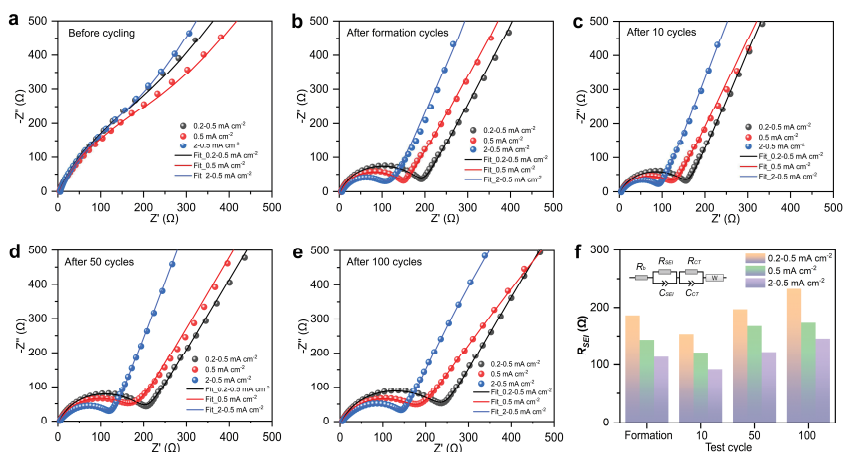


Fig. S3.10. EIS measurements of the cells cycled with different formation current densities. (a) Before cycling and after (b) 5 formation cycles, (c) 10 working cycles, (d) 50 working cycles, and (e) 100 working cycles. (f) comparison of SEI resistance after formation and 10, 50, 100 working cycles. Insert is the equivalent circuit. R_b is the bulk electrolyte resistance, R_{SEI} is the SEI resistance, R_{ct} is the charge-transfer resistance, CPE is constant phase element, the respective CPE describes the capacitance of the corresponding process, and W is Warburg diffusion term.

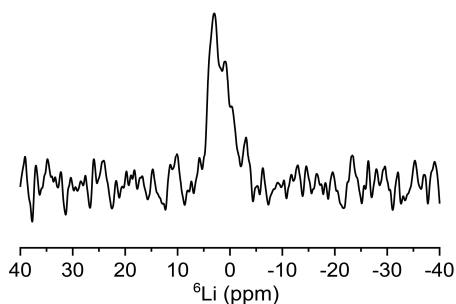


Fig. S3.11. 1D single-pulse ⁶Li spectrum of the SEI from the sample plated at 2 mA cm⁻² (ED-2).

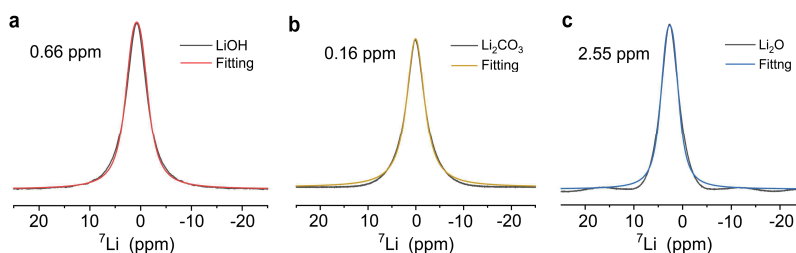


Fig. S3.12. 1D single-pulse ⁷Li spectra. (a) LiOH, (b) Li₂CO₃, and (c) Li₂O.

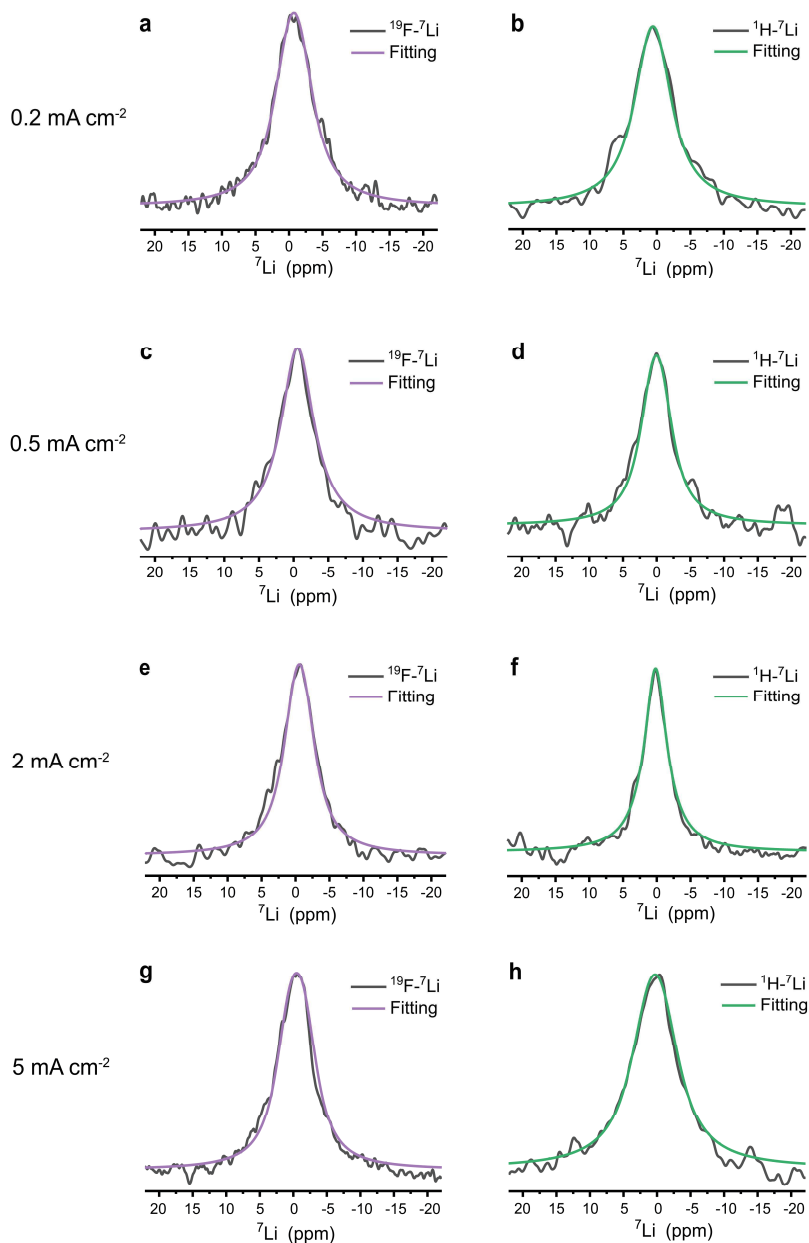


Fig. S3.13. CP MAS spectra and the fitting of $^{19}\text{F} \rightarrow ^7\text{Li}$, $^1\text{H} \rightarrow ^7\text{Li}$ of the SEI peak plated at different current densities. (a and b) 0.2 mA cm⁻², (c and d) 0.5 mA cm⁻², (e and f) 2 mA cm⁻², and (g and h) 5 mA cm⁻².

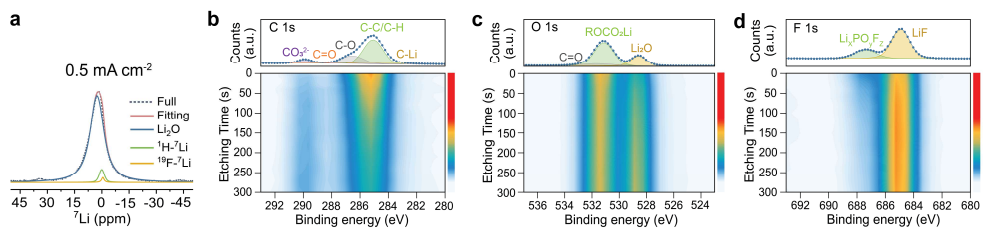


Fig. S3.14. Determining the composition of the SEI on ED-Li initially plated at 0.5 mA cm^{-2} using ssNMR and XPS. (a) SEI peak deconvolution for the plating current densities of 0.5 mA cm^{-2} by combining the fitting of the CP MAS spectra of ${}^1\text{H}\text{-}{}^7\text{Li}$ (Li near H), ${}^{19}\text{F}\text{-}{}^7\text{Li}$ (Li near F) and one-pulse measurement of bulk Li_2O . Depth-profiled XPS measurements of (b) C 1s, (c) O 1s, and (d) F 1s for the ED-Li and SEI plated on Cu at 0.5 mA cm^{-2} . Color bar indicates the intensity from weak to strong from bottom to top.

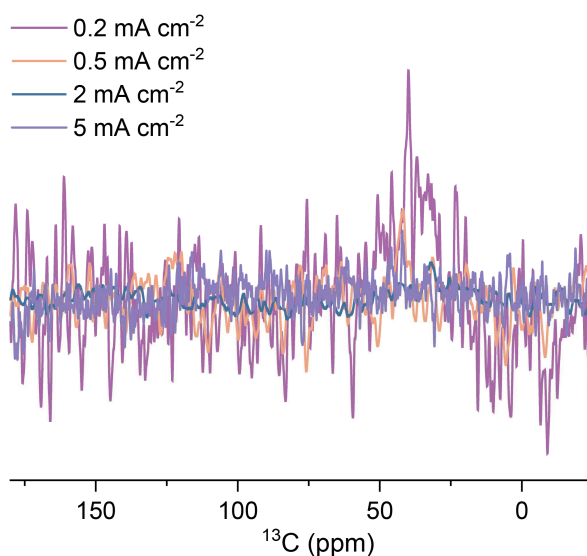


Fig. S3.15. ${}^1\text{H}\text{-}{}^{13}\text{C}$ CP MAS NMR spectra of the ED-Li and the corresponding SEI on plating at 0.2 , 0.5 , 2 , and 5 mA cm^{-2} , respectively.

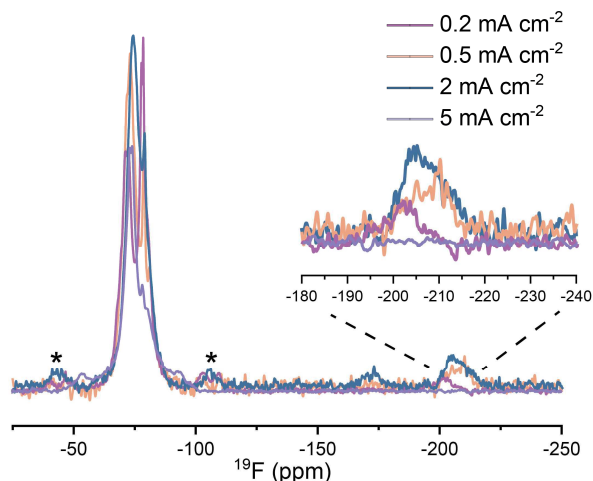


Fig. S3.16. 1D single-pulse ^{19}F spectra of the ED-Li and the corresponding SEI on plating at 0.2, 0.5, 2, and 5 mA cm^{-2} , respectively. Asterisks denote spinning sidebands.

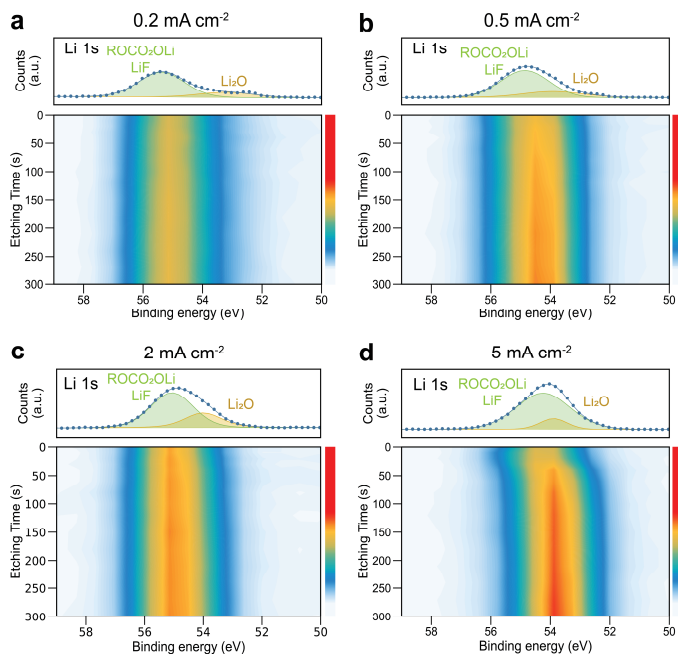


Fig. S3.17. Depth-profiled XPS measurements of Li 1s for the ED-Li plated on Cu. (a) 0.2 mA cm^{-2} , (b) 0.5 mA cm^{-2} , (c) 2 mA cm^{-2} , and (d) 5 mA cm^{-2} . Color bar indicates the intensity from weak to strong from bottom to top.

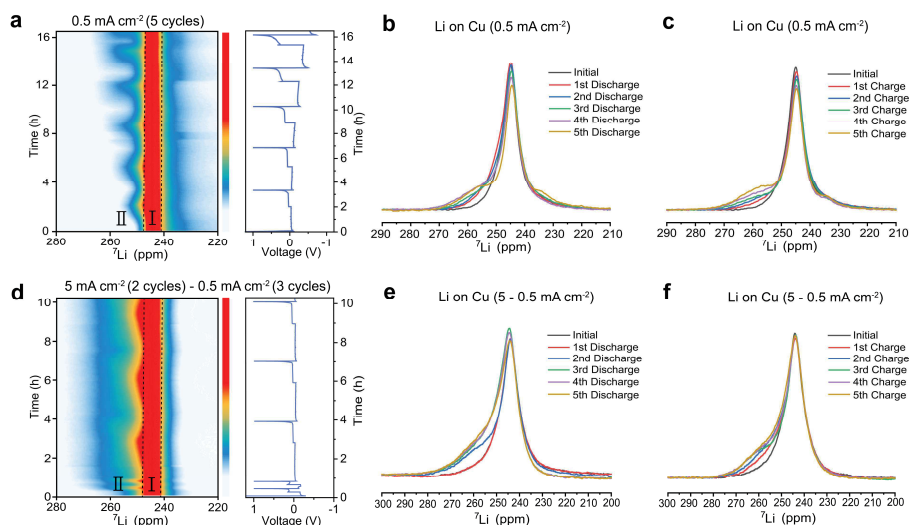


Fig. S3.18. Operando NMR study of the evolution of dead Li for the Li||Cu cells cycled with different formation current densities. Contour plots of the ${}^7\text{Li}$ NMR spectra acquired during the plating and stripping of Li metal at (a) 0.5 mA cm^{-2} , and (b) 5 to 0.5 mA cm^{-2} (precycled at 5 mA cm^{-2} for two cycles and followed by three working cycles at 0.5 mA cm^{-2}), along with the electrochemical voltage profile. ${}^7\text{Li}$ NMR spectra at the end of (b and e) discharge and (c and f) charge for the five cycles, along with the initial Li peak. Color bar indicates the intensity from weak to strong from bottom to top.

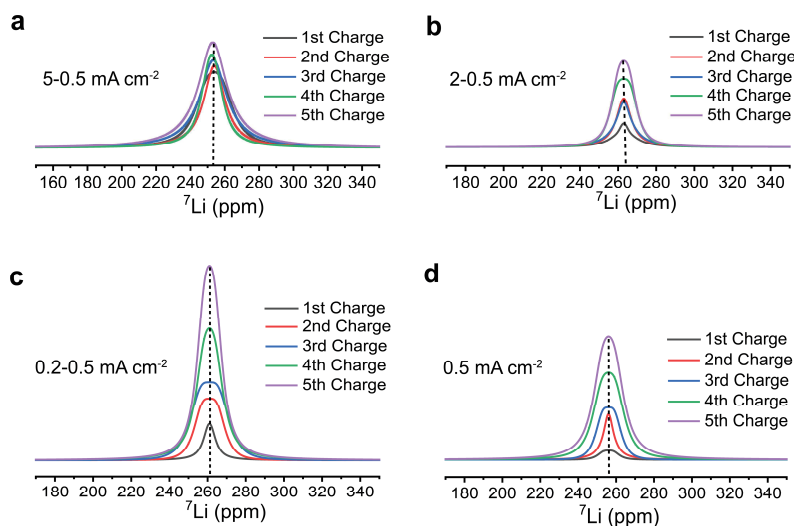


Fig. S3.19. ${}^7\text{Li}$ NMR signals at the end of charge (stripping) of the operando NMR cells. (a) 5 to 0.5 mA cm^{-2} , (b) 2 to 0.5 mA cm^{-2} , (c) 0.2 to 0.5 mA cm^{-2} , and (d) 0.5 mA cm^{-2} . The spectra are extracted from the fitting results of the corresponding ${}^7\text{Li}$ NMR slices for the cells cycled in Fig. 3.5. a and d, and Fig. S18. a and d, respectively.

3

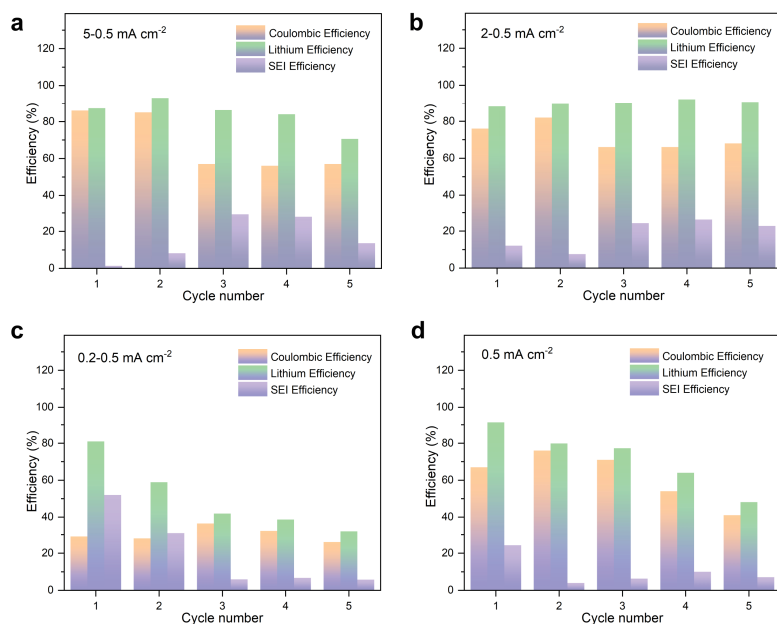


Fig. S3.20. Lithium efficiency (LE_{Li}) and SEI efficiency (CE_{SEI}) obtained from the operando NMR measurements, and CE from the electrochemistry of the cells cycled with different formation current densities. (a) 5 to 0.5 mA cm⁻², (b) 2 to 0.5 mA cm⁻², (c) 0.2 to 0.5 mA cm⁻², and (d) 0.5 mA cm⁻².

Supplementary Tables

Table S3.1. Average CE for the operando NMR cells

Cycling protocol (mA cm ⁻²)	Average CE (×100%)
0.2-0.5	0.302
0.5	0.618
2-0.5	0.716
5-0.5	0.682

References

- Xu, W., Wang, J., Ding, F., Chen, X., Nasybulin, E., Zhang, Y. & Zhang, J. G. Lithium metal anodes for rechargeable batteries. *Energy & Environmental Science* **7**, 513-537 (2014).
- Whittingham, M. S. Electrical energy storage and intercalation chemistry. *Science* **192**,

- 1126–1127 (1976).
- Zheng, J., Kim, M. S., Tu, Z., Choudhury, S., Tang, T. & Archer, L. A. Regulating electrodeposition morphology of lithium: towards commercially relevant secondary Li metal batteries. *Chemical Society Reviews* **49**, 2701–2750 (2020).
 - He, X., Bresser, D., Passerini, S., Baakes, F., Krewer, U., Lopez, J. & Kostecki, R. The passivity of lithium electrodes in liquid electrolytes for secondary batteries. *Nature Reviews Materials* **6**, 1036–1052 (2021).
 - Peled, E. & Menkin, S. Review—SEI: past, present and future. *Journal of The Electrochemical Society* **164**, A1703–A1719 (2017).
 - Lin, D., Liu, Y., & Cui, Y. Reviving the lithium metal anode for high-energy batteries. *Nature Nanotechnology* **12**, 194–206 (2017).
 - Wu, H., Jia, H., Wang, C., Zhang, J. & Xu, W. Recent progress in understanding solid electrolyte interphase on lithium metal anodes. *Advanced Energy Materials* **11**, 2003092 (2021).
 - Boyle, D. T., Li, Y., Pei, A., Vilá, R. A., Zhang, Z., Sayavong, P. & Cui, Y. Resolving current-dependent regimes of electroplating mechanisms for fast charging lithium metal anodes. *Nano Letters* **22**, 8224–8232 (2022).
 - Fang, C., Wang, X. & Meng, Y. S. Key issues hindering a practical lithium-metal anode. *Trends Chem* **1**, 152–158 (2019).
 - Cheng, X. B., Zhang, R., Zhao, C. Z., Wei, F., Zhang, J. G. & Zhang, Q. A Review of solid electrolyte interphases on lithium metal anode. *Advanced Science* **3**, 1500213 (2016).
 - Cheng, X.-B., Zhang, R., Zhao, C.-Z. & Zhang, Q. Toward safe lithium metal anode in rechargeable batteries: a review. *Chemical Reviews* **117**, 10403–10473 (2017).
 - Boyle, D. T., Kim, S. C., Oyakhire, S. T., Vilá, R. A., Huang, Z., Sayavong, P. & Cui, Y. Correlating kinetics to cyclability reveals thermodynamic origin of lithium anode morphology in liquid electrolytes. *Journal of the American Chemical Society* **144**, 20717–20725 (2022).
 - Shi, F., Pei, A., Boyle, D. T., Xie, J., Yu, X., Zhang, X. & Cui, Y. Lithium metal stripping beneath the solid electrolyte interphase. *Proceedings of the National Academy of Sciences* **115**, 8529–8534 (2018).
 - Oyakhire, S. T., Zhang, W., Yu, Z., Holmes, S. E., Sayavong, P., Kim, S. C. & Bent, S. F. Correlating the formation protocols of solid electrolyte interphases with practical performance metrics in lithium metal batteries. *ACS Energy Letters* **8**, 869–877 (2023).
 - Wang, H., Yu, Z., Kong, X., Kim, S. C., Boyle, D. T., Qin, J. & Cui, Y. Liquid electrolyte: The nexus of practical lithium metal batteries. *Joule* **6**, 588–616 (2022).
 - Zhao, Y., Zhou, T., Jeurgens, L. P., Kong, X., Choi, J. W. & Coskun, A. Electrolyte engineering for highly inorganic solid electrolyte interphase in high-performance lithium metal batteries. *Chem* **9**, 682–697 (2023).
 - Hobold, G. M., Kim, K.-H. & Gallant, B. M. Beneficial vs. inhibiting passivation by the

- native lithium solid electrolyte interphase revealed by electrochemical Li⁺ exchange. *Energy & Environmental Science* **16**, 2247–2261 (2023).
18. Jin, D., Park, J., Ryou, M. H. & Lee, Y. M. Structure-controlled Li metal electrodes for post-Li-ion batteries: recent progress and perspectives. *Advanced Materials Interfaces* **7**, 1902113 (2020).
19. Jie, Y., Ren, X., Cao, R., Cai, W. & Jiao, S. Advanced liquid electrolytes for rechargeable Li metal batteries. *Advanced Functional Materials* **30**, 1910777 (2020).
20. Horstmann, B., Shi, J., Amine, R., Werres, M., He, X., Jia, H. & Latz, A. Strategies towards enabling lithium metal in batteries: interphases and electrodes. *Energy & Environmental Science* **26**, 5289–5314 (2021).
21. Li, J., Kong, Z., Liu, X., Zheng, B., Fan, Q. H., Garratt, E. & Jin, H. Strategies to anode protection in lithium metal battery: A review. *InfoMat* **3**, 1333–1363 (2021).
22. Xu, Y., Wu, H., Jia, H., Zhang, J. G., Xu, W. & Wang, C. Current density regulated atomic to nanoscale process on li deposition and solid electrolyte interphase revealed by cryogenic transmission electron microscopy. *ACS Nano* **14**, 8766–8775 (2020).
23. Pei, A., Zheng, G., Shi, F., Li, Y. & Cui, Y. Nanoscale nucleation and growth of electrodeposited lithium metal. *Nano Letters* **17**, 1132–1139 (2017).
24. Wood III, D. L., Li, J. & An, S. J. Fast Formation Cycling for Rechargeable Batteries. *U.S. Patent No. 10,910,628*. Washington, DC: U.S. Patent and Trademark Office. (2021).
25. Rehnlund, D., Ihrfors, C., Maibach, J. & Nyholm, L. Dendrite-free lithium electrode cycling via controlled nucleation in low LiPF₆ concentration electrolytes. *Materials Today* **21**, 1010–1018 (2018).
26. Li, Q., Tan, S., Li, L., Lu, Y. & He, Y. Understanding the molecular mechanism of pulse current charging for stable lithium-metal batteries. *Science Advances* **3**, e1701246 (2017).
27. García, G., Dieckhöfer, S., Schuhmann, W. & Ventosa, E. Exceeding 6500 cycles for LiFePO₄/Li metal batteries through understanding pulsed charging protocols. *Journal of Materials Chemistry A* **6**, 4746–4751 (2018).
28. Lv, S., Verhallen, T., Vasileiadis, A., Ooms, F., Xu, Y., Li, Z. & Wagemaker, M. Operando monitoring the lithium spatial distribution of lithium metal anodes. *Nature Communications* **9**, 2152 (2018).
29. Zhang, Z., Zhou, X. & Liu, Z. Optimization of lithium nucleation by current density toward dendrite-free Li metal anode. *Journal of Alloys and Compounds* **893**, 162389 (2022).
30. Boyle, D. T., Kong, X., Pei, A., Rudnicki, P. E., Shi, F., Huang, W. & Cui, Y. Transient voltammetry with ultramicroelectrodes reveals the electron transfer kinetics of lithium metal anodes. *ACS Energy Letters* **5**, 701–709 (2020).
31. Xu, Y., Wu, H., He, Y., Chen, Q., Zhang, J. G., Xu, W. & Wang, C. Atomic to nanoscale origin of vinylene carbonate enhanced cycling stability of lithium metal anode revealed by cryo-transmission electron microscopy. *Nano Letters* **20**, 418–425 (2020).

32. Wang, X., Pawar, G., Li, Y., Ren, X., Zhang, M., Lu, B. & Liaw, B. (2020). Glassy Li metal anode for high-performance rechargeable Li batteries. *Nature Materials* **19**, 1339–1345 (2020).
33. Huang, W., Wang, H., Boyle, D. T., Li, Y. & Cui, Y. Resolving nanoscopic and mesoscopic heterogeneity of fluorinated species in battery solid-electrolyte interphases by cryogenic electron microscopy. *ACS Energy Letters* **5**, 1128–1135 (2020).
34. Han, B., Zhang, Z., Zou, Y., Xu, K., Xu, G., Wang, H. & Gu, M. Poor stability of Li_2CO_3 in the solid electrolyte interphase of a lithium-metal anode revealed by cryo-electron microscopy. *Advanced materials* **33**, 2100404 (2021).
35. Columbus, D., Arunachalam, V., Glang, F., Avram, L., Haber, S., Zohar, A. & Leskes, M. Direct detection of lithium exchange across the solid electrolyte interphase by ^7Li chemical exchange saturation transfer. *Journal of the American Chemical Society* **144**, 9836–9844 (2022).
36. May, R., Fritzsche, K. J., Livitz, D., Denny, S. R. & Marbella, L. E. Rapid interfacial exchange of Li ions dictates high coulombic efficiency in Li metal anodes. *ACS Energy Lett.* **6**, 1162–1169 (2021).
37. Gunnarsdóttir, A. B., Amanchukwu, C. V., Menkin, S. & Grey, C. P. Noninvasive in situ NMR study of “dead lithium” formation and lithium corrosion in full-cell lithium metal batteries. *Journal of the American Chemical Society* **142**, 20814–20827 (2020).
38. Xiang, Y., Tao, M., Zhong, G., Liang, Z., Zheng, G., Huang, X. & Yang, Y. Quantitatively analyzing the failure processes of rechargeable Li metal batteries. *Science advances* **7**, eabj3423 (2021).
39. Sano, H., Sakaebe, H., Senoh, H. & Matsumoto, H. Effect of current density on morphology of lithium electrodeposited in ionic liquid-based electrolytes. *Journal of The Electrochemical Society* **161**, A1236–A1240 (2014).
40. Zhang, C., Lan, Q., Liu, Y., Wu, J., Shao, H., Zhan, H. & Yang, Y. A dual-layered artificial solid electrolyte interphase formed by controlled electrochemical reduction of LiTFSI/DME-LiNO_3 for dendrite-free lithium metal anode. *Electrochimica Acta* **306**, 407–419 (2019).
41. Liu, M., Zhang, S., van Eck, E. R., Wang, C., Ganapathy, S. & Wagemaker, M. Improving Li-ion interfacial transport in hybrid solid electrolytes. *Nature Nanotechnology* **19**, 959–967 (2022).
42. Yu, C., Ganapathy, S., Eck, E. R. V., Wang, H., Basak, S., Li, Z. & Wagemaker, M. Accessing the bottleneck in all-solid state batteries, lithium-ion transport over the solid-electrolyte-electrode interface. *Nature communications* **8**, 1086 (2017).
43. Ganapathy, S., Yu, C., van Eck, E. R. H. & Wagemaker, M. Peeking across grain boundaries in a solid-state ionic conductor. *ACS Energy Letters* **4**, 1092–1097 (2019).
44. Ganapathy, S., van Eck, E. R. H., Kentgens, A. P. M., Mulder, F. M. & Wagemaker, M. equilibrium lithium-ion transport between nanocrystalline lithium-inserted anatase TiO_2 and the electrolyte. *Chemistry—A European Journal* **17**, 14811–14816 (2011).

45. Liu, M., Wang, C., Zhao, C., van der Maas, E., Lin, K., Arszewska, V. A. & Wagemaker, M. Quantification of the Li-ion diffusion over an interface coating in all-solid-state batteries via NMR measurements. *Nature Communications* **12**, 5943 (2021).
46. Cheng, Z., Liu, M. & Ganapathy, S. Revealing the impact of space-charge layers on the Li-ion transport in all-solid-state batteries. *Joule* **4**, 1311–1323 (2020).
47. Yu, C., Ganapathy, S., De Klerk, N. J., Roslon, I., van Eck, E. R., Kentgens, A. P. & Wagemaker, M. Unravelling Li-ion transport from picoseconds to seconds: bulk versus interfaces in an argyrodite $\text{Li}_6\text{PS}_5\text{Cl}$ – Li_2S all-solid-state Li-ion battery. *Journal of the American Chemical Society* **138**, 11192–201 (2016).
48. Wagemaker, M., Kentgens, A. P. M. & Mulder, F. M. Equilibrium lithium transport between nanocrystalline phases in intercalated TiO_2 anatase. *Nature* **418**, 397–399 (2002).
49. Xu, K. Electrolytes and interphases in Li-ion batteries and beyond. *Chemical Reviews* **114**, 11503–11618 (2014).
50. Zhang, Z., Li, Y., Xu, R., Zhou, W., Li, Y., Oyakhire, S. T. & Cui, Y. Capturing the swelling of solid-electrolyte interphase in lithium metal batteries. *Science* **375**, 66–70 (2022).
51. Guo, R. & Gallant, B. M. Li_2O solid electrolyte interphase: probing transport properties at the chemical potential of lithium. *Chemistry of Materials* **32**, 5525–5533 (2020).
52. Ma, Q., Zhang, X., Wang, A., Xia, Y., Liu, X. & Luo, J. Stabilizing solid electrolyte interphases on both anode and cathode for high areal capacity, high-voltage lithium metal batteries with high Li utilization and lean electrolyte. *Advanced Functional Materials* **30**, 2002824 (2020).
53. Li, F., Liu, J., He, J., Hou, Y., Wang, H., Wu, D. & Ma, J. Additive-assisted hydrophobic Li^+ -solvated structure for stabilizing dual electrode electrolyte interphases through suppressing LiPF_6 hydrolysis. *Angewandte Chemie International Edition* **61**, e202205091 (2022).
54. Guan, D., Hu, G., Peng, Z., Cao, Y., Wu, J., Huang, M. & Du, K. A nonflammable low-concentration electrolyte for lithium-ion batteries. *Journal of Materials Chemistry A* **10**, 12575–12587 (2022).
55. Zheng, J., Yan, P., Mei, D., Engelhard, M. H., Cartmell, S. S., Polzin, B. J. & Xu, W. Highly stable operation of lithium metal batteries enabled by the formation of a transient high-concentration electrolyte layer. *Advanced Energy Materials* **6**, 1502151 (2016).
56. Menkin, S., O’Keefe, C. A., Gunnarsdóttir, A. B., Dey, S., Pesci, F. M., Shen, Z. & Grey, C. P. Toward an understanding of SEI formation and lithium plating on copper in anode-free batteries. *The Journal of Physical Chemistry C* **125**, 16719–16732 (2021).
57. Liu, S., Ji, X., Piao, N., Chen, J., Eidson, N., Xu, J. & Wang, C. An inorganic-rich solid electrolyte interphase for advanced lithium-metal batteries in carbonate electrolytes. *Angewandte Chemie International Edition* **60**, 3661–3671 (2021).
58. Seong, I. W., Hong, C. H., Kim, B. K. & Yoon, W. Y. The effects of current density and amount of discharge on dendrite formation in the lithium powder anode electrode. *J.*

- Power Sources* **178**, 769–773 (2008).
59. Chang, H. J., Trease, N. M., Ilott, A. J., Zeng, D., Du, L. S., Jerschow, A. & Grey, C. P. Investigating Li microstructure formation on Li anodes for lithium batteries by in situ ^6Li / ^7Li NMR and SEM. *The Journal of Physical Chemistry C* **119**, 16443–16451 (2015).
60. Hsieh, Y. C., Leißing, M., Nowak, S., Hwang, B. J., Winter, M. & Brunklaus, G. Quantification of dead lithium via in situ nuclear magnetic resonance spectroscopy. *Cell Reports Physical Science*, **1**, 100139 (2020).
61. Kayser, S. A., Mester, A., Mertens, A., Jakes, P., Eichel, R. A. & Granwehr, J. Long-run in operando NMR to investigate the evolution and degradation of battery cells. *Physical Chemistry Chemical Physics* **20**, 13765–13776 (2018).
62. Küpers, V., Kolek, M., Bieker, P., Winter, M. & Brunklaus, G. In situ ^7Li -NMR analysis of lithium metal surface deposits with varying electrolyte compositions and concentrations. *Physical Chemistry Chemical Physics*, **21**, 26084–26094 (2019).
63. Kanamura, K., Shiraishi, S. & Takehara, Z. Electrochemical deposition of very smooth lithium using nonaqueous electrolytes containing HF. *Journal of the Electrochemical Society* **143**, 2187–2197 (1996).
64. Tan, J., Matz, J., Dong, P., Shen, J. & Ye, M. A growing appreciation for the role of LiF in the solid electrolyte interphase. *Advanced Energy Materials* **11**, 2100046 (2021).
65. Spees, W. M., Buhl, N., Sun, P., Ackerman, J. J., Neil, J. J. & Garbow, J. R. Quantification and compensation of eddy-current-induced magnetic-field gradients. *Journal of Magnetic Resonance* **212**, 116–123 (2011).
66. Pecher, O., Bayley, P. M., Liu, H., Liu, Z., Trease, N. M. & Grey, C. P. Automatic tuning matching cyclus (ATMC) in situ NMR spectroscopy as a novel approach for real-time investigations of Li- and Na-ion batteries. *Journal of Magnetic Resonance* **265**, 200–209 (2016).

4

Revealing Local Diffusive Dynamics in Hybrid Solid Electrolytes

“曲径通幽处，禅房花木深”

“Winding paths lead to secluded spots, where the flowers and trees grow deep in the Zen courtyard.”

常建《题破山寺后禅院》(Zen Retreat Behind the Mountain Temple)

This chapter has been submitted as: **Zhang, S.**, Mueller, L. F., Macray, L., Wagemaker, M., Bannenberg, L. J. & Ganapathy, S. Revealing local diffusive dynamics in hybrid solid electrolytes. (2024).

Abstract

Hybrid solid electrolytes (HSEs) offer key advantages over their organic or inorganic counterparts. However, developing effective HSEs requires optimizing ion transport and component compatibility, necessitating a better fundamental understanding of the complex ion transport mechanisms from intricate phase interactions. Here, macroscopic charge transport is correlated with local lithium (Li)-ion diffusivity in HSEs, using polyethylene oxide (PEO) as matrix and argyrodite-type $\text{Li}_6\text{PS}_5\text{Cl}$ electrolytes as filler. Both solvent and dry processing methods were explored to assess the morphological impact on Li-ion transport. Through multiscale and multinuclear solid-state nuclear magnetic resonance, we reveal that the filler enhances local Li-ion diffusivity within the slow polymer segmental dynamics. Phase transitions from crystalline to amorphous states at lower temperatures indicated inhibited crystallization in HSEs, corroborated by decreased Li-ion diffusion barriers compared to polymer electrolytes alone. This is attributed to the enhanced segmental motion and a more conductive polymer conformation in the HSEs. Relaxometry measurements reveal a highly mobile component unique to the hybrid system, indicating fast Li-ion transport along polymer-filler interfaces. Comparative analysis of solvent and dry processing methods suggest that the solvent-processed HSEs exhibit better morphological uniformity, which also shows enhanced compatibility towards the Li-metal anode with the formation of an inorganic-rich solid electrolyte interphase (SEI).

4.1 Introduction

In response to the growing demand for high-energy-density and high-safety energy storage systems, current research effort is increasingly focused on moving away from traditional liquid Li-ion batteries to all-solid-state Li-metal batteries^{1,2}. To achieve this, it is crucial to develop solid-state electrolytes that offer desirable features like high ionic conductivity, flexibility, mechanical stability, and a wide operating temperature range^{3,4}. Among many solid-state electrolytes, polyethylene oxide (PEO)-based systems show superior mechanical flexibility, processability, and electrode wettability. However, the low ionic conductivity at room temperature and insufficient mechanical strength pose challenges for practical use⁵⁻⁸. As a combinational strategy, hybrid solid electrolytes (HSEs) that incorporate ceramic fillers into the PEO-lithium salt (LiX) matrix have proven effective in improving ionic conductivity and mechanical properties. The added fillers can be either passive or active (ion-conductive). While passive fillers function similarly to molecular plasticizers by reducing the crystallinity of the polymer, active fillers have an additional role that contribute to higher ionic conductivity by forming extra Li-ion transport pathways. These pathways can be established through the filler phase and the polymer-filler interface⁹. Previous research has confirmed enhanced ion transportation in the PEO-based HSEs when using active fillers such as garnet-type oxides^{10,11}, NASICON-type phosphates¹⁰, and sulfides¹²⁻¹⁴. Most research focuses on macroscopic and interfacial Li-ion conduction to access the contributions of each phase to ion transport^{13,15-17}, yet an in-depth understanding of local Li-ion dynamics, which are also closely correlated to overall conductivity, is still lacking. Local Li-ion dynamics in HSEs pertain to the behavior of Li-ions at a microscopic level, which provides essential insight into the mechanisms governing ion movement and polymer-filler interactions within the HSEs.

The transport of Li-ions in the PEO phase involves both intermolecular and intramolecular hopping, which occurs through continuous formation and dissociation of EO-Li bonds, along with chain movement^{5,18}. This constant segmental reorganization aids in long-rang Li-ion diffusion, which primarily occurs in the amorphous region of the polymer. Consequently, the ionic conductivity of the PEO-LiX complexes is typically below 10^{-5} S cm^{-1} at room temperature as PEO chains readily crystallize below 65 °C⁶. Also in PEO-based HSEs, room temperature conductivity remains unsatisfactory despite the use of active fillers

that are expected to contribute with their high ionic conductivity. This is typically attributed to the poor ionic conductivity of the PEO matrix and the limited participation of the inorganic particles. It is worth noting that while increasing the filler concentration can enhance ionic conductivity, the resulting filler agglomeration may impede Li-ion transport and reduce overall conductivity¹⁹. Especially in a system with a low inorganic fraction, although previous research has often attributed inadequate conductivity to limited Li-ion transport at the polymer-filler interface^{12,17,20,21}, ion conduction within the polymer matrix itself plays a crucial role. This aspect has not received sufficient attention, yet it can greatly affect overall conductivity and often being the dominant mechanism. In addition, fundamental understanding of the impact of fillers on Li-ion motion within the polymer matrix is essential for advancing interface engineering in the HSEs.

Given these considerations, solid-state Nuclear Magnetic Resonance (ssNMR) stands out as an effective technique being able to probe local chemical environments and dynamic behavior, providing detailed insight into motions across a wide range of time and length scales with isotope selectivity and non-destructive analysis^{22,23}. Specifically, in the PEO-based HSEs systems with Li-containing active fillers, ssNMR allows us to distinguish various chemical environments and provides detailed information into their individual structure and dynamics. Several studies have investigated interfacial Li-ion diffusion in the PEO-based HSEs using one/two-dimensional exchange spectroscopy (1/2D-EXSY NMR)^{11,15,24,25}, or isotope labelling ssNMR with ⁷Li replaced by ⁶Li^{16,19,26}, enabling the tracking of Li-ion transport pathways. However, comprehensive studies on the local structure and ion dynamics in the HSEs are still lacking, particularly regarding the impact of the formulation method on the polymer phase, which can lead to large disparity in results. Many reports describe the use of solvent-assisted preparation for formulating HSEs, which generally outperforms dry-mixing in terms of homogeneity and ease of processing. However, the disadvantage is that solvent-processing typically induces side reactions between the electrolytes and the solvent^{27,28}.

In this work, we aim to understand the local Li-ion mobility across different dynamic ranges in the HSE system built on PEO-LiTFSI (lithium-bis (trifluoromethane-sulfonyl) imide) and the fast ion-conducting Li₆PS₅Cl filler, with a particular focus on the polymer phase. The impact of the Li₆PS₅Cl filler on local Li-ion dynamics in the PEO phase is

compared to that of the non-filled PEO electrolyte, alongside an evaluation of solvent and dry processing methods in formulating the HSEs. These aspects are analyzed using temperature-dependent line-width and spin-lattice relaxation time (T_1) ssNMR measurements. Fitting the data to different diffusion models enables quantification of local Li-ion mobility and provides insight into the ion transport mechanisms. In combination with electrochemical impedance spectroscopy (EIS), this enables the correlation of local molecular dynamics with macroscopic charge transport. We find that incorporating $\text{Li}_6\text{PS}_5\text{Cl}$ filler particles into the PEO-based polymer electrolyte improves Li-ion diffusion at both bulk and local length scales. This improvement is associated with the altered phase transition behavior and the polymer chain configuration in the polymer phase by the addition of fillers, which inhibits crystallization and promotes a predominance of the *cis*-PEO conformation. When comparing solvent and dry processing methods, the dry-processed electrolytes display slower local Li-ion dynamics and an inhomogeneous phase distribution, which is attributed to the morphological heterogeneity introduced by the dry mixing. Finally, adding $\text{Li}_6\text{PS}_5\text{Cl}$ fillers has proven to enhance the compatibility of the PEO-based polymer electrolytes with the Li-metal anode by forming a more conductive SEI layer.

It is worth noting that $\text{Li}_6\text{PS}_5\text{Cl}$ was selected as a filler in this study for its high intrinsic ionic conductivity and ductility. It was anticipated that $\text{Li}_6\text{PS}_5\text{Cl}$ would not only enhance Li-ion mobility within the PEO-LiTFSI matrix but also contribute to overall conductivity by establishing additional fast ion-conducting pathways. While this chapter primarily focuses on the impact of $\text{Li}_6\text{PS}_5\text{Cl}$ on the local Li-ion dynamics within the PEO phase, the question of whether $\text{Li}_6\text{PS}_5\text{Cl}$ actively contributes to ion conduction with the HSEs remains unresolved. This aspect will be further explored in more detail in Chapter 5, where we investigate the polymer-filler interface and assess the use of additives to improve this interface.

4.2 Results

4.2.1 Li-ion conduction

The HSEs composed of PEO-LiTFSI (EO:Li = 18:1) and $\text{Li}_6\text{PS}_5\text{Cl}$ (10 wt%) were fabricated using both solvent and dry methods, referred to as HSE and DHSE, respectively (see details in section 4.4 Methods). To investigate the impact of $\text{Li}_6\text{PS}_5\text{Cl}$ fillers on the PEO-LiTFSI

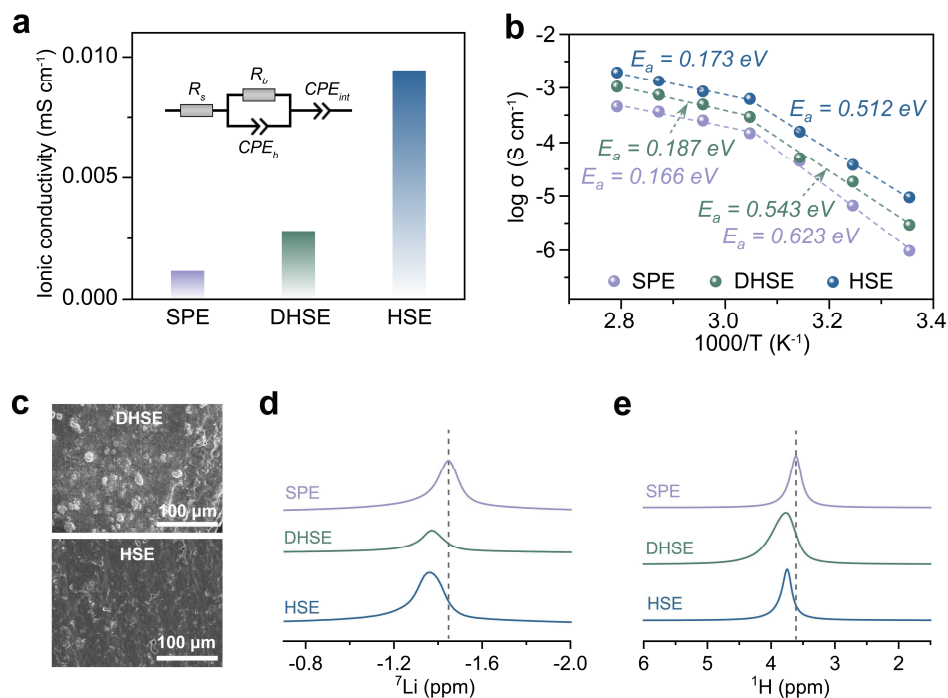


Fig. 4.1. Characterization of the SPE and (D)HSE. (a) Ionic conductivity obtained by EIS of the cells using SPE, DHSE, and HSE at 25 °C. (b) Arrhenius plots of the SPE, DHSE, and HSE with fitted activation energies (E_a) corresponding to different processes. (c) SEM images of the DHSE and HSE. 1D (d) ^7Li , and (e) ^1H magic angle spinning (MAS) ssNMR spectra of the SPE, DHSE, and HSE electrolytes. The ^7Li spectra correspond to the LiTFSI-PEO resonance, with peak positions at 1.45, 1.38, and 1.37 ppm for SPE, DHSE, and HSE, respectively. ^7Li spectra over a broader range, including the $\text{Li}_6\text{PS}_5\text{Cl}$ peak, are shown in Fig. S4.1. The ^1H peak positions for SPE, DHSE, and HSE are 3.61, 3.77, and 3.75 ppm, respectively.

solid polymer electrolyte (SPE) and evaluate the feasibility of the dry-processing approach for fabricating HSEs, their ionic conductivities at variable temperatures were measured. Evidently, the addition of the $\text{Li}_6\text{PS}_5\text{Cl}$ filler notably improved the ionic conductivity of the SPE, with the solvent-processed HSE showing the highest ionic conductivity (Fig. 4.1a). In the Arrhenius plot, two linear fits were applied due to a noticeable deflection after the melting temperature (T_m) of the polymer matrix (Fig. 4.1b). This deflection can be attributed to either the melting of the crystalline phase or the rearrangement of the -EO- moieties²⁹. The obtained activation energies (E_a) reveal more distinct differences in the lower temperature region, with values of 0.623 (± 0.02), 0.543 (± 0.03), and 0.512 (± 0.01) eV for the SPE, DHSE, and HSE, respectively. This indicates that incorporating the $\text{Li}_6\text{PS}_5\text{Cl}$ filler lowers the energy

barrier for Li-ion diffusion in the SPE, particularly when the polymer matrix is more rigid. Furthermore, the solvent-processing method exhibits a lower E_a compared to the dry-processed counterparts, likely due to the better homogeneity of the HSE, as illustrated in the scanning electron microscope (SEM) images in **Fig. 4.1c**. The HSE displays a much smoother surface than the DHSE, potentially increasing the interface area and optimizing the Li-ion conduction pathway.

Expanding on the aforementioned observations, one-pulse ^7Li and ^1H ssNMR experiments were conducted on the pristine membrane electrolytes. This aims to gain insight into how $\text{Li}_6\text{PS}_5\text{Cl}$ interacts with the polymer matrix and to assess the influence of the processing method. A downfield shift of the LiTFSI-PEO peak is detected in the ^7Li NMR spectra for both the HSE and DHSE (**Fig. 4.1d**). The de-shielded Li-ion indicates reduced electron density around the Li atoms, resulting from decreased coordination with the -EO- units in the polymer backbone^{30,31}. Correspondingly, the ^1H NMR spectra show a downfield shift of the ^1H peak in samples containing $\text{Li}_6\text{PS}_5\text{Cl}$, signifying a more de-shielded ^1H environment due to the less tightly bonded EO-Li coordination (**Fig. 4.1e**). Although the chemical shifts were similar across different processing methods, the DHSE displays a weaker LiTFSI-PEO peak and a stronger $\text{Li}_6\text{PS}_5\text{Cl}$ peak, indicating sample heterogeneity and possible filler agglomeration (**Fig. S4.1**). In addition, the broader ^1H peak in the DHSE suggests poorer uniformity within the sample.

4.2.2 Local Li-ion dynamics

Having established the impact of filler addition and processing methods on the bulk ionic conductivity and the interaction between the polymer matrix and $\text{Li}_6\text{PS}_5\text{Cl}$ filler, it is crucial to understand the underlying dynamic changes at the molecular level that contribute to these observations. To this end, the NMR line-width measurements were employed to analyze the local structure and ion mobility within the electrolytes, providing insights into the mechanism behind the improved bulk conductivity and the influence of processing method on local Li-ion diffusion in the HSEs. In the line-width measurements, increased mobility averages out dipolar interactions, resulting in narrower lines³⁵. **Fig. S4.2** shows the deconvolution of the overlapping LiTFSI-PEO and $\text{Li}_6\text{PS}_5\text{Cl}$ peaks, enabling for more accurate determination of both line-widths and amplitudes. The PEO phase is the primary focus of this study, as it serves as the matrix and has a greater impact on the overall ionic conductivity of the HSEs.

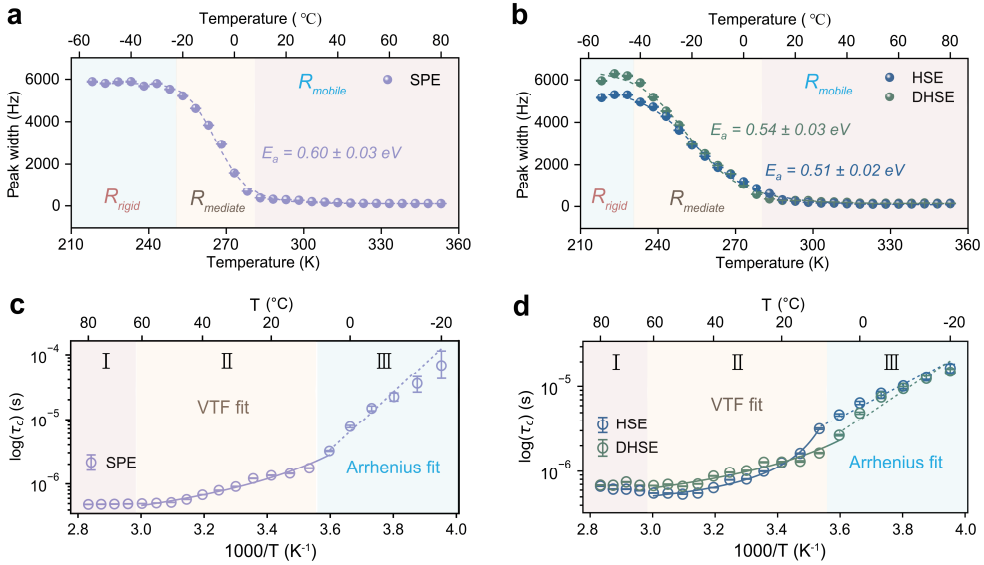


Fig. 4.2. Probing local Li-ion dynamics using ${}^7\text{Li}$ line-width measurements. Temperature-dependent ${}^7\text{Li}$ line-widths fitted with the Hendrickson-Bray model³² (dashed line, see details in Supplementary Text S4.1) for (a) SPE, and (b) (D)HSE. Semilogarithmic plot of the correlation time (τ_c) against the reciprocal temperature for (c) SPE, and (d) (D)HSE, fitted with the Abragam model (see details in Supplementary Text S4.2)³³. The different dynamical regimes (I-III) of the ${}^7\text{Li}$ correlation times are marked by distinct fill colors: regime I corresponds to the polymer melt regime with fast Li-ion motion and correspondingly short τ_c , regimes II and III are mixed-phase regimes fitted by the Vogel-Tamman-Flucher (VTF) and Arrhenius laws³⁴, respectively.

Fig. 4.2a, b show the change in line-width as a function of temperature, distinguishing three behavioral regimes for both the SPE and (D)HSE: (i) The rigid lattice regime (R_{rigid}): In this regime, the line-widths are very broad ($\geq 5000 \text{ Hz}$) and remain constant as the temperature decreases. This indicates low Li mobility, where the hopping frequency is slower than the rate of magnetic environment fluctuations responsible for line-broadening, which occurs when the system is below the glass transition temperature (T_g). The broad peaks observed are a result of quadrupolar and dipole-dipole interactions³⁶. (ii) The intermediate regime (R_{mediate}): This regime signals the onset of motional narrowing, characterized by a gradual decrease in line-width. As the temperature increases, the Li-ion motion increases to a rate where the ion motion becomes comparable to the timescale of the NMR experiment (related to the Larmor frequency). Consequently, the local magnetic fields experienced by the nuclei start to average out. (iii) The fully narrowed regime (R_{mobile}): In this regime, the line-width becomes very narrow ($\leq 100 \text{ Hz}$). Here, the Li-ions exhibit high mobility, leading

to a complete averaging of the local magnetic fields. The rapid Li-ion motion causes the NMR measurements to detect only an averaged and diminished magnetic interaction. This indicates a high level of segmental motion and dynamic behavior within the PEO matrix. Comparing the SPE and (D)HSE reveals differences in the temperature ranges of their respective regimes. In the SPE, the onset of R_{rigid} occurs at a temperature of $-20\text{ }^{\circ}\text{C}$, whereas in the (D)HSE, the onset of the rigid lattice regime occurs at temperatures as low as $-45\text{ }^{\circ}\text{C}$. This corresponds to a wider temperature range (ΔT) for the $R_{mediate}$ in the (D)HSE ($\Delta T_{(D)HSE} = 40\text{ }^{\circ}\text{C}$), compared to the SPE where narrowing occurs faster ($\Delta T_{SPE} = 25\text{ }^{\circ}\text{C}$). However, the fully narrowed regime R_{mobile} begins at approximately $5\text{ }^{\circ}\text{C}$ for both samples. In the SPE, the shorter intermediate regime indicates a rapid decrease in Li-ion motion within the amorphous polymer phase below $5\text{ }^{\circ}\text{C}$, due to the immobilization induced by the growing crystalline phase. In contrast, the (D)HSE exhibit inhibited growth of the crystalline phase, allowing Li-ion motion to persist across a broader temperature range. This is attributed to the plasticizing effect and the inhibition of crystallization with the presence of fillers^{37,38}. In addition, the two processing methods also display a visible difference, notably with the dry method showing broader peaks compared to the solvent method at temperatures below $-20\text{ }^{\circ}\text{C}$ (**Fig. 4.2b**). The broader peak suggests additional heteronuclear dipolar line-broadening arising from closer interactions between Li^+ and TFSI. This hints that the inherent morphology of the DHSE is characterized by incomplete Li salt solvation within the PEO domains due to inhomogeneous particle distribution, which in turn influences the charge distribution near the Li nuclei.

Taking a closer look at line-widths in the R_{mobile} regime (**Fig. S4.3**), even at these very small line-widths, a two-step decrease is visible for both the SPE and (D)HSE. This decrease can be attributed to a gradual increase of the amorphous phase in the PEO matrix before T_m , which is consistent with the T_m obtained from the Differential Scanning Calorimetry (DSC) measurements (**Fig. S4.4**). After reaching T_m , the line-width remains constant for all samples. It is noteworthy that before reaching T_m , the HSE exhibits the smallest line-width of all the samples, indicating accelerated Li dynamics and a more homogeneous chemical environment for Li-ions within the PEO matrix of the HSE at typical operational temperatures. Notably, the line-width of the dry-processed sample remains larger also after melting, suggesting greater heterogeneity in chemical environments due to the dry-processing procedure. This indicates that the Li mobility in this temperature range is predominantly influenced by

polymer segmental motion, with well-mixed $\text{Li}_6\text{PS}_5\text{Cl}$ fillers enhancing local chain mobility. Fitting the temperature-dependent line-width using Hendrickson Bray phenomenological equation (see details in **Supplementary Text S4.1**)³², the activation energy (E_a) of the motional process responsible for the line-narrowing can be determined. The E_a obtained from the NMR line-width measurement corresponds to local ion dynamics on the timescale of several microseconds³⁵. Both HSE and DHSE show a lower E_a and a different curve shape compared to the SPE, with DHSE exhibiting slightly higher E_a than HSE. This suggests that the addition of $\text{Li}_6\text{PS}_5\text{Cl}$ filler enhances the Li-ion diffusion and lowers the energy barrier for Li-ion transport.

This local Li-ion dynamics were further analyzed by the Abragam model (see details in **Supplementary Text S4.2**), where the line-width proportional correlation time (τ_c) can be determined^{33,39}. This reveals how quickly ions can reorient themselves or move between different sites. In the temperature range analyzed, all the electrolytes exhibit three distinct regimes of τ_c , as indicated in **Fig. 4.2c, d**. Within regime (I), the polymer phase exists in a melted, fully amorphous state, where τ_c is short and segmental dynamics dominate. Thermal motion of both the polymer backbone and Li, leads to high-frequency changes in the EO-Li coordination shell. In the intermediate temperature regime (II), a noticeable curved trend emerges as the temperature decreases, indicating that Li-ion reorientation follows a Vogel-Tammann-Fulcher (VTF) process³⁴. This VTF curvature reflects increasing heterogeneity in the sample as it cools⁴⁰. The as-formed regions thus show distinct mobility characteristics: high-mobility amorphous fractions and low-mobility crystalline fractions. Cooperative rearrangement of larger polymer chain regions is crucial for Li-ion motion. In this semi-crystalline state, the motion follows a super-exponential behavior rather than an Arrhenius-type exponential relationship, attributed to increased cooperativity and heterogeneity within the system⁴¹. While the polymer crystallizes, Li-ions do not remain within the crystalline fraction. Instead, a phase segregation occurs, as noted by M. Marzantowicz et al.⁴², where the dissolved Li salt does not integrate well into the PEO crystallite structure and accumulates in the amorphous phase. A concentrated salt front develops at the boundary of the crystal phase, leading to increased formation of PEO:LiTFSI complexes in the amorphous phase. This process creates domains of PEO:LiTFSI complexes within a semi-crystalline electrolyte. Despite this phase formation, the semi-crystalline electrolyte only marginally reduces

mobility, as ions are infrequently trapped within the crystalline phase⁴². Regime (III) is marked by a rapid change in line-width. The τ_c of the Li nuclei now exhibits an Arrhenius temperature dependency, suggesting the presence of another phase transition. The steepness of the Arrhenius plot indicates a high energy barrier for altering the Li coordination shell. In this regime, the increase in τ_c is influenced not only by the crystalline fraction of the PEO phase but also by the crystallization of the PEO:LiTFSI complexes. Consequently, these crystalline phases contribute to a solid-like mechanism of ion transport⁴³.

From the EIS measurements and the Hendrickson-Bray fits of the line-width, the addition of Li₆PS₅Cl fillers demonstrates a reduced E_a for Li-ion diffusion. This reduction is also evident from the E_a values obtained from both regime (II) and regime (III) (see **Table S4.1**) using the VTF and Arrhenius fits. Furthermore, solvent processing of the membranes increases the onset temperature for the transition to Arrhenius behavior compared to dry processing (**Fig. 4.2d**). This difference suggests variations in the microstructural uniformity of HSE and DHSE. Previous studies have highlighted the impact of solvents on polymer-ceramic composites, showing that degradation increases with the dielectric constant of the solvent²⁸. Therefore, dry-processed samples are expected to exhibit weakened polymer-filler interfacial interactions. Nonetheless, the prolonged VTF behavior indicates less uniform dispersion of the filler particles in the DHSE, leading to large PEO bulk regions devoid of filler particles. These observations are also consistent with the DSC measurements (**Fig. S4.4**), which show an additional melting point (T_m) at a lower temperature in DHSE. This implies that the filler does not integrate uniformly into the polymer matrix, resulting in a microstructure that varies in PEO crystallinity and the distribution of Li₆PS₅Cl particles.

To further investigate the impact of fillers and processing methods on the dynamic coupling of Li-ions and polymer chains at local scales, spin-lattice relaxation (SLR) analysis at various temperatures was applied. This provides deeper insights into how local interactions fluctuate at frequencies that cause the probed Li nuclei to relax longitudinally. Relaxation rates ($1/T_1$) are sensitive to motion on a timescale comparable to the inverse of the NMR Larmor frequency (116.6 MHz for this study), i.e., several nanoseconds. Hence, SLR focuses on more localized motion compared to the previous line-width analysis. **Fig. 4.3a-c** shows the relaxation rates measured at increasing temperatures for the SPE, HSE, and DHSE, respectively. The relaxation rates for the SPE can be fit with the modified Bloembergen-

Purcell-Pound (BPP) spectral density function⁴⁴, which exhibits a broad peak with a maximum within the thermal window of 40 to 45 °C (see details in **Supplementary Text S4.3**). At this maximum, the Li hopping frequency is of the same order as the Larmor frequency. The BPP fit gives an E_a value of 0.35 ± 0.01 eV, which is much smaller than the E_a obtained from the Hendrickson-Bray fit for the line-width measurements (**Fig. 4.2a**, 0.60 ± 0.03 eV). This difference arises as T_1 measurements capture short-range Li-ion dynamics, whereas line-width measurements reflect environmental inhomogeneities and constraints on broader ionic motion.

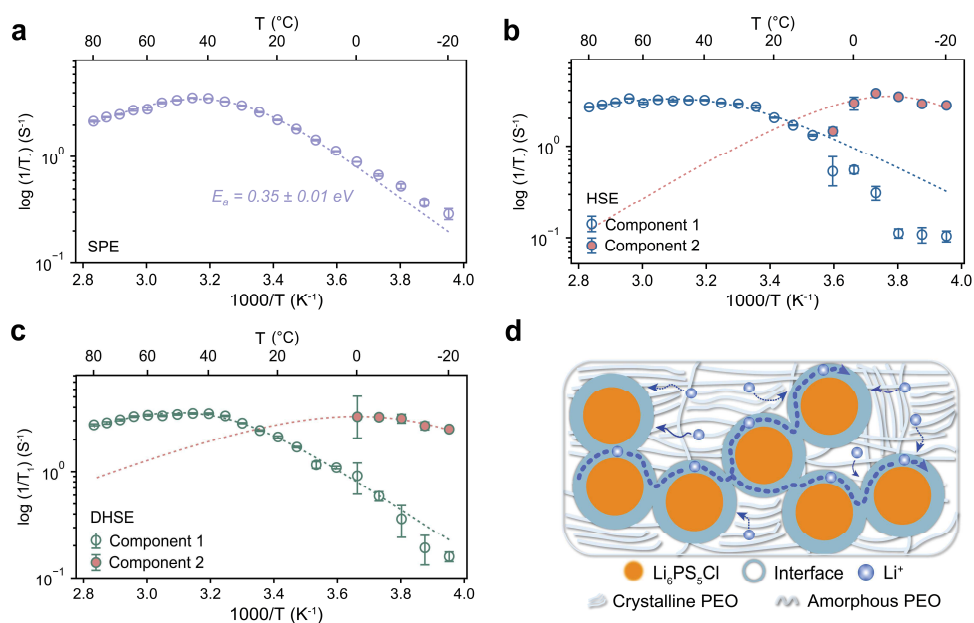


Fig. 4.3. Probing local Li-ion dynamics through ^7Li T_1 relaxometry measurements. ^7Li relaxation rates measured for (a) SPE, (b) HSE, and (c) DHSE. The fit in (a) represents a modified Bloembergen-Purcell-Pound (BPP) type spectral density, while the fits in (b) and (c) use the Richards spectral density model for 2D diffusion, showing both single and two-component regions (see details in Supplementary Text S4.3). (d) Schematic showing the Li-ion diffusion pathways within the (D)HSE at low temperatures, with the polymer-filler interfaces gaining more Li-ions during the cooling process, leading to a fast Li-ion diffusion pathways along the interfaces at lower temperatures.

The relaxation rates of the (D)HSE show a similar trend to the SPE when the temperature ≥ 10 °C (**Fig. 4.3b, c**). However, a separate Li-ion relaxation process from the polymer phase arises when the temperature ≤ 5 °C, as depicted by the filled circles (denoted as Component 2). The relaxation rate of the newly emerging component differs from the primary PEO

component (denoted as Component 1) due to its considerably shorter relaxation times, and it is not identifiable in the pure polymer electrolyte system shown in **Fig. 4.3a**. Examples of the individual T_1 fits at 0 °C are shown in **Fig. S4.5**. The HSE and DHSE yield the best fits using a bi-exponential model, while the second exponential fit for the SPE data fails, indicating the presence of only one component. This secondary relaxation mechanism, nested within the LiTFSI-PEO peak, suggests a variant of EO-Li coordination with shorter relaxation times, which is unaffected by the mobility of the polymer chains. Correlating these observations with the Abragam model analysis shown in **Fig. 4.2c, d** suggests that a concentrated salt phase develops at the polymer-filler interfaces, as this feature is not present in the SPE sample. Comparing the two processing methods, notable differences were observed, especially at temperatures ≤ 10 °C. The trend line for Component 1 in the DHSE shows a more linear behavior compared to that of the HSE, indicating that the Li-ion diffusion in this phase resembles that observed in the SPE more closely. This divergence can be attributed to filler aggregation in the DHSE, leading to larger regions of the polymer phase lacking filler particles, thus locally behaving similarly to the SPE. Moreover, these agglomerates result in less developed polymer-filler interactions.

The BPP spectral density fits for the SPE indicate a reasonable fits to a single relaxation mechanism. However, the BPP model is not feasible for fitting the relaxation data of the (D)HSE, as the appearance of Component 2 causes substantial deviations. Comparison with the τ_c data from the line-width measurements (**Fig. 4.2c, d**) also shows a change in diffusion behavior at around 5 to 10 °C. This indicates the need for a different spectral density function to accurately fit the data. In this context, we attempted to fit the components 1 and 2 individually using the Richards spectral density function for two-dimensional (2D) diffusion. This provides a better fit to the measured data (see details in **Supplementary Text S4.3**)⁴⁵, although the deviation for HSE in Component 1 remains large below 10 °C. This indicates that the influence of the filler on the local dynamics of the polymer phase is more pronounced at and below this temperature. Any quantitative analysis for the (D)HSE relaxation rate curves is challenging due to the limited number of data points and the less defined maximum in the relaxation rate curves compare to the SPE. However, these observations clearly show a second relaxation process within the polymer matrix induced by filler addition. This is possibly associated with 2D diffusion of Li-ions both within/between the polymer segments

and along the polymer-filler interfaces, which is more evident at low temperatures due to polymer-filler interactions. The observation of the fast local dynamics of Li-ions from this second component can be leveraged to better understand and expand the operating temperature range of HSEs.

4.2.3 Polymer structure and dynamics

Given the distinctive differences in Li-ion dynamics between SPE and the HSEs, a detailed study of the polymer conformation was conducted using ^{13}C NMR spectra, to investigate the impact of the $\text{Li}_6\text{PS}_5\text{Cl}$ filler and the processing method on the bulk structure. Deconvolution of the ^{13}C spectra reveals that the ^{13}C environments are dominated by *trans*-PEO, *cis*-PEO, and crystalline PEO in both the SPE and (D)HSE (**Fig. 4.4a-c**)⁴⁶. The slight downfield shift (to higher ppm value) of the ^{13}C chemical shift in the (D)HSE is likely attributed to enhanced polymer chain mobility, as evidenced by the normalized peak intensity in **Fig. S4.6**. The crystalline phase ratios in the SPE, DHSE, and HSE are 30%, 25%, and 22%, respectively. This occurs since the addition of fillers increases the amorphous region of the polymer phase, leading to increased Li-ion coordination with EO groups and a consequent de-shielding effect on the ^{13}C environment. The SPE is predominantly composed of *trans*-PEO, whereas the HSE is dominated by *cis*-PEO, with the DHSE lying between the two. For the oxygen atoms adjacent to the *cis*-PEO carbon atoms, the shorter distance and smaller steric hindrance facilitate the coordination of Li-ions with these oxygens, as depicted in **Fig. S4.7**. This enhanced coordination improves the Li-ion conductivity of the polymer chains, which corresponds to increased ionic conductivity and improved local Li-ion dynamics in the (D)HSE, as discussed in the previous sections.

The structural change also coincides with alterations in polymer dynamics, as evidenced by the faster proton relaxation rates detected in the HSE from the ^1H SLR measurements (**Fig. S4.8**). This could be explained by an inherently higher mobility of the amorphous phase resulting from the addition of fillers. In addition, one-dimensional (1D) $^1\text{H} \rightarrow ^7\text{Li}$ cross-polarization MAS (^7Li CP MAS) experiments were conducted to distinguish local ^1H and ^7Li dynamics (**Fig. S4.9**). In these experiments, the magnetization from the abundant protons (^1H) is transferred to nearby ^7Li nuclei during a defined contact time, enabling the analysis of ^1H dynamics. Focusing on the sharp LiTFSI-PEO peak, the buildup of the peak intensity can be

fitted using their characteristic proton spin-lattice relaxation time in the rotating frame ($T_{1\rho H}$) values (fitting details in **Supplementary Text S4.4**). Among the three samples, HSE displays a notably faster cross-relaxation time (**Fig. 4.4d** and **Table S4.2**), suggesting a more mobile proton environment. This variation is also reflected in the $T_{1\rho H}$ values, as presented in **Table S4.2**. Despite the improvement in polymer dynamics with the addition of fillers, noticeable differences remain between the two processing methods. Consequently, the proton dynamics in the DHSE are more similar to those in the SPE due to the inhomogeneous particle distribution, as shown in **Fig. 4.4d**.

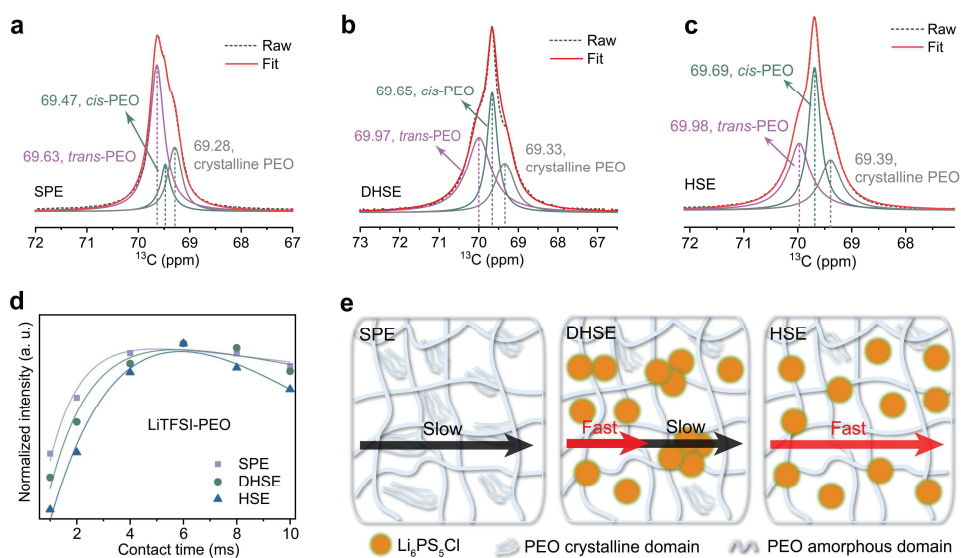


Fig. 4.4. Characterizing the polymer configuration and dynamics in the SPE and (D)HSE. Fitting of the high power decoupling (hpdec) ^{13}C single-pulse MAS ssNMR spectra for (a) SPE, (b) DHSE, and (c) HSE. (d) Integrated intensities and the corresponding fits extracted from 1D $^1\text{H}\rightarrow^7\text{Li}$ CP MAS spectra obtained for SPE, DHSE, and HSE, expressed in arbitrary units (a.u.), with a focus on the LiTFSI-PEO environment (individual spectra at contact times ranging from 0.05 to 10 ms are shown in **Fig. S4.6**, see fitting details in Supplementary Text S4.4). (e) Schematic showing the Li-ion transport modes in the SPE, DHSE, and HSE.

The impact of $\text{Li}_6\text{PS}_5\text{Cl}$ fillers and processing method on the polymer structure and dynamics in the PEO-based electrolytes is summarized in **Fig. 4.4e**. In a typical PEO-LiTFSI polymer electrolyte system, the high crystallinity of the polymer chains impedes efficient Li-ion transport. Introducing $\text{Li}_6\text{PS}_5\text{Cl}$ fillers into the SPE system through solvent processing

has proven effective in improving Li-ion conduction by altering the polymer chain configuration and chain dynamics in a homogeneous mixed phase. In contrast, the electrolytes produced by dry processing resulted in an inhomogeneous membrane characterized by phase separation and discontinuous Li-ion transport channels. This underscores the importance of uniformity to create continuous Li-ion pathways when designing hybrid electrolytes.

4.2.4 Compatibility towards the Li-metal anode

Having established an understanding of Li-ion dynamics and polymer configuration in the HSE, it is crucial to explore its practical applicability. Therefore, the compatibility of the PEO-based electrolytes with and without Li₆PS₅Cl fillers towards Li-metal anode has been investigated using Li|Li symmetrical cells. During long-term cycling at 0.05 mA cm⁻² and 40 °C (**Fig. 4.5a**), the cell cycled with SPE consistently shows a higher overpotential compared to HSE, which is ascribed to insufficient Li-ion conductivity of the SPE. In contrast, the cell using HSE maintained a stable overpotential at ~50 mV and remained stable for over 800 h, whereas the cell using SPE failed at ~237 h (**Fig. 4.5a, insert**). When increasing the current density, the Li|HSE|Li cell exhibits a much more stable overpotential, whereas the Li|SPE|Li cell already fails as low as 0.05 mA cm⁻² (**Fig. 4.5b**). The improved performance is attributed to the addition of Li₆PS₅Cl fillers, which enhances both the ionic conductivity and mechanical strength of the SPE, thereby effectively suppressing Li dendrites.

To further understand the enhanced interfacial stability of the HSE towards Li metal, both the pristine electrolytes and the SEI formed on the Li anode disk after cycling were investigated using depth-profiling X-ray photoelectron spectroscopy (XPS). **Fig. 4.5c-h** depict the depth-dependent evolution of the C 1s, F 1s, and O 1s XPS spectra for both the SPE and HSE. Within the C 1s spectra (**Fig. 4.5c, f**), the peak corresponding to C-C/C-H is attributed to the ether groups of the PEO residues, while the smaller peaks of C-O and C=O arise from the decomposition products of PEO^{47,48}. It is evident that a noticeably organic outer layer is present on the surface of the SEI formed with SPE. In the F 1s spectra (**Fig. 4.5d, g**), the LiF peak and the C-F peak originate from the decomposition and residuals of LiTFSI⁴⁹⁻⁵¹. The evolution of the LiF peak intensity contrast between these two samples indicates the formation of a LiF-rich SEI layer of the Li-metal cycled with HSE. Tracking the relative spectral contribution of the O 1s species as a function of the etching time (**Fig.**

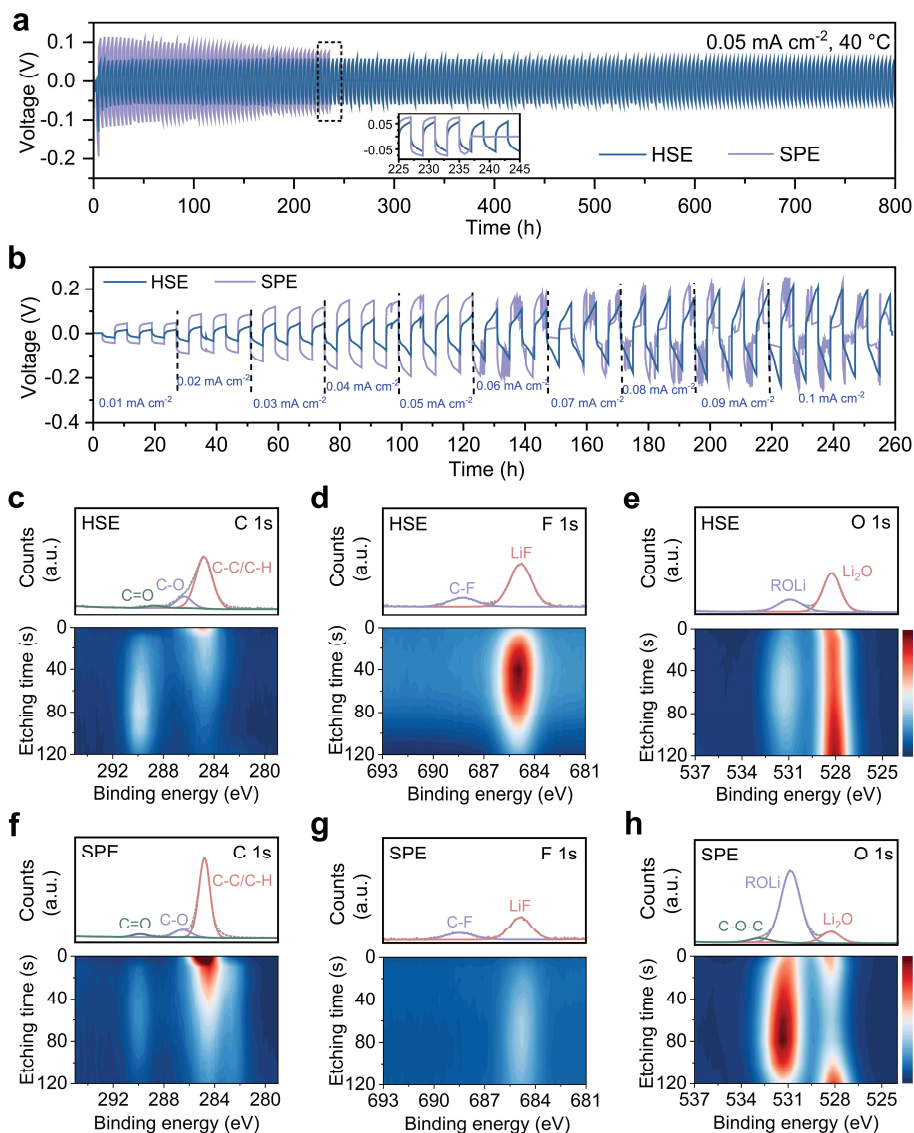


Fig. 4.5. Electrochemical performance and interfacial properties with Li-metal of the SPE and HSE. (a) Galvanostatic voltage profiles of the Li||Li symmetric cells measured at 0.05 mA cm⁻² and 40 °C (0.05 mAh cm⁻², with inserts showing the voltage profiles at ~235 h). (b) Plating and stripping curves of the Li||Li symmetric cells measured at variable current densities and 40 °C. Depth-profiling XPS measurements of C 1s, F 1s, and O 1s for the Li-metal anode cycled with (c-e) HSE and (f-h) SPE. Each plot comprises of two individual figures, i.e., the point before etching (up) and depth profiling spectrum (down). The dash lines represent the raw data and the continuous lines are from the fits. The color bar indicates the intensity from weak to strong from bottom to top. The Li-metal electrodes were obtained by disassembling the Li||Li symmetrical cells cycled with SPE or HSE electrolytes at 0.05 mA cm⁻¹ for 10 cycles (0.05 mAh cm⁻¹, 40 °C).

4.5e, h) indicates that the predominant presence of Li_2O in the SEI layer formed with HSE^{52,53}. In contrast, the SEI layer formed with SPE shows a prevalent distribution of the organic ROCO_2Li species^{54–56}. When correlating the observed SEI compositions with the surface properties of the pristine electrolytes, SPE shows a higher distribution of the PEO-LiTFSI phase and LiF on its surface (**Fig. S4.10**). This can be due to the addition of filler in the HSE weakening the signal from the polymer phase.

4.3 Conclusions

In summary, incorporating $\text{Li}_6\text{PS}_5\text{Cl}$ inorganic fillers into the PEO-LiTFSI polymer electrolyte, especially when processed using a solvent-assisted method, considerably improves the ionic conductivity of the SPE. The underlying mechanism is elucidated through an analysis of local Li-ion mobility, leveraging NMR's capability to provide dynamic and structural insights. The line-width measurements indicate that the incorporation of the $\text{Li}_6\text{PS}_5\text{Cl}$ filler suppresses crystallization in the polymer phase as the temperature decreases. The activation energies obtained from the Hendrickson-Bray and Abragam model fits of the line-width data suggest enhanced local Li-ion mobility in the HSEs compared to the SPE. The temperature dependence of the correlation time, τ_c , captures the characteristic phase transitions of the PEO phase, which reveals typical VTF behavior in the intermediate temperature range and Arrhenius behavior in the fully crystallized state. At low temperatures, the second T_1 relaxation component in the hybrid systems indicates two distinct dynamic modes within the polymer matrix, likely attributed to the presence of the filler. The fits from the 2D Richards spectral density function hints that the Li-ion transport occurs along the salt-rich polymer-filler interfaces. Despite the enhancement in local Li-ion mobility achieved through the addition of fillers, morphological inhomogeneities may counteract this effect, as evidenced by the lower conductivity and Li-ion dynamics observed in the dry-processed electrolyte compared to its solvent-processed counterpart. The improvement in local Li-ion dynamics from incorporating fillers is correlated with enhanced Li salt dissociation, altered polymer chain configuration, and increased segmental mobility. Finally, the formation of an inorganic-rich SEI layer at the Li/HSE interface can be adopted in designing high-performance HSEs for enabling Li-metal anode. The present work provides an in-depth understanding of local ion conduction and polymer-filler interactions in the PEO-sulfide

hybrid electrolyte system, with broad applicability to other electrolyte systems.

4.4 Methods

Preparation of PEO-based solid-state electrolytes

For both the SPE and (D)HSE, 384 mg PEO powder ($M_w = 600,000$ g/mol, Sigma-Aldrich) and 140 mg LiTFSI (Sigma-Aldrich) were used. SPE was prepared by mixing PEO and LiTFSI in 7 mL acetonitrile (Sigma-Aldrich) and stirring for 24 hours. The obtained homogenized slurry was cast onto a Teflon plate and dried in the glove box at room temperature for 24 hours, followed by additional drying under vacuum for 48 hours. HSE was fabricated by first grinding the PEO, LiTFSI, and 52.4 mg $\text{Li}_6\text{PS}_5\text{Cl}$ (10 wt%, NEI Corporation) in a mortar. The obtained mixture was then added to 7 ml of acetonitrile and stirred for 24 hours. The subsequent casting and drying procedures are the same as those used for the SPE.

The DHSE films were prepared using a hot-press method. The aforementioned amount of LiTFSI and $\text{Li}_6\text{PS}_5\text{Cl}$ were first mixed by grinding in a mortar for over 15 minutes, then the PEO powder was added gradually in approximately 50 mg increments, with 2 minutes of grinding between each addition. After all the PEO powder has been added, grind the mixture for over 15 minutes until a homogeneous dough forms. The resulting dough is then sandwiched between two polytetrafluoroethylene (PTFE) sheets, with a 150 μm spacer in between to control the thickness, and placed in a two-plate stainless steel assembly. This assembly is then heated on a hot plate set to 110°C. Once the target temperature is reached, it is held at that temperature for 10 minutes. Afterwards, the assembly is removed and compressed under a hydraulic press at 35 bar. Following compression, the dough is flattened into a membrane and then folded to improve mixing. The process of heating, compressing, and folding is repeated three times to ensure uniformity. Finally, the assembly is cooled under continuous compression for 12 hours. This extended cooling period ensures that the membrane cools gradually and uniformly, reducing exposure to external temperatures.

Material characterizations

For SEM imaging, the samples were transferred into an SEM (JEOL JSM-6010LA) machine using an airtight Argon-filled sample holder. The images were acquired with a 10 kV

accelerating voltage (secondary electron). DSC measurements were performed at $10^\circ \text{ min}^{-1}$ steps using a commercial TA-Q2000 DSC calorimeter (TA instruments). XPS measurements were carried out with a Thermo Fisher K-Alpha spectrometer. The samples were transferred to the XPS machine under vacuum using an air-tight sample holder. The spectrometer is equipped with a focused monochromatic Al $k\alpha$ source (1486.6 eV) anode operating at 36 W (12 kV, 3 mA), and a flood gun operating at 1 V (100 μA). The base pressure of the analysis chamber was approximately 2×10^{-9} mbar and the spot size was approximately 800×400 (μm^2). For the detailed scan collected before etching, a pass energy of 50 eV was used. Depth profiling was performed with an Ar^+ ion gun operated at 3 kV, corresponding to about 0.5 nm s^{-1} as calibrated on Ta_2O_5 , and a pass energy of 200 eV was used. In the analysis, the binding energy was corrected for the charge shift relative to the primary C 1s hydrocarbon peak at $BE = 284.8$ eV. For each sample, at least three points were measured which showed consistent results. The data were fitted using 70% Gaussian and 30% Lorentzian line shapes (weighted least-squares fitting method) and nonlinear Shirley-type background using the Thermo Fisher Avantage software.

Batteries assembly and electrochemical measurements

4 The ionic conductivity of the SPE and (D)HSE were calculated based on EIS data obtained using an electrochemical station (Autolab PGSTAT302N). The measurements were conducted from 10 MHz to 1 kHz with a sinusoidal signal ($V_{rms} = 10$ mV). The electrolytes were sandwiched between two stainless steels (SS) in coin cells, and each test temperature was maintained for more than 30 minutes to ensure thermal equilibrium. The EIS data was fitted using an Equivalent Circuit (EC) model that included R_s as the series resistance, R_b as the bulk electrolyte resistance, and CPE_b as a Constant Phase Element (CPE) representing the bulk capacitance of the electrolyte. In addition, CPE_{int} was introduced to account for the capacitance associated with the blocking electrodes at low frequencies. Subsequently, the bulk resistance (R_b) and ionic conductivity (σ) were determined using the formula $\sigma = d/(R_b \times A)$, with d representing the thickness of the electrolytes and A denoting the area of the electrolytes in contact with the stainless steels. The galvanostatic charge-discharge tests of the $\text{Li}||\text{Li}$ symmetrical cells were performed on a Maccor 4000 battery cycler at 40°C .

Solid-state NMR measurements

The temperature-dependent ${}^7\text{Li}$ line-width and T_1 relaxometry measurements were conducted using a Bruker Avance 300 MHz wide-bore spectrometer ($B_0 = 7.1$ T) equipped with an NEO console, operating at frequencies of 116.64 MHz for ${}^7\text{Li}$. A 90° pulse optimization was performed for each sample, and the probe was matched and tuned at every other temperature increment. The protocol began at ambient temperature (25°C) and involved temperature decrements of 5°C down to -20°C . Before each measurement, the system was equilibrated for at least 10 minutes to ensure thermal stability. The T_1 relaxation constants were measured using a saturation recovery experiment. The one-pulse ${}^7\text{Li}$ measurements were extended to lower temperatures (-55°C). Post-completion of the low-temperature series, the system was gradually returned to room temperature. High-temperature experiments were then performed, with the temperature progressively increased by 5°C up to a maximum of 80°C for high temperature experiments.

Additional MAS ssNMR measurements were performed on Bruker Ascend 500 MHz magnet ($B_0 = 11.7$ T), also equipped with an NEO console, operating at frequencies of 194.37 MHz for ${}^7\text{Li}$, 500.130 MHz for ${}^1\text{H}$, and 125.758 MHz for ${}^{13}\text{C}$. One-pulse ${}^7\text{Li}$ and ${}^1\text{H}$ experiments were performed with 90° pulse lengths of $3.25\ \mu\text{s}$ and $4\ \mu\text{s}$. A recycle delay of about four times T_1 was used for each nuclei, where the T_1 was determined using saturation recovery experiments. For ${}^1\text{H} \rightarrow {}^7\text{Li}$ CP MAS experiments, a radio frequency (r.f.) field strengths of 81 kHz and various contact times were applied, the r.f. field amplitude of ${}^1\text{H}$ during CP experiments was ramped from 70 to 100% and 128 scans were acquired for each sample with a recycle delay of 7 s. High power decoupling (hpdec) one-pulse ${}^{13}\text{C}$ measurements were conducted with a 90° pulse length of $5.95\ \mu\text{s}$ and an recycle delay of 1 s, and the data were fitted using MestReNova 11.

All measurements were conducted using a Bruker three-channel MAS 4 mm direct variable temperature (DVT) probe. The chemical shifts of ${}^7\text{Li}$ were referenced with respect to a 0.1 M LiCl solution (0 ppm), while the chemical shifts of ${}^1\text{H}$ and ${}^{13}\text{C}$ were referenced to solid adamantane (${}^1\text{H}$ at 1.81 ppm and ${}^{13}\text{C}$ at 38.48 ppm). Individual samples were prepared by cutting the electrolyte membranes into small pieces, which were then transferred into 4 mm zirconia rotors and sealed with a Vespel cap. A MAS frequency of 10 kHz was used for the MAS measurements. For the ${}^7\text{Li}$ line-width and T_1 relaxometry measurements, the cap

was modified by filing down its drive fins to prevent rotation, thus enabling static measurements.

4.5 Supplementary information

Supplementary Texts

Text S4.1: Hendrickson Bray's phenomenological equation

This approach is based on the paper by J. R. Hendrickson and P. Bray³², which employs a phenomenological method to NMR motional narrowing. The model considers the system to consist of two states, the first component to consist of thermally non-excited ions, each characterized by a spin-spin relaxation time T_{2A} related to a broad line-width of A :

$$T_{2A} = \frac{1}{A} \quad (4.1)$$

and the second component is that of thermally excited ions with a spin-spin relaxation time T_{2B} and a narrow line-width of B :

$$T_{2B} = \frac{1}{B} \quad (4.2)$$

Experimentally, only a single NMR line with a line-width ω is observed, which is attributed to the rapid exchange between the two states. Consequently, the line-width is a combination of both fractions f_A and f_B , each weighted by their respective T_2 values:

$$T_2 = f_A T_{2A} + f_B T_{2B} = \frac{1}{\omega} \quad (4.3)$$

The total fraction of ions is unity, and the fraction of thermally activated ions f_B can be approximated using the Arrhenius equation, which is given by:

$$f_B = \exp\left(-\frac{E_a}{kT}\right) \quad (4.4)$$

where E_a is the energy barrier or activation energy, k is Boltzmann constant and T is the absolute temperature in Kelvin.

Combining equations (4.1), (4.2), (4.3), and (4.4), the equation for the temperature-

dependent line-width $\omega(T)$ becomes:

$$\omega(T) = A \left[\left(1 + \left(\left(\frac{A}{B} - 1 \right) \exp \left(-\frac{E_a}{kT} \right) \right) \right) \right] + D \quad (4.5)$$

where D is the correction factor.

Text S4.2: Abragam model

The rate of fluctuations in the local field of a spin can be described by a characteristic rotational correlation time, τ_c . Fast fluctuations, which average out interactions, are given with respect to the instantaneous Larmor precession (ω_0) in the local field, and are typically categorized as³³:

$$\omega_0 \tau_c \ll 1 \quad (4.6)$$

The product of the Larmor frequency and correlation time should be much less than 1 for the fast regime. If this inequality is true, there will be appreciable narrowing. Conversely, when $\omega_0 \tau_c$ is large, the NMR signals are influenced by slower motions, and the regime is often termed the “slow exchange” regime. Qualitatively the line-width ($\Delta\nu$) can be defined as the inverse of the time (t), after which spins precessing in their respective local field, which were initially in phase, are now out of phase:

$$t \cong \frac{1}{\nu} \quad (4.7)$$

where ν is the line-width. Motional narrowing starts when the rate of fluctuation, described by the correlation time, τ_c , is fast enough to start averaging out interactions, thus:

$$\omega_0 \ll \frac{1}{\tau_c} \quad (4.8)$$

From this assumption, an estimation for the correlation time at any line-width can be obtained by the following relationship³³:

$$\tau_c = \frac{\alpha}{\nu} \tan \left[\frac{\pi}{2} \left(\frac{\nu}{\nu_{rigid}} \right)^2 \right] \quad (4.9)$$

where v is the line-width [usually characterized by full width half maximum (FWHM)] at a given temperature, v_{rigid} is the FWHM of the rigid phase, or the FWHM measured at the lowest temperature in this case, and α is a constant close to 1. It should be noted that when $v \approx v_{rigid}$, the term $\tan\left[\frac{\pi}{2}\left(\frac{v}{v_{rigid}}\right)\right]^2$ becomes very large, which causes significant uncertainties in τ_c . Therefore, R_{rigid} is excluded from detailed analysis in **Fig. 4.2c, d**. In some cases, τ_c is a thermally activated jump process described by Arrhenius:

$$\tau_c = \tau_0 \exp\left(\frac{E_a}{kT}\right) \quad (4.10)$$

where τ_0 is the pre-exponential constant. However, in polymers, diffusion processes are not governed by a strict Arrhenius behavior. The Vogel-Tamman-Flucher (VTF) equation is often employed to describe the conductivity behavior of materials approaching their T_g ³⁹. Hence, a modified equation is used to describe the correlation time:

$$\tau_c = \tau_0 \exp\left(\frac{A}{k(T - T_0)}\right) \quad (4.11)$$

where τ_0 is the pre-exponential constant, A is the pseudo-activation energy, and T_0 is the ideal glass transition temperature. The VTF equation assumes that mobility is affected by free volume of the polymer, which has a non-linear dependence on temperature and goes to zero at T_0 , where polymer chain motion ceases.

Text S4.3: Spectral density fitting

Interpreting the shape of relaxation data and its implications for the motional processes of the probed Li-ions is not straightforward. The measured T_1 needs to be linked to the correlation time, τ_c , of the probed nucleus in its environment, to determine the activation energy for the observed motional process. Spectral density fitting plays a pivotal role in understanding of the complex interplays. The spectral density function $J(\omega)$ is the Fourier transform (in the frequency domain) of the autocorrelation function $G(t)$ (in the time domain), which quantifies how the local magnetic field at one time correlates with its magnitude and orientation at a later point in time^{35,57}. The spectral densities reveal patterns of spin fluctuations, and characterizing these patterns provides a deeper understanding of the

system's dynamics.

Redfield equation

In a sample that is mostly dominated by dipolar relaxation, the spin-lattice relaxation rates can be described by the Redfield equation³³:

$$\frac{1}{T_1} = K_D [J(\omega_0) + 4J(2\omega_0)] \quad (4.12)$$

This expresses the spin-lattice relaxation rate $1/T_1$ as a function of the spectral density function with a proportionality constant K_D , which is related to the strength of the dominant spin interaction, whether dipolar or quadrupolar. Spectral density fitting involves adjusting the parameters of a chosen model of $J(\omega_0)$ so that the model accurately reflects the experimentally measured relaxation times. This process enables us to infer details about the molecular motions that influence the relaxation behaviour.

Bloembergen-Purcell- Pound (BPP) model

The simplest and most common spectral density model is the Bloembergen-Purcell-Pound (BPP) model. This model assumes isotropic random three dimensional (3D) molecular motion with a single thermally activated correlation time, τ_c ⁵⁷.

$$J_{BPP}(\omega_0, \tau_c) = \frac{2\tau_c}{1 + (\tau_c\omega_0)^2} \quad (4.13)$$

where τ_c can be described with the Arrhenius equation or VTF equation. The position of the maxima or, where the relaxation rate is highest, is when $\omega\tau_c = 1$ (when the correlation time is the inverse of the Larmor frequency). The spectral density then has limiting values far away from the maxima. At the low temperature limit ($\omega\tau_c \ll 1$) and high temperature limit ($\omega\tau_c \gg 1$), the spectral density reduced to a simpler form:

$$J_{BPP}(\omega_0, \tau_c) = \begin{cases} 2\tau_c, & \omega_0\tau_c \ll 1; \\ 2/(\tau_c\omega_0^2), & \omega_0\tau_c \gg 1. \end{cases} \quad (4.14)$$

When substituting into equation (4.12) and plotting the natural log of $(1/T_1)$ against $(1/k_bT)$, the slopes of the low and high temperature regions correspond to $-E_a$ and $+E_a$, respectively. In more complex systems, deviations from this model often arise due to factors

such as system disorder or strong Coulomb interactions among the moving ions, leading to asymmetrical slopes⁵⁸. To account for this asymmetry, an asymmetry parameter β is introduced:

$$\beta = \frac{E_{a,LT}}{E_{a,HL}} + 1 \quad (4.15)$$

The overall spectral density is given by:

$$J_{BPP}(\omega_0, \tau_c) \propto \frac{\tau_c}{1+(\omega_0\tau_c)^\beta} \quad (4.16)$$

This is often referred to as the modified BPP model. The full expression that is fit to the relaxation rates reads as follows:

$$\frac{1}{T_1} = K_D \left[\frac{2\tau_c}{1+(\omega_0\tau_c)^\beta} + \frac{4\tau_c}{1+(2\omega_0\tau_c)^\beta} \right] \quad (4.17)$$

Richards model

In some systems, diffusion may be restricted to two dimensions. Unlike the symmetric peaks observed with 3D diffusion-induced relaxation rates, 2D diffusion exhibits an asymmetric profile, typically with a lower slope on the high-temperature side. This can occur in cases such as conduction along an interface or surface. To model such systems, Richards proposed an empirical expression that combines the two limiting cases for low and high temperatures⁴⁵:

$$J_{2D}(\omega_0, \tau_c) \propto \begin{cases} \omega_0^{-2}\tau_c^{-1}, & \omega_0\tau_c \gg 1; \\ \tau_c \ln(1/\omega_0\tau_c), & \omega_0\tau_c \ll 1. \end{cases} \quad (4.18)$$

combined into the empirical expression:

$$J_{2D}(\omega_0, \tau_c) \propto \tau_c \ln \left(1 + \frac{1}{(\omega_0\tau_c)^\beta} \right) \quad (4.19)$$

Here, the parameter β is expected to be equal to 2 for following the BPP behavior. If this accurately approximates the underlying dynamics, the frequency and temperature dependencies are described by a single equation $J(\omega_0, \tau_c)$. This results in a slightly asymmetric rate peak, with the high-temperature slope being somewhat reduced compared to the low-temperature slope.

The full expression that is fit to the relaxation rates reads as follows:

$$\frac{1}{T_1} = K_D \left[\tau_c \ln \left(1 + \frac{1}{(\omega_0 \tau_c)^\beta} \right) + 4\tau_c \ln \left(1 + \frac{1}{(2\omega_0 \tau_c)^\beta} \right) \right] \quad (4.20)$$

Multiple correlation times

Electrolytes often exhibit multiple simultaneous diffusion processes within the system. In such systems, where different thermally activated processes have distinct rates and activation energies, these processes contribute additively, assuming they do not interfere with one another. Mathematically, this can be expressed as:

$$\frac{1}{T_{1,total}} = \frac{1}{T_{1,a}} + \frac{1}{T_{1,b}} + \dots + \frac{1}{T_{1,N}} \quad (4.21)$$

This means that it is possible to fit complex T_1 data as a sum of superimposed individual processes.

Text S4.4: Cross polarization MAS ssNMR

CP dynamics depend on the effective heteronuclear dipolar interaction ($T_{I-S} \approx 1/r^6$, r : distance) between ^1H and ^7Li , as well as on local mobilities that affect the relaxation of magnetization ($T_{1\rho}$ of ^7Li and ^1H). A stronger effective dipolar interaction leads to a faster buildup, while motions can reduce the effectiveness of transfer and enhance the decay of magnetization if they fall within the range of strength of the CP locking fields. The broad peaks observed near the main LiTFSI-PEO resonance in the spectra of HSE and DHSE correspond to the interfacial products that are in close proximity to the neighboring protons (**Fig. S4.9**). Focusing on the main LiTFSI-PEO environment (in the dotted box), both the HSE and DHSE have much smaller cross-relaxation time (T_{H-Li}) than that for the SPE, with the DHSE showing slower cross-relaxation than the HSE. These differences are also reflected in their distinct proton $T_{1\rho}$ ($T_{1\rho H}$) values (**Table S4.2**). This effect is attributed to changes in the proton environment due to the disruption of the PEO structure by fillers, which alters the proton dynamics on a time scale that does not affect the transfer rate but results in different $T_{1\rho H}$ values for both samples. This suggests that the polymer-filler interactions improve local proton dynamics, with this improvement closely associated with local morphological homogeneity.

Supplementary Figures

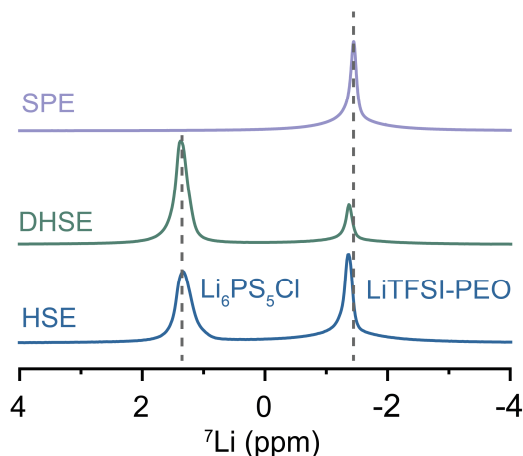


Fig. S4.1. ${}^7\text{Li}$ environments in the SPE and (D)HSE. 1D ${}^7\text{Li}$ MAS ssNMR spectra of the SPE, DHSE, and HSE electrolytes. The relatively low intensity of the LiTFSI-PEO environment in the DHSE is indicative of the sample heterogeneity, which is attributed to more $\text{Li}_6\text{PS}_5\text{Cl}$ and less polymer phase in the sample holder. Since the MAS measurement captures an average signal, the peak intensity reflects the absolute amount of each environment.

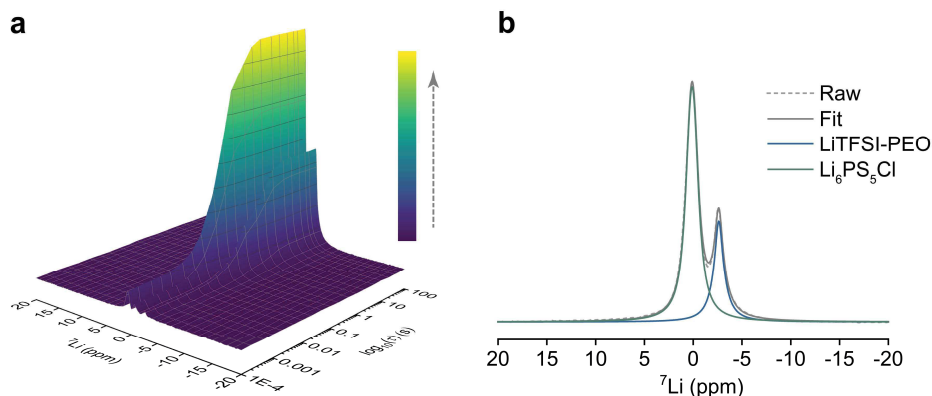


Fig. S4.2. Peak deconvolution of the obtained ${}^7\text{Li}$ NMR spectra from the line-width and T_1 relaxometry measurements for the (D)HSE. Using the T_1 measurement for the HSE at 30°C as an example. Breaking down the spectrum into individual Lorentzian functions for each peak allows for a more accurate determination of both line-widths and amplitudes, effectively separating the contributions from the PEO and $\text{Li}_6\text{PS}_5\text{Cl}$ phases. (a) 3D plot of the T_1 measurement before deconvolution, with the chemical shift in ppm on the x -axis, the logarithm of the recovery time (τ) on the y -axis, and the peak intensity on the z -axis. (b) The spectrum after deconvolution, showing the same T_1 measurement at $\tau = 100$ s. The color bar indicates the intensity from weak to strong from bottom to top.

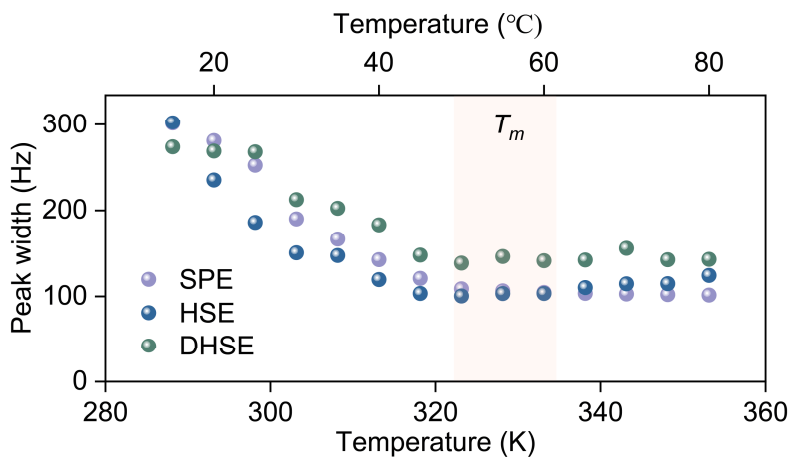


Fig. S4.3. Probing local Li-ion dynamics using ^7Li line-width measurements. Zoomed-in view of the temperature-dependent ^7Li line-width measurements in Fig. 4.2a, b for the SPE and (D)HSE, within a temperature range of 15 to 80 $^{\circ}\text{C}$.

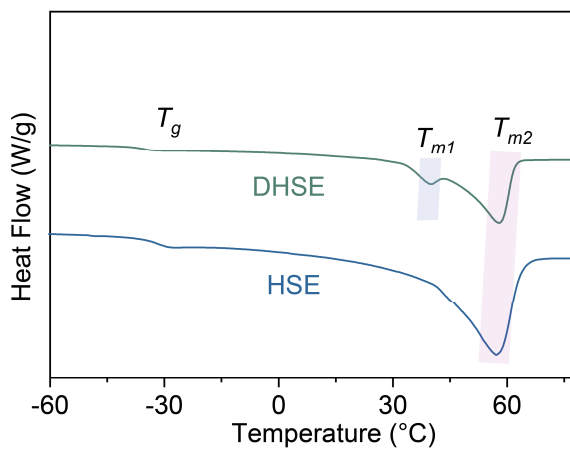


Fig. S4.4. DSC measurements showing the heat flow of HSE and DHSE. DSC curves of HSE and DHSE under heating, with the glass transition temperature (T_g) and melting temperatures (T_{m1} and T_{m2}) are highlighted.

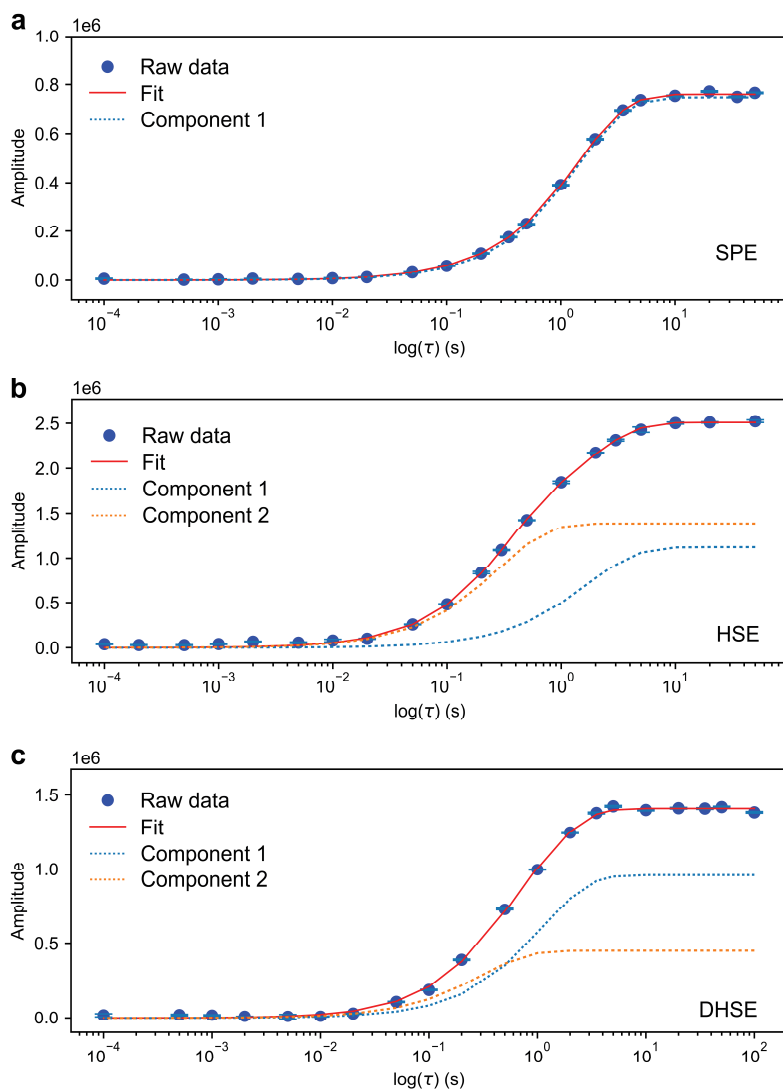


Fig. S4.5. Probing local Li-ion dynamics through ${}^7\text{Li}$ T_1 relaxometry measurements. Bi-exponential recovery fit for (a) SPE, (b) HSE, and (c) DHSE. For all samples, the data were obtained at 0 °C, with τ representing the recovery time in the saturation recovery experiments⁹ for the T_1 measurements. For the HSE and DHSE, optimal fits were achieved using a bi-exponential recovery model, where each component corresponds to distinct T_1 dynamics. In contrast, the fitting of the second component for the SPE data failed, indicating the presence of only one component.

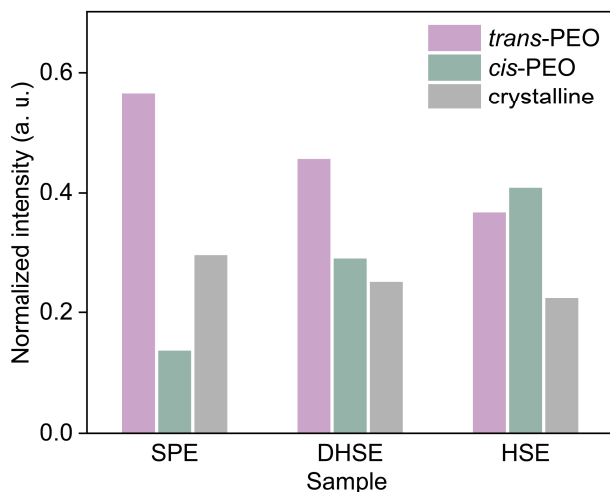


Fig. S4.6. Characterizing the polymer configuration. Normalized peak intensity of the hpdec ^{13}C single-pulse MAS ssNMR spectra in Fig. 4.4a-c. The data were fitted using MestReNova 11. The normalized intensity for each individual sample was derived from the peak areas obtained from the fits.

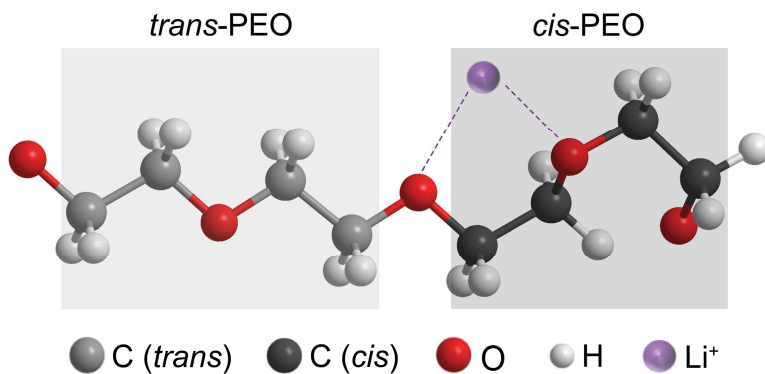


Fig. S4.7. Carbon conformation diagram. Schematic showing the typical carbon conformation of the PEO chains.

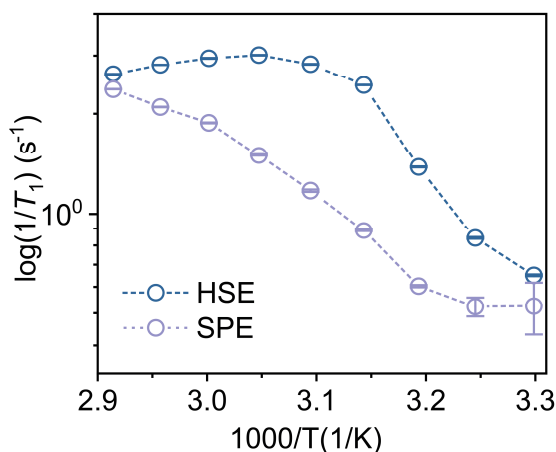


Fig. S4.8. Probing local proton dynamics through ^1H T_1 relaxometry measurements. ^1H relaxation rates measured for the SPE and HSE.

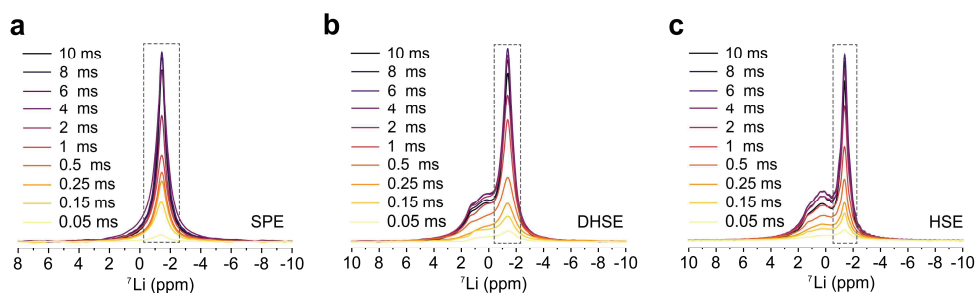


Fig. S4.9. 1D $^1\text{H} \rightarrow ^7\text{Li}$ CP MAS ssNMR spectra of the SPE and (D) HSE. 1D $^1\text{H} \rightarrow ^7\text{Li}$ CP MAS ssNMR spectra of (a) SPE, (b) DHSE, and (c) HSE with contact times ranging from 0.05 to 10 ms. The LiTFSI-PEO peak is highlighted in the dotted box.

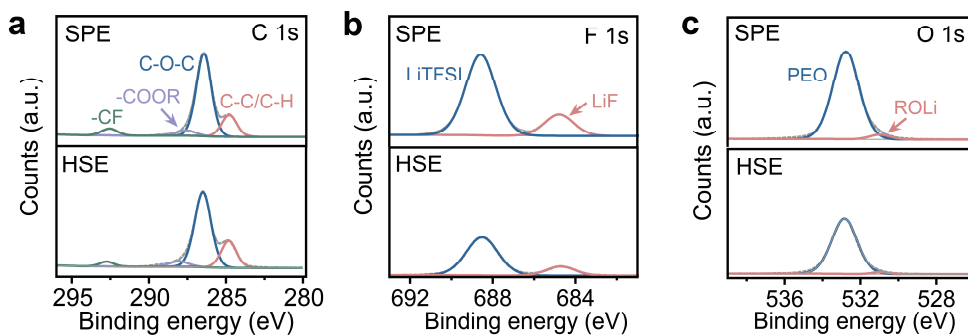


Fig. S4.10. Characterizing the surface properties of the pristine SPE and HSE. XPS measurements of (a) C 1s, (b) F 1s, and (c) O 1s for the pristine SPE and HSE.

Supplementary Tables

Table S4.1. Activation energies (E_a) obtained from the Hendrickson Bray and Abragam model fits in the line-width measurements in Fig. 4.2.

Sample	E_a from HB model (eV)	E_a from Abragam model (eV)	
		Arrhenius fit	VTF fit
SPE	0.60 ± 0.03	0.89 ± 0.03	$(13.3 \pm 0.5) \times 10^{-3}$
HSE	0.51 ± 0.02	0.37 ± 0.01	$(2.7 \pm 0.1) \times 10^{-3}$
DHSE	0.54 ± 0.03	0.46 ± 0.01	$(8.2 \pm 0.5) \times 10^{-3}$

Table S4.2. Fitting results of the $^1\text{H} \rightarrow ^7\text{Li}$ CP MAS curves in Fig. S4.9.

		T_{H-Li} (ms)	$T_{1\rho H}$ (ms)
SPE	LiTFSI-PEO	3.43	83.54
HSE	LiTFSI-PEO	1.15	11.42
DHSE	LiTFSI-PEO	1.59	52.69

References

1. Ye, L. & Li, X. A dynamic stability design strategy for lithium metal solid state batteries. *Nature* **593**, 218–222 (2021).
2. Janek, J. & Zeier, W. G. Challenges in speeding up solid-state battery development. *Nature Energy* **8**, 230–240 (2023).
3. Zhao, Q., Stalin, S., Zhao, C.-Z. & Archer, L. A. Designing solid-state electrolytes for safe, energy-dense batteries. *Nature Reviews Materials* **5**, 229–252 (2020).
4. Manthiram, A., Yu, X. & Wang, S. Lithium battery chemistries enabled by solid-state electrolytes. *Nature Reviews Materials* **2**, 16103 (2017).
5. Xue, Z., He, D. & Xie, X. Poly(ethylene oxide)-based electrolytes for lithium-ion batteries. *Journal of Materials Chemistry A* **3**, 19218–19253 (2015).
6. Zhou, D., Shanmukaraj, D., Tkacheva, A., Armand, M. & Wang, G. Polymer electrolytes for lithium-based batteries: advances and prospects. *Chem* **5**, 2326–2352 (2019).
7. Zhang, D., Meng, X., Hou, W., Hu, W., Mo, J., Yang, T. & Li, M. Solid polymer electrolytes: Ion conduction mechanisms and enhancement strategies. *Nano Research Energy* **2**, e9120050 (2023).
8. Lu, X., Wang, Y., Xu, X., Yan, B., Wu, T. & Lu, L. Polymer-based solid-state electrolytes for high-energy-density lithium-ion batteries—review. *Advanced Energy Materials* **13**, 2301746 (2023).
9. Liu, S., Liu, W., Ba, D., Zhao, Y., Ye, Y., Li, Y. & Liu, J. Filler-integrated composite polymer electrolyte for solid-state lithium batteries. *Advanced Materials* **35**, 2110423 (2022).
10. Xue, S., Chen, S., Fu, Y., Zhu, H., Ji, Y., Song, Y. & Yang, L. Revealing the role of active fillers in Li-ion conduction of composite solid electrolytes. *Small* **19**, 2305326 (2023).
11. Zhang, X., Cheng, S., Fu, C., Yin, G., Zuo, P., Wang, L. & Huo, H. Unveiling the structure and diffusion kinetics at the composite electrolyte interface in solid-state batteries. *Advanced Energy Materials* **14**, 2401802 (2024).
12. Liu, M., Zhang, S., van Eck, E. R., Wang, C., Ganapathy, S. & Wagemaker, M. Improving Li-ion interfacial transport in hybrid solid electrolytes. *Nature Nanotechnology* **19**, 959–967 (2022).
13. Zheng, J., Wang, P., Liu, H. & Hu, Y.-Y. Interface-enabled ion conduction in $\text{Li}_{10}\text{GeP}_2\text{S}_{12}$ -poly (ethylene oxide) hybrid electrolytes. *ACS Applied Energy Materials* **2**, 1452–1459 (2019).
14. Simon, F. J., Hanauer, M., Richter, F. H. & Janek, J. Interphase formation of $\text{PEO}_{20}\text{:LiTFSI-Li}_6\text{PS}_5\text{Cl}$ composite electrolytes with lithium metal. *ACS Applied Materials & Interfaces* **12**, 11713–11723 (2020).
15. Zheng, J., Tang, M. & Hu, Y.-Y. Lithium ion pathway within $\text{Li}_7\text{La}_3\text{Zr}_2\text{O}_{12}$ -polyethylene

- oxide composite electrolytes. *Angewandte Chemie International Edition* **55**, 12538–12542 (2016).
16. Zheng, J., Dang, H., Feng, X., Chien, P.-H. & Hu, Y.-Y. Li-ion transport in a representative ceramic–polymer–plasticizer composite electrolyte: $\text{Li}_7\text{La}_3\text{Zr}_2\text{O}_{12}$ –polyethylene oxide–tetraethylene glycol dimethyl ether. *Journal of Materials Chemistry A* **5**, 18457–18463 (2017).
17. Spencer Jolly, D., Melvin, D. L., Stephens, I. D., Brugge, R. H., Pu, S. D., Bu, J. & Bruce, P. G. Interfaces between ceramic and polymer electrolytes: a comparison of oxide and sulfide solid electrolytes for hybrid solid-state batteries. *Inorganics* **10**, 60 (2022).
18. Yang, X., Liu, J., Pei, N., Chen, Z., Li, R., Fu, L. & Zhao, J. The critical role of fillers in composite polymer electrolytes for lithium battery. *Nano-Micro Letters* **15**, 74 (2023).
19. Zheng, J. & Hu, Y.-Y. New insights into the compositional dependence of Li-ion transport in polymer–ceramic composite electrolytes. *ACS Applied Materials & Interfaces* **10**, 4113–4120 (2018).
20. Miao, X., Guan, S., Ma, C., Li, L. & Nan, C. W. Role of interfaces in solid-state batteries. *Advanced Materials* **35**, 2206402 (2023).
21. Pan, K., Zhang, L., Qian, W., Wu, X., Dong, K., Zhang, H. & Zhang, S. A flexible ceramic/polymer hybrid solid electrolyte for solid-state lithium metal batteries. *Advanced Materials* **32**, 2000399 (2020).
22. Popovic, J., Brandell, D., Ohno, S., Hatzell, K. B., Zheng, J. & Hu, Y.-Y. Polymer-based hybrid battery electrolytes: theoretical insights, recent advances and challenges. *Journal of Materials Chemistry A* **9**, 6050–6069 (2021).
23. Böhmer, R., Jeffrey, K. R. & Vogel, M. Solid-state Li NMR with applications to the translational dynamics in ion conductors. *Progress in Nuclear Magnetic Resonance Spectroscopy* **50**, 87–174 (2007).
24. Ranque, P., Zagórski, J., Devaraj, S., Aguesse, F. & López del Amo, J. M. Characterization of the interfacial Li-ion exchange process in a ceramic–polymer composite by solid state NMR. *Journal of Materials Chemistry A* **9**, 17812–17820 (2021).
25. Ghorbanzade, P., Pesce, A., Armand, M., Gómez, K., Devaraj, S., López-Aranguren, P. & López del Amo, J. M. Unveiling the reactivity and the Li-ion exchange at the PEO– $\text{Li}_6\text{PS}_5\text{Cl}$ interphase: Insights from solid-state NMR. *Small Structures* **5**, 2400139 (2024).
26. Liu, M., Cheng, Z., Ganapathy, S., Wang, C., Haverkate, L. A., Tułodziecki, M. & Wagemaker, M. Tandem interface and bulk Li-ion transport in a hybrid solid electrolyte with micro-sized active filler. *ACS Energy Letters* **4**, 2336–2342 (2019).
27. Ruhl, J., Riegger, L. M., Ghidui, M. & Zeier, W. G. Impact of solvent treatment of the superionic argyrodite $\text{Li}_6\text{PS}_5\text{Cl}$ on solid-state battery performance. *Advanced Energy and Sustainability Research* **2**, 2000077 (2021).
28. Tan, D. H., Banerjee, A., Deng, Z., Wu, E. A., Nguyen, H., Doux, J. M. & Chen, Z. Enabling thin and flexible solid-state composite electrolytes by the scalable solution process. *ACS Applied Energy Materials* **2**, 6542–6550 (2019).

29. Porcarelli, L., Gerbaldi, C., Bella, F. & Nair, J. R. Super soft all-ethylene oxide polymer electrolyte for safe all-solid lithium batteries. *Scientific Reports* **6**, 19892 (2016).
30. Ao, X., Wang, X., Tan, J., Zhang, S., Su, C., Dong, L. & Wang, H. Nanocomposite with fast Li⁺ conducting percolation network: Solid polymer electrolyte with Li⁺ non-conducting filler. *Nano Energy* **79**, 105475 (2021).
31. Mackanic, D. G., Michaels, W., Lee, M., Feng, D., Lopez, J., Qin, J. & Bao, Z. Crosslinked poly(tetrahydrofuran) as a loosely coordinating polymer electrolyte. *Advanced Energy Materials* **8**, 1800703 (2018).
32. Hendrickson, J. R. & Bray, P. J. A phenomenological equation for NMR motional narrowing in solids. *Journal of Magnetic Resonance* **9**, 341–357 (1973).
33. Abragam, A. *The Principles of Nuclear Magnetism*. (Clarendon Press, Oxford, 1989).
34. Quartarone, E. & Mustarelli, P. Electrolytes for solid-state lithium rechargeable batteries: recent advances and perspectives. *Chemical Society Reviews* **40**, 2525 (2011).
35. Levitt, M. H. *Spin Dynamics: Basics of Nuclear Magnetic Resonance*. (John Wiley & Sons, Chichester, England, 2008).
36. Chung, S. H., Jeffrey, K. R. & Stevens, J. R. A ⁷Li nuclear magnetic resonance study of LiCF₃SO₃ complexed in poly(propylene-glycol). *The Journal of Chemical Physics* **94**, 1803–1811 (1991).
37. Manuel Stephan, A. Review on gel polymer electrolytes for lithium batteries. *European Polymer Journal* **42**, 21–42 (2006).
38. Lin, C.-L., Kao, H.-M., Wu, R.-R. & Kuo, P.-L. Multinuclear solid-state NMR, DSC, and conductivity studies of solid polymer electrolytes based on polyurethane/poly(dimethylsiloxane) segmented copolymers. *Macromolecules* **35**, 3083–3096 (2002).
39. Ries, M. E., Klein, P. G., Brereton, M. G. & Ward, I. M. Proton NMR study of rouse dynamics and ideal glass transition temperature of poly(ethylene oxide) LiCF₃SO₃ complexes. *Macromolecules* **31**, 4950–4956 (1998).
40. Ikeda, M. & Aniya, M. Understanding the Vogel–Fulcher–Tammann law in terms of the bond strength–coordination number fluctuation model. *Journal of Non-Crystalline Solids* **371**, 53–57 (2013).
41. Jeon, J.-D. & Kwak, S.-Y. Variable-temperature ⁷Li solid-state NMR investigation of Li-ion mobility and its correlation with conductivity in pore-filling polymer electrolytes for secondary batteries. *Macromolecules* **39**, 8027–8034 (2006).
42. Marzantowicz, M., Dygas, J. R., Krok, F., Nowiński, J. L., Tomaszewska, A., Florjańczyk, Z. & Zygadło-Monikowska, E. Crystalline phases, morphology and conductivity of PEO:LiTFSI electrolytes in the eutectic region. *Journal of Power Sources* **159**, 420–430 (2006).
43. Epp, V., Gün, Ö., Deiseroth, H.-J. & Wilkening, M. Highly mobile ions: Low-temperature NMR directly probes extremely fast Li⁺ hopping in argyrodite-type Li₆PS₅Br. *Journal of*

- Physical Chemistry Letters* **4**, 2118–2123 (2013).
44. Beckmann, P. A. Spectral densities and nuclear spin relaxation in solids. *Physics Reports* **171**, 85–128 (1988).
45. Myron B. Salamon. *Physics of Superionic Conductors*. vol. 15 (Springer Berlin Heidelberg, Berlin, Heidelberg, 1979).
46. Xu, S., Sun, Z., Sun, C., Li, F., Chen, K., Zhang, Z. & Li, F. Homogeneous and fast ion conduction of peo-based solid-state electrolyte at low temperature. *Advanced Functional Materials* **30**, 2007172 (2020).
47. Li, X., Zheng, Y. & Li, C. Y. Dendrite-free, wide temperature range lithium metal batteries enabled by hybrid network ionic liquids. *Energy Storage Materials* **29**, 273–280 (2020).
48. Pan, Q., Barbash, D., Smith, D. M., Qi, H., Gleeson, S. E. & Li, C. Y. Correlating electrode–electrolyte interface and battery performance in hybrid solid polymer electrolyte-based lithium metal batteries. *Advanced Energy Materials* **7**, 1701231 (2017).
49. Xu, C., Sun, B., Gustafsson, T., Edström, K., Brandell, D. & Hahlin, M. Interface layer formation in solid polymer electrolyte lithium batteries: an XPS study. *Journal of Materials Chemistry A* **2**, 7256–7264 (2014).
50. Huo, H., Jiang, M., Mogwitz, B., Sann, J., Yusim, Y., Zuo, T. T. & Janek, J. Interface design enabling stable polymer/thiophosphate electrolyte separators for dendrite-free lithium metal batteries. *Angewandte Chemie International Edition* **62**, e202218044 (2023).
51. Tan, J., Matz, J., Dong, P., Shen, J. & Ye, M. A growing appreciation for the role of LiF in the solid electrolyte interphase. *Advanced Energy Materials* **11**, 2100046 (2021).
52. Zeng, H., Yu, K., Li, J., Yuan, M., Wang, J., Wang, Q. & Chi, S. S. Beyond LiF: Tailoring Li₂O-dominated solid electrolyte interphase for stable lithium metal batteries. *ACS Nano* **18**, 1969–1981 (2024).
53. Guo, R. & Gallant, B. M. Li₂O solid electrolyte interphase: probing transport properties at the chemical potential of lithium. *Chemistry of Materials* **32**, 5525–5533 (2020).
54. Xu, J., Li, J., Li, Y., Yang, M., Chen, L., Li, H. & Wu, F. Long-life lithium-metal all-solid-state batteries and stable li plating enabled by in situ formation of Li₃PS₄ in the SEI layer. *Advanced Materials* **34**, 2203281 (2022).
55. Zhang, J., Li, S., Wang, X., Mao, S., Guo, J., Shen, Z. & Lu, Y. Construction of stable Li₂O-rich solid electrolyte interphase for practical PEO-based Li-metal batteries. *Advanced Energy Materials* **14**, 2302587 (2023).
56. Fang, R., Xu, B., Grundish, N. S., Xia, Y., Li, Y., Lu, C. & Goodenough, J. B. Li₂S₆-integrated peo-based polymer electrolytes for all-solid-state lithium-metal batteries. *Angewandte Chemie* **133**, 17842–17847 (2021).
57. Beckmann, P. A. Spectral densities and nuclear spin relaxation in solids. *Physics Reports* **171**, 85–128 (1988).

58. Hanghofer, I., Brinek, M., Eisbacher, S. L., Bitschnau, B., Volck, M., Hennige, V. & Wilkening, H. M. R Substitutional disorder: structure and ion dynamics of the argyrodites $\text{Li}_6\text{PS}_5\text{Cl}$, $\text{Li}_6\text{PS}_5\text{Br}$ and $\text{Li}_6\text{PS}_5\text{I}$. *Physical Chemistry Chemical Physics* **21**, 8489–8507 (2019).
59. Keeler, J. J. *Understanding NMR Spectroscopy*. (Wiley, Chichester, West Sussex, 2011).

5

Improving Li-ion Interfacial Transport in Hybrid Solid Electrolytes

“山重水复疑无路，柳暗花明又一村”

“After endless mountains and rivers that leave doubt whether there is a path out, suddenly one encounters the shade of a willow, bright flowers and a lovely village.”

陆游《游山西村》(In the Shanxi Mountains)

This chapter has been published as: Liu, M., **Zhang, S.**, van Eck, E. R., Wang, C., Ganapathy, S. & Wagemaker, M. Improving Li-ion interfacial transport in hybrid solid electrolytes, *Nature Nanotechnology* 17, 959-967 (2022).

Abstract

The development of commercial solid-state batteries has to date been hindered by the individual limitations of inorganic and organic solid electrolytes, motivating hybrid concepts. However, the room-temperature conductivity of hybrid solid electrolytes is still insufficient to support the required battery performance. A key challenge is to assess the lithium (Li)-ion transport over the inorganic and organic interfaces and relate this to surface chemistry. Here we study the interphase structure and the Li-ion transport across the interface of hybrid solid electrolytes using solid-state nuclear magnetic resonance spectroscopy. In a hybrid solid polyethylene oxide polymer-inorganic electrolyte, we introduce two representative types of ionic liquid that have different miscibilities with the polymer. The poorly miscible ionic liquid wets the polymer-inorganic interface and increases the local polarizability. This lowers the diffusional barrier, resulting in an overall room-temperature conductivity of $2.47 \times 10^{-4} \text{ S cm}^{-1}$. A critical current density of 0.25 mA cm^{-2} versus a Li-metal anode shows improved stability, allowing cycling of a LiFePO_4 -Li-metal solid-state cell at room temperature with a Coulombic efficiency of 99.9%. Tailoring the local interface environment between the inorganic and organic solid electrolyte components in hybrid solid electrolytes seems to be a viable route towards designing highly conducting hybrid solid electrolytes.

5.1 Introduction

Solid-state batteries are recognized as a key candidate for next generation batteries because of their potential to improve both energy density and safety^{1,2}. However, the progress in solid-state battery development is hindered by the many criteria that solid electrolytes need to satisfy to become commercially viable. These include high ionic conductivity, flexibility, (electro)chemical stability, compatibility with electrode materials, and processability, conditions that are often hard to fulfill with an individual organic or inorganic solid electrolyte material³⁻⁷. This has led to the investigation of hybrid electrolyte that typically combine an organic and an inorganic phase⁸⁻¹¹. One of the most intensively investigated hybrid solid electrolytes (HSEs) comprises of inorganic filler particles embedded in a conductive organic polymer matrix. The use of polyethylene oxide (PEO) as the organic polymer component together with a lithium (Li)-containing salt is especially attractive because of its relative stability towards Li-metal, excellent contact/adhesion with electrodes, superior mechanical properties, and good flexibility, allowing facile production as thin films on a large scale¹²⁻¹⁷. Properties such as particle size, relative amount, and morphology of the inorganic component influence the conductivity of the HSEs. Typically, inorganic fillers are added to lower the glass transition temperature (T_g) of PEO. This enhances the polymer chain segmental mobility and results in higher ionic conductivity^{13,18-20}.

More recently, HSEs with inorganic ionic conductors as additives have been investigated with the aim to provide highly conductive pathways for Li-ion transport, a promising route to improve the overall conductivity of the HSEs^{18,20-24}. However, despite the high ionic conductivity of these inorganic fillers, the room temperature Li-ion conductivity of the HSEs remains far from what is demanded for all-solid-state-batteries ($\sim 1 \text{ mS cm}^{-1}$). This raises questions about the Li-ion transport pathway through the heterogeneous HSE, and especially on the role of the interface between the organic and inorganic components. However, it is challenging to monitor the Li-ion transport in HSEs at the sub-nano scale of interfaces. Several approaches have been reported that explore the correlation between interface environment and Li-ion movement in HSEs^{5,18,25-28}. Three-dimensional (3D) structural reconstruction of HSEs obtained from synchrotron experiments and physics-based modelling indicate that the inorganic particles are highly aggregated in the electrolyte, which would

affect the internal Li-ion transport between different phases^{5,25}. Four-point electrochemical impedance measurements and surface-sensitive X-ray photoelectron spectroscopy revealed decomposition reactions between the organic and inorganic phases, which may significantly affect the Li-ion transport^{26,27}. Recently, combining selective isotope labelling with high-resolution solid-state nuclear magnetic resonance (ssNMR), Li-ion diffusion pathways were tracked within a $\text{Li}_7\text{La}_3\text{Zr}_2\text{O}_{12}$ (LLZO)-PEO HSE^{18,28}. While these studies provide insight into Li-ion transport in HSEs, it is also evident that it remains a challenge to directly access the interfacial structure, correlate this to the Li-ion transport across the interface and use this to develop strategies to improve the conductivity of HSEs¹⁰.

To gain deeper insight into the Li-ion transport in HSEs in conjunction with the organic/inorganic interface structure, we employed an experimental approach using electrochemical impedance spectroscopy (EIS) and multinuclear ssNMR. This allows us to measure the bulk conductivity as well as directly access the interface structure and interfacial Li-ion diffusion in an HSE comprising of an PEO-LiTFSI [lithium bis (trifluoromethane sulfonyl)imide] organic and argyrodite $\text{Li}_6\text{PS}_5\text{Cl}$ inorganic components. We find that the ionic conductivity of the HSE is impeded by the chemical structure of the decomposition layer between the organic and inorganic phases. To overcome this, the interface is ‘activated’ by adding an ionic liquid that settles at the organic/inorganic interface of the HSE because it is poorly miscible with PEO. This enables Li-ion diffusion over the interface, which increases the overall ionic conductivity of the HSE as visualized by two-dimensional (2D) ^7Li exchange NMR. SsNMR is demonstrated to be a powerful method for resolving the sub-nano domains of the interface, which is impossible by other traditional characterization techniques. In this manner, the bottleneck for Li-ion transport in HSEs is revealed and new design strategies are proposed towards future solid electrolytes.

5.2 Results

5.2.1 Interface structure and Li-ion diffusion in the hybrid LiTFSI-PEO- $\text{Li}_6\text{PS}_5\text{Cl}$ solid electrolyte

With the aim of improving the overall Li-ion conductivity of a PEO-LiTFSI polymer electrolyte, highly conductive micron-sized argyrodite $\text{Li}_6\text{PS}_5\text{Cl}$ was mixed into the LiTFSI-PEO with a weight fraction of 10 % [see scanning electron microscope (SEM) images in **Fig.**

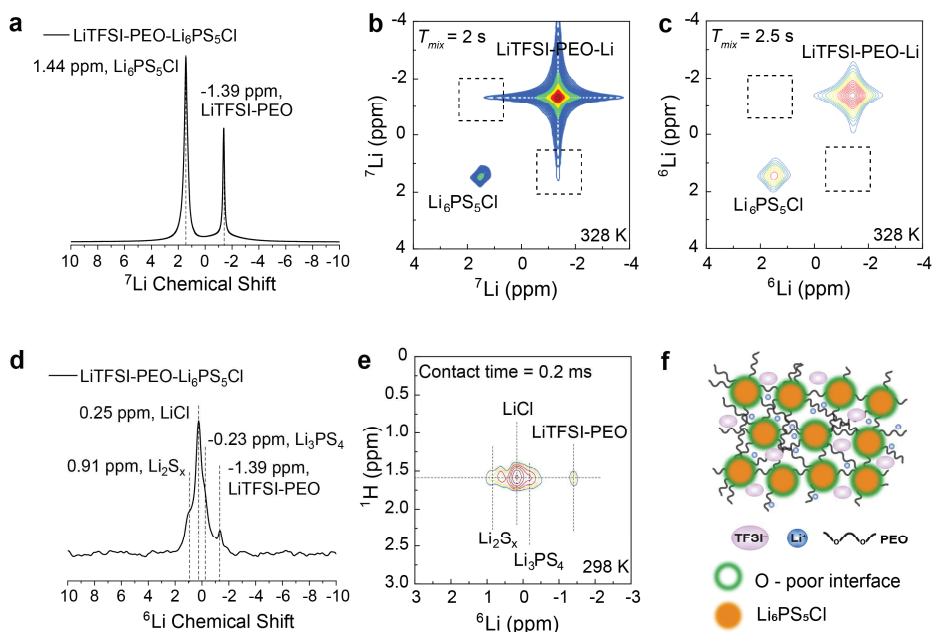


Fig. 5.1. Li-ion interphase diffusion between LiTFSI-PEO and $\text{Li}_6\text{PS}_5\text{Cl}$. (a) 1D ^7Li MAS, (b) ^7Li - ^7Li , and (c) ^6Li - ^6Li 2D-EXSY spectra corresponding to the LiTFSI-PEO- $\text{Li}_6\text{PS}_5\text{Cl}$ HSE with mixing times of 2 and 2.5 s at 328 K, where no obvious off-diagonal cross-peak intensity is observed, indicating that the exchange flux of Li-ions over the solid-solid LiTFSI-PEO- $\text{Li}_6\text{PS}_5\text{Cl}$ interface is very small. (d) 1D $^1\text{H} \rightarrow ^6\text{Li}$ CP MAS spectrum with a contact time of 6 ms (see 0.2 to 6 ms in Fig. S5.2). (e) 2D ^1H - ^6Li HETCOR spectrum measured with a CP contact time of 0.2 ms. (f) Schematic figure of Li-ion diffusion pathway in the HSE. Intensity from low to high is depicted as blue to red in (b), (c), and (e).

S5.1]. For $\text{Li}_6\text{PS}_5\text{Cl}$ to contribute to the bulk conductivity of this HSE, facile Li-ion diffusion over the interfaces between the PEO-LiTFSI phase and the $\text{Li}_6\text{PS}_5\text{Cl}$ particles is a prerequisite. This is because a 10% weight fraction (8% volume fraction) will not result in percolating transport pathways through the $\text{Li}_6\text{PS}_5\text{Cl}$ phase. The high ductility of $\text{Li}_6\text{PS}_5\text{Cl}$ is expected to enhance interfacial transport, with its softness promoting the formation of more adaptable interfaces that facilitate interfacial Li-ion diffusion²⁹. To study the Li-ion diffusion across the PEO-LiTFSI- $\text{Li}_6\text{PS}_5\text{Cl}$ interface and to resolve the interphase structure between the organic and inorganic phases, magic angle spinning (MAS) $^6,^7\text{Li}$ ssNMR was employed. This allows us to discriminate between Li-ions in different chemical environments, in this case in the PEO and $\text{Li}_6\text{PS}_5\text{Cl}$ phases^{18,29}. One-dimensional (1D) ^7Li MAS NMR spectra and two-dimensional ^7Li - ^7Li and ^6Li - ^6Li exchange spectra (2D-EXSY) of the hybrid LiTFSI-PEO-

$\text{Li}_6\text{PS}_5\text{Cl}$ electrolyte are shown in **Fig. 5.1a-c**. As seen in **Fig. 5.1a**, the LiTFSI-PEO and $\text{Li}_6\text{PS}_5\text{Cl}$ show two clear resonances with ^7Li chemical shifts of -1.39 and 1.44 ppm, respectively. Based on the difference in $^{6,7}\text{Li}$ chemical shift of the PEO-LiTFSI and $\text{Li}_6\text{PS}_5\text{Cl}$ phases, 2D-EXSY experiments provide selective and non-invasive quantification of the spontaneous Li-ion diffusion over the solid-solid interphase between these phases^{29,30}. Li-ion exchange between these two chemical environments would result in off-diagonal cross-peaks at the positions indicated with dotted boxes in **Fig. 5.1b** and **c**. Increasing the mixing time, T_{mix} , therefore providing more time for the Li-ions to diffuse from one phase to the other, as well as increasing the temperature, is expected to increase the Li-ion exchange flux and thus the intensity of the off-diagonal cross-peaks²⁹. In this case the absence of cross-peaks, even for the maximum T_{mix} and temperature ($T_{\text{mix}} = 2$ s and 2.5 s, 328 K) that can be achieved, indicates that the Li-ion exchange (flux) between PEO-LiTFSI and $\text{Li}_6\text{PS}_5\text{Cl}$ phases does not occur at the timescale of T_{mix} , indicating very slow Li-ion diffusion across the interfaces within this HSE.

To discern the origin of the poor Li-ion diffusion across the interfaces between the organic and inorganic phases, 1D ^6Li ($^1\text{H} \rightarrow ^6\text{Li}$) cross-polarization (CP) MAS and 2D ^1H - ^6Li heteronuclear correlation (HETCOR) experiments were carried out (**Fig. 5.1d, e**), which allows us to resolve the interface composition and structure. In these experiments, transfer of polarization occurs from protons (^1H), in this case abundantly present in the polymer, to any ^6Li environment in its near vicinity (within the range of a few bonds). This takes place during a varying time interval referred to as the contact time, typically in the range of 0.2 to 6 ms (**Fig. S5.2**). With the direct $^{6,7}\text{Li}$ excitation, only two peaks are resolved as shown in **Fig. 5.1a** for ^7Li (**Fig. S5.3** for ^6Li). However, in the ^6Li CP MAS spectrum several additional resonances between 1 ppm and -1.5 ppm (**Fig. 5.1d**) are resolved. The additional peaks are assigned to Li-containing polysulfides and phosphorus sulfide species^{31,32}, based on previous literature^{26,27}. This indicates that inorganic decomposition products that could inhibit interfacial Li-ion transport accumulate at the interface. The 2D ^1H - ^6Li HETCOR experiment at a short contact time shows correlations between ^1H and ^6Li species either directly bonded to, or in very close proximity to, each other. At a short contact time of 0.2 ms (**Fig. 5.1e**, in **Fig. S5.2** peaks are also visible at 0.2 ms), the different Li species observed are in contact with a single ^1H environment at a chemical shift of ~ 1.6 ppm, which can be assigned to the -

OCH₂- group. This has been identified from X-ray photoelectron spectroscopy studies^{26,27,33} as the main decomposition product of PEO chains when in contact with Li₆PS₅Cl and indicates that there are interfacial reactions between Li₆PS₅Cl and PEO. These reactions result in an inert environment deficient in etheral oxygen that is known to mediate the Li-ion diffusion in PEO (**Fig. 5.1f**). The poorly Li-ion conducting interface environment is held responsible for the absence of Li-ion exchange (**Fig. 5.1b, c**), indicating sluggish Li-ion diffusion between the two electrolyte phases. These findings can potentially explain the difficulties in activating inorganic particles in HSEs¹⁸, suggesting that the interface needs to be improved to enhance the interfacial Li-ion diffusion.

5.2.2 Addition of ionic liquids to enhance the conductivity of the PEO-Li₆PS₅Cl hybrid solid electrolyte

Based on the above findings, it is clear that an inert interphase is formed between PEO-LiTFSI and Li₆PS₅Cl which impedes charge transport in the HSE. Traditionally, ionic liquids (ILs) have been used to enhance the segmental motion of PEO chains to increase the Li-ion mobility^{9,34}. These ILs do not form strong ionic bonds between their cation and anion moieties and hence possess low solvation energy and remain in a dissociated state. It has been shown in previous studies that imidazole-based ILs are effective in improving the conductivity of PEO because of their low viscosity and miscibility in PEO³⁴.

To determine whether an IL added to the HSE has impact on the conductivity and interfacial charge diffusivity between the organic and inorganic phases, two ILs that differ significantly in their viscosity and miscibility with PEO were selected. The first was an imidazole-based IL, 1-ethyl-3-methylimidazolium bis(trifluoromethylsulfonyl)imide (denoted as EMIM-TFSI) (**Fig. 5.2a**) and the second was a piperidinium-based IL, 1-methyl-1-propylpiperidinium bis(trifluoromethylsulfonyl)imide (denoted as PP13-TFSI) (**Fig. 5.2b**). These ILs each have a very different miscibility in PEO³⁵, where the hypothesis is that the poorly miscible PP13-TFSI will be preferably located at the interface with the inorganic Li₆PS₅Cl phase, with the aim to improve the Li-ion diffusion across the interface. By contrast, the highly miscible EMIM-TFSI is anticipated to be distributed homogenously in the HSE and to not specifically influence Li-ion transport across the organic/inorganic interface. To test this, fixed amounts of EMIM-TFSI and PP13-TFSI (0.25:1 molar ratio IL:LiTFSI) were

added to the PEO-LiTFSI-Li₆PS₅Cl mixture. The HSEs subsequently formed are henceforth referred to as HSE-EMIM and HSE-PP13, respectively.

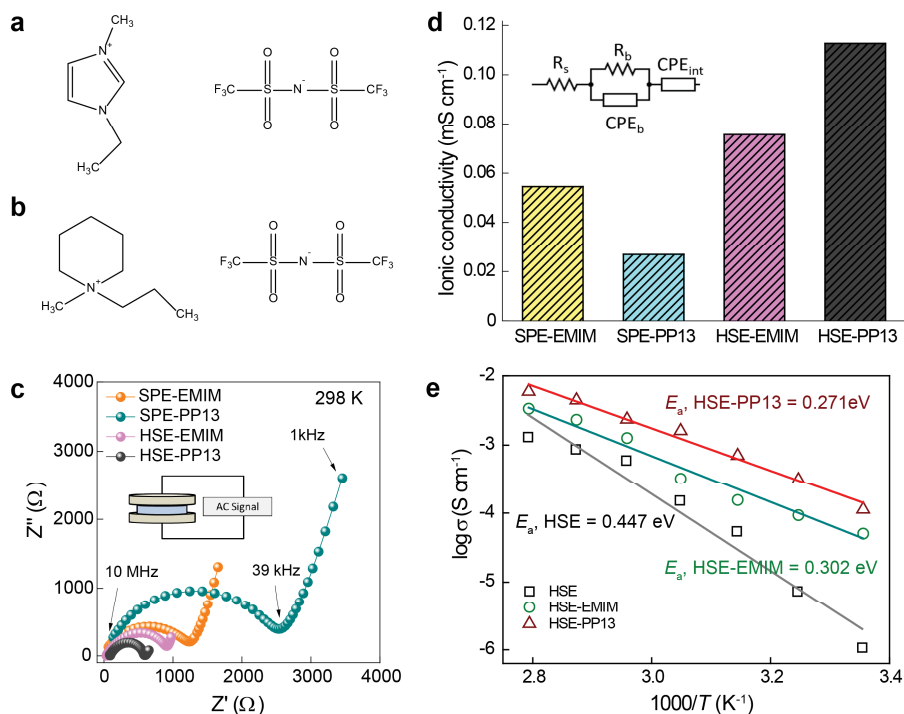


Fig. 5.2. Macroscopic diffusion in HSE with PP13-TFSI and EMIM-TFSI IL additives. Molecular structure of (a) EMIM-TFSI and (b) PP13-TFSI ILs. (c, d) EIS measurements and ionic conductivity of cells with PEO-LiTFSI solid polymer electrolytes with PP13-TFSI (SPE-PP13, $2.69 \times 10^{-5} \text{ S cm}^{-1}$ at 25 °C), and EMIM-TFSI (SPE-EMIM, $5.45 \times 10^{-5} \text{ S cm}^{-1}$ at 25 °C) ILs. And PEO-LiTFSI-Li₆PS₅Cl HSEs with PP13-TFSI (HSE-PP13, $1.12 \times 10^{-4} \text{ S cm}^{-1}$ at 25 °C), and EMIM-TFSI (HSE-EMIM, $7.57 \times 10^{-5} \text{ S cm}^{-1}$ at 25 °C) ILs. (e) Ionic conductivity determined by EIS measurements of PEO-LiTFSI-Li₆PS₅Cl HSE ($E_a = 0.447 \text{ eV}$), and with PP13-TFSI (HSE-PP13, $E_a = 0.271 \text{ eV}$) and EMIM-TFSI (HSE-EMIM, $E_a = 0.302 \text{ eV}$) ILs at various temperatures. AC, alternating current.

To establish how the addition of the ILs improves the macroscopic conductivity of the PEO electrolyte (non-filled) and of the HSEs, EIS measurements were performed. **Fig. 5.2c, d** demonstrate that the conductivity of a mixture of a PEO-LiTFSI solid polymer electrolyte (SPE) with EMIM-TFSI (SPE-EMIM) is higher than that of the mixture with PP13-TFSI (SPE-PP13), as expected due to the high miscibility of EMIM-TFSI with PEO and in good agreement with previous literature³⁴. However, when Li₆PS₅Cl is introduced into the system,

the opposite result is found. HSE-PP13 displays a higher conductivity compared to HSE-EMIM, also noting that both the HSEs have a higher conductivity than the materials without $\text{Li}_6\text{PS}_5\text{Cl}$. In addition, the activation energy indicates better conductivity for the HSE-PP13 electrolyte, where the various temperature measurements shown in **Fig. 5.2e** give a lower activation energy for HSE-PP13. Clearly, introduction of the inorganic $\text{Li}_6\text{PS}_5\text{Cl}$ in the PEO matrix improved the overall conductivity, indicating that the $\text{Li}_6\text{PS}_5\text{Cl}$ actively contributes to the conductivity¹⁰. Notably, the poorly miscible PP13-TFSI IL results in a higher conductivity of the HSE as compared to the more miscible EMIM-TFSI IL.

5.2.3 Impact of the ionic liquid on the bulk PEO and PEO- $\text{Li}_6\text{PS}_5\text{Cl}$ interface structure

To understand the improved conductivity of the HSE upon addition of the poorly miscible PP13-TFSI IL, the structure and kinetics of the PEO- $\text{Li}_6\text{PS}_5\text{Cl}$ interface, which appears to play a critical role in activating the high conductivity of the $\text{Li}_6\text{PS}_5\text{Cl}$ phase in the HSE, were investigated. The impact of adding the ILs to the bulk PEO structure was investigated first by comparing the ^1H and ^{13}C NMR spectra of the individual components. As shown in **Fig. 5.3a**, the ^1H resonances of EMIM in HSE-EMIM for the peak positions between 6 to 10 ppm shows a clear shift compared to pristine EMIM-TFSI, indicating a change in the ^1H environments on the imidazole ring³⁶. The ^1H peaks corresponding to PP13 in HSE-PP13 retain the same chemical shifts compared to pristine PP13-TFSI (**Fig. 5.3b**), reflecting the better miscibility of EMIM-TFSI in PEO. The chemical shift in the 1D ^{13}C ($^1\text{H}\rightarrow^{13}\text{C}$) CP MAS spectra (**Fig. 5.3c, d**) indicates less crystalline PEO in HSE-EMIM (70 ppm) compared to HSE-PP13 (72 ppm). This is consistent with the better miscibility of EMIM-TFSI in PEO³⁷. Differential scanning calorimetry (DSC) measurements were performed to determine the impact of the EMIM-TFSI and PP13-TFSI ILs on the melting temperature and crystallinity of PEO in the HSE (**Fig. S5.4** and **Supplementary Text S5.1**), indicating that the presence of EMIM results in a larger decrease in melting temperature and crystallinity, consistent with the larger miscibility of EMIM in PEO, in agreement with the NMR observations.

To understand the role of the IL in activating the PEO-LiTFSI- $\text{Li}_6\text{PS}_5\text{Cl}$ interface, the interface structure was explored using 2D ^1H - ^1H nuclear Overhauser effect spectroscopy

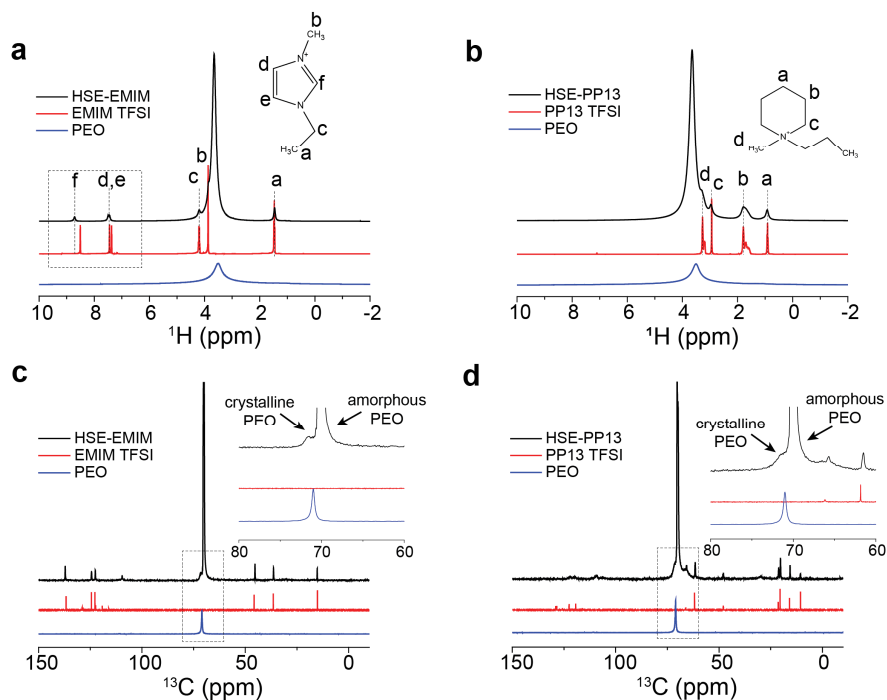


Fig. 5.3. Structural characterization of HSE with PP13-TFSI and EMIM-TFSI IL additives. (a, b) 1D ^1H spectra of PEO-LiTFSI-Li₆PS₅Cl HSEs with EMIM-TFSI (HSE-EMIM) and PP13-TFSI (HSE-PP13) ILs. (c, d) 1D ^1H → ^{13}C CP MAS spectra of PEO-LiTFSI-Li₆PS₅Cl HSEs with EMIM-TFSI (HSE-EMIM) and PP13-TFSI (HSE-PP13) ILs. ^{13}C spectra of PEO (solid, CP MAS), EMIM-TFSI (liquid), and PP13-TFSI (liquid) are included in for comparison.

(NOESY) NMR measurements (Fig. 5.4a-f). NOESY is a commonly used method to elucidate polymer structures and configurations³⁸. The cross-peaks that arise, especially for short mixing times, are typically between protons that are in close spatial proximity (< 1 nm) to each other. As seen from Fig. 5.4a-c, all the cross-peaks between EMIM-TFSI and PEO-LiTFSI appear at nearly the same mixing time, also reflected in the intensity buildup of these cross-peaks shown in Fig. S5.5, indicating that there is no preferred orientation of the EMIM-TFSI species with respect to PEO. This confirms the earlier finding that these species mix well, and that the EMIM-TFSI is mobile within the HSE-EMIM showing no preferred orientation. For the HSE-PP13 seen in Fig. 5.4d-f, the dotted region displays a sequence of cross-peaks that evolve with increasing mixing times. At the shortest mixing times, ^1H - ^1H correlations are first observed between ^1H resonances at positions *a* and *b* on the piperidine ring of PP13-TFSI and the -OCH₂- protons from PEO. This is especially clear from the

intensity buildup shown in **Fig. S5.5**. These ring protons are the furthest away from the bulky propyl and methyl groups attached to the nitrogen (N) atom on the piperidium ring. This indicated that the positively charged N atom on the piperidine ring, along with the functional groups it carries, are oriented away from the PEO segments.

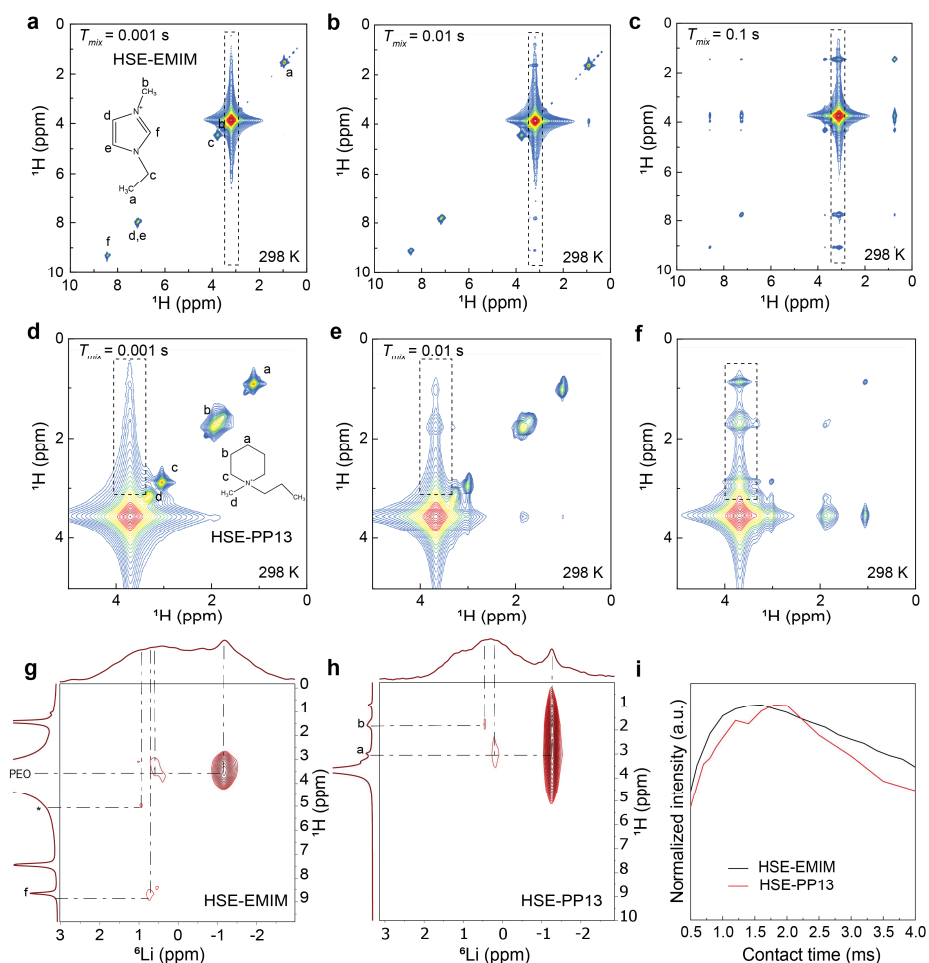


Fig. 5.4. Locating the position of PP13-TFSI and EMIM-TFSI ILs additives in the HSEs. (a-f) 2D ^1H - ^1H NOESY spectra of the mixture of PEO-LiTFSI-Li₆PS₅Cl with (a-c) EMIM-TFSI, and (d-f) PP13-TFSI ILs measured at a spinning speed of 5 kHz at 298 K with T_{mix} of 0.001, 0.01, and 0.1 s. The dotted regions indicate the evolution of a series of cross-peaks as a function of T_{mix} . (g, h) 2D ^1H - ^6Li HETCOR spectra of HSE-EMIM and HSE-PP13. (i) Integrated intensities, denoted in arbitrary units (a.u.), taken from 1D ^1H \rightarrow ^7Li CP MAS spectra measured for the HSE-EMIM and HSE-PP13 (representative spectra given in the **Fig. S5.6**) at contact times from 0.2 to 12 ms of the interface Li environment (located at ~ 0.26 ppm). Intensity from low to high is depicted from blue to red in a-f.

Next, the interface environments in both HSEs are explored by 2D ^1H - ^6Li HETCOR measurements (**Fig. 5.4g, h**). This technique makes it possible to establish which Li-containing species are in proximity to the protons present in PEO and the ILs. For HSE-EMIM (**Fig. 5.4g**), a strong correlation is found between PEO and LiTFSI, consistent with the solvation of EMIM in the PEO matrix. Additionally, PEO and EMIM correlate with the decomposed $\text{Li}_6\text{PS}_5\text{Cl}$ surface species (observed for the HSE without IL, **Fig. 5.1d**), indicating that a fraction of the PEO + EMIM is in contact with the $\text{Li}_6\text{PS}_5\text{Cl}$ particles. For HSE-PP13 (**Fig. 5.4h**), no correlation between PEO and LiTFSI or the decomposed $\text{Li}_6\text{PS}_5\text{Cl}$ species are observed, the former consistent with poor solvation of this IL in PEO. However, correlations between the protons on the piperidine ring (**Fig. 5.2b**) and LiTFSI as well as between the same protons of PP13 with the decomposed $\text{Li}_6\text{PS}_5\text{Cl}$ surface environments are observed, indicating that PP13 is in contact with $\text{Li}_6\text{PS}_5\text{Cl}$.

After identifying the position and orientation of the PP13-TFSI IL with respect to the PEO chains, the interface between PEO and $\text{Li}_6\text{PS}_5\text{Cl}$ is further probed using 1D ^7Li ($^1\text{H} \rightarrow ^7\text{Li}$) CP MAS experiments (**Fig. 5.4i**). The CP process depends on the effective heteronuclear dipolar interaction between ^1H and ^7Li , thus is typically most efficient when these species are in close proximity to each other (< 1 nm) and is reduced when mobility increases¹⁰. For both HSE-EMIM and HSE-PP13, the ^7Li CP MAS NMR spectra show narrow LiTFSI signal (**Fig. S5.6**), indicating the close proximity between PEO (and, in the case of EMIM, also between this IL) and LiTFSI. The broad $\text{Li}_6\text{PS}_5\text{Cl}$ interface environment is also observed in the CP MAS spectra for both HSE-EMIM and HSE-PP13, suggesting the interface decomposition products that are also observed in the absence of the IL (**Fig. 5.1d** and **Fig. S5.6**). This indicates that this interface is also in close proximity with neighboring protons, though there is a difference in proton kinetics between the two interfaces (the fitting details are analogous to **Supplementary Text S4.4**, and see the fitting results in **Supplementary Table S5.1**). Between HSE-EMIM and HSE-PP13, HSE-EMIM exhibits a faster buildup of the broad component as a function of contact time (**Fig. 5.4i**). This is attributed to the abundance of protons from the proton-rich PEO (and its decomposed segments) at the interface (**Fig. 5.4g**). In contrast, the slower buildup of the broad component's intensity in HSE-PP13 can be explained by the higher local mobility of the PP13 present at the interface, which limits the efficiency of polarization transfer.

To summarize, addition of EMIM-TFSI and PP13-TFSI results in a very different PEO bulk and interphase structures in the HSEs. ^1H and ^{13}C NMR, as well as DSC measurements, demonstrate that EMIM resides dominantly within the PEO, consistent with its higher solubility, thereby lowering the PEO crystalline fraction. The ^1H - ^1H NOESY spectra provide more details, showing that EMIM has no preferred orientation towards PEO, whereas PP13 does. 2D ^1H - ^6Li HETCOR spectra demonstrate that PP13 is at the surface of the $\text{Li}_6\text{PS}_5\text{Cl}$, which in combination with the poor miscibility of PP13 in PEO established above, indicates that PP13 is predominantly located at the PEO- $\text{Li}_6\text{PS}_5\text{Cl}$ interface, as initially hypothesized. Additionally, the ^7Li CP MAS buildup curves suggest a more mobile PEO- $\text{Li}_6\text{PS}_5\text{Cl}$ interface environment due to the presence of the PP13 that will be investigated in more detail in the next section.

5.2.4 Impact of the ionic liquid on the interfacial diffusion between PEO-LiTFSI and $\text{Li}_6\text{PS}_5\text{Cl}$

To understand how the Li-ion diffusion (due to equilibrium charge transfer) over the PEO- $\text{Li}_6\text{PS}_5\text{Cl}$ interface of the HSE is affected by both ILs, 1D and 2D NMR techniques were utilized, noting that in the HSE without IL, no Li-ion diffusion was detected (**Fig. 5.1b, c**). In the 1D ^7Li spectra of HSE-EMIM and HSE-PP13 (**Fig. S5.7**), a notable difference in the peak position of the LiTFSI-PEO component is observed. This difference arises from the varying miscibilities of PP13-TFSI and EMIM-TFSI in PEO. The peak appears at -1.27 ppm for HSE-PP13 and shifts downfield to -1.17 ppm for HSE-EMIM, indicating that the Li in LiTFSI-PEO is less shielded by EMIM. To quantify the spontaneous charge transfer at the PEO-LiTFSI- $\text{Li}_6\text{PS}_5\text{Cl}$ interface and evaluate the impact of ILs on this process, $^6,7\text{Li}$ - $^6,7\text{Li}$ 2D-EXSY NMR measurements are conducted (**Fig. 5.1b, c**). For HSE-EMIM (**Fig. S5.8a, b**), no cross-peaks are observed with mixing times as long as 2 s, indicating that there is no significant Li-ion diffusion over the PEO-LiTFSI- $\text{Li}_6\text{PS}_5\text{Cl}$ interface at this timescale. By contrast, clear cross-peaks corresponding to Li-ion diffusion between the PEO-LiTFSI and $\text{Li}_6\text{PS}_5\text{Cl}$ phases appear for HSE-PP13 (**Fig. 5.5** and **Fig. S5.8c, d**). This indicates more facile diffusion over the organic/inorganic interface in the HSE-PP13, which is associated with the presence of the PP13 at the PEO- $\text{Li}_6\text{PS}_5\text{Cl}$ interface established in the previous section.

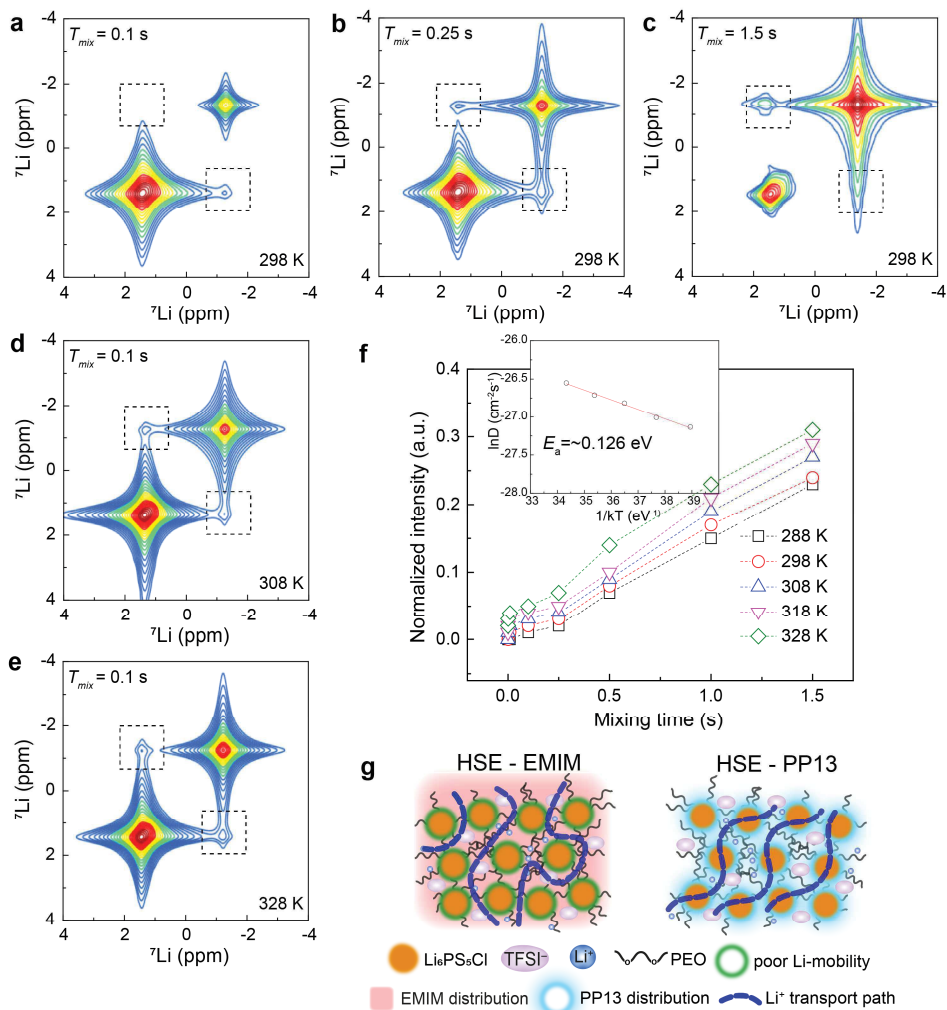


Fig. 5.5. Quantification of Li-ion diffusion across phase boundaries in the HSE with the PP13-TFSI IL. 2D ${}^7\text{Li}$ - ${}^7\text{Li}$ EXSY spectra of the mixture of PEO-LiTFSI-Li₆PS₅Cl with PP13-TFSI IL measured at spinning speed of 5 kHz at (a-c) 298 K with mixing times T_{mix} of 0.1, 0.25, and 1.5 s, and (d, e) at 308 and 328 K with a T_{mix} of 0.1 s. (f) Evolution of cross-peak intensity as a function of T_{mix} obtained from the 2D-EXSY measurements performed at the temperatures indicated in the graph. The line passing through the symbols is a guide to the eye. The inset figure is the dependence of the diffusion coefficient (D) obtained from fitting the data in (f) to a diffusion model described by us in detail elsewhere³⁰ and **Supplementary Text S5.2**. The normalized intensity is denoted in arbitrary units (a.u.). These can be fit with the Arrhenius law, yielding an E_a of 0.126 eV. (g) Proposed mechanism for Li-ion diffusion in the HSEs with EMIM-TFSI and PP13-TFSI IL additives. Intensity from low to high is shown from blue to red in a-e.

An advantage offered by ssNMR is that Li-ion diffusion can be quantified between Li

environments, under the condition that the chemical shifts can be distinguished and that T_1 relaxation times are sufficiently long^{29,30}. Upon increasing the mixing time and the temperature, a clear increase in cross-peak intensity is observed (**Fig. 5.5a-e**). The Li-ion exchange between the PEO-LiTFSI and $\text{Li}_6\text{PS}_5\text{Cl}$ phases was quantified by fitting the evolution of the cross-peak intensity as a function of T_{mix} to a diffusion model derived from Fick's law, described in **Supplementary Text S5.2** and elsewhere^{29,30,39}. The diffusion coefficient as a function of temperature obtained from the fit (**Fig. 5.5f**, insert), reflects the Li-ion self-diffusion across the PEO-LiTFSI- $\text{Li}_6\text{PS}_5\text{Cl}$ interface. Fitting with an Arrhenius law yields an activation energy of 0.126 eV for diffusion between the organic and inorganic components, which is much lower than that reported with impedance measurements^{26,27}. This suggests that the addition of PP13-TFSI IL 'activates' the PEO-LiTFSI- $\text{Li}_6\text{PS}_5\text{Cl}$ interface, even though micron-sized inorganic argyrodite filler particles are used in the HSE. Thus, there is a relatively small ionic contact area.

Based on these observations, we can now link the PEO- $\text{Li}_6\text{PS}_5\text{Cl}$ interface nanostructure with the Li-ion mobility over the interface. The poor Li-ion diffusivity over the interface between PEO and $\text{Li}_6\text{PS}_5\text{Cl}$ in the HSE can be rationalized by the observed $-\text{OCH}_2-$ groups at the interface (**Fig. 5.1**) that annihilates the conducting etheral oxygen positions that mediate the Li-ion conductivity in PEO. The consequence is that Li-ion transport will be forced through the polymer phase and will not utilize the high conductivity of the $\text{Li}_6\text{PS}_5\text{Cl}$ phase (**Fig. 5.1f**). In contrast to the miscible EMIM-TFSI, which improves the conductivity of the PEO, the much less miscible PP13-TFSI settles at the interface with the $\text{Li}_6\text{PS}_5\text{Cl}$ phase (**Fig. 5.5g**) where it leads to a higher local mobility. This is held responsible for the facile Li-ion diffusivity over the PEO- $\text{Li}_6\text{PS}_5\text{Cl}$ interface as quantified by the 2D-EXSY experiments in **Fig. 5.5** and can be explained by the higher local mobility induced by the PP13-TFSI IL. The higher dielectric constant of the IL ($\epsilon > 20$) compared to that of PEO ($\epsilon \approx 5$) may also play a role⁴⁰, which can be expected to enhance the local polarizability. Facilitated by the higher Li-ion diffusivity over the organic/inorganic interface in the presence of PP13-TFSI, long-range Li-ion transport can now make use of the much higher conductivity of the $\text{Li}_6\text{PS}_5\text{Cl}$ phase (**Fig. 5.5g**). This explains the higher overall conductivity of the HSE-PP13 electrolyte observed with EIS (**Fig. 5.2c, d**).

5.2.5 Electrochemical evaluation of the hybrid solid electrolyte upon introduction of ionic liquids

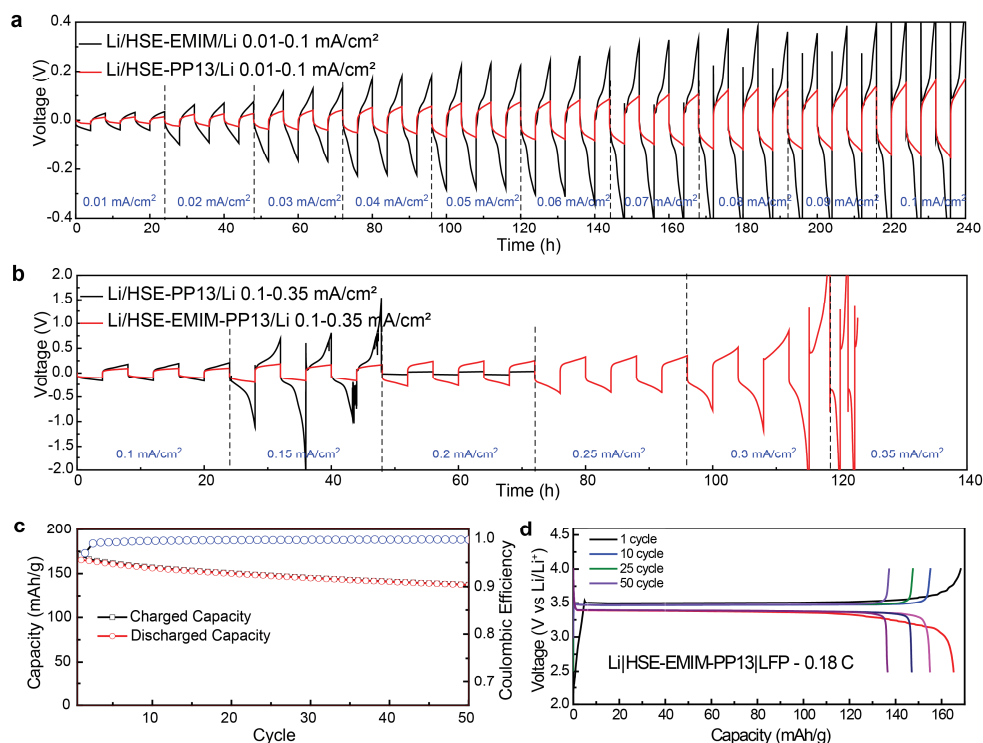


Fig. 5.6. Electrochemical characterization of the HSEs with PP13-TFSI and EMIM-TFSI IL additives. (a) Plating and stripping curves of a Li-metal symmetrical cell with PEO-LiTFSI-Li₆PS₅Cl HSEs containing PP13-TFSI (HSE-PP13) or EMIM-TFSI (HSE-EMIM) ILs measured at room temperature. (b) Plating and stripping curves of a symmetrical cell with PEO-LiTFSI-Li₆PS₅Cl HSE only with PP13-TFSI and with a mixture of PP13-TFSI and EMIM-TFSI (PP13-TFSI and EMIM-TFSI, 0.25:1 molar ratio IL:Li-ion, HSE-PP13-EMIM) ILs measured at room temperature. (c) Specific charge and discharge capacity (red circle) and Coulombic efficiency (blue circle) as a function of cycle number. (d) Charge and discharge voltage curves of a LiFePO₄ (LFP)|HSE-EMIM-PP13|Li battery cycled at 0.18 C and at room temperature.

As Li-metal is the ultimate anode from the perspective of battery energy density, the impact of the IL on the interface of the HSE with Li-metal was evaluated in Li-metal symmetrical cells for both HSE-PP13 and HSE-EMIM electrolytes (Fig. 5.6). The overpotential of the symmetrical cell is an indicative parameter of the interface stability and ability to conduct Li-ions²⁵. In Fig. 5.6a, the Li|HSE-EMIM|Li cell shows a continuous increase in overpotential when the current density is higher than 0.05 mA cm⁻², indicating insufficient

Li-ion conductivity. By contrast, the Li|HSE-PP13|Li cell shows a much more stable overpotential, increasing with current density up to a relatively small value not exceeding 200 mV at 0.1 mA cm⁻². A similar trend is observed upon cycling (**Fig. S5.9**). The cell with HSE-EMIM shows rapid polarization after 300 hours of cycling at a current density of 0.05 mA cm⁻². In contrast, the cell with HSE-PP13 maintains a stable overpotential (below 200 mV) during 800 hours of cycling, indicating higher ionic conductivity and better interfacial stability against Li-metal.

Taking it one step further, we can assume that in the HSE-PP13 electrolyte the conductivity is no longer limited by the PEO-Li₆PS₅Cl interface due to the presence of PP13-TFSI but by the polymer phase. To evaluate this, an HSE was prepared with both the PP13-TFSI and EMIM-TFSI additives. In this HSE, PP13-TFSI will enhance the interfacial Li-ion diffusivity while EMIM-TFSI is expected to enhance the Li-ion diffusivity in the PEO phase by improving the chain mobility. Indeed, the small fraction of IL increases the ionic conductivity to 2.47×10^{-4} S cm⁻¹ at 25 °C as measured by EIS (**Fig. S5.10**). The higher conductivity upon adding both ILs is accompanied by a higher critical current density of 0.25 mA cm⁻² (**Fig. 5.6b**) as compared to addition of the individual IL additives (**Fig. 5.6a**). In theory, a critical current density of 0.25 mA cm⁻² could already enable a solid-state Li-metal battery using sulfur as the cathode, having an energy density of more than 500 Wh/kg⁴¹. The HSE with both ILs added demonstrates a critical current density that can be compared to those state-of-the-art solid-state electrolytes reported in the literature (**Supplementary Table S5.2**), although it should be realized that our result is achieved using a small fraction of a liquid (IL) phase.

Before evaluation a full cell configuration, the oxidative stability of both HSE-EMIM and HSE-PP13 were investigated by linear-sweep voltammetry (LSV, **Fig. S5.11**). The HSE-EMIM exhibits electrochemical stability of up to 4.75 V, while oxidation in the HSE-PP13 occurs at around 4.5 V. This can be attributed to the phase separation in the HSE-PP13 between PEO and PP13-TFSI, where the isolated PEO chains may be more susceptible to oxidation. Finally, the HSE with the dual IL additive was electrochemically cycled in a Li-metal battery in combination with a LiFePO₄ cathode (**Fig. 5.6c, d**). The battery delivers a capacity of more than 0.8 mAh (120 mAh g⁻¹) after 50 cycles, with an average Coulombic efficiency of ~99.9% and an overpotential of 150 mV, indicating the feasibility of this HSE

to function as a solid-state electrolyte for a room-temperature Li-metal battery.

5.3 Conclusions

In conclusion, we propose that the bottleneck for Li-ion transport in HSEs comprising PEO polymer and inorganic solid electrolyte phases is across the organic/inorganic phase boundaries, where the deficiency of ethereal oxygen species and absence of local mobility are held responsible for the poor local Li-ion conductivity at the interface. The interface diffusivity can be improved by making use of an IL additive as a wetting agent, in this case, PP13-TFSI, whose low miscibility in PEO forces it to be positioned at the phase boundaries where it functions as a bridge for Li-ion transport. The ssNMR investigation reveals the structure of the interface between the organic and inorganic phases in the HSE and how this affects the Li-ion diffusion pathway. This sheds light on the development of interface strategies, such as the one proposed with non-miscible ILs, leading to highly improved conductivities and compatibility with Li-metal anodes.

5.4 Methods

The solid-state electrolyte $\text{Li}_6\text{PS}_5\text{Cl}$ was prepared by a simple solid-state reaction. The stoichiometric raw materials LiCl (Sigma-Aldrich), P_2S_5 (Sigma-Aldrich), and Li_2S (Sigma-Aldrich) were used as the starting materials and were ball-milled at 110 rpm for 2 hours with the ZrO_2 -coated jars using 18 ZrO_2 balls. After the ball milling, the precursor was sealed in a quartz tube containing Ar and then annealed at 550 °C for 15 hours to obtain the $\text{Li}_6\text{PS}_5\text{Cl}$ solid electrolyte.

HSE films were prepared by mixing 0.768 g PEO (Sigma-Aldrich, $M_w = 600,000$ g/mol), 0.28 g LiTFSI (Sigma-Aldrich), 0.1048 g $\text{Li}_6\text{PS}_5\text{Cl}$, and 0.25:1 molar ratio IL:Li-ion of ionic liquid together in 10 ml acetonitrile (Sigma-Aldrich) and stirring for 24 hours. The prepared solution was evenly casted on a Teflon plate and dried in the glove box at room temperature for 24 hours, then transferred into reduced pressure environment in the glove box for 48 hours. DSC measurements were carried out at $10^\circ \text{ min}^{-1}$ steps using a commercial TA-Q2000 DSC calorimeter (TA instruments). The morphology of HSE was analysed using an SEM (JEOL JSM IT100LA).

LSV was performed to cell of Li|HSE|SS with stainless steel (SS) area of 1.13 cm². The LSV curves were recorded from the open-circuit voltage (OCV) to 5.5 V versus Li/Li-ion at a scanning rate of 0.1 mV s⁻¹ using an Autolab PGSTAT302N (Metrohm-Autolab). The ionic conductivities of the HSEs were measured by EIS, where the HSE was sandwiched between two SS blocking electrodes (area of 1.13 cm²), and kept at each test temperature (from 25 to 85 °C) for at least 30 minutes, in order to reach thermal equilibrium before the electrochemical impedance measurements were acquired. The EIS measurements were obtained using an Autolab PGSTAT302N in the frequency range of 10 MHz-1 kHz with a sinusoidal signal with $V_{\text{rms}} = 10$ mV. EIS spectra were fit with an Equivalent Circuit (EC) model, where R_S is the series resistance, R_b is the bulk polymer resistance, CPE_b is a constant phase element (CPE) which accounts for the bulk capacitance of the polymer film, and CPE_{int} accounts for the capacitance associated with the blocking electrodes at low frequencies. From this, the bulk resistance (R_b) and the ionic conductivity (σ) are calculated using the equation $\sigma = d / (R_b \times A)$, where d is the thickness, and A is the area of the electrolyte in contact with the SS (area of 1.13 cm²). The HSE-based all-solid-state cells were assembled in an Ar-filled glove box. These cells consisted of Li-metal (Aldrich) and LiFePO₄ (LFP, mass loading: ~6.5 mg cm⁻²) as electrodes, and the HSE as the electrolyte. It should be noted that 50 μ L of the HSE solution prepared with above methods was dropped into an LFP electrode and then allowed to fully dry. LiFePO₄ (Sigma-Aldrich) cathodes were prepared by mixing the active material with Super P and polyvinylidene fluoride (PVDF) in a mass ratio of 8:1:1, and N-Methylpyrrolidone (NMP) was used as a solvent. Charge-discharge tests of the HSE-based all-solid-state cells were performed using a Maccor 4000 battery cyclers at room temperature.

SsNMR measurements were performed using a Bruker Ascend 500 magnet ($B_0 = 11.7$ T) with a NEO console operating at frequencies of 500.130 MHz for ¹H, 194.37 MHz for ⁷Li, 73.6 MHz for ⁶Li, and 125.758 for ¹³C. ^{6,7}Li chemical shifts were referenced with respect a 0.1 M LiCl solution (0 ppm), and ¹H and ¹³C chemical shifts were referenced with respect to solid adamantane (¹H at 1.81 ppm and ¹³C at 38.48 ppm). A Bruker three-channel MAS 4 mm direct variable temperature (DVT) probe was used for all measurements. The PEO-LiTFSI-Li₆PS₅Cl (HSE), HSE-EMIM, and HSE-PP13 membranes were cut into tiny pieces and filled in 4 mm zirconia rotors that were spun at spinning speeds of 5 kHz for all measurements. One-pulse ¹H, ⁷Li, and ⁶Li experiments were performed with $\pi/2$ pulse lengths

of 3.5, 2.7, and 4.75 μs , respectively. A recycle delay of three times of T_1 was used each time, where T_1 was determined using saturation recovery experiments. 2D ^7Li - ^7Li and ^6Li - ^6Li EXSY measurements were performed for these samples at various mixing times from 1 ms up to 2.5 s and at temperatures from 10 to 50 $^\circ\text{C}$. Each spectrum consisted of 8 (16) scans for each of the 1,200-1,500 (400-800) transients, and each transient was incremented by 200 (400) μs with a recycle delay of up to 5 (10) s. The ^6Li CP MAS experiments were performed with an initial ^1H $\pi/2$ pulse of 5 μs . During CP, for ^6Li , radio frequency (r.f.) field strengths of 25 kHz and contact times of up to 12 ms were utilized. The r.f. field amplitude of ^1H during CP was ramped from 70 to 100%. 256 (1,024) scans were acquired for each sample with a recycle delay of 2 (3) s. 2D ^1H - ^6Li HETCOR measurements were performed with a short CP contact time of 0.2 ms for the HSE and long contact times of 10 ms each for the HSE-EMIM and HSE-PP13. For each of the 128 transients in the indirect ^1H dimension, 128 ^6Li scans were accumulated. A recycle delay of 3 s was applied after each scan. The ^{13}C CP MAS experiments were measured with an initial ^1H $\pi/2$ pulse of 3.65 μs . During CP for ^{13}C , an r.f. field strengths of 58 kHz was utilized and 40,000 scans were acquired for each sample with a recycle delay of 2 s. For both the CP MAS and HETCOR experiments, proton decoupling was performed during acquisition using the SPINAL-64 decoupling sequence⁴². 2D ^1H - ^1H NOESY measurements were performed at various mixing times from 1 to 100 ms at room temperature. Each spectrum consisted of 8 scans for each of the 800 transients, with each transient incremented by 100 μs with a recycle delay of 2 s. ^7Li CP MAS experiments were performed on an Agilent 400 MHz spectrometer operating at 155.422 MHz for ^7Li and 399.915 MHz for ^1H . A 4 mm HXY Chemagnetics pencil design probe was used at a MAS speed of 5 kHz. For CP, both the ^1H and ^7Li r.f. field strengths were set at 40 kHz, and SPINAL-64 proton decoupling at the same field strength with 12.5 μs pulse length and an 8° phase shift was used during acquisition.

5.5 Supplementary information

Supplementary Texts

Text S5.1: Differential Scanning Calorimetry

DSC measurements were performed to determine the impact of the EMIM and PP13 ILs on

the melting temperature and crystallinity of PEO in the HSE (relative crystallinity defined as % change in enthalpy compared to fully crystalline PEO (193 J g⁻¹, **Fig. S5.4**). For the HSE, HSE-PP13, and HSE-EMIM, this results in 52.6 °C/17.9%, 50.3 °C/14.9%, and 47.1 °C/9.8%, indicating that the presence of EMIM results in a larger decrease in melting temperature and crystallinity, consistent with the larger miscibility of EMIM in PEO, in agreement with the NMR observations.

Text S5.2: Quantification of interphases Li-ion exchange

Quantification of exchange between PEO and Li₆PS₅Cl was performed by fitting the growing exchange signal to a diffusion model where in a solution to Fick's law for diffusion is determined $\frac{\partial m(\vec{r}, \vec{t})}{\partial t} = \vec{\nabla} \cdot \{D(\vec{r})m(\vec{r}, \vec{t})\}$, where $m(\vec{r}, \vec{t})$ is the magnetization of Li at position \vec{r} and t , and D is the Li-ion self-diffusion coefficient. By using the mathematical models of Schmidt-Rohr and co-workers for spin diffusion, and by assuming the overall diffusivity to be equal to the effective diffusion coefficient, the rate of demagnetization of Li-ions in the Li₆PS₅Cl can be set equal to the initial magnetization minus the rate of magnetization in the PEO. Assuming the Li₆PS₅Cl phase embedded in an infinite PEO phase, this leads to the following analytical expression for the rate of demagnetization from the Li₆PS₅Cl into PEO as:

$$m(t_{mix}) = 1 - \left\{ \frac{m_0}{2} \sqrt{4Dt_{mix}} \left[\text{ierfc} \left(\frac{d}{\sqrt{4Dt_{mix}}} \right) + \text{ierfc} \left(\frac{-d}{\sqrt{4Dt_{mix}}} \right) - \frac{2}{\sqrt{\pi}} \right] \right\}^3 \quad (5.1)$$

where $\text{ierfc}(x) = 1/\sqrt{\pi} \exp(-x^2) - x[l - \text{erf}(x)]$ and d is the Li-ion diffusion distance from the Li₆PS₅Cl phase to the PEO phase.

Supplementary Figures

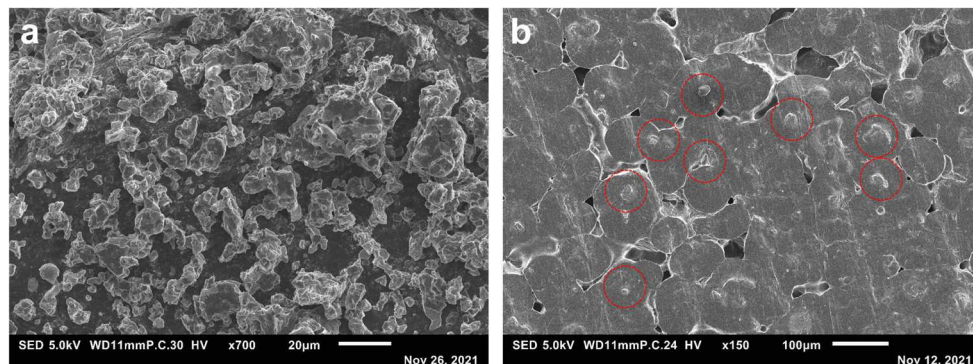


Fig. S5.1. SEM image of the pristine micron-sized $\text{Li}_6\text{PS}_5\text{Cl}$ and PEO-LiTFSI- $\text{Li}_6\text{PS}_5\text{Cl}$ HSE. (a) SEM image of the pristine micron-sized $\text{Li}_6\text{PS}_5\text{Cl}$. (b) SEM image showing the morphology of the HSE where the $\text{Li}_6\text{PS}_5\text{Cl}$ particles are marked with circles.

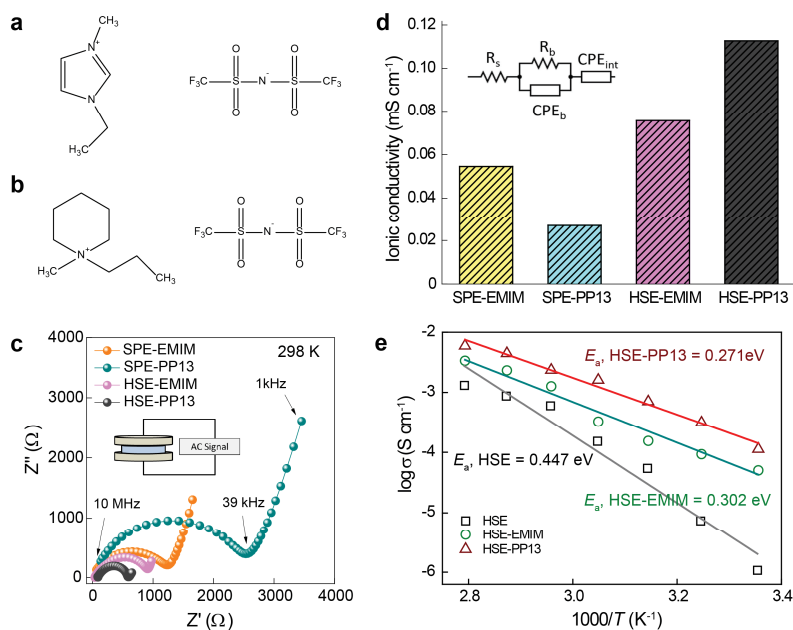


Fig. S5.2. $1\text{D } ^6\text{Li}$ CP MAS spectra of the PEO-LiTFSI- $\text{Li}_6\text{PS}_5\text{Cl}$ HSE. $1\text{D } ^6\text{Li}$ CP MAS spectra of the PEO-LiTFSI- $\text{Li}_6\text{PS}_5\text{Cl}$ HSE measured at contact times ranging from 0.2 (lightest grey) to 6 ms (black).

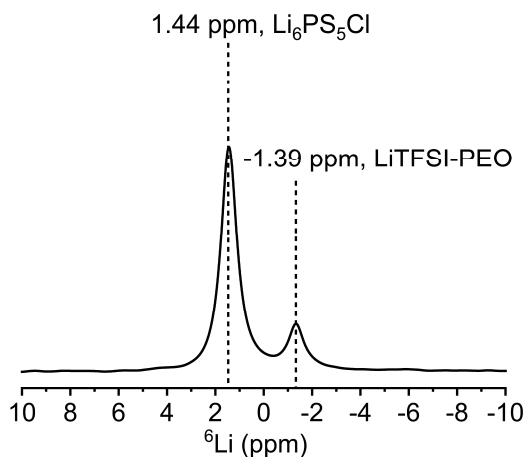
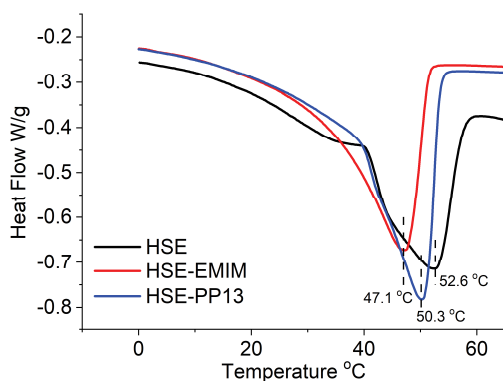
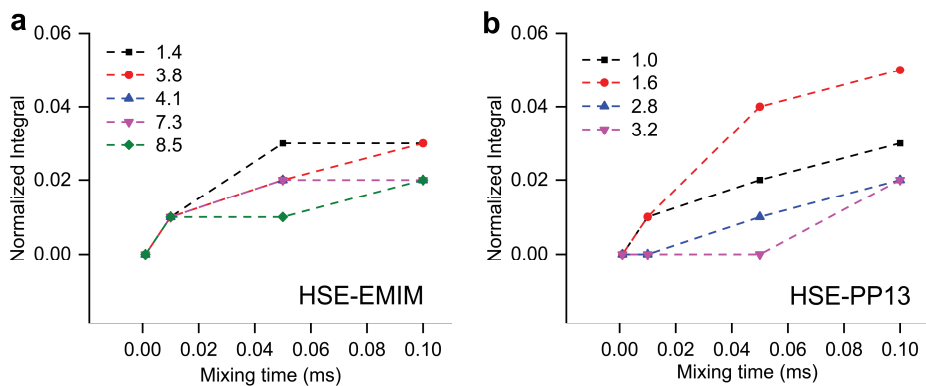
Fig. S5.3. 1D ${}^6\text{Li}$ MAS spectrum corresponding to the PEO-LiTFSI- $\text{Li}_6\text{PS}_5\text{Cl}$ HSE.Fig. S5.4. DSC measurements showing the heat flow of the HSE, HSE-EMIM, and HSE-PP13 under heating up from 0 to 65 $^{\circ}\text{C}$.

Fig. S5.5. ^1H - ^1H cross peak intensity buildup of protons in EMIM-TFSI and PP13-TFSI correlated to PEO from the 2D ^1H - ^1H NOESY spectra of HSE-PP13 and HSE-EMIM. ^1H - ^1H cross peak intensity buildup of protons in (a) EMIM-TFSI, and (b) PP13-TFSI correlated to PEO from the 2D ^1H - ^1H NOESY spectra of HSE-PP13 and HSE-EMIM given in Fig. 5.4. All the cross-peaks between EMIM-TFSI and LiTFSI-PEO appear at nearly at the same mixing time which means that there is no preferred orientation of the EMIM-TFSI species with respect to PEO. While a sequence of cross-peak evolution with mixing time is observed in HSE-PP13. At the shortest mixing times, ^1H - ^1H correlations are first observed between ^1H resonances at positions 1.0 ppm and 1.6 ppm on the piperidine ring of PP13-TFSI and the $-\text{OCH}_2-$ protons from PEO. These ring protons are the furthest away from the bulky propyl and methyl groups attached to the nitrogen (N) atom on the piperidine ring.

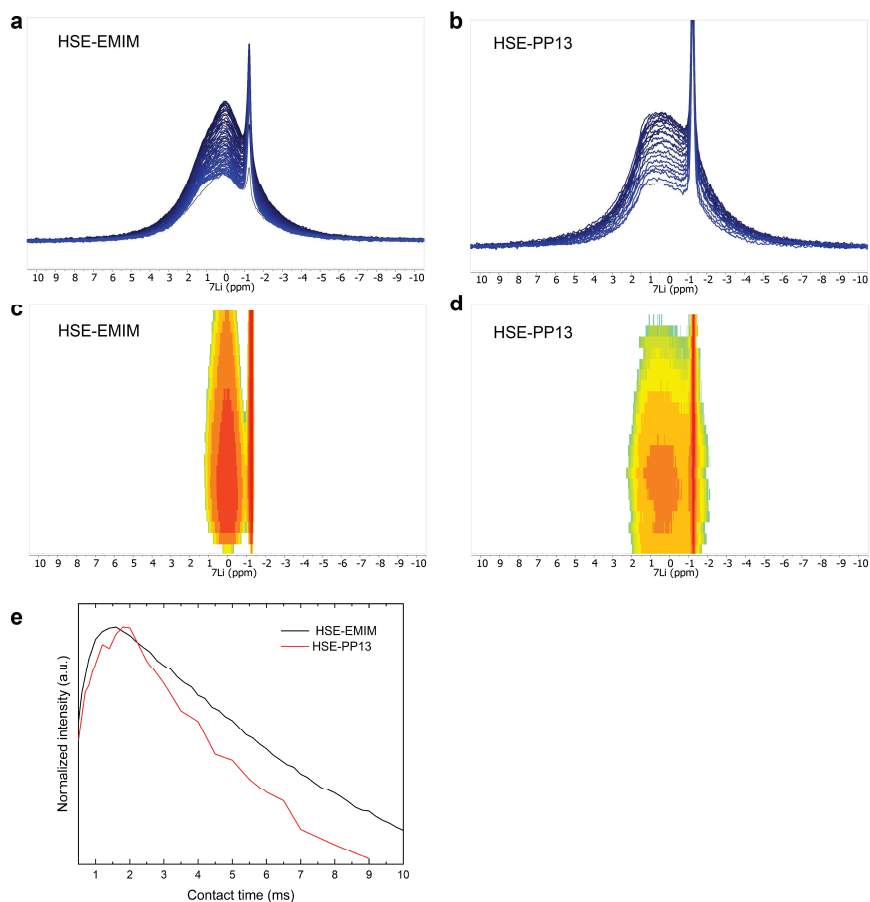


Fig. S5.6. 1D ^7Li CP MAS spectra and intensity plots measured of the HSE-EMIM and HSE-PP13, and the full buildup of the peak intensity of the broad component. 1D ^7Li CP MAS spectra and intensity plots measured of the (a, c) HSE-EMIM, and (b, d) HSE-PP13 at contact times between 0.2 μs and 12 ms. (e) Full buildup of peak intensity at 0.2 to 0.7 ppm as function of contact time of the spectra given in (a) and (b).

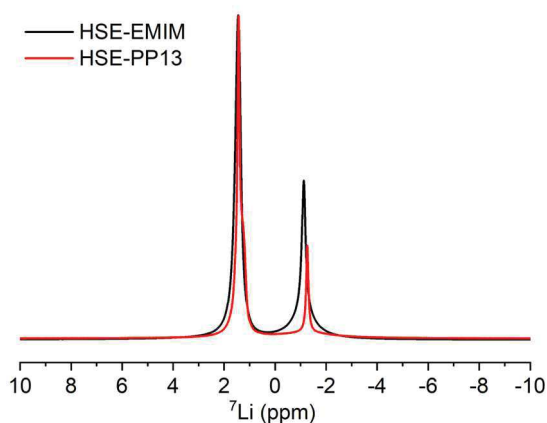


Fig. S5.7. 1D ^7Li MAS spectra of HSE-EMIM and HSE-PP13.

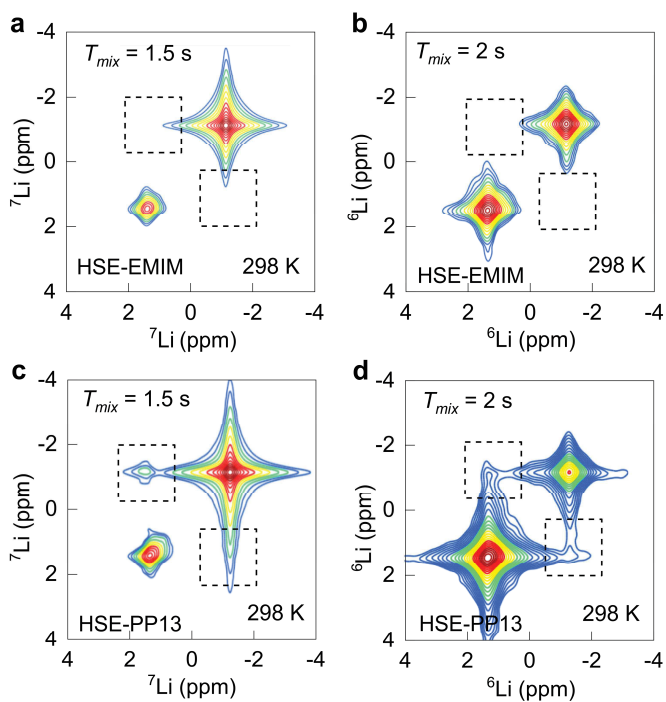


Fig. S5.8. Li-ion transport characterization in HSE with HSE-PP13 and HSE-EMIM using $^{6,7}\text{Li}$ - $^{6,7}\text{Li}$ 2D-EXSY NMR. ^7Li - ^7Li , ^6Li - ^6Li 2D-EXSY corresponding to the (a, b) HSE-EMIM, and (c, d) HSE-PP13 measured under MAS at a spinning speed of 5 kHz with mixing times of 1.5 s and 2 s at 298 K.

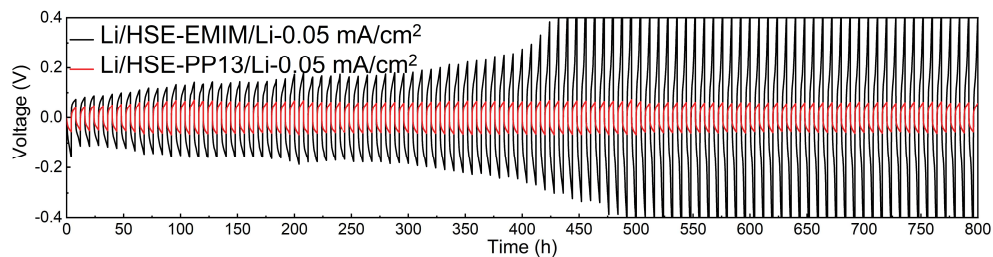


Fig. S5.9. Plating and stripping curves of a Li-metal symmetrical cell with HSE-EMIM and HSE-PP13.

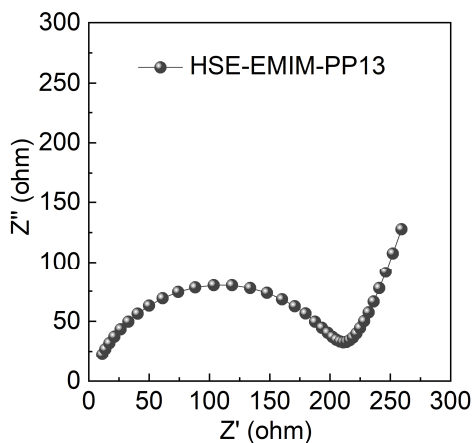


Fig. S5.10. EIS measurement of the cell with PEO-LiTFSI-Li₆PS₅Cl HSE with both PP13-TFSI and EMIM-TFSI ILs (HSE-EMIM-PP13).

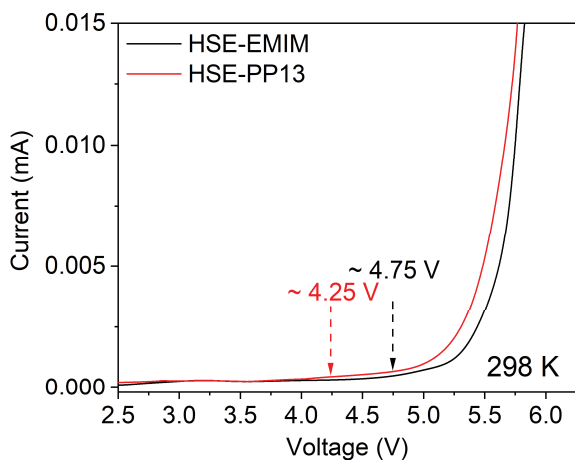


Fig. S5.11. LSV measurements of cells with HSE-PP13 and HSE-EMIM.

5

Supplementary Tables

Table S5.1. Fitting results of the 1D ^7Li ($^1\text{H} \rightarrow ^7\text{Li}$) CP curves from Fig. S5.6.

		T_{H-Li} (ms)	$T_{1\rho H}$ (ms)	$T_{1\rho Li}$ (ms)
HSE-EMIM	Decomposition products	0.42	12.1	18.6
	Li-PEO	2.35	35.5	16.3
HSE-PP13	Decomposition products	0.38	7.5	19.5
	Li-PEO	1.06	15	34

Table S5.2. Comparison of the recently reported electrochemical performances of PEO-based Li||Li symmetric cells for critical current density (CCD), areal capacity, duration time and temperature.

Method	CCD (mA/cm ²)	Areal Capacity (mAh/cm ²)	Duration time (per cycle, h)	Temperature	Ref.
PEO-SN-LAGP	0.1	0.4	4	25	10
PEO-Li ₂ S ₆	0.9	0.15	0.16	40	42
PEO-LLZO	0.5	0.5	1	55	22
PEO-RGO-LLZO	1	1	1	60	43
PEO-PMA	0.1	0.1	1	65	44
PEO-LiZr ₂ (PO ₄) ₃	0.3	0.05	0.16	40	45
PEO-Li ₃ PS ₄	0.1	0.1	1	60	46
MOF-PEO-IL	0.2	0.2	1	60	47
PEO-Nanowire LLZO	0.5	0.5	1	25	48
PEO-LLZO	0.1	–	–	60	49
PEO-Li ₆ PS ₅ Cl-EMIM-PP13	0.25	1	4	25	This work

References

1. Armand, M. & Tarascon, J. M. Building better batteries. *Nature* **451**, 652–657 (2008).
2. Dunn, B., Kamath, H. & Tarascon, J.-M. Electrical energy storage for the grid: a battery of choices. *Science* **334**, 928–935 (2011).
3. Cheng, X.-B., Zhao, C.-Z., Yao, Y.-X., Liu, H. & Zhang, Q. Recent advances in energy chemistry between solid-state electrolyte and safe lithium-metal anodes. *Chem* **5**, 74–96 (2019).
4. Armand, M. The history of polymer electrolytes. *Solid State Ionics* **69**, 309–319 (1994).
5. Zaman, W., Hortance, N., Dixit, M. B., De Andrade, V. & Hatzell, K. B. Visualizing percolation and ion transport in hybrid solid electrolytes for Li–metal batteries. *Journal of Materials Chemistry A* **7**, 23914–23921 (2019).
6. Bouchet, R., Maria, S., Meziane, R., Aboulaich, A., Lienafa, L., Bonnet, J. P. & Armand, M. Single-ion BAB triblock copolymers as highly efficient electrolytes for lithium-metal batteries. *Nature Materials* **12**, 452–457 (2013).
7. Ma, Q., Zhang, H., Zhou, C., Zheng, L., Cheng, P., Nie, J. & Zhou, Z. Single lithium-ion conducting polymer electrolytes based on a super-delocalized polyanion. *Angewandte Chemie International Edition* **55**, 2521–2525 (2016).
8. Dixit, M. B., Zaman, W., Bootwala, Y., Zheng, Y., Hatzell, M. C. & Hatzell, K. B. Scalable manufacturing of hybrid solid electrolytes with interface control. *ACS Applied Materials & Interfaces* **11**, 45087–45097 (2019).
9. Osada, I., de Vries, H., Scrosati, B. & Passerini, S. Ionic-liquid-based polymer electrolytes for battery applications. *Angewandte Chemie International Edition* **55**, 500–513 (2016).
10. Liu, M., Cheng, Z., Ganapathy, S., Wang, C., Haverkate, L. A., Tułodziecki, M. & Wagemaker, M. Tandem interface and bulk Li-ion transport in a hybrid solid electrolyte with micro-sized active filler. *ACS Energy Letters* **4**, 2336–2342 (2019).
11. Yang, K., Chen, L., Ma, J., Lai, C., Huang, Y., Mi, J. & He, Y. B. Stable interface chemistry and multiple ion transport of composite electrolyte contribute to ultra-long cycling solid-state $\text{LiNi}_{0.8}\text{Co}_{0.1}\text{Mn}_{0.1}\text{O}_2$ /lithium metal batteries. *Angewandte Chemie International Edition* **60**, 24668–24675 (2021).
12. Croce, F., Sacchetti, S. & Scrosati, B. Advanced, lithium batteries based on high-performance composite polymer electrolytes. *Journal of Power Sources* **162**, 685–689 (2006).
13. Syzdek, J., Armand, M., Gizowska, M., Marcinek, M., Sasim, E., Szafran, M. & Wiczorek, W. Ceramic-in-polymer versus polymer-in-ceramic polymeric electrolytes—A novel approach. *Journal of Power Sources* **194**, 66–72 (2009).
14. Hassoun, J. & Scrosati, B. A high-performance polymer tin sulfur lithium ion battery. *Angewandte Chemie International Edition* **49**, 2371–2374 (2010).

15. Płcharski, J. & Weiczorek, W. PEO based composite solid electrolyte containing nasicon. *Solid State Ionics* **28**, 979–982 (1988).
16. Xu, K. Electrolytes and interphases in Li-ion batteries and beyond. *Chemical Reviews* **114**, 11503–11618 (2014).
17. Lei, D., He, Y. B., Huang, H., Yuan, Y., Zhong, G., Zhao, Q. & Kang, F. Cross-linked beta alumina nanowires with compact gel polymer electrolyte coating for ultra-stable sodium metal battery. *Nature Communications* **10**, 4244 (2019).
18. Zheng, J., Tang, M. & Hu, Y.-Y. Lithium Ion Pathway within $\text{Li}_7\text{La}_3\text{Zr}_2\text{O}_{12}$ -Polyethylene Oxide Composite Electrolytes. *Angewandte Chemie International Edition* **55**, 12538–12542 (2016).
19. Wang, S., Li, Q., Bai, M., He, J., Liu, C., Li, Z. & Zhang, L. A dendrite-suppressed flexible polymer-in-ceramic electrolyte membrane for advanced lithium batteries. *Electrochimica Acta* **353**, 136604 (2020).
20. Fergus, J. W. Ceramic and polymeric solid electrolytes for lithium-ion batteries. *Journal of Power Sources* **195**, 4554–4569 (2010).
21. Blanga, R., Burstein, L., Berman, M., Greenbaum, S. G. & Golodnitsky, D. Solid polymer-in-ceramic electrolyte formed by electrophoretic deposition. *Journal of The Electrochemical Society* **162**, D3084–D3089 (2015).
22. Chen, L., Li, Y., Li, S. P., Fan, L. Z., Nan, C. W. & Goodenough, J. B. PEO/garnet composite electrolytes for solid-state lithium batteries: From “ceramic-in-polymer” to “polymer-in-ceramic”. *Nano Energy* **46**, 176–184 (2018).
23. Huo, H., Chen, Y., Luo, J., Yang, X., Guo, X. & Sun, X. Rational design of hierarchical “ceramic-in-polymer” and “polymer-in-ceramic” electrolytes for dendrite-free solid-state batteries. *Advanced Energy Materials* **9**, 1804004 (2019).
24. Bonizzoni, S., Ferrara, C., Berbenni, V., Anselmi-Tamburini, U., Mustarelli, P. & Tealdi, C. NASICON-type polymer-in-ceramic composite electrolytes for lithium batteries. *Physical Chemistry Chemical Physics* **21**, 6142–6149 (2019).
25. Dixit, M. B., Zaman, W., Hortance, N., Vujic, S., Harkey, B., Shen, F. & Hatzell, K. B. Nanoscale mapping of extrinsic interfaces in hybrid solid electrolytes. *Joule* **4**, 207–221 (2020).
26. Simon, F. J., Hanauer, M., Henss, A., Richter, F. H. & Janek, J. Properties of the Interphase Formed between Argyrodite-Type $\text{Li}_6\text{PS}_5\text{Cl}$ and Polymer-Based $\text{PEO}_{10}:\text{LiTFSI}$. *ACS Applied Materials & Interfaces* **11**, 42186–42196 (2019).
27. Simon, F. J., Hanauer, M., Richter, F. H. & Janek, J. Interphase formation of $\text{PEO}_{20}:\text{LiTFSI}-\text{Li}_6\text{PS}_5\text{Cl}$ composite electrolytes with lithium metal. *ACS Applied Materials & Interfaces* **12**, 11713–11723 (2020).
28. Zheng, J., Wang, P., Liu, H. & Hu, Y.-Y. Interface-enabled ion conduction in $\text{Li}_{10}\text{GeP}_2\text{S}_{12}$ -poly(ethylene oxide) hybrid electrolytes. *ACS Applied Energy Materials* **2**, 1452–1459 (2019).

29. Yu, C., Ganapathy, S., Eck, E. R. V., Wang, H., Basak, S., Li, Z. & Wagemaker, M. Accessing the bottleneck in all-solid state batteries, lithium-ion transport over the solid-electrolyte-electrode interface. *Nature Communications* **8**, 1086 (2017).
30. Ganapathy, S., Yu, C., van Eck, E. R. H. & Wagemaker, M. Peeking across grain boundaries in a solid-state ionic conductor. *ACS Energy Letters* **4**, 1092–1097 (2019).
31. Schwieter, T. K., Arszlewska, V. A., Wang, C., Yu, C., Vasileiadis, A., de Klerk, N. J. & Wagemaker, M. Clarifying the relationship between redox activity and electrochemical stability in solid electrolytes. *Nature Materials*, **19**, 428–435 (2020).
32. Hoefling, A., Nguyen, D. T., Partovi-Azar, P., Sebastiani, D., Theato, P., Song, S. W. & Lee, Y. J. Mechanism for the stable performance of sulfur-copolymer cathode in lithium–sulfur battery studied by solid-state NMR spectroscopy. *Chemistry of Materials* **30**, 2915–2923 (2018).
33. Rataboul, F., Baudouin, A., Thieuleux, C., Veyre, L., Copéret, C., Thivolle-Cazat, J. & Emsley, L. Molecular understanding of the formation of surface zirconium hydrides upon thermal treatment under hydrogen of $[(\text{SiO})\text{Zr}(\text{CH}_2\text{tBu})_3]$ by using advanced solid-state NMR techniques. *Journal of the American Chemical Society* **126**, 12541–12550 (2004).
34. Zhu, C., Cheng, H. & Yang, Y. Electrochemical characterization of two types of peo-based polymer electrolytes with room-temperature ionic liquids. *Journal of the Electrochemical Society* **155**, A569 (2008).
35. Kodama, K., Tsuda, R., Niitsuma, K., Tamura, T., Ueki, T., Kokubo, H. & Watanabe, M. Structural effects of polyethers and ionic liquids in their binary mixtures on lower critical solution temperature liquid-liquid phase separation. *Polymer journal* **43**, 242–248 (2011).
36. Cesare Marincola, F., Piras, C., Russina, O., Gontrani, L., Saba, G. & Lai, A. NMR investigation of imidazolium-based ionic liquids and their aqueous mixtures. *ChemPhysChem* **13**, 1339–1346 (2012).
37. Wang, B.-H., Xia, T., Chen, Q. & Yao, Y.-F. Probing the dynamics of Li^+ ions on the crystal surface: A solid-state NMR study. *Polymers* **12**, 391 (2020).
38. Zhao, Z., Li, F., Zhao, J., Ding, G., Wang, J., Du, X. & Cui, G. Ionic-association-assisted viscoelastic nylon electrolytes enable synchronously coupled interface for solid batteries. *Advanced Functional Materials* **30**, 2000347 (2020).
39. Ganapathy, S., van Eck, E. R. H., Kentgens, A. P. M., Mulder, F. M. & Wagemaker, M. Equilibrium lithium-ion transport between nanocrystalline lithium-inserted anatase TiO_2 and the electrolyte. *Chemistry – A European Journal* **17**, 14811–14816 (2011).
40. Kumar, M. & Sekhon, S. S. Role of plasticizer’s dielectric constant on conductivity modification of PEO– NH_4F polymer electrolytes. *European Polymer Journal* **38**, 1297–1304 (2002).
41. Liu, M., Zhou, D., He, Y. B., Fu, Y., Qin, X., Miao, C. & Kang, F. Novel gel polymer electrolyte for high-performance lithium–sulfur batteries. *Nano Energy* **22**, 278–289 (2016).

42. Fang, R., Xu, B., Grundish, N. S., Xia, Y., Li, Y., Lu, C. & Goodenough, J. B. Li₂S₆-integrated PEO-based polymer electrolytes for all-solid-state lithium-metal batteries. *Angewandte Chemie* **133**, 17842–17847 (2021).
43. Liu, Y., Lin, D., Jin, Y., Liu, K., Tao, X., Zhang, Q. & Cui, Y. Transforming from planar to three-dimensional lithium with flowable interphase for solid lithium metal batteries. *Science Advances* **3**, eaao0713 (2017).
44. Zhou, W., Wang, Z., Pu, Y., Li, Y., Xin, S., Li, X. & Goodenough, J. B. Double-layer polymer electrolyte for high-voltage all-solid-state rechargeable batteries. *Advanced Materials* **31**, 1805574 (2019).
45. Wu, N., Chien, P. H., Li, Y., Dolocan, A., Xu, H., Xu, B. & Goodenough, J. B. Fast Li⁺ Conduction Mechanism and Interfacial Chemistry of a NASICON/Polymer Composite Electrolyte. *Journal of the American Chemical Society* **142**, 2497–2505 (2020).
46. Chen, S., Wang, J., Zhang, Z., Wu, L., Yao, L., Wei, Z. & Xu, X. In-situ preparation of poly(ethylene oxide)/Li₃PS₄ hybrid polymer electrolyte with good nanofiller distribution for rechargeable solid-state lithium batteries. *Journal of Power Sources* **387**, 72–80 (2018).
47. Wu, J. & Guo, X. Nanostructured metal–organic framework (mof)-derived solid electrolytes realizing fast lithium ion transportation kinetics in solid-state batteries. *Small* **15**, 1804413 (2019).
48. Fu, K., Gong, Y., Dai, J., Gong, A., Han, X., Yao, Y. & Hu, L. Flexible, solid-state, ion-conducting membrane with 3D garnet nanofiber networks for lithium batteries. *Proceedings of the National Academy of Sciences* **113**, 7094–7099 (2016).
49. Zhao, C. Z., Zhang, X. Q., Cheng, X. B., Zhang, R., Xu, R., Chen, P. Y. & Zhang, Q. An anion-immobilized composite electrolyte for dendrite-free lithium metal anodes. *Proceedings of the National Academy of Sciences* **114**, 11069–11074 (2017).

6

Elucidating the Impact of Functional Additives on the Structure and Ion Dynamics of Hybrid Solid Electrolytes

“横看成岭侧成峰，远近高低各不同”

“Viewed from the front, it appears as a ridge; from the side, it stands as a peak; near or far, high or low, all appear different.”

苏轼《题西林壁》(On the West Forest Wall)

This chapter has been published as: **Zhang, S.**, Li, Y., Bannenberg, L.J., Liu, M., Wagemaker, M. & Ganapathy, S. Elucidating the impact of functional additives on the structure and ion dynamics of hybrid solid electrolytes. *Advanced Energy Materials*, accepted (2025).

Abstract

One of the major challenges in advancing polymer-inorganic hybrid solid electrolytes (HSEs) lies in comprehending and controlling their internal structure. In addition, the intricate interplay between multiple phases further complicates efforts to establish the structure-property relationships. In this study, by introducing a multifunctional LiI additive to a HSE comprising of polyethylene oxide (PEO) polymeric electrolyte and the fast lithium-ion conductor $\text{Li}_6\text{PS}_5\text{Cl}$, we disentangle the relationship between the bulk and interface structure and ascertain their impact on lithium-ion dynamics within the HSE. Using multidimensional solid-state nuclear magnetic resonance, we find that the addition of LiI stabilizes the internal interfaces and enhances lithium-ion mobility. A kinetically stable solid-electrolyte interphase is formed at the lithium-metal anode, increasing the critical current density to 1.3 mA cm^{-2} , and enabling long-term stable cycling of lithium symmetric cells ($> 1200 \text{ h}$). This work sheds light on tailoring the structure of HSEs to improve their conductivity and stability for enabling all-solid-state lithium-metal batteries.

6.1 Introduction

Solid-state electrolytes (SSEs) are investigated for their superior safety, i.e., inflammable and leak-proof, compared to conventional liquid electrolytes. SSEs with high ionic conductivity, (electro)chemical stability, and easy processability are required to enable high-energy-density all-solid-state lithium (Li)-metal batteries (ASSLMBs), which appears to be one of the most appealing next-generation battery technologies¹⁻⁴. However, the practical utilization of SSEs remains challenging due to the absence of a comprehensive single electrolyte possessing all the required properties. Among currently investigated SSEs, inorganic solid electrolytes typically suffer from severe sensitivity to ambient atmosphere, high resistance at the electrode/electrolyte interface, and instability in contact with Li, despite their remarkable ionic conductivity and mechanical strength⁵⁻⁷. Conversely, solid polymer electrolytes offer greater flexibility and favorable compatibility with lithium, yet their room temperature conductivity tends to be relatively low ($< 10^{-5}$ S cm⁻¹ at room temperature)^{8,9}. In this context, a hybrid concept which seeks to combine the advantages of both inorganic and organic solid electrolytes, appears to be a promising solution for advancing the application of ASSLMBs¹⁰⁻¹². In principle, this combination can result in a wide variety of combinations of different ion conductors and their respective ratios. One of the most extensively studied systems is a composition of inorganic electrolyte fillers within the polyethylene oxide (PEO)-lithium salt (LiX) matrix.

In the PEO-LiX matrix, Li-ion conduction occurs via segmental motion of the polymer, which relies on the solvation of Li-ions through the lone electron pair donated from the oxygen atom of the PEO chain (via the bonding and fracturing of ethylene oxide-Li bonds), allowing for the transport of Li-ions^{13,14}. However, the molecular segmental motion is confined to the amorphous region, resulting in limited ionic conductivity. Embedding inorganic electrolyte fillers, thus forming hybrid solid electrolytes (HSEs), can reduce the degree of crystallinity of the polymer matrix and create additional fast Li-ion transport channels¹⁵⁻¹⁸. An ideal triple Li-ion conduction network is envisioned: (i) within the PEO-LiX phase; (ii) along the organic/inorganic interface; and (iii) through the inorganic electrolyte phase. However, achieving this ideal scenario remains challenging as the Li-ion conductivity of the obtained HSEs still falls short of the requirements for ASSLMBs. This is

primarily due to the formation of an inert interface between the inorganic fillers and the polymer matrix, and the persistently high crystallinity of the polymer matrix. Various approaches have been proposed to address the aforementioned interlinked issues and reduce the crystallinity of the polymer phase. One of the most common ways is the addition of plasticizers (e.g., tetraethylene glycol dimethyl ether, succinonitrile, ionic liquid), which mainly work on reducing the crystallinity of the polymer matrix^{19–23}. However, this typically sacrifices the mechanical strength as well as the thermal and electrochemical stability of the HSEs.

To address these issues, identifying additives for PEO-based HSEs that enable a conductive organic/inorganic interface, and reduce the crystallinity of the polymer matrix while maintaining certain mechanical strength presents a viable strategy. Simultaneously, it is necessary that the HSEs interact synergistically with Li-metal to form a mechanically and chemically stable solid-electrolyte interphase (SEI) layer with high conductivity. Recently, the incorporation of a binary LiI additive into sulfide solid electrolytes has been found to be advantageous, as iodine improves the Li-ion conductivity and Li-metal compatibility by suppressing the reductive decomposition of the sulfide solid electrolytes^{24–27}. This suggests that the introduction of LiI in the PEO-LiX/sulfide-ISE can be highly advantageous. LiI is expected to lower the internal resistance by altering the interface structure of the PEO-LiX/sulfides.

Herein, as a continuation of the study from Chapter 5, we incorporated LiI (5 wt%) into the PEO-LiTFSI-Li₆PS₅Cl hybrid system, aiming to unveil how this secondary Li salt phase modifies the interface structure between the organic/inorganic phases and how it changes the Li solvation structure in the PEO-LiX matrix. Targeted at activating the high conductivity of the inorganic Li₆PS₅Cl, multinuclear and multiscale solid-state nuclear magnetic resonance (ssNMR) are employed to address the major experimental challenge of disentangling the local Li-ion transport across the polymer phase, the inorganic phase, and the interface between these two phases. Building on previous research, a combination of two-dimensional (2D) exchange (2D-EXSY)^{28,29}, pulsed field gradient (PFG), and one-dimensional (1D) direct excitation with/without decoupling and cross-polarization (CP) dynamics experiments are utilized^{28,30,31}. A clearly improved self-diffusion process between the organic and inorganic phases is visualized and quantified by 2D ⁶Li-⁶Li EXSY, rationalizing the increased ionic

conductivity observed with electrochemical impedance spectroscopy (EIS) measurements. Unravelling the bulk and local interfacial structures of the HSEs demonstrates that the addition of LiI facilitates Li dissociation in the bulk, while impeding detrimental reactions between PEO and $\text{Li}_6\text{PS}_5\text{Cl}$. Through X-ray photoelectron spectroscopy (XPS) and time-of-flight secondary ion mass spectrometry (TOF-SIMS) analysis, a stable interface with Li-metal, rich in inorganic species, was identified that is instrumental in inhibiting the formation and aggregation of Li dendrites, thereby facilitating stable and long cycling Li|HSE|Li symmetrical cells and enabling the use of sulfur cathodes.

6.2 Results

6.2.1 Improving Li-ion diffusion between PEO-LiTFSI and $\text{Li}_6\text{PS}_5\text{Cl}$ with a LiI additive

Given that the interfacial Li-ion diffusion determines whether the inorganic phase contributes to the overall Li-ion conductivity, 2D-EXSY experiments under magic angle spinning (MAS) conditions are employed to investigate the impact of LiI on the interfacial Li-ion conduction in the PEO-LiTFSI- $\text{Li}_6\text{PS}_5\text{Cl}$ hybrid system. The exchange between distinct Li environments (in this case, LiTFSI-PEO and $\text{Li}_6\text{PS}_5\text{Cl}$, as depicted in **Fig. 6.1a**) within the NMR time scale generates off-diagonal (cross) peaks in the 2D contour plots, the position of which we indicate with the dotted boxes in **Fig. 6.1a-c**. With increasing the mixing time (T_{mix}) or elevating the temperatures, more Li-ions spontaneously diffuse between these environments, either using a longer contact time or through faster dynamics, leading to the emergence or growth of cross-peak intensity.

For $\text{PEO}_{18}\text{LiTFSI-Li}_6\text{PS}_5\text{Cl}$ [EO:Li = 18:1, denoted as HSE (18:1)], no cross-peaks are visible in the 2D-EXSY spectrum (**Fig. S6.1a**) despite a long T_{mix} at an elevated temperature (338 K). Building on the study in Chapter 5, the accumulation of interfacial decomposition products on the $\text{Li}_6\text{PS}_5\text{Cl}$ surface acts as a barrier layer that impedes the Li-ion diffusion, preventing this phase from contributing to long-range conductivity of the HSE²⁸. To address this limitation, LiI was introduced to the HSE system, with the initial goal of improving interfacial conductivity by modifying the composition and structure of the interface. When LiI is added to the HSE (18:1) forming $\text{PEO}_{18}\text{LiTFSI-Li}_6\text{PS}_5\text{Cl-LiI}$ (denoted as HSE-LiI), cross-peaks are directly observed between Li in the PEO phase and in the $\text{Li}_6\text{PS}_5\text{Cl}$ phase at

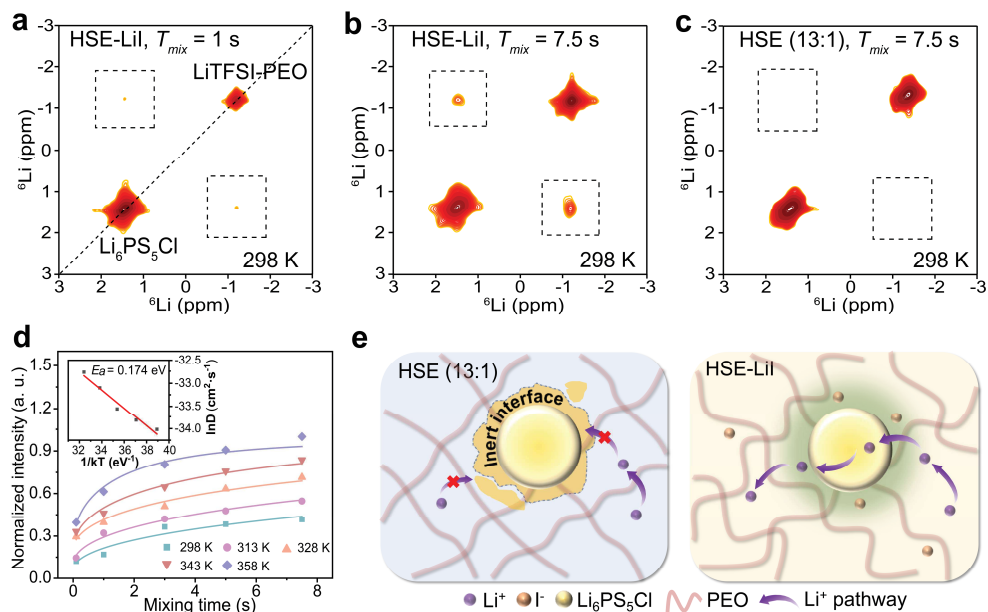


Fig. 6.1. Measuring and quantifying Li-ion transport between the PEO-LiTFSI and Li₆PS₅Cl phases in the HSEs. 2D ⁶Li-⁶Li EXSY spectra measured at a spinning speed of 10 kHz at 298 K for HSE-LiI with (a) $T_{mix} = 1$ s and (b) $T_{mix} = 7.5$ s, and for (c) HSE (13:1) with a mixing time $T_{mix} = 7.5$ s. (d) Evolution of the normalized cross-peak intensity as a function of T_{mix} at the temperatures indicated in the graph. The inset figure illustrates the dependence of the diffusion coefficient (D), obtained by fitting the 2D ⁶Li-⁶Li EXSY data to a diffusion model described in detail in **Supplementary Text S5.2** and elsewhere^{32,33}. The normalized intensity is denoted in arbitrary units (a.u.). Fitting the temperature dependence of D to the Arrhenius law provides an activation energy (E_a) of 0.174 eV. (e) Schematic figure of Li-ion diffusion pathway in HSE (13:1) and HSE-LiI.

room temperature already at a relatively short T_{mix} (**Fig. 6.1a**). In addition, an evident rise in cross-peak intensity with an increasing T_{mix} is observed as illustrated in **Fig. S6.1b-d** and **Fig. 6.1b**. Given the LiI peak (~ -4.56 ppm) is not observed in the one-pulse ⁶Li NMR spectrum (**Fig. S6.2**), it is plausible that the LiI dissociates in the PEO matrix, consistent with other reports³⁴⁻³⁶. As a result, the EO:Li ratio varies between these two samples, with the HSE-LiI sample effectively having an EO:Li ratio of 13:1, assuming all LiI dissociates in the PEO matrix. To have a more fair comparison, we prepared an additional material with the same EO:Li ratio, i.e., PEO₁₃LiTFSI-Li₆PS₅Cl [EO:Li = 13:1, denoted as HSE (13:1)], serving as a more appropriate reference for examining the impact of LiI in the HSEs system. Hence from hereon we compare the HSE-LiI with HSE (13:1), unless otherwise specified. Despite observing no exchange in the HSE (13:1) at room temperature with a long T_{mix} (**Fig. 6.1c**),

cross-peaks begin to appear at an elevated temperature of 313 K (**Fig. S6.1e**). The appearance of cross-peaks in the HSE (13:1) sample suggests that the Li-ion concentration affects the interfacial Li-ion transport between the organic/inorganic phases. This may be attributed to the increased segmental motion of the PEO chains resulting from a higher amorphous phase fraction, caused by the addition of more Li salt^{37–39}. The enhanced mobility of Li-ions and/or improved contact may contribute to overcoming the interfacial barrier for Li-ion transport between both phases, alluding to a complex interplay between bulk and interfacial Li-ion dynamics. However, this enhancement comes at the cost of a noticeable reduction in the mechanical strength of the HSE membrane. As seen in **Fig. S6.3d, e**, the HSE (13:1) membrane is very sticky and challenging to handle and process. In contrast, the HSE-LiI membrane still retains sufficient mechanical strength to be handled (**Fig. S6.3a-c**). For a more comprehensive comparison, a series of measurements with varying T_{mix} are conducted at 313 K for the HSE (13:1) to quantify equilibrium Li-ion exchange between these two phases (**Fig. S6.1f**). Clearly, a faster buildup of cross-peaks with much higher intensity is observed for the HSE-LiI sample, which demonstrates that the addition of LiI effectively promotes the interfacial Li-ion diffusion between the organic and inorganic phases.

Fitting the normalized intensity of the cross-peak evolution to a diffusion model derived from Fick's law, as described in **Supplementary Text S5.2** and previous work^{32,33}, leads to diffusion coefficients as a function of temperature (**Fig. 6.1d**, inset). The local Li-ion diffusion between the organic and inorganic species in the HSE-LiI can thus be quantified. Fitting the diffusion coefficients with the Arrhenius law results in an activation energy (E_a) of 0.174 eV for this process, which is notably lower than that obtained from the EIS measurements (vide infra, 0.201 eV and 0.557 eV from **Fig. 6.4b**). This indicates that the incorporation of LiI improves Li-ion transport between the organic and inorganic components in the hybrid electrolyte system (**Fig. 6.1e**), while simultaneously maintaining the mechanical integrity of the membrane.

6.2.2 Impact of LiI on bulk and local structures of the HSE

To understand how LiI interacts with the organic and inorganic phases in the HSE-LiI system and consequently improves the Li-ion mobility, it is essential to characterize both the bulk and local structure of the HSEs. The ⁷Li NMR spectra in **Fig. 6.2a** show that the Li-ion resonances are shifted downfield for the HSE-LiI electrolyte. The downfield shift of the

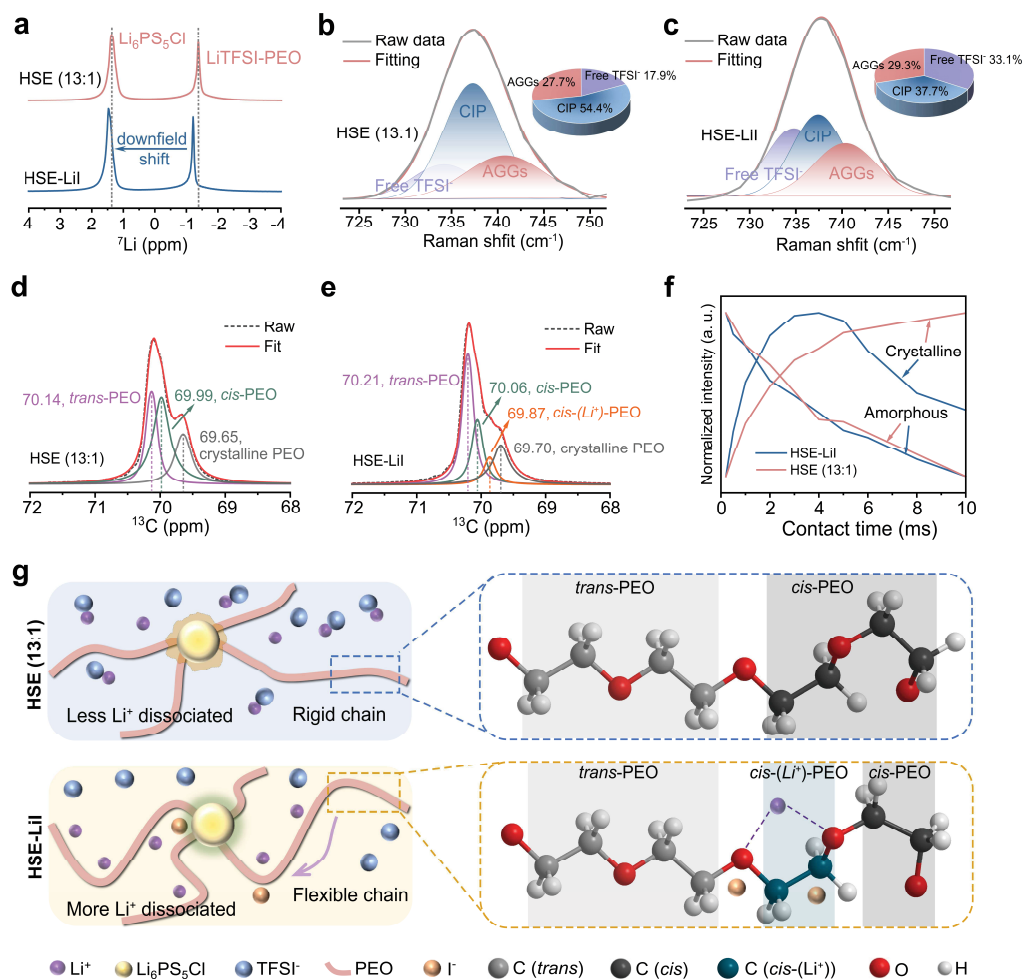


Fig. 6.2. Characterizing the bulk structure of the HSEs with and without LiI. (a) 1D ^7Li MAS ssNMR spectra. Raman spectra of (b) HSE (13:1) and (c) HSE-LiI electrolytes, and corresponding quantification results of the TFSI $^-$ anion states in the HSEs. CIP, contact ion pairs; AGGs, aggregate clusters. Fitting of the high power decoupling (hpdec) ^{13}C single-pulse ssNMR spectra for (d) HSE (13:1), and (e) HSE-LiI. (f) Integrated intensities extracted from the 1D $^1\text{H}\rightarrow^{13}\text{C}$ CP MAS ssNMR spectra obtained for HSE-LiI and HSE (13:1), expressed in arbitrary units (a.u.), with a focus on both the amorphous and crystalline ^{13}C environments as highlighted in Fig. S6.10. (g) Schematic showing the influence of LiI on the bulk structure of the HSE, with the carbon conformation of HSE-LiI and HSE (13:1) assigned in Fig. 6.2d, e.

LiTFSI-PEO peak is indicative of reduced electron density around the Li atoms, suggesting improved Li mobility within the PEO, which is a result of the enhanced dissociation degree of the LiTFSI 35,40,41 . The shift of the $\text{Li}_6\text{PS}_5\text{Cl}$ peak possibly stems from greater local disorder

and potentially excess I⁻ intercalating in the structure or exchanging with the Cl⁻.⁴² To determine whether this shift is observed in the absence of the PEO-LiTFSI, a control mixture of Li₆PS₅Cl@LiI in acetonitrile was prepared. The Li₆PS₅Cl peak in the Li₆PS₅Cl@LiI mixture also shows a downfield shift compared to pristine Li₆PS₅Cl (**Fig. S6.4**). Notably, the ¹H peak also shifts to higher ppm for the HSE-LiI sample in the ¹H NMR spectrum (**Fig. S6.5**), signifying the interaction between the PEO chains and I⁻ anions^{34,35}. Furthermore, Raman analysis was conducted to identify the TFSI⁻ states (**Fig. 6.2b, c**)⁴³. In HSE (13:1), the content of free TFSI⁻, contact ion pairs (CIP), and aggregate clusters (AGGs) are 17.9%, 54.5%, and 27.7% respectively, while the corresponding values for HSE-LiI are 33.1%, 37.7%, and 29.3%, respectively. The nearly doubled amount of free TFSI⁻ suggests the presence of more “free” Li-ions due to the improvement in dissociation of the Li salt by the addition of LiI (**Fig. 6.2g**), which is consistent with the peak shift shown in the ⁷Li spectra (**Fig. 6.2a**).

The bulk structure of the HSEs was further explored by X-ray photoelectron spectroscopy (XPS, **Fig. S6.6 and S6.7**). The signal at ~292.8 eV and ~288.2 eV in the C 1s spectra are attributable to the -CF₃ group of LiTFSI and the small amount of -COOR from the PEO decomposition, such as Li₂CO₃ and ROCO₂Li^{44,45}. The intensities of the peaks at ~286.6 eV and ~284.8 eV, corresponding to C-O-C and C-C/C-H of the PEO backbone, show a clear difference in ratio between HSE-LiI and HSE (13:1). This difference has not yet been addressed in publications, and presently we attributed it to the interaction between I⁻ and C-C/C-H³⁴. Two doublets centred around ~168.68 eV (S 2p_{3/2}) and ~166.88 eV (S 2p_{3/2}) correspond to LiTFSI and its decomposition products, such as -SO₂CF₂⁺ and Li_xS_yO_z^{44,46}. A weak intensity doublet of polysulfides (-S_x⁰⁻) is present in both samples, while additional P-S-Li bonds from Li₆PS₅Cl are observed in HSE (13:1)⁴⁷. Comparing the intensities of PEO and LiTFSI peaks in the XPS spectra implies a relatively higher coverage of organic phase on the surface of HSE-LiI, accompanied by less salt decomposition. This corresponds to the scanning electron microscope (SEM) images in **Fig. S6.8**, where HSE-LiI displays a smoother surface and HSE (13:1) shows obvious agglomeration of Li₆PS₅Cl particles. Further characterization of the bulk structure of the HSEs was conducted using time-of-flight secondary ion mass spectrometry (TOF-SIMS, **Fig. S6.9**). Secondary-ion fragments such as NS₂O₄C₂F₆⁻, NSO₂CF₃⁻, and C₂H₃O⁻ are identified as representing the PEO-LiTFSI phase,

while S^- and PS^- fragments originated from the Li_6PS_5Cl phase (with SO_2^- attributed to the oxidation of PS_x^- species)⁴⁸. Three-dimensional (3D) reconstruction and top-down depth profiles of the species of interest indicate that HSE-LiI exhibits a higher degree of organic coverage, providing further evidence supporting the aforementioned results.

A detailed study of the organic phase conformation is conducted using ^{13}C NMR. This is realized by 1D ^{13}C NMR and ^{13}C ($^1H \rightarrow ^{13}C$) CP MAS (**Fig. 6.2d, e** and **Fig. S6.10**). Deconvoluting the ^{13}C spectra reveal that the ^{13}C environments are dominated by *trans*-PEO, *cis*-PEO, and crystalline PEO in both the HSE-LiI and HSE (13:1) (**Fig. 6.2d, e**)⁴⁹. The slight downfield shift of the ^{13}C chemical shift (to higher ppm value) in the HSE-LiI is likely attributed to the de-shielding effect by the I (**Fig. 6.2e**). An additional ^{13}C environment is present in the HSE-LiI spectrum, with a chemical shift close to that of the *cis*-PEO. This is attributed to the enhanced coordination between *cis*-PEO and Li-ion in the presence of I, which causes an upfield shift of part of the *cis*-PEO peak due to a more pronounced shielding effect [designated as *cis*-(Li^+)-PEO]. In analyzing the PEO matrix, it becomes crucial to discern the crystalline and amorphous phases, as the Li-ion transport within the PEO phase is governed by the segmental motion within the amorphous phase. This can be readily accomplished using ^{13}C CP MAS NMR, as both the crystalline and amorphous phases exhibit distinct dependencies on contact time⁵⁰. In the evolution of the ^{13}C CP MAS spectra, the peak intensity, varying with contact time, significantly relies on the local environments and dynamics of the investigated system. The signal from the amorphous PEO phase is detectable only with a short contact time, attributed to its high mobility, which makes the dipolar coupling less efficient^{50,51}. In contrast, the crystalline phase experiences an increase in peak intensity with an extended contact time. Therefore, in **Fig. S6.10**, the sharp peak can be assigned to crystalline phase, while the broad peak is associated with the amorphous phase, determined by their intensity evolution and linewidth (**Table S6.1**). Comparing the buildup of their peak intensity (**Fig. 6.2f**), despite similar decay rates for the amorphous phase, the decay of the crystalline phase is accelerated by the presence of LiI, suggesting improved local 1H dynamics of the HSE-LiI. Based on 7Li , 1H , ^{13}C , ^{13}C CP MAS and Raman data, a conformation diagram is proposed in **Fig. 6.2g**, illustrating that the addition of LiI increases the dissociation of Li salt, enhancing polymer chain mobility and altering the polymer configuration to one more favorable for Li-ion transport [the formation of *cis*-(Li^+)-PEO].

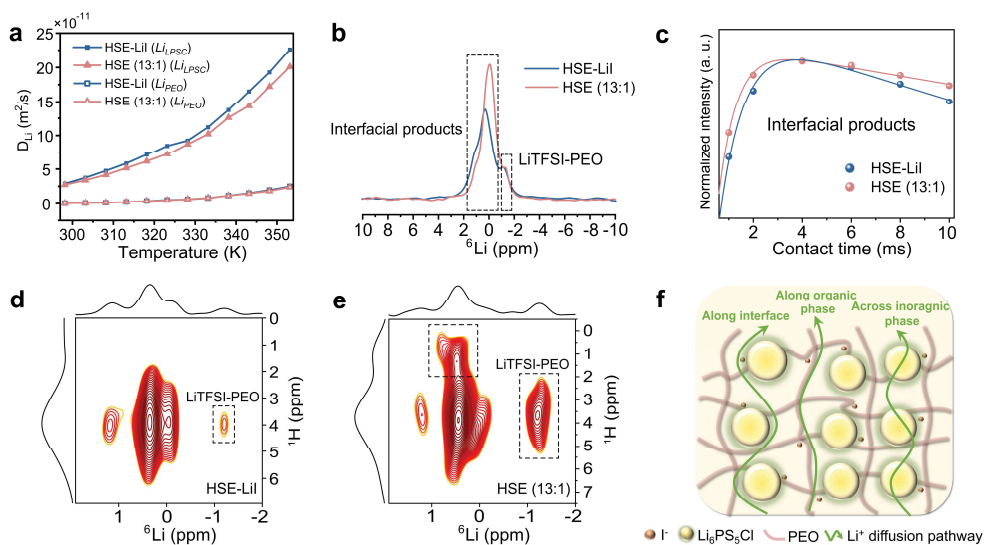


Fig. 6.3. Identifying the interface structure of the HSEs with and without LiI. Self-diffusion coefficients of ${}^7\text{Li}$ from 298 K to 353 K obtained by (a) PFG-NMR, where the Li-ion diffusion in the PEO-LiTFSI phase and the $\text{Li}_6\text{PS}_5\text{Cl}$ phase are deconvoluted. (b) 1D ${}^1\text{H}\rightarrow{}^6\text{Li}$ CP MAS spectra with a contact time of 8 ms (0.2 to 8 ms in Fig. S6.13). (c) Integrated intensities and the corresponding fits extracted from 1D ${}^1\text{H}\rightarrow{}^7\text{Li}$ CP MAS spectra obtained for HSE-LiI and HSE (13:1), expressed in arbitrary units (a.u.), with a focus on the interfacial Li environment as highlighted in (b) (individual spectra at contact times ranging from 0.05 to 10 ms are shown in Fig. S6.15). 2D ${}^1\text{H}\text{-}{}^6\text{Li}$ HETCOR spectra acquired with a CP contact time of 0.5 ms of (d) HSE-LiI, and (e) HSE (13:1). (f) Proposed Li-ion diffusion pathway in the HSE-LiI.

The individual mobility of cations and anions were studied by pulsed field gradient (PFG)-NMR. The Li-ion diffusion in the PEO-LiTFSI phase and the $\text{Li}_6\text{PS}_5\text{Cl}$ phase can be readily distinguished as there is appreciable difference between their ${}^7\text{Li}$ chemical shifts. The self-diffusion coefficients of ${}^7\text{Li}$ (D_{Li}) and ${}^{19}\text{F}$ (D_{F}) were measured at various temperatures (Fig. 6.3a and Fig. S6.11). The D_{Li} in the LiTFSI-PEO phase is virtually identical in the HSEs regardless of the presence of LiI, but a higher D_{Li} is observed for the $\text{Li}_6\text{PS}_5\text{Cl}$ phase in the HSE-LiI sample. This suggests that the increased conductivity resulting from the addition of LiI is associated better participation of the $\text{Li}_6\text{PS}_5\text{Cl}$ phase and/or better conductivity of the $\text{Li}_6\text{PS}_5\text{Cl}$ phase itself. From the X-ray diffraction (XRD) patterns (Fig. S6.12), no obvious difference is observed between the $\text{Li}_6\text{PS}_5\text{Cl}$ phase in these two samples. This suggests that the higher D_{Li} of the $\text{Li}_6\text{PS}_5\text{Cl}$ phase in the HSE-LiI, as obtained from PFG-NMR, is unlikely due to any major structural changes in $\text{Li}_6\text{PS}_5\text{Cl}$. Instead, it is more likely associated with

changes in the surface properties of the $\text{Li}_6\text{PS}_5\text{Cl}$ particles, particularly at the interface between PEO-LiTFSI and $\text{Li}_6\text{PS}_5\text{Cl}$, which could improve Li-ion transport between the two phases. In both samples, D_F is generally higher than D_{Li} in the PEO-LiTFSI phase, as expected for the PEO-based polymer electrolyte, where Li-ions strongly coordinate with the EO groups⁵². The introduction of LiI does not significantly affect the dynamics of the TFSI anion, as the D_F remains similar for both samples (**Fig. S6.11c**). The E_a for each component was determined by fitting the self-diffusion coefficients of ^7Li in the PEO (Li_{PEO}) and $\text{Li}_6\text{PS}_5\text{Cl}$ phases (Li_{LPSC}), and ^{19}F in the TFSI (D_F) phase using the Arrhenius equation. For the HSE-LiI, both the Li_{PEO} and Li_{LPSC} show a slightly smaller E_a than the HSE (13:1), in contrast, the E_a obtained from fitting the D_F is higher for the HSE (13:1), especially in the lower temperature region (**Fig. S6.11a, b and S6.11d**). This is expected as TFSI⁻ is competing with I⁻ for adsorption sites in the HSE-LiI system, leading to weakened binding of F⁻ to the polymer segments, thereby reducing their diffusion rates. The difference is more pronounced in the lower temperature range as the polymer segments and Li-ions are less mobile, potentially impeding the diffusion of the counter ions.

The results from the PFG-NMR motivate an in-depth study on the impact of the added LiI to the interface between the organic and inorganic phases. For this, 1D $^1\text{H} \rightarrow ^{6,7}\text{Li}$ CP MAS and 2D $^1\text{H}-^6\text{Li}$ ($^1\text{H}-^{13}\text{C}$) heteronuclear correlation (HETCOR) experiments were performed (**Fig. 6.3b-e, Fig. S6.13 and S6.14**). In these experiments, the abundant protons (^1H) are utilized to identify $^{6,7}\text{Li}$ (^{13}C) in their close vicinity (within a few atomic bond lengths), through the transfer of magnetization within a specific time duration called the contact time. Consequently, this aids in elucidating the interfacial ion dynamics and structure. In comparison to the ^6Li single-pulse excitation spectra (**Fig. S6.2**), additional resonances are resolved in the ^6Li CP MAS spectra within the -0.7 to 1.2 ppm range for both electrolytes (**Fig. 6.3b**). These signals can be attributed to: (i) impurities on the $\text{Li}_6\text{PS}_5\text{Cl}$ surface given its inherently high reactivity, and (ii) the reaction products between PEO-LiTFSI and $\text{Li}_6\text{PS}_5\text{Cl}$ particles, delineated as interfacial products in **Fig. 6.3b**^{46,48,53,54}. Similar to the single-pulse spectrum, a downfield shift of the ^6Li signal is also observed in the ^6Li CP MAS spectrum of HSE-LiI. In addition, fewer interfacial products are detected in the HSE-LiI system. Examining the development of the ^6Li CP MAS signal with varying contact time from 0.2 to 8 ms (**Fig. S6.13**), a distinctly quicker buildup of the LiTFSI-PEO peak is evident

in the HSE (13:1) sample, suggesting a lower mobility of Li-ions in the proximity of the PEO, or that the Li-ions are more tethered to the PEO segments (the more mobile it is, the harder it is to detect)²⁸.

To better resolve the ${}^6\text{Li}$ signals arising from the interfacial Li-containing species in the ${}^6\text{Li}$ CP MAS experiments, 2D ${}^1\text{H}$ - ${}^6\text{Li}$ HETCOR experiments were conducted with a short contact time of 0.5 ms (**Fig. 6.3d, e**). This enables the detection of ${}^6\text{Li}$ directly bonded to ${}^1\text{H}$ or in its immediate proximity, and provides better resolved ${}^6\text{Li}$ signals. Considerably stronger correlations between PEO and LiTFSI, as well as the interfacial products in the HSE (13:1) are observed, suggesting stronger coordination between Li-ions and EO units, and lower mobility of the Li-containing species in close proximity to ${}^1\text{H}$ (**Fig. 6.3e**). These findings are consistent with the ${}^6\text{Li}$ CP MAS spectra. The ${}^6\text{Li}$ signal in the HETCOR spectrum is dominated by the correlations between the ${}^1\text{H}$ in the main PEO chains ($-\text{CH}_2-\text{CH}_2-$) and ${}^6\text{Li}$ in its proximity. An additional ${}^1\text{H}$ environment is present in the HSE (13:1) sample ($\sim 1 - 1.2$ ppm, in the left dotted box in **Fig. 6.3e**), and this ${}^1\text{H}$ resonance is correlated to the main ${}^6\text{Li}$ peak at ~ 0.43 ppm as well. This can be assigned to the degradation products of PEO chains into shorter chains resulting from side reactions with $\text{Li}_6\text{PS}_5\text{Cl}$ ^{48,55}. This is also reflected in the ${}^1\text{H}$ - ${}^{13}\text{C}$ HETCOR spectra (**Fig. S6.14**), where additional ${}^1\text{H}$ - ${}^{13}\text{C}$ correlations emerge in HSE (13:1) aside from the main correlation from the methylene groups in the PEO chains. And the ${}^1\text{H}$ chemical shift also aligns with what is observed from the ${}^1\text{H}$ - ${}^6\text{Li}$ HETCOR spectrum (**Fig. 6.3e**). While the Li-containing interfacial products can be assumed to be similar regardless of the presence of LiI, the ${}^1\text{H}$ environments are different as evidenced from the additional ${}^1\text{H}$ environment detected for HSE (13:1) in the HETCOR spectra. Therefore, various ${}^7\text{Li}$ CP MAS experiments at different contact times were performed to differentiate the ${}^1\text{H}$ dynamics (**Fig. S6.15**). Fits of the buildup of the interfacial products indicate a significantly faster cross-relaxation time for HSE-LiI compared to HSE (13:1) as shown in **Fig. 6.3c**, which implies a more mobile interfacial Li environment in this sample. This disparity also leads to differences in proton $T_{1\rho}$ ($T_{1\rho H}$) values, as shown in **Table S6.2** (see fitting details in **Supplementary Text S4.4**).

In summary, the introduction of LiI in the PEO-LiTFSI- $\text{Li}_6\text{PS}_5\text{Cl}$ HSE system induces a downfield shift in the ${}^7\text{Li}$ ssNMR spectra for both the LiTFSI-PEO and $\text{Li}_6\text{PS}_5\text{Cl}$ resonances, implying that the Γ interacts with both the PEO-LiTFSI and $\text{Li}_6\text{PS}_5\text{Cl}$ phases. Dynamics

derived from the PFG-NMR measurements reveal improved Li-ion diffusion in the $\text{Li}_6\text{PS}_5\text{Cl}$ phase, suggesting improved interfacial properties between the PEO-LiTFSI and $\text{Li}_6\text{PS}_5\text{Cl}$ phases, thus facilitating Li-ion diffusion. The 1D $^{6/7}\text{Li}$ CP MAS spectra indicate that the Li-ion transport over the organic/inorganic interface is facilitated by “cleaner” interfaces with faster local kinetics. Additionally, the 2D ^1H - ^6Li and ^1H - ^{13}C HETCOR spectra suggest that the structural stability is improved by suppressing side reactions between PEO and $\text{Li}_6\text{PS}_5\text{Cl}$. This indicates that LiI extends its impact on the PEO-LiTFSI- $\text{Li}_6\text{PS}_5\text{Cl}$ HSE system from bulk to interfaces: improving PEO chain mobility, mechanical stability, and Li salt dissociation in the bulk, while also stabilizing the interfaces between the organic and inorganic phases, thereby facilitating the Li-ion conduction along the interface, organic and inorganic phases (**Fig. 6.3f**).

6.2.3 Evaluation of ionic conductivity and electrochemical performance of the HSEs

Based on the aforementioned findings, it is evident that LiI positively activates the inert interface between the PEO-LiTFSI and $\text{Li}_6\text{PS}_5\text{Cl}$ phases in the HSE. To complete the picture, electrochemical characterization of the HSE-LiI, HSE (13:1), and HSE (18:1) were performed. EIS results demonstrate that the addition of LiI in the HSE effectively improves the ionic conductivity compared to the HSEs with or without an increase in salt concentration (**Fig. 6.4a**). The ionic conductivity of HSE (13:1) shows improvement only in the low-temperature range compared to HSE (18:1), which can be expected as the Li-ion transport is governed by the segmental motions of the PEO chains in these two samples. Increasing the salt concentration to a certain extent can reduce the crystallinity of the PEO phase^{39,56}. However, at higher temperatures, almost all the PEO chains become mobile, resulting in no discernible differences in the Li-ion conducting ability in the polymer phase. In both HSEs, temperature-dependent conductivities reveal two processes with distinct slopes (**Fig. 6.4a**). In the HSE-LiI, the critical temperature for these processes is lower than that in the other two HSEs, indicating a more amorphous structure in this sample. This is consistent with the differential scanning calorimetry (DSC) measurements, where HSE-LiI exhibits lower glass transition temperature (T_g) and melting temperature (T_m), as well as reduced crystallinity (**Fig.**

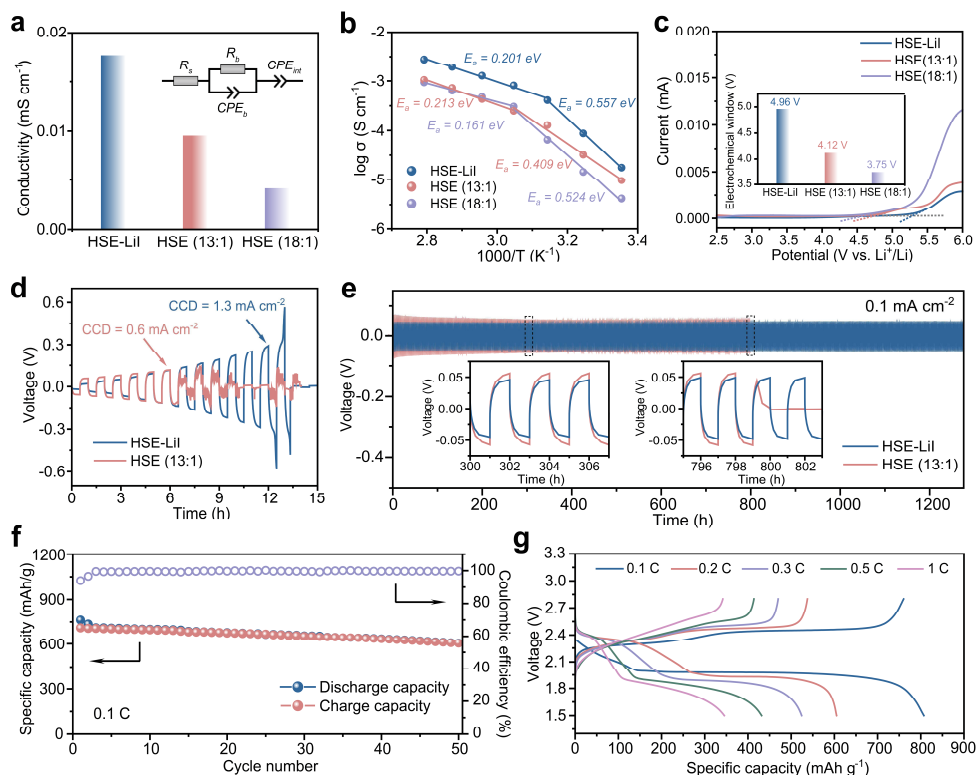


Fig. 6.4. Macroscopic Li-ion diffusion and electrochemical characterizations of the HSEs. (a) Ionic conductivity obtained from the fits in (Fig. S6.16) of the cells using different HSEs measured at 25 °C by EIS. (b) Arrhenius plots of the HSEs with fitted activation energies corresponding to different processes. (c) LSV measurements of the Li|HSE|SS (SS: stainless steel) cells using different HSEs. (d) CCD measurements for the HSE-LiI and HSE (13:1) with a stripping/plating period of 30 minutes. (e) Galvanostatic voltage profiles of the Li|HSE|Li symmetric cells measured at 0.1 mA cm⁻² and 40 °C (0.1 mAh cm⁻², with inserts showing the voltage profiles at ~303 h and ~800 h). (f) Cycling performance and CE of the all-solid-state Li|HSE-LiI|S@CNTs cells at 0.1 C and 60 °C. (g) Galvanostatic charge/discharge profiles of the all-solid-state Li|HSE-LiI|S@CNTs cells at various C-rates and 60 °C.

S6.17 and Table S6.3)⁴⁶. Also, from the Fourier transform infrared spectroscopy (FT-IR) spectra, the peaks corresponding to CH₂ stretching (ν) and wagging (ω) vibrations show a decrease in intensity for the HSE-LiI (Fig. S6.18), indicating the crystallinity of the polymer matrix reduces due to the interactions between HSE and LiI^{34,57,58}. In addition, the peak ~1620 cm⁻¹ indicates the formation of C=C peak for the HSE without LiI additive. This is indicative of the degradation of PEO, via deprotonation through series of fragment reactions^{53,59}. The E_a of the HSE-LiI is not notably lower than that of the HSEs without LiI, particularly in the low temperature range (Fig. 6.4b). This is attributed to the activated interfacial Li-ion

conduction after adding LiI in the HSE system, which introduces three processes in the calculation of the energy barrier: Li-ion diffusion in the LiTFSI-PEO phase, at the interfaces, and in the $\text{Li}_6\text{PS}_5\text{Cl}$ phase. In contrast, the other two samples lack the latter two diffusion pathways, resulting in a relatively lower E_a especially in the low-temperature region. The electrochemical stability window of the HSEs was determined by linear-sweep voltammetry (LSV) measurements (**Fig. 6.4c**), where the HSE-LiI exhibits the highest stability window up to 4.96 V, and the HSEs without LiI show much narrower stability window of 4.12 V [HSEs (13:1)], and 3.75 V [HSE (18:1)], respectively. The narrow window in the PEO-LiTFSI- $\text{Li}_6\text{PS}_5\text{Cl}$ HSE system is attributed to the unstable interfaces between PEO-LiTFSI and $\text{Li}_6\text{PS}_5\text{Cl}$, which intensify the decomposition of the $\text{Li}_6\text{PS}_5\text{Cl}$ particles and the degradation of the PEO chains, consequently resulting in incomplete Li-ion transport channels^{28,48,53}. The widened window of the HSE-LiI therefore also indicates that the addition of LiI is beneficial for suppressing the side reactions between the PEO-LiTFSI and the $\text{Li}_6\text{PS}_5\text{Cl}$ particles.

The impact of LiI on the interfacial stability between the HSEs and Li-metal anodes are conducted in Li|HSE|Li symmetrical cells. During long-term cycling (0.1 mA cm⁻² and 40 °C, **Fig. 6.4e**), the cell cycled with HSE (13:1) consistently shows a higher overpotential than HSE-LiI, especially at the beginning of the cycling (from ~87 to ~58 mV), which is ascribed to insufficient Li-ion conductivity and severe side reactions. In contrast, the cell using HSE-LiI maintained a stable overpotential at ~48 mV and remained stable for over 1200 h, while the cell with HSE (13:1) failed at ~800 h (**Fig. 6.4e**). Additionally, the cell using HSE-LiI presents a critical current density (CCD) of 1.3 mA cm⁻², which is much higher than that for HSE (13:1) (0.6 mA cm⁻², **Fig. 6.4d**), suggesting that the interfacial stability towards Li-metal and the ability to suppress Li dendrites can be effectively improved by the presence of LiI. To further assess the interfacial compatibility of the HSE-LiI with the cathode, and considering the high theoretical capacity (1675 mAh g⁻¹) and abundance of sulfur cathode⁶⁰, ASSLMs were assembled with a cathode composite of sulfur with carbon nanotubes (S@CNTs) and a Li-metal anode using the HSE-LiI electrolyte. The cell delivers a discharge capacity of ~610 mAh g⁻¹ after 50 cycles at 0.1 C and 60 °C, with an average Coulombic efficiency (CE) of ~99.6% after first two cycles (**Fig. 6.4f**). The rate capability depicted in **Fig. 6.4g** shows that the Li|HSE-LiI|S@CNTs cell exhibits the discharge capacities of 807,

605, 523, 429, and 345 mAh g⁻¹ at 0.1 C, 0.2 C, 0.3 C, 0.5 C, and 1 C, respectively. This indicates that the HSE-LiI shows promise in enabling ASSLMBs due to the stable electrolyte/electrode interfaces.

6.2.4 Interfacial stability of HSE-LiI with Li-metal

To understand the origin of the improved interfacial stability of the HSEs towards Li-metal, both the pristine HSEs and the SEI formed on the Li anode disk after cycling (20 cycles at 0.1 mA cm⁻²) were investigated by depth-profiling XPS in conjunction with TOF-SIMS. **Fig. 6.5a-d** shows the depth-dependent evolution of the C 1s and F 1s XPS spectra for the HSE-LiI and HSE (13:1). In the C 1s spectra, similar to the pristine HSEs shown in **Fig. S6.6**, the C-C/C-H peak arises from the ether groups of the PEO residues, while the small C-O and C=O peaks originate from the decomposition products of PEO^{44,45}. The PEO residues and the decomposition products of PEO form the amorphous outer layer of the SEI and continue deeper into the HSE (13:1) sample. It is worth noting that in the HSE (13:1), part of the decomposed species (C=O) are distributed in the inner layer of the SEI, implying the formation of an organic-rich SEI layer between Li and the HSE (13:1).

In the F 1s spectra (**Fig. 6.5c, d**), two peaks centred at ~684.5 eV (LiF from the decomposition of LiTFSI) and ~688.08 eV (-CF₃ group from the residual LiTFSI) were observed for both samples^{48,61}. Apparently a more LiF-rich SEI was formed on the Li disk cycled with HSE-LiI, with LiF distributed across both the outer and inner layers. Furthermore, upon tracking the relative spectral contribution of the O 1s species with etching (**Fig. S6.19**), a dominant distribution of the Li₂O component inside, accompanied by a small amount of organic ROCO₂Li and C-O-C species on the surface, were observed in the SEI formed with HSE-LiI^{44,62}. In the S 2p spectra (**Fig. S6.20a, b**), the doublet at ~160 eV is attributed to the S²⁻ ions within Li₆PS₅Cl^{48,63}. Besides, smaller doublets of -SO₂CF₃ (at ~168.8 eV, S 2p_{3/2}) and -SO₂CF₂⁺/Li_xS_yO_z (at ~167.5 eV, S 2p_{3/2}) associated with the LiTFSI decomposition were observed^{44,46}. Apparently, there is more “free” S²⁻ and decomposed residual Li salt remaining on the surface of the SEI formed with HSE (13:1). A weaker LiTFSI signal (at ~398.6 eV) was detected in the SEI formed with HSE (13:1), as indicated by the N 1s spectra (**Fig. S6.20c, d**)³⁴. This is in agreement with the rougher surface morphology of the HSE (13:1) electrolyte, as depicted in **Fig. S6.8**, suggesting a lower amount of polymer phase distributed over the surface. A doublet at ~618.6 eV and ~630.1 eV were observed in the I 3d spectra, confirming

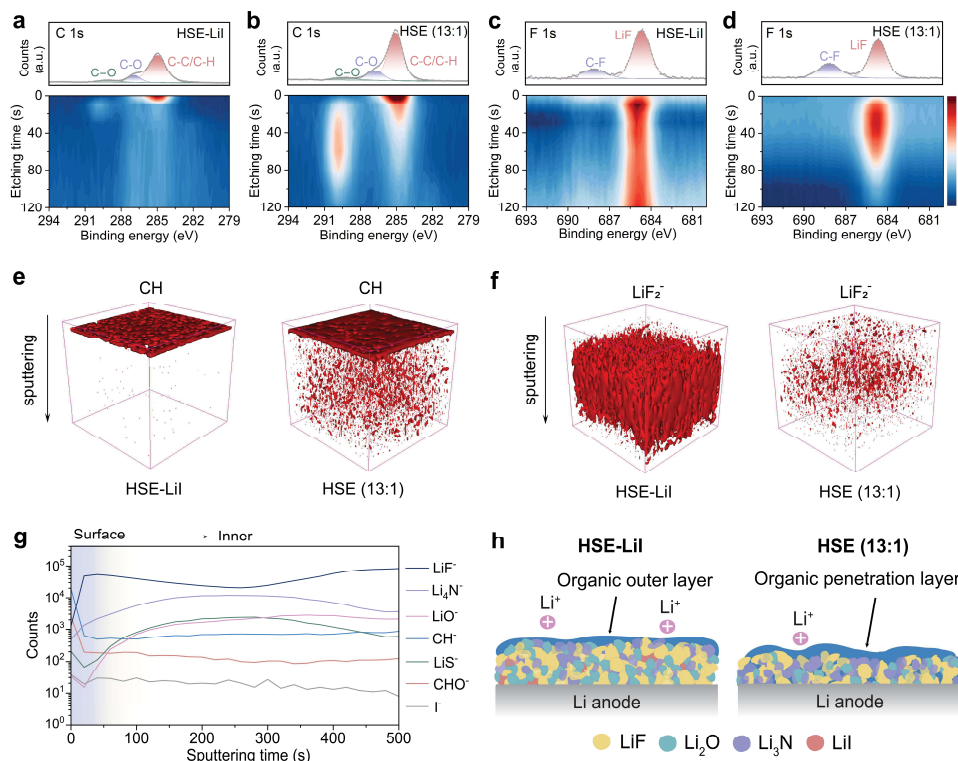


Fig. 6.5. Assessing the interfacial properties of the HSEs with Li-metal anode. Depth-profiling XPS measurements of C 1s and F 1s for the Li-metal anode cycled with (a and c) HSE-LiI, (b and d) HSE (13:1). Each plot comprises of two individual figures, i.e., the point before etching (up) and depth profiling spectrum (down). The color bar indicates the intensity from weak to strong from bottom to top. 3D reconstruction of TOF-SIMS secondary-ion fragments sputtered from the Li-metal anode cycled with HSE-LiI and HSE (13:1) electrolytes, respectively. The sputtered area is $100 \times 100 \mu\text{m}^2$. The species containing (e) CH and (f) LiF_2^- signals were selected, which are the main compounds of the investigated SEI layer. (g) TOF-SIMS depth profiles of representative components of the SEI formed at the Li/HSE-LiI interface. (h) Schematic showing the main components in the SEI formed at the Li/HSE-LiI and the Li/HSE (13:1) interfaces. For both the depth-profiling XPS and TOF-SIMS measurements, the Li-metal electrodes were obtained by disassembling the Li|HSE|Li symmetrical cells cycled with HSE-LiI or HSE (13:1) electrolytes at 0.1 mA cm^{-1} for 20 cycles (0.1 mAh cm^{-1} , $40 \text{ }^\circ\text{C}$).

the formation of LiI compound in the Li/HSE-LiI interface (Fig. S6.21)^{35,64}.

TOF-SIMS top-down depth profiles and their corresponding 3D reconstruction for the species of interest were conducted to further detail the SEI composition and microstructure (Fig. 6.5e, f). It is evident that CH mainly disperses on the top of the SEI, while a large amount of LiF is concentrated in the interior part, with some iodide ions (I^-) being

homogeneously distributed within the SEI formed after cycling with HSE-LiI (**Fig. S6.22**). In contrast, for the SEI obtained by cycling with HSE (13:1), more concentrated CH with less LiF is distributed in the inner layer. The depth profiles of the main chemical compounds of the investigated SEI cycled with HSE-LiI are depicted in **Fig. 6.5g**. As the sputtering time increases, the evolution of these fragments initially exhibits a signal attenuation but stabilizes as the sputtering progresses. Inorganic species such as LiF, Li₃N, and Li₂O dominate in the SEI, which is in stark contrast with the SEI formed in Li/HSE (13:1) (**Fig. S6.23**). These observations are consistent with the XPS results, where a more inorganic-rich SEI was also detected for HSE-LiI. A schematic interpretation is provided in **Fig. 6.5h**, which illustrates the SEI structures formed for the HSE-LiI and HSE (13:1), respectively, as determined by depth-profiling XPS and TOF-SIMS. This inorganic-rich SEI layer is considered pivotal in improving the interfacial stability of the Li/HSEs, which plays a prominent role in inhibiting dendrite propagation and accelerating Li-ion conduction across the Li/SEI/HSE interfaces.

6.2.5 Impact of local and bulk structures in HSEs

Both the interface between the two conducting solid electrolyte phases within the HSE, as well as the interface with the Li-metal anode play a critical role in the battery performance. Here we introduce LiI to improve both aspects in the PEO-LiTFSI-Li₆PS₅Cl hybrid system, and study in detail the structure-property relationship. The influence of LiI on the HSE manifests in two aspects: Li-ion diffusivity and the stability of the Li/HSE interface. The improvement of Li-ion diffusion on adding LiI is seen via the higher ionic conductivity obtained from the EIS measurements on the macroscopic scale (**Fig. 6.4a, b**). This result is supported by the intensified equilibrium Li-ion exchange between the organic phase (PEO-LiTFSI) and the inorganic phase (Li₆PS₅Cl), a phenomenon visualized and quantified by 2D ⁶Li-⁶Li EXSY NMR (**Fig. 6.1**). It is worth noting that the E_a derived from the 2D-EXSY experiments (0.174 eV, **Fig. 6.1d**) is lower than that obtained from the EIS measurements (0.201 eV and 0.557 eV, **Fig. 6.4b**). This disparity arises because the 2D-EXSY measurement detects local Li-ion diffusion across the organic/inorganic interfaces, whereas the EIS measurement primarily assesses bulk Li-ion conduction. Furthermore, the ¹H dynamics have been differentiated by ⁷Li CP MAS experiments with various contact times, from which the faster cross-relaxation time for HSE-LiI compared to HSE (13:1) suggests a more mobile interfacial Li environment between PEO-LiTFSI and Li₆PS₅Cl in the presence of LiI (**Fig.**

6.3c and **Fig. S6.15**). This is further supported by the improved local ^1H dynamics in the HSE-LiI sample, as evidenced through ^{13}C CP MAS measurements at varying contact times (**Fig. 6.2f**). Nonetheless, the individual ^7Li mobility detected by PFG-NMR indicates that the Li-ion self-diffusion over the polymer matrix remains similar, regardless of the presence of LiI, though appears to differ for the inorganic phase or at the inorganic/organic interfaces (**Fig. 6.3a**). Another pertinent aspect is the stabilized Li/HSE-LiI interface. This is seen via the widened stability window (4.96 V), higher CCD (1.3 mA cm^{-2}), and more stable long-term cycling in the Li|HSE-LiI|Li symmetric cells. This renders the HSE applicable to the Li-S battery system (**Fig. 6.4c-g**).

Combining the above results, it becomes clear that the addition of LiI facilitates both the Li salt dissociation in the bulk HSE and interfacial Li-ion diffusion across the organic/inorganic interfaces. This illustrates that the effect of LiI extends from the bulk to the inner interfaces, impacting both structure and ion-dynamics. Additionally, the interactions between the HSE and LiI also improve its stability towards the Li-metal anode. XPS and TOF-SIMS suggest more PEO phase coverage on the surface of HSE-LiI, also seen from its smoother surface morphology in SEM (**Fig. S6.6-6.9**). This explains the more stable Li/HSE-LiI interface, as typically a PEO-based SPE is more compatible with the Li-metal anode than $\text{Li}_6\text{PS}_5\text{Cl}^{11}$. The single-pulse ^{67}Li ssNMR spectra indicate that LiI has fully dissociated in the HSE. The change in the chemical shift of the ^7Li peak suggests that the occurrence of more mobile Li-ions, as evidenced in the Raman spectra, leads to an increase in the amount of Li-ions coordinated to the PEO chains^{35,40,41} (**Fig. 6.2a-c**). Besides, the downfield shift of the ^1H peaks and the appearance of the additional ^{13}C peak indicate an interaction between the F anions and the PEO chains^{34,35} (**Fig. S6.5** and **Fig. 6.2e**). The local interfacial structure, as detected by ^6Li CP MAS and ^1H - ^6Li HETCOR experiments, suggests suppressed side reactions between PEO and $\text{Li}_6\text{PS}_5\text{Cl}$ phases due to the addition of LiI, which has been further supported by 2D ^1H - ^{13}C HETCOR spectra (**Fig. 6.3b-e** and **Fig. S6.14**). Discriminating between the local amorphous and crystalline phases based on their respective contact time dependence in the ^{13}C CP MAS experiments, higher local ^1H dynamics is observed in HSE-LiI based on the accelerated decay of its crystalline phase (**Fig. 6.2f**), implying improved chain mobility.

The depth-profiling XPS and TOF-SIMS data suggest that the addition of LiI changes

the decomposition subsequence of LiTFSI, tuning the growth dynamics of the SEI and leading to the formation of an inorganic-rich SEI layer abundant in LiF, Li₂O, and Li₃N, coupled with an organic outer layer (**Fig. 6.5h**). This SEI structure, rich in inorganic species, is well-known to be beneficial for effective Li-ion transport and uniform Li-metal deposition. LiF is electronically insulating and can prevent excessive electrolyte oxidation, while Li₂O promotes the formation of an anion-derived SEI by facilitating electron transfer^{65–68}. Additionally, thermodynamically favoured Li-Li₃N interactions guide uniform Li deposition^{69,70}.

It is evident that the local and bulk structures jointly determine the properties of the HSEs. An effective percolation network of ionic conduction within the HSEs requires active interfacial Li-ion diffusion as well as a favourable bulk structure. The structure-property relationship of HSEs, investigated by incorporating LiI into the PEO-LiTFSI-Li₆PS₅Cl hybrid system, suggests that fine-tuning the bulk properties synergistically stabilizes the interfaces within the polymer-salt-filler system, an aspect that was previously poorly understood. The influence of the LiI additive is also reflected in the improved stability of the Li/HSEs interface, further highlighting the importance of regulating and stabilizing interfaces to enable ASSLMBs. Reflecting on the structure-property-performance relationship, the present work provides insights into rational regulation of various aspects of the HSE structure, from bulk to interface, with potential applicability to other electrolyte systems.

6.3 Conclusions

In summary, this work investigates the structure-property relationship of HSEs through the introduction of an LiI additive into the PEO-LiTFSI-Li₆PS₅Cl HSE system. The interaction between the HSE and LiI improves the Li salt dissociation in the bulk PEO matrix, while also stabilizing the organic/inorganic interfaces, thus activating interfacial Li-ion diffusion. The bulk and interface structures revealed by multidimensional NMR experiments suggest that the addition of LiI mitigates the degradation of the PEO phase and its reactions with Li₆PS₅Cl, leading to a more Li-ion conductive interface environment and thereby improving the overall ionic conductivity. Besides, given by the altered decomposition sequence of LiTFSI, an inorganic-rich (i.e., LiF, Li₂O, and Li₃N) SEI layer was formed at the Li/HSE-LiI interface, which facilitates the Li-ion transport and suppresses dendrite formation. The introduction of

the multifunctional LiI additive provides perspective on the rational design of the organic/inorganic interfaces in the HSE system, as well as the Li/HSE/cathode interfaces, shedding light for the practical application of high-safety and high-energy-density ASSLMBs.

6.4 Methods

Preparation of hybrid solid electrolytes

For the HSE-LiI and HSE (18:1) membranes, 384 mg PEO powder ($M_w = 600,000$ g/mol, Sigma-Aldrich), 140 mg LiTFSI (Sigma-Aldrich), and 52.4 mg $\text{Li}_6\text{PS}_5\text{Cl}$ (10 wt%, NEI Corporation) were first homogeneously mixed with and without 26.2 mg LiI (5 wt%, Sigma-Aldrich) in a mortar by grinding, then added into 10 ml acetonitrile (Sigma-Aldrich) and stirring for 24 hours. The obtained homogenized slurry was cast onto a Teflon plate and dried in the glove box at room temperature for 24 hours, and further dried under vacuum for 48 hours. The HSE (13:1) membranes were prepared using the same procedures with 347 mg of PEO powder, 177 mg of LiTFSI, and 52.4 mg of $\text{Li}_6\text{PS}_5\text{Cl}$ (10 wt%, NEI Corporation). The $\text{Li}_6\text{PS}_5\text{Cl@LiI}$ mixture was prepared by mixing 52.4 mg $\text{Li}_6\text{PS}_5\text{Cl}$ and 26.2 mg LiI in 10 mL acetonitrile at room temperature for 24 hours, then dried in the glove box for 24 hours, and further dried under vacuum for 48 hours.

Material characterizations

Raman spectra were acquired using a miniature laser confocal Raman spectrometer (Renishaw inVia Qontor) with a 785 nm laser at room temperature. For SEM imaging, the samples were transferred into an SEM (JEOL JSM-6010LA) machine under dry Argon (Ar) conditions by an air-tight Ar-filled sample holder. The images were taken using an accelerating voltage of 10 kV (secondary electron). Bragg-Brentano XRD measurements were conducted on an X'Pert Pro X-ray diffractometer (PANalytical) with Cu $K\alpha$ radiation ($\lambda_1 = 1.540598$ Å and $\lambda_2 = 1.544426$ Å, at 45 kV and 40 mA) using an in-house air-tight sample holder. DSC measurements were carried out at $10^\circ \text{ min}^{-1}$ steps using a commercial TA-Q2000 DSC calorimeter (TA instruments). FT-IR spectra were collected on Bruker VERTEX 70 spectrometer in an attenuated total reflection (ATR) mode. XPS measurements were performed with a Thermo Fisher K-Alpha spectrometer to investigate the chemical compositions of both the pristine HSEs and the cycled Li electrodes. The samples were

transferred into the XPS machine under vacuum using an air-tight sample holder. The spectrometer is equipped with a focused monochromatic Al $K\alpha$ source (1486.6 eV) anode operating at 36 W (12 kV, 3 mA), a flood gun operating at 1 V, 10 μ A. The base pressure of the analysis chamber was approximately 2×10^{-9} mbar and the spot size was approximately $800 \times 400 \mu\text{m}^2$. For the detailed scan collected before etching, a pass energy of 50 eV was used. Depth profiling was performed with an Ar^+ ion gun operated at 3 kV, corresponding to about 0.5 nm s^{-1} as calibrated on Ta_2O_5 and a pass energy of 200 eV was used. In the analysis, the binding energy was corrected for the charge shift relative to the primary C 1s hydrocarbon peak at $BE = 284.8 \text{ eV}$. For each sample, at least 3 points were measured which showed similar results. The data were fitted using 70% Gaussian and 30% Lorentzian line shapes (weighted least-squares fitting method) and nonlinear Shirley-type background using the Thermo Fisher Avantage software. TOF-SIMS measurements were carried out on a Nano TOF-2 instrument (ULVAC- PHI, Japan) equipped with a Bi^{3++} beam (30 kV, 2 nA) cluster primary-ion gun for analysis, and an Ar^+ beam (3 keV, 100 nA) using a sputtering rate of 0.1 nm s^{-1} to obtain the desired depth profile. The area of analysis was $100 \times 100 \mu\text{m}^2$, whereas the sputtering area was $400 \times 400 \mu\text{m}^2$. For depth-profiling XPS and TOF-SIMS measurements of Li-metal anode, the Li-metal electrodes were obtained by disassembling the Li|HSE|Li symmetrical cells cycled with HSE-LiI or HSE (13:1) electrolytes at 0.1 mA cm^{-1} for 20 cycles (0.1 mAh cm^{-1} , $40 \text{ }^\circ\text{C}$).

Batteries assembly and electrochemical measurements

The ionic conductivity of the HSEs was calculated based on EIS data obtained using an electrochemical station (Autolab PGSTAT302N). The measurements were conducted from 10 MHz to 1 kHz with a sinusoidal signal ($V_{rms} = 10 \text{ mV}$). The HSEs were sandwiched between two stainless steels (SS) in coin cells (with surface area of 1.13 cm^2), and each test temperature was maintained for more than 30 minutes to ensure thermal equilibrium. The EIS data was fitted using an Equivalent Circuit (EC) model that included R_S as the series resistance, R_b as the bulk HSE resistance, and CPE_b as a Constant Phase Element (CPE) representing the bulk capacitance of the HSE membranes. Additionally, CPE_{int} was introduced to account for the capacitance associated with the blocking electrodes at low frequencies. Subsequently, the bulk resistance (R_b) and ionic conductivity (σ) were determined using the formula $\sigma = d/(R_b \times A)$, with d representing the thickness and A denoting

the area of the HSEs in contact with the SS.

LSV curves were measured at a scan rate of 0.1 mV s^{-1} using an Autolab PGSTAT302N with Li|HSE|SS cells. The galvanostatic charge/discharge tests of the Li||Li symmetrical cell were performed on a Maccor 4000 battery cycler at $40 \text{ }^\circ\text{C}$. The S@CNTs cathode mixture was made by first grinding sulfur powder and CNTs in a mortar with a mass ratio of 2:8, then transferring the mixture to a quartz ampule and heated to $155 \text{ }^\circ\text{C}$ for 6 hours in an Ar atmosphere. The cathode slurry was prepared by mixing S@CNTs, PEO, LiTFSI, and Super P with a mass ratio of 8 : 0.5 : 0.5 : 1 in acetonitrile. Then, the slurry was spread evenly on aluminium foil to create a cathode film with loadings of $\sim 0.6 \text{ mg cm}^{-2}$, and dried under vacuum at $60 \text{ }^\circ\text{C}$ for 48 h. The solid-state Li|HSE|S@CNTs coin cells were assembled in a glove box filled with Ar. Galvanostatic cycling was performed on a Maccor 4000 battery cycler at $60 \text{ }^\circ\text{C}$.

Solid-state NMR measurements

SsNMR measurements were performed on a Bruker Ascend 500 MHz magnet ($B_0 = 11.7 \text{ T}$) equipped with an NEO console, operating at frequencies of 194.37 MHz for ^7Li , 73.6 MHz for ^6Li , 500.130 MHz for ^1H , and 125.758 MHz for ^{13}C . The chemical shifts of $^{6,7}\text{Li}$ were referenced with respect to a 0.1 M LiCl solution (0 ppm), while the ^1H and ^{13}C chemical shifts were referenced to solid adamantane (^1H at 1.81 ppm and ^{13}C at 38.48 ppm). A Bruker three-channel MAS 4 mm direct variable temperature (DVT) probe was used for all the measurements. Individual samples were prepared by cutting the HSEs membranes into small pieces, which were then transferred into 4 mm zirconia rotors and sealed with a Vespel cap. A MAS frequency of 10 kHz was applied for all the measurements.

One-pulse ^7Li and ^6Li experiments were performed with $\pi/2$ pulse lengths of 3.3 μs and 9 μs . A recycle delay of about four times T_1 (spin-lattice relaxation time) was used for each nuclei, where the T_1 was determined using saturation recovery experiments. Variable temperature (VT) ^6Li - ^6Li 2D-EXSY measurements were performed for the HSE-LiI and HSE (13:1) samples at different mixing times. All 2D spectra consisted of 8 scans for each of the 1,950 transients, and each transient was incremented by 8.5 μs . For 1D ^7Li CP MAS experiments, a radio frequency (r.f.) field strengths of 81 kHz and various contact times were applied, the r.f. field amplitude of ^1H during CP experiments was ramped from 70 to 100%, and 128 scans were acquired for each sample with a recycle delay of 6 s. The 1D ^6Li CP MAS

experiments were performed with a contact time of up to 8 ms, the r.f. field amplitude of ^1H during CP experiments was ramped from 70 to 100%, and 10,240 scans were acquired for each sample with a recycle delay of 6 s. 2D ^1H - ^6Li HETCOR measurements were performed with a short CP contact time of 0.5 ms for HSE-LiI and HSE (13:1). For each of the 128 transients in the indirect ^1H dimension, 1,024 scans were accumulated. A recycle delay of 5 s was applied after each scan. One-pulse ^{13}C measurements were conducted with a $\pi/2$ pulse length of 6.2 μs and an recycle delay of 1 s. The 1D ^{13}C CP MAS experiments were measured with an initial ^1H $\pi/2$ pulse of 3.8 μs and various contact times. An r.f. field strength of 64 kHz was utilized and 2,048 scans were acquired for each sample with a recycle delay of 2 s. 2D ^1H - ^{13}C HETCOR measurements were measured with a contact time of 2 ms for both HSE-LiI and HSE (13:1). For each of the 128 transients in the indirect ^1H dimension, 256 ^{13}C scans were accumulated. A recycle delay of 2 s was applied after each scan. For both the CP MAS and HETCOR experiments, proton decoupling was performed during acquisition using the SPINAL-64 decoupling sequence.

PFG-NMR was used to determine the diffusion coefficients of ^7Li and ^{19}F for all the HSEs at VT (ranging from 25 to 80 °C) using a Bruker Avance NEO 600 MHz narrow bore NMR spectrometer equipped with a diffusion probe. A stimulated Echo sequence was used for all diffusion measurements. Typical diffusion time for both nuclei was 20 to 200 ms, gradient pulse duration was 2 ms. The maximum field strength was 7.05 T on a log scale. The diffusion coefficients were obtained by fitting the pulse data obtained with the Stejskal-Tanner Equation⁷¹.

6.5 Supplementary information

Supplementary Texts

Text S6.1. Cross polarization MAS ssNMR

The interface environment between the LiTFSI-PEO phase and the $\text{Li}_6\text{PS}_5\text{Cl}$ phase is observed for both HSE-LiI and HSE (13:1) in the $^1\text{H} \rightarrow ^{67}\text{Li}$ CP MAS ssNMR spectra, suggesting that this interface is in close proximity with neighboring protons. Fitting the CP curves shows that the cross-relaxation times (T_{H-Li}) and the proton $T_{1\rho}$ ($T_{1\rho H}$) are distinct

for the Li-PEO and the interface environments (**Supplementary Table S6.2**). For both HSE-LiI and HSE (13:1), the Li-containing decomposition products can be assumed to be similar but the proton environment differs because of the interactions between the LiI additive and the HSE. This will give different proton dynamics apparently on a time-scale not affecting the transfer rate but giving rise to different $T_{1\rho}$ values for both samples. In the $^1\text{H}\rightarrow^7\text{Li}$ CP MAS spectra, both HSE-LiI and HSE (13:1) show the expected narrow LiTFSI signal (**Fig. S6.15**), indicating the close proximity between PEO and LiTFSI. Fits of CP data show that the cross-relaxation time for the HSE (13:1) membrane is much slower than for HSE-LiI, in line with the higher mobility of both Li and PEO. Differences in PEO chain and Li-TFSI mobility are also reflected in different $T_{1\rho\text{H}}$ values (**Supplementary Table S6.2**).

Supplementary Figures

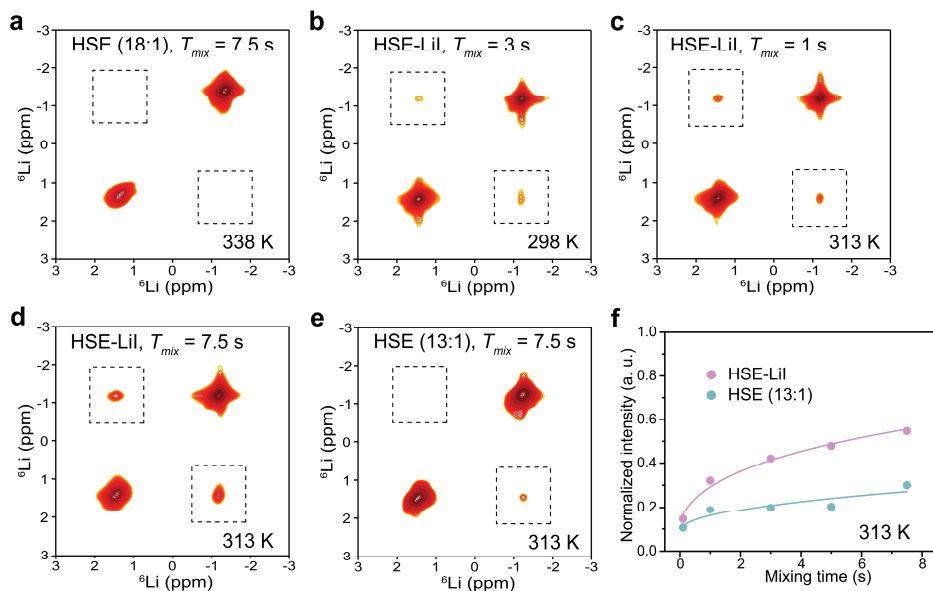


Fig. S6.1. Measurements of the Li-ion transport between the PEO-LiTFSI phase and the $\text{Li}_6\text{PS}_5\text{Cl}$ phase. 2D ${}^6\text{Li}$ - ${}^6\text{Li}$ EASY spectra measured at a spinning speed of 10 kHz for (a) HSE (18:1) with $T_{mix} = 7.5$ s at 338 K; for HSE-LiI with (b) $T_{mix} = 3$ s at 298 K, (c) $T_{mix} = 1$ s at 313 K, and (d) $T_{mix} = 7.5$ s at 313 K; and for (e) HSE (13:1) with $T_{mix} = 7.5$ s at 338 K. (f) Evolution of normalized cross-peak intensity as a function of T_{mix} at 313 K for HSE-LiI and HSE (13:1).

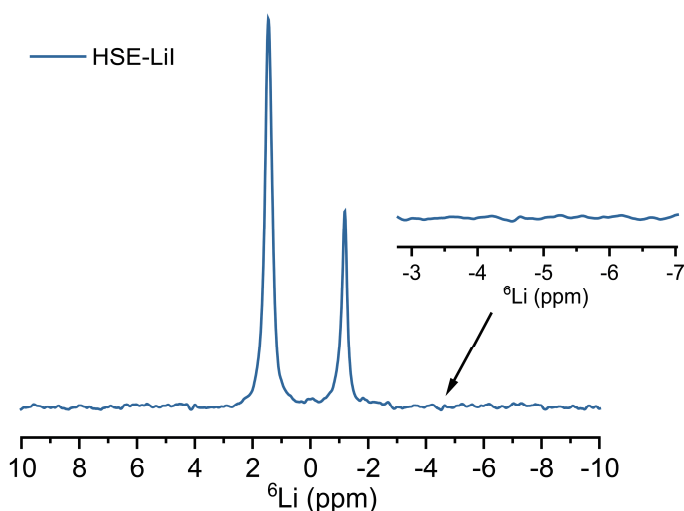


Fig. S6.2. One-pulse ${}^6\text{Li}$ MAS spectrum of HSE-LiI. No LiI signal (~ -4.56 ppm) is observed.

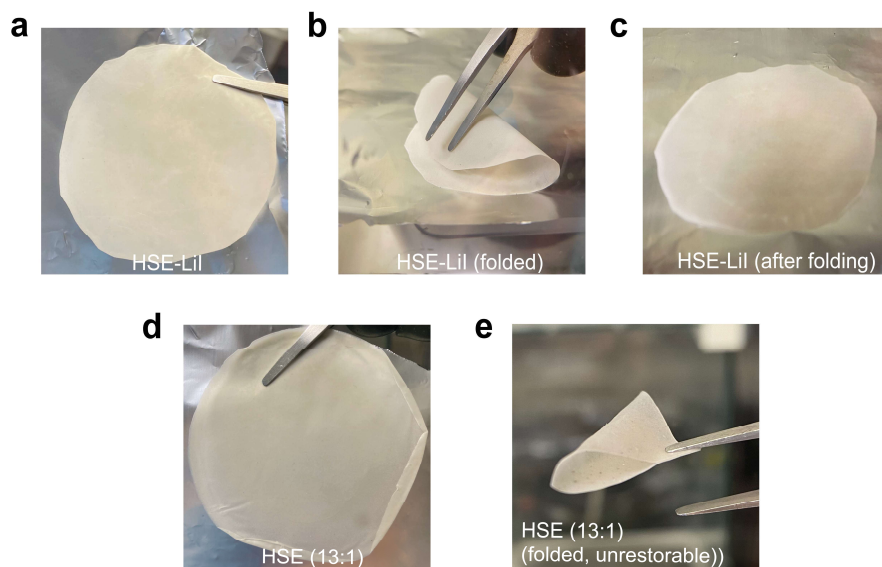


Fig. S6.3. Optical images showing the mechanical properties of HSE-LiI and HSE (13:1). (a) Before folding, (b) folded, and (c) after folding images of HSE-LiI. (d) Before folding, and (e) folded images of HSE (13:1). The folded HSE (13:1) membrane is unrestorable because of excessive adhesion and lack of mechanical operability, while the HSE-LiI is flexible and with sufficient mechanical strength.

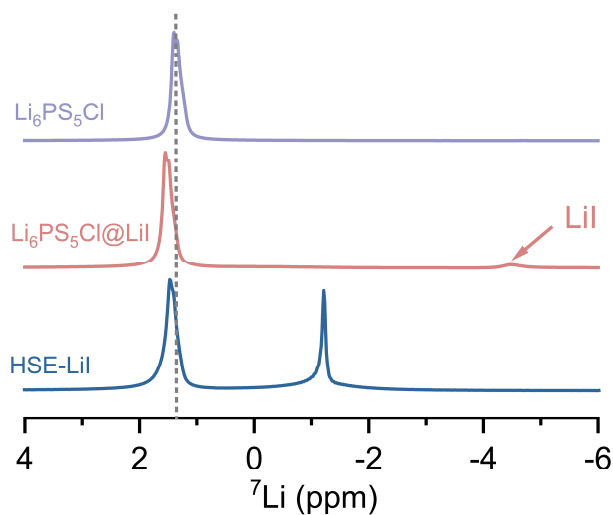


Fig. S6.4. Identifying the peak shift of $\text{Li}_6\text{PS}_5\text{Cl}$ in HSE-LiI. 1D ^7Li MAS ssNMR spectra of $\text{Li}_6\text{PS}_5\text{Cl}$, $\text{Li}_6\text{PS}_5\text{Cl}@LiI$ mixture, and HSE-LiI. (The $\text{Li}_6\text{PS}_5\text{Cl}@LiI$ mixture was prepared using the same method as the HSEs but without adding PEO-LiTFSI, see details in Section 6.4 Methods).

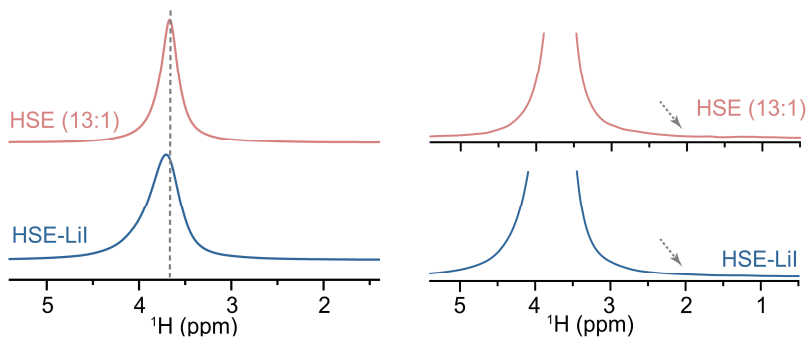


Fig. S6.5. Characterizing the bulk structure of the HSEs with and without LiI. 1D ^1H MAS ssNMR spectra of HSE-LiI and HSE (13:1) electrolytes. The spectra on the right provide a zoomed-in view of the spectra on the left to check for residual solvent. The arrows indicate the ^1H chemical shift position corresponding to acetonitrile solvent, where no signal is observed, confirming the absence of residual acetonitrile.

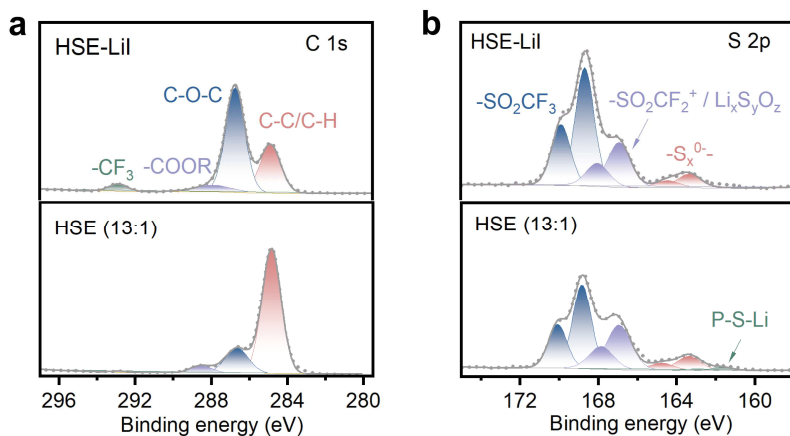


Fig. S6.6. Characterizing the surface properties of the HSEs with and without LiI. XPS measurements of (a) C 1s, and (b) S 2p for the pristine HSE-LiI and HSE (13:1).

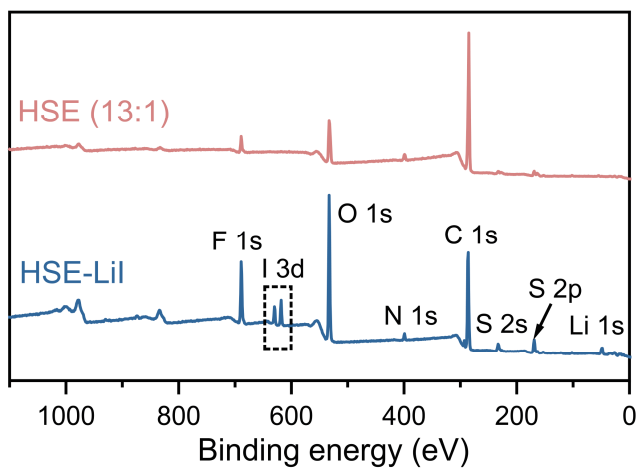


Fig. S6.7. Characterizing the surface properties of the HSEs with and without LiI. XPS survey spectra for the pristine HSE-LiI and HSE (13:1).

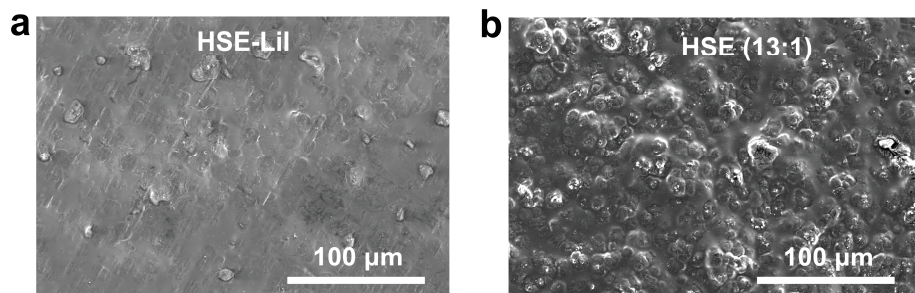


Fig. S6.8. SEM images of HSE-LiI and HSE (13:1). (a) HSE-LiI, and (b) HSE (13:1).

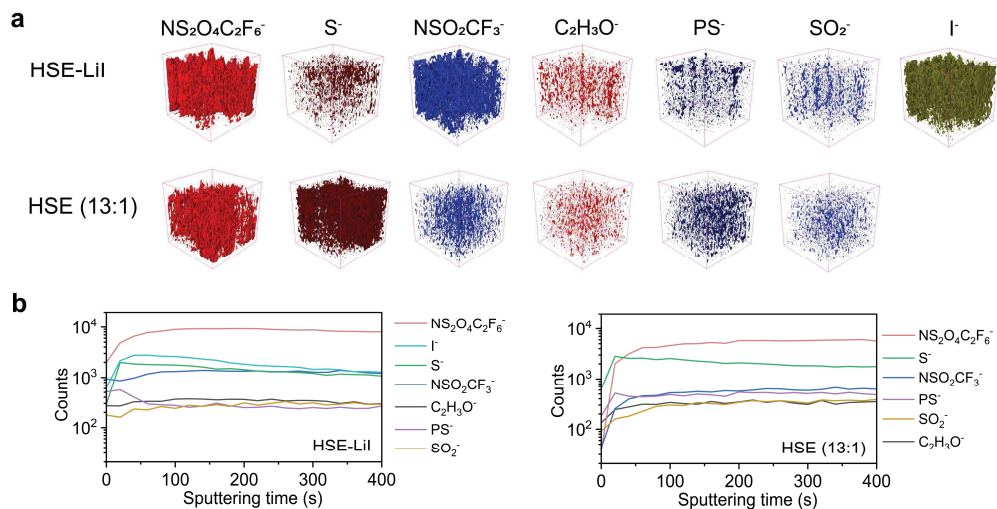


Fig. S6.9. 3D reconstruction of TOF-SIMS secondary-ion fragments sputtered from pristine HSE-LiI and HSE (13:1) electrolytes, respectively. The sputtered area is $100 \times 100 \mu\text{m}^2$. The species displayed in (a) are the main compounds of the investigated PEO-LiTFSI-Li₆PS₅Cl system. (b) TOF-SIMS depth profiles of the representative components of HSE-LiI and HSE (13:1).

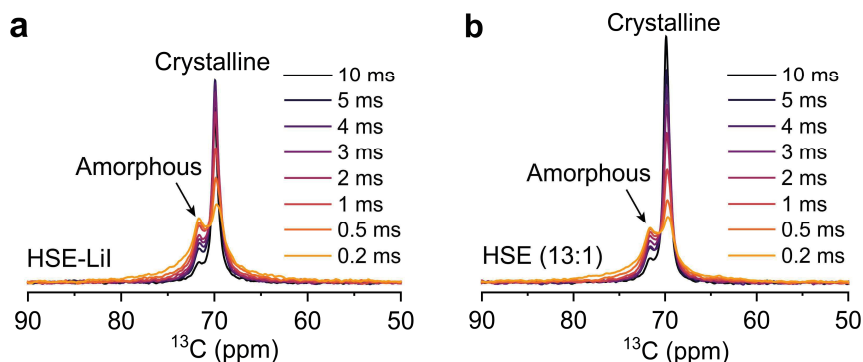


Fig. S6.10. Studying the organic phase conformation in the HSEs using 1D ^{13}C ssNMR. 1D ^{13}C CP MAS spectra of (a) HSE-LiI, and (b) HSE (13:1) with contact times ranging from 0.2 to 10 ms.

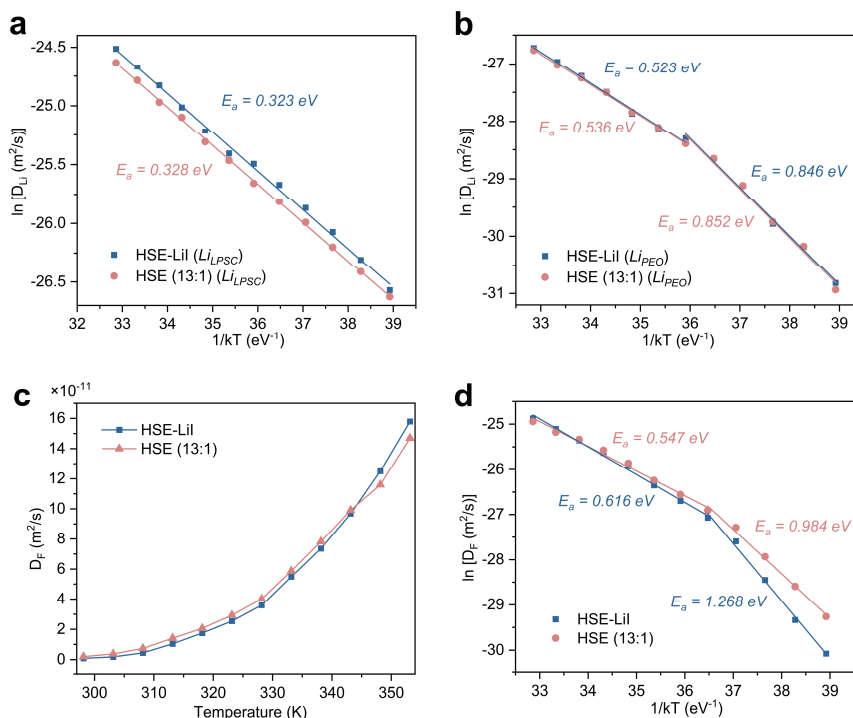


Fig. S6.11. PFG-NMR of HSE-LiI and HSE (13:1). Fits of diffusion coefficient of ${}^7\text{Li}$ (D_{Li}) in (a) $\text{Li}_6\text{PS}_5\text{Cl}$ phase (L_{LPSC}), and (b) PEO phase (L_{PEO}) using the Arrhenius equation. (c) Diffusion coefficients of ${}^{19}\text{F}$ (D_{F}) from 298 to 353 K, and (d) fits of D_{F} using the Arrhenius equation.

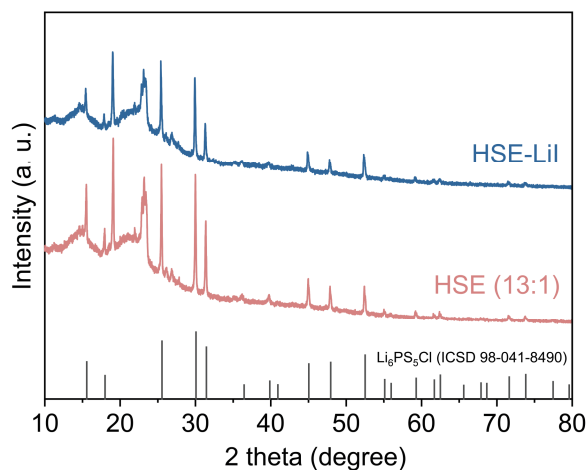


Fig. S6.12. XRD patterns of HSE-LiI and HSE (13:1).

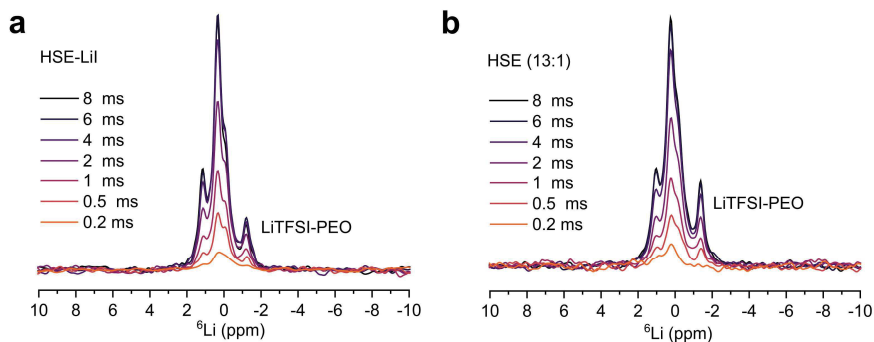


Fig. S6.13. 1D ^6Li CP MAS spectra of the studied HSEs. 1D ^6Li CP MAS ssNMR spectra of (a) HSE-LiI, and (b) HSE (13:1) with contact times ranging from 0.2 to 8 ms.

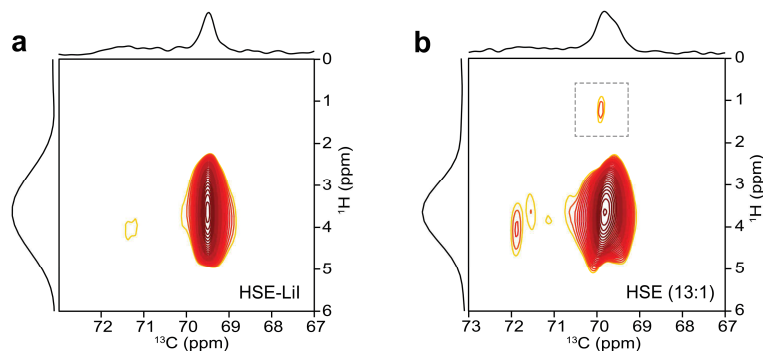


Fig. S6.14. Studying the organic phase conformation stability in the HSEs using 2D ^{13}C ssNMR. 2D ^1H - ^{13}C HETCOR spectra acquired with a CP contact time of 2 ms for (a) HSE-LiI, and (b) HSE (13:1). Additional ^1H - ^{13}C correlations show in the dotted box.

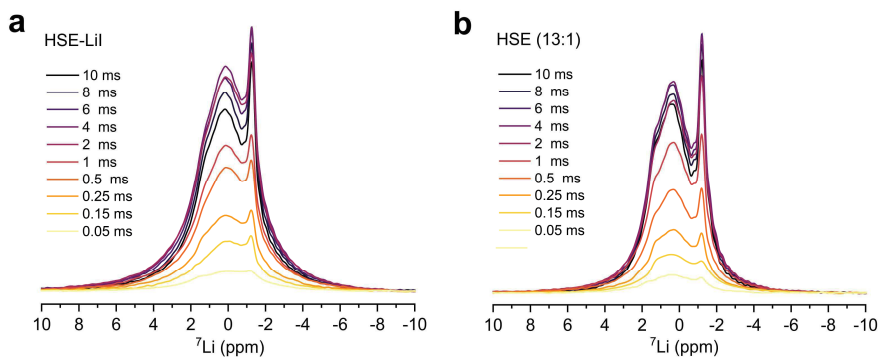


Fig. S6.15. 1D ^7Li CP MAS spectra of the studied HSEs. 1D ^7Li CP MAS ssNMR spectra of (a) HSE-LiI, and (b) HSE (13:1) with contact times ranging from 0.05 to 10 ms.

6

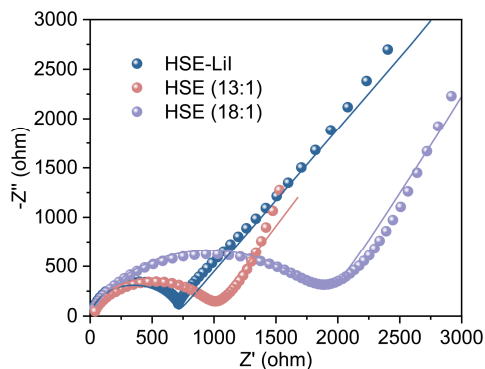


Fig. S6.16. EIS spectra with representative fits. The SS|HSE|SS cells were measured at 25 °C with different HSEs.

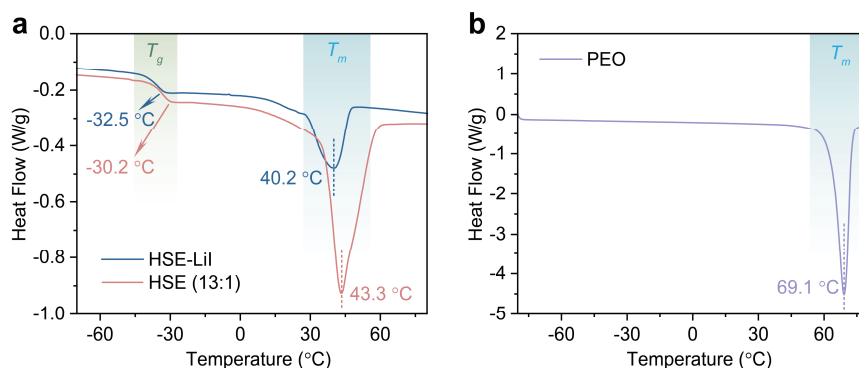


Fig. S6.17. DSC measurements showing the heat flow of HSE-LiI and HSE (13:1). DSC curves of (a) HSE-LiI, HSE (13:1), and (b) pristine PEO under heating. Glass transition temperature (T_g) and melting points (T_m) are highlighted, see details in Supplementary Table S6.3.

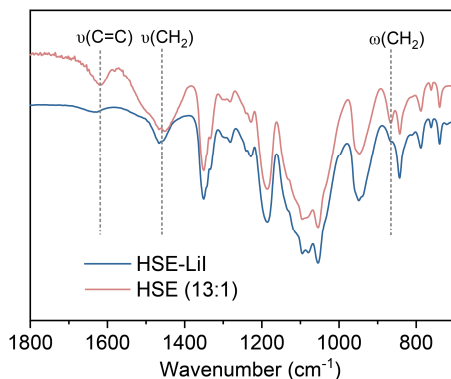


Fig. S6.18. FT-IR spectra of HSE-LiI and HSE (13:1). FT-IR spectra of HSE-LiI and HSE (13:1) showing the impact of LiI on the chemical structure of the HSE.

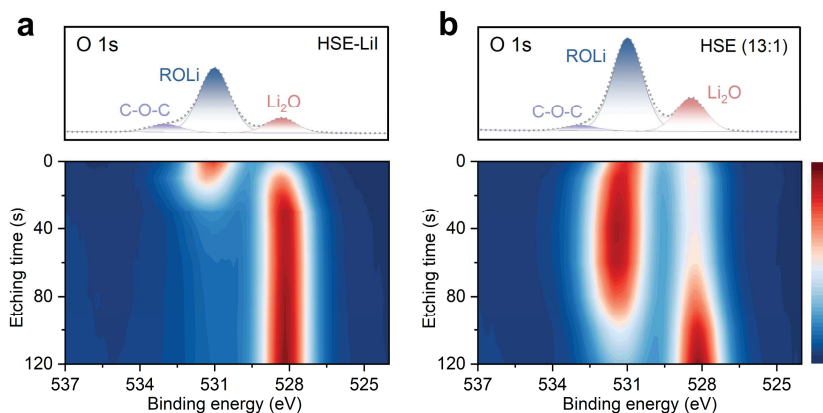


Fig. S6.19. Depth-profiling XPS measurements of O 1s for the Li-metal anode cycled with HSE-LiI and HSE (13:1). Each plot comprises of two individual figures, i.e., the point before etching (up) and depth profiling spectrum (down). The color bar indicates the intensity from weak to strong from bottom to top.

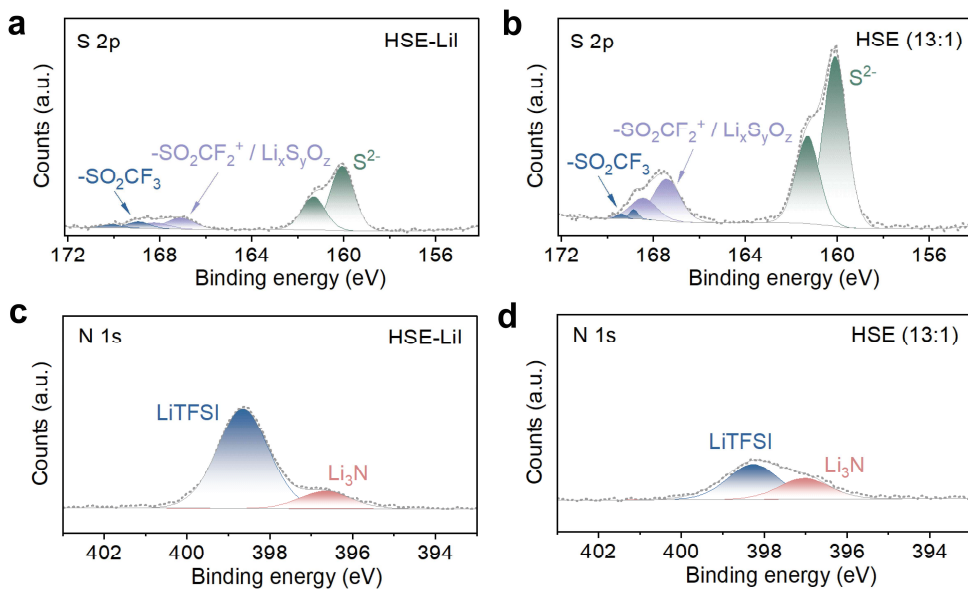


Fig. S6.20. XPS spectra of S 2p and N 1s for the Li-metal anode cycled with HSE-LiI and HSE (13:1). S 2p XPS spectra for the Li-metal anode cycled with (a) HSE-LiI, and (b) HSE (13:1). N 1s XPS spectra for the Li-metal anode cycled with (c) HSE-LiI, and (d) HSE (13:1).

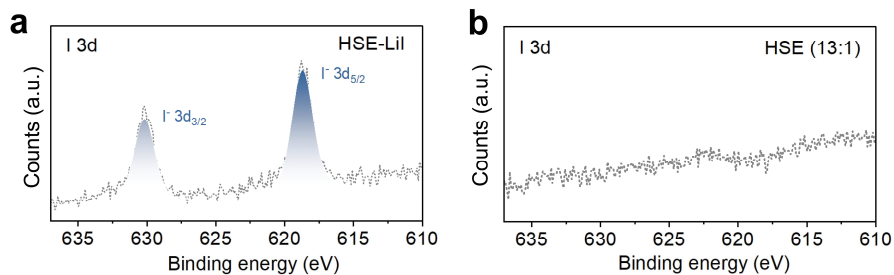


Fig. S6.21. XPS spectra of I 3d for the Li-metal anode cycled with HSE-LiI and HSE (13:1). I 3d XPS spectra for the Li-metal anode cycled with (a) HSE-LiI, and (b) HSE (13:1).

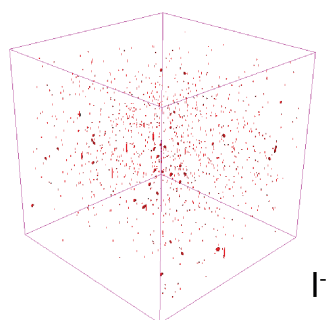


Fig. S6.22. 3D reconstruction of TOF-SIMS secondary-ion fragments sputtered from the Li-metal anode cycled with HSE-LiI. The sputtered area is $100 \times 100 \mu\text{m}^2$. The species containing I⁻ signals were selected.

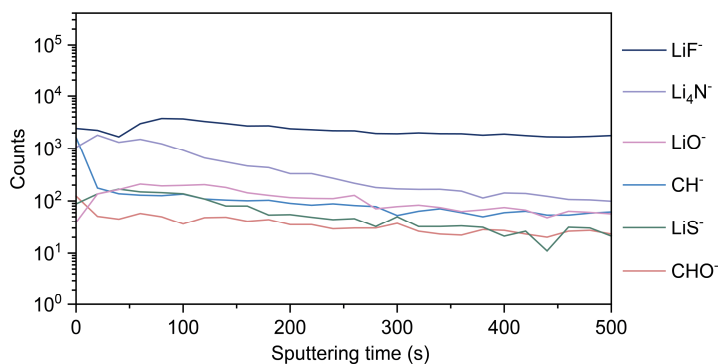


Fig. S6.23. TOF-SIMS depth profiles of representative components of the SEI formed at the Li/HSE (13:1) interface.

Supplementary Tables

Table S6.1. Deconvolution of 1D ^{13}C ($^1\text{H}\rightarrow^{13}\text{C}$) CP MAS spectra in Fig. S6.10 with a contact time of 2 ms.

Sample	Chemical shift (ppm)	Line-width (Hz)
HSE-LiI	71.49	385
	69.80	148
HSE (13:1)	71.68	214
	69.75	167

Table S6.2. Fitting results of 1D ^7Li ($^1\text{H}\rightarrow^7\text{Li}$) CP MAS curves in Fig. S6.15.

Sample		T_{H-Li} (ms)	$T_{1\rho H}$ (ms)
HSE-LiI	Interface	0.74	38.45
	Li-PEO	1.29	32.52
HSE (13:1)	Interface	1.02	72.43
	Li-PEO	1.47	72.80

Table S6.3. Thermal behavior of the HSE-LiI and HSE (13:1)

Sample	T_g ($^{\circ}\text{C}$)	T_m ($^{\circ}\text{C}$)	ΔH_m (J g^{-1})	*Crystallinity (%)
HSE-LiI	-32.5	40.2	20.37	12.0%
HSE (13:1)	-30.2	43.3	37.22	22.9%

*The relative crystallinity defined as % change in enthalpy compared to fully crystalline PEO (170 J g^{-1} , Fig. S6.17b). The presence of LiI in the HSE results in a decrease in melting temperature and crystallinity, which is consistent with the ssNMR observations.

References

1. Zhao, Q., Stalin, S., Zhao, C.-Z. & Archer, L. A. Designing solid-state electrolytes for safe, energy-dense batteries. *Nature Reviews Materials* **5**, 229–252 (2020).
2. Janek, J. & Zeier, W. G. A solid future for battery development. *Nature Energy* **1**, 16141 (2016).
3. Manthiram, A., Yu, X. & Wang, S. Lithium battery chemistries enabled by solid-state electrolytes. *Nature Reviews Materials* **2**, 16103 (2017).
4. Cheng, X.-B., Zhao, C.-Z., Yao, Y.-X., Liu, H. & Zhang, Q. Recent advances in energy chemistry between solid-state electrolyte and safe lithium-metal anodes. *Chem* **5**, 74–96 (2019).
5. Famprikis, T., Canepa, P., Dawson, J. A., Islam, M. S. & Masquelier, C. Fundamentals of inorganic solid-state electrolytes for batteries. *Nature Materials* **18**, 1278–1291 (2019).
6. Banerjee, A., Wang, X., Fang, C., Wu, E. A. & Meng, Y. S. Interfaces and interphases in all-solid-state batteries with inorganic solid electrolytes. *Chemical Reviews* **120**, 6878–6933 (2020).
7. Gao, Z., Sun, H., Fu, L., Ye, F., Zhang, Y., Luo, W. & Huang, Y. Promises, Challenges, and recent progress of inorganic solid-state electrolytes for all-solid-state lithium batteries. *Advanced Materials* **30**, 1705702 (2018).
8. Lu, X., Wang, Y., Xu, X., Yan, B., Wu, T. & Lu, L. Polymer-based solid-state electrolytes for high-energy-density lithium-ion batteries – Review. *Advanced Energy Materials* **13**, 2301746 (2023).
9. Zhang, D., Meng, X., Hou, W., Hu, W., Mo, J., Yang, T. & Li, M. Solid polymer electrolytes: Ion conduction mechanisms and enhancement strategies. *Nano Research Energy* **2**, e9120050 (2023).
10. Zhang, Z., Wang, X., Li, X., Zhao, J., Liu, G., Yu, W. & Wang, J. Review on composite solid electrolytes for solid-state lithium-ion batteries. *Materials Today Sustainability* **21**, 100316 (2023).
11. Vu, T. T., Cheon, H. J., Shin, S. Y., Jeong, G., Wi, E. & Chang, M. Hybrid electrolytes for solid-state lithium batteries: Challenges, progress, and prospects. *Energy Storage Materials* **61**, 102876 (2023).
12. Nguyen, A.-G. & Park, C.-J. Insights into tailoring composite solid polymer electrolytes for solid-state lithium batteries. *Journal of Membrane Science* **675**, 121552 (2023).
13. Xue, Z., He, D. & Xie, X. Poly(ethylene oxide)-based electrolytes for lithium-ion batteries. *Journal of Materials Chemistry A* **3**, 19218–19253 (2015).
14. Feng, J., Wang, L., Chen, Y., Wang, P., Zhang, H. & He, X. PEO based polymer-ceramic hybrid solid electrolytes: a review. *Nano Convergence* **8**, 2 (2021).
15. Huo, H., Chen, Y., Luo, J., Yang, X., Guo, X. & Sun, X. Rational design of hierarchical

- “ceramic-in-polymer” and “polymer-in-ceramic” electrolytes for dendrite-free solid-state batteries. *Advanced Energy Materials* **9**, 1804004 (2019).
16. Zhang, M., Yusuf, A. & Wang, D.-Y. A novel hierarchical “ceramic in polymer - polymer in ceramic” structure composite solid-state electrolyte for safer lithium ion batteries. *Journal of Power Sources* **591**, 233812 (2024).
17. Xue, S., Chen, S., Fu, Y., Zhu, H., Ji, Y., Song, Y., Pan, F. & Yang, L. Revealing the role of active fillers in li-ion conduction of composite solid electrolytes. *Small* **19**, 2305326 (2023).
18. Fu, Y., Yang, K., Xue, S., Li, W., Chen, S., Song, Y. & Sun, X. Surface defects reinforced polymer-ceramic interfacial anchoring for high-rate flexible solid-state batteries. *Advanced Functional Materials* **33**, 2210845.
19. Zhang, X., Fu, C., Cheng, S., Zhang, C., Zhang, L., Jiang, M. & Huo, H. Novel PEO-based composite electrolyte for low-temperature all-solid-state lithium metal batteries enabled by interfacial cation-assistance. *Energy Storage Materials* **56**, 121–131 (2023).
20. Zheng, J. & Hu, Y.-Y. New insights into the compositional dependence of li-ion transport in polymer–ceramic composite electrolytes. *ACS Applied. Materials Interfaces* **10**, 4113–4120 (2018).
21. Wang, H.-R., Yang, Y.-N. & Zhang, T. Tape-casting method of hybrid solid electrolytes with a residual active solvent of tetraethylene glycol dimethyl ether. *ACS Applied Energy Materials* **6**, 2031–2038 (2023).
22. Liu, W., Deng, F., Song, S., Ji, G., Hu, N. & Xu, C. LLZO@EmimFSI@PEO derived hybrid solid electrolyte for high-energy lithium metal batteries. *Materials Technology* **35**, 618–624 (2020).
23. Yang, G., Song, Y., Wang, Q., Zhang, L. & Deng, L. Review of ionic liquids containing, polymer/inorganic hybrid electrolytes for lithium metal batteries. *Materials & Design* **190**, 108563 (2020).
24. Su, H., Zhong, Y., Wang, C., Liu, Y., Hu, Y., Li, J. & Tu, J. Deciphering the critical role of interstitial volume in glassy sulfide superionic conductors. *Nature Communications* **15**, 2552 (2024).
25. Takahashi, M., Watanabe, T., Yamamoto, K., Ohara, K., Sakuda, A., Kimura, T. & Uchimoto, Y. Investigation of the suppression of dendritic lithium growth with a lithium-iodide-containing solid electrolyte. *Chemistry of Materials* **33**, 4907–4914 (2021).
26. Choi, S. J., Choi, S. H., Bui, A. D., Lee, Y. J., Lee, S. M., Shin, H. C. & Ha, Y. C. Li-doped sulfide solid electrolyte: enabling a high-capacity slurry-cast electrode by low-temperature post-sintering for practical all-solid-state lithium batteries. *ACS Applied Materials Interfaces* **10**, 31404–31412 (2018).
27. Wang, G., Xiong, X., Xie, D., Fu, X., Ma, X., Li, Y. & Liu, M. Suppressing dendrite growth by a functional electrolyte additive for robust Li metal anodes. *Energy Storage Materials* **23**, 701–706 (2019).
28. Liu, M., Zhang, S., van Eck, E. R., Wang, C., Ganapathy, S. & Wagemaker, M. Improving

- Li-ion interfacial transport in hybrid solid electrolytes. *Nature Nanotechnology* **19**, 959–967 (2022).
29. Ranque, P., Zagórski, J., Devaraj, S., Aguesse, F. & López del Amo, J. M. Characterization of the interfacial Li-ion exchange process in a ceramic–polymer composite by solid state NMR. *Journal of Materials Chemistry A* **9**, 17812–17820 (2021).
30. Zheng, J., Dang, H., Feng, X., Chien, P.-H. & Hu, Y.-Y. Li-ion transport in a representative ceramic–polymer–plasticizer composite electrolyte: Li₇La₃Zr₂O₁₂–polyethylene oxide–tetraethylene glycol dimethyl ether. *Journal of Materials Chemistry A* **5**, 18457–18463 (2017).
31. Zheng, J., Tang, M. & Hu, Y.-Y. Lithium Ion Pathway within Li₇La₃Zr₂O₁₂–Polyethylene Oxide Composite Electrolytes. *Angewandte Chemie International Edition* **55**, 12538–12542 (2016).
32. Wagemaker, M., Kentgens, A. P. M. & Mulder, F. M. Equilibrium lithium transport between nanocrystalline phases in intercalated TiO₂ anatase. *Nature* **418**, 397–399 (2002).
33. Ganapathy, S., van Eck, E. R. H., Kentgens, A. P. M., Mulder, F. M. & Wagemaker, M. Equilibrium lithium-ion transport between nanocrystalline lithium-inserted anatase TiO₂ and the electrolyte. *Chemistry—A European Journal* **17**, 14811–14816 (2011).
34. Wang, H., Hou, T., Cheng, H., Jiang, B., Xu, H. & Huang, Y. Bifunctional LiI additive for poly(ethylene oxide) electrolyte with high ionic conductivity and stable interfacial chemistry. *Journal of Energy Chemistry* **71**, 218–224 (2022).
35. Han, Q., Wang, S., Wang, L., Ren, W., Zhang, F., Lu, J. & Wang, H. Exploiting iodine redox chemistry for achieving high-capacity and durable peo-based all-solid-state LiFePO₄/Li Batteries. *Advanced Energy Materials* **13**, 2301462 (2023).
36. Liu, M., Wang, C., Zhao, C., van der Maas, E., Lin, K., Arszewska, V. A. & Wagemaker, M. Quantification of the Li-ion diffusion over an interface coating in all-solid-state batteries via NMR measurements. *Nature Communications* **12**, 5943 (2021).
37. Zhang, H., Judez, X., Santiago, A., Martínez-Ibañez, M., Muñoz-Márquez, M. Á., Carrasco, J. & Armand, M. Fluorine-free noble salt anion for high-performance all-solid-state lithium–sulfur batteries. *Advanced Energy Materials* **9**, 1900763 (2019).
38. Gupta, A. & Sakamoto, J. Controlling ionic transport through the PEO-LiTFSI/LLZTO Interface. *Electrochemical Society Interface* **28**, 63–69 (2019).
39. Lascaud, S., Perrier, M., Vallee, A., Besner, S., Prud'Homme, J. & Armand, M. Phase Diagrams and conductivity behavior of poly(ethylene oxide)-molten salt rubbery electrolytes. *Macromolecules* **27**, 7469–7477 (1994).
40. Ao, X., Wang, X., Tan, J., Zhang, S., Su, C., Dong, L. & Wang, H. Nanocomposite with fast Li⁺ conducting percolation network: Solid polymer electrolyte with Li⁺ non-conducting filler. *Nano Energy* **79**, 105475 (2021).
41. Mackanic, D. G., Michaels, W., Lee, M., Feng, D., Lopez, J., Qin, J. & Bao, Z. Crosslinked poly(tetrahydrofuran) as a loosely coordinating polymer electrolyte. *Advanced Energy Materials* **8**, 1800703 (2018).

42. Hanghofer, I., Brinek, M., Eisbacher, S. L., Bitschnau, B., Volck, M., Hennige, V. & Wilkening, H. M. R. Substitutional disorder: structure and ion dynamics of the argyrodites $\text{Li}_6\text{PS}_5\text{Cl}$, $\text{Li}_6\text{PS}_5\text{Br}$ and $\text{Li}_6\text{PS}_5\text{I}$. *Physical Chemistry Chemical Physics* **21**, 8489–8507 (2019).
43. Chen, B., Wang, T., Liu, C., Li, T. & Liu, X. Build a high-performance all-solid-state lithium battery through introducing competitive coordination induction effect in polymer-based electrolyte. *Angewandte Chemie International Edition* **63**, e202400960 (2024).
44. Xu, J., Li, J., Li, Y., Yang, M., Chen, L., Li, H. & Wu, F. Long-life lithium-metal all-solid-state batteries and stable Li plating enabled by in situ formation of Li_3PS_4 in the SEI layer. *Advanced Materials* **34**, 2203281 (2022).
45. Yusim, Y., Trevisanello, E., Ruess, R., Richter, F. H., Mayer, A., Bresser, D. & Henss, A. Evaluation and improvement of the stability of poly(ethylene oxide)-based solid-state batteries with high-voltage cathodes. *Angewandte Chemie International Edition* **62**, e202218316 (2023).
46. Simon, F. J., Hanauer, M., Richter, F. H. & Janek, J. Interphase formation of $\text{PEO}_{20}:\text{LiTFSI}-\text{Li}_6\text{PS}_5\text{Cl}$ composite electrolytes with lithium metal. *ACS Applied Materials & Interfaces* **12**, 11713–11723 (2020).
47. Aktekin, B., Kataev, E., Riegger, L. M., Garcia-Diez, R., Chalkley, Z., Becker, J. & Janek, J. Operando photoelectron spectroscopy analysis of $\text{Li}_6\text{PS}_5\text{Cl}$ electrochemical decomposition reactions in solid-state batteries. *ACS Energy Letters* **9**, 3492–3500 (2024).
48. Simon, F. J., Hanauer, M., Henss, A., Richter, F. H. & Janek, J. Properties of the interphase formed between argyrodite-type $\text{Li}_6\text{PS}_5\text{Cl}$ and polymer-based $\text{PEO}_{10}:\text{LiTFSI}$. *ACS Applied Materials & Interfaces* **11**, 42186–42196 (2019).
49. Xu, S., Sun, Z., Sun, C., Li, F., Chen, K., Zhang, Z. & Li, F. Homogeneous and fast ion conduction of peo-based solid-state electrolyte at low temperature. *Advanced Functional Materials* **30**, 2007172 (2020).
50. Koster, T. & Vanwullen, L. Phase separation and local cation coordination in $\text{PEO}_n\text{LiNTf}_2$ polymer electrolytes: Lessons from solid state NMR. *Solid State Ionics* **178**, 1879–1889 (2008).
51. Wickham, J. R., Mason, R. N. & Rice, C. V. Solid-state NMR studies of the crystalline and amorphous domains within PEO and $\text{PEO}:\text{LiTf}$ systems. *Solid State Nuclear Magnetic Resonance* **31**, 184–192 (2007).
52. Boaretto, N., Ghorbanzade, P., Perez-Furundarena, H., Meabe, L., Lopez del Amo, J. M., Gunathilaka, I. E. & Martinez-Ibañez, M. Transport properties and local ions dynamics in LATP-based hybrid solid electrolytes. *Small* **20**, 2305769 (2023).
53. Huo, H., Jiang, M., Mogwitz, B., Sann, J., Yusim, Y., Zuo, T.T., Moryson, Y., Minnmann, P., Richter, F.H., Veer Singh, C. & Janek, J. Interface Design Enabling Stable Polymer/Thiophosphate Electrolyte Separators for Dendrite-Free Lithium Metal Batteries. *Angewandte Chemie International Edition* **62**, e202218044 (2023).
54. Huo, H., Jiang, M., Mogwitz, B., Sann, J., Yusim, Y., Zuo, T. T. & Janek, J. Clarifying

- the relationship between redox activity and electrochemical stability in solid electrolytes. *Nature Materials* **62**, e202218044 (2020).
55. Spencer Jolly, D., Melvin, D. L., Stephens, I. D., Brugge, R. H., Pu, S. D., Bu, J. & Bruce, P. G. Interfaces between ceramic and polymer electrolytes: a comparison of oxide and sulfide solid electrolytes for hybrid solid-state batteries. *Inorganics* **10**, 60 (2022).
56. Wieczorek, W., Raducha, D., Zalewska, A. & Stevens, J. R. Effect of salt concentration on the conductivity of peo-based composite polymeric electrolytes. *The Journal of Physical Chemistry B* **102**, 8725–8731 (1998).
57. Fang, R., Xu, B., Grundish, N. S., Xia, Y., Li, Y., Lu, C. & Goodenough, J. B. Li₂S₆-integrated peo-based polymer electrolytes for all-solid-state lithium-metal batteries. *Angewandte Chemie* **133**, 17842–17847 (2021).
58. Kulasekarapandian, K., Jayanthi, S., Muthukumari, A., Arulsankar, A. & Sundaresan, B. Preparation and characterization of PVC-PEO based polymer blend electrolytes complexed with lithium perchlorate. *Journal of Engineering Research and Development* **5**, 30–39 (2013).
59. Hester, T. H., Castillo, D. E. & Goebbert, D. J. Fragmentation of deprotonated polyethylene glycols, [PEG – H]⁻. *Rapid Communications in Mass Spectrometry* **27**, 1643–1648 (2013).
60. Zhao, M., Li, B.-Q., Zhang, X.-Q., Huang, J.-Q. & Zhang, Q. A perspective toward practical lithium–sulfur batteries. *ACS Central Science* **6**, 1095–1104 (2020).
61. Xu, C., Sun, B., Gustafsson, T., Edström, K., Brandell, D. & Hahlin, M. Interface layer formation in solid polymer electrolyte lithium batteries: an XPS study. *Journal of Materials Chemistry A* **2**, 7256–7264 (2014).
62. Zhang, J., Li, S., Wang, X., Mao, S., Guo, J., Shen, Z. & Lu, Y. Construction of stable Li₂O-rich solid electrolyte interphase for practical PEO-based Li-metal batteries. *Advanced Energy Materials* **14**, 2302587 (2023).
63. Walther, F., Koerver, R., Fuchs, T., Ohno, S., Sann, J., Rohnke, M. & Janek, J. Visualization of the interfacial decomposition of composite cathodes in argyrodite-based all-solid-state batteries using time-of-flight secondary-ion mass spectrometry. *Chemistry of Materials* **31**, 3745–3755 (2019).
64. Sheng, O., Hu, H., Liu, T., Ju, Z., Lu, G., Liu, Y. & Tao, X. Interfacial and ionic modulation of poly(ethylene oxide) electrolyte via localized iodization to enable dendrite-free lithium metal batteries. *Advanced Functional Materials* **32**, 2111026 (2022).
65. Li, M., An, H., Song, Y., Liu, Q., Wang, J., Huo, H. & Wang, J. Ion–dipole-interaction-induced encapsulation of free residual solvent for long-cycle solid-state lithium metal batteries. *Journal of the American Chemical Society* **145**, 25632–25642 (2023).
66. Gong, C., Pu, S. D., Gao, X., Yang, S., Liu, J., Ning, Z. & Robertson, A. W. Revealing the role of fluoride-rich battery electrode interphases by operando transmission electron microscopy. *Advanced Energy Materials* **11** 2003118 (2021).
67. Guo, R. & Gallant, B. M. Li₂O solid electrolyte interphase: probing transport properties

- at the chemical potential of lithium. *Chemistry of Materials* **32**, 5525–5533 (2020).
68. Kim, M. S., Zhang, Z., Rudnicki, P. E., Yu, Z., Wang, J., Wang, H. & Cui, Y. Suspension electrolyte with modified Li^+ solvation environment for lithium metal batteries. *Nature Materials* **21**, 445–454 (2022).
69. Kim, M. S., Zhang, Z., Wang, J., Oyakhire, S. T., Kim, S. C., Yu, Z. & Cui, Y. Revealing the multifunctions of Li_3N in the suspension electrolyte for lithium metal batteries. *ACS Nano* **17**, 3168–3180 (2023).
70. Liu, S., Ji, X., Piao, N., Chen, J., Eidson, N., Xu, J. & Wang, C. An inorganic-rich solid electrolyte interphase for advanced lithium-metal batteries in carbonate electrolytes. *Angewandte Chemie International Edition* **60**, 3661–3671 (2021).
71. Stejskal, E. O. & Tanner, J. E. Spin diffusion measurements: spin echoes in the presence of a time-dependent field gradient. *The Journal of Chemical Physics* **42**, 288–292 (1965).

Summary

Rechargeable lithium (Li)-metal batteries (LMBs) stand out as a top contender for next-generation high-energy-density storage solutions, originating from the high theoretical specific capacity and low redox potential of metallic Li. However, developing LMBs is hindered by safety issues arising from dendrite growth as well as electrolyte decomposition reactions during Li plating/stripping. These dendrites can cause short-circuits that may start thermal runaway, greatly amplifying fire hazards. The rapid reaction between the electrolyte and Li-metal leads to the formation of the solid electrolyte interphase (SEI), whose structure and Li-ion conduction properties are crucial for the uniformity of Li deposition. This affects dendrite formation and cycling efficiency, which in turn influences battery life. Yet very little is known about the Li-ion kinetics through the SEI and how these correlate with the structure and composition of the SEI.

To advance LMBs, it is essential to develop a fundamental understanding of Li exchange kinetics across the SEI, and implement practical electrolyte engineering solutions to tailor the structure and properties of SEI, as well as improve battery safety. Compared to liquid electrolytes, solid-state electrolytes (SSEs) have the unique advantage of lowering or even eliminating safety concerns and improving energy density. Among them, hybrid solid electrolytes (HSEs), which combine an organic polymer electrolyte with an inorganic solid electrolyte, have the potential to leverage the strengths of both types while addressing their individual limitations. Despite their promising prospects, HSEs present intrinsic complexities, such as the interaction between the components, filler ratios and sizes, film-forming structures, and how these impact their functional properties, which are not yet thoroughly understood. Thus, fundamental research is critically required to better understand the ion transport phenomena in HSEs at an atomic-scale.

This thesis seeks to deepen the fundamental understanding of the Li-ion diffusion

through the SEI chemistry for liquid electrolytes, and of alternative HSEs to support the development of safe and efficient (solid-state) LMBs. The main research questions explored in this thesis cover two main aspects, which refer to the study objectives:

(i) *Li-ion kinetics of the SEI*: Specifically, how does the electrochemical formation protocol affect Li-ion kinetics at the Li/SEI interface, and what are its implications for the cycling performance in subsequent cycles?

(ii) *Li-ion dynamics in HSEs*: Li-ion conductivity in HSEs is a result of a complex diffusion pathway that involves several phases and interphases. To gain more insight, we probe the Li-ion dynamics across various length scales within HSEs and correlate this behavior with their structural characteristics. When an inorganic Li-ion conductor is incorporated into the polymeric matrix, to what extent does it modify the polymer configuration and phase distribution? Furthermore, does it actively contribute to the overall ion conduction? If not, what factors contribute to this limitation, and how can we improve it?

The questions outlined above are investigated and summarized in four chapters:

In **Chapter 3**, complementary techniques have been used to perform a dynamically-resolved and quantitative assessment of the lasting impact of the formation current density on Li-metal anodes. By combining ssNMR with XPS, SEM, and TEM, the chemical composition and microstructure of the formed SEI are unveiled. Quantification of the spontaneous Li-ion diffusion between electrochemically deposited Li-metal and the as-formed SEI indicates a strong dependency on the formation current density. Employing a moderately high formation current density (2 mA cm^{-2}) increases Li-ion mobility between the Li-metal and the corresponding SEI. This improvement is attributed to the compact Li microstructure and favorable SEI composition, which lead to more uniform Li deposition and reduce the buildup of inactive Li. The lasting impact of this optimal SEI improves the Li-ion diffusion between distinct solid phases, creating favorable conditions for subsequent cycling and leading to great improvement in the stability and efficiency of the Li-metal anode. This study provides in-depth understanding into the impact of formation cycles in LMBs, revealing how the spontaneous Li-ion diffusion dynamics between Li-metal and the SEI can inform various optimization strategies, including electrolyte design, current collector engineering, and the development of new electrode materials.

Chapter 4 discusses how incorporating $\text{Li}_6\text{PS}_5\text{Cl}$ inorganic fillers into the PEO-LiTFSI

polymer electrolyte (SPE) considerably enhances the ionic conductivity of the SPE, in particular when using a solvent-assisted processing method. Leveraging NMR's capability to provide dynamic and structural insights, the local Li-ion mobility and the structure of the polymer phase were studied to elucidate the Li-ion transport mechanism in the HSEs. The line-width measurements suggest that incorporating the $\text{Li}_6\text{PS}_5\text{Cl}$ filler inhibits crystallization in the polymer phase when temperature decreases. The activation energies derived from the Hendrickson-Bray and Abragam model fits of the line-width data point to improved local Li-ion mobility in the HSEs compared to the SPE. The temperature dependence of the correlation time, τ_c , reveals the characteristic phase transitions of the PEO phase, which shows typical Vogel-Tamman-Flucher (VTF) behavior at the intermediate temperatures and Arrhenius behavior in the fully crystallized state. At low temperatures, the second T_1 relaxation component in the hybrid systems suggests the emergence of two distinct dynamic modes in the polymer matrix, likely due to the presence of the filler. Fits from the 2D Richards spectral density function imply that the Li-ion transport occurs along the salt-rich polymer-filler interfaces. Although the incorporation of fillers enhances local Li-ion mobility, morphological inhomogeneities may offset these improvements, as reflected by the reduced conductivity and Li-ion dynamics observed in the dry-processed electrolyte relative to its solvent-processed counterpart. While the improvement in conductivity cannot be directly attributed to the active role of $\text{Li}_6\text{PS}_5\text{Cl}$ in Li-ion conduction, it promotes local Li-ion dynamics, which are further linked to: (i) increased Li salt dissociation; (ii) alterations in polymer configuration; and (iii) enhanced mobility of the polymer chains. Additionally, the formation of an inorganic-rich SEI layer at the Li/HSE interface is found to be beneficial for its application in solid-state LMBs.

Building on the HSE system (PEO-LiTFSI- $\text{Li}_6\text{PS}_5\text{Cl}$) studied in Chapter 4. **Chapter 5** delves into the organic/inorganic interface, aiming to establish whether the $\text{Li}_6\text{PS}_5\text{Cl}$ actively participates in the HSE conductivity and, if not, to uncover the underlying reasons. Here, we identify the phase boundary between these two ion conductors as the key bottleneck for Li-ion transport in the HSEs. The observed poor local Li-ion conductivity at these interfaces is associated with a deficiency of ethereal oxygen species and insufficient local Li-ion mobility. Using an ionic liquid additive as a wetting agent is an effective approach to improve the interface diffusivity. An ionic liquid with low miscibility in PEO, i.e., PP13-TFSI, localizes

at the phase boundaries and acts as a bridge for Li-ion transport. In contrast, an ionic liquid that is miscible with PEO, i.e., EMIM-TFSI, enhances the conductivity by distributing throughout the PEO phase, thereby increasing both chain and Li-ion mobility, but only within the polymer phase. In this case, the polymer-filler interface remains the bottleneck for Li-ion transport. The NMR analysis resolves the interface structure between the organic and inorganic phases in the HSE and its effect on Li-ion diffusion. These insights can lead to the development of interface strategies, such as using non-miscible ionic liquids, which highly improve conductivity and compatibility with Li-metal anodes. This study also highlights the potential of using multinuclear NMR for detecting interface properties, particularly in HSEs.

Taking the investigation further, **Chapter 6** explores the structure-property relationship of HSEs by introducing a functional LiI additive into the aforementioned hybrid system, aiming to promote Li-ion diffusivity between the PEO matrix and the $\text{Li}_6\text{PS}_5\text{Cl}$ filler, thereby improving overall conductivity. The interaction between LiI and the HSE improves the Li salt dissociation within the bulk PEO matrix, while also stabilizing the organic/inorganic interfaces, thereby promoting organic/inorganic interfacial Li-ion diffusion. Multidimensional NMR experiments reveal that the addition of LiI reduces the degradation of the PEO phase and its interactions with the $\text{Li}_6\text{PS}_5\text{Cl}$ phase, creating a more conductive interface environment, which consequently enhances the overall ionic conductivity. Furthermore, the altered decomposition sequence of LiTFSI leads to an inorganic-rich SEI at the Li/HSE-LiI interface, which facilitates the Li-ion transport and inhibits dendrite formation. The addition of the multifunctional LiI additive offers valuable insight into the design of organic/inorganic interfaces within the HSE system and at the Li/HSE/cathode interfaces, further guiding the development of high-safety and high-energy-density solid-state LMBs.

In conclusion, the crucial role of formation cycling in shaping the initial SEI and its conductive properties has been revealed, highlighting its lasting impact on cycling performance over extended cycles. For HSEs, three aspects of the polymer-filler interaction have been explored, the local Li-ion dynamics of the polymer phase, the organic/inorganic interface, and the polymer bulk structure, as well as the correlation between these aspects. Incorporating additives is presented as promising strategy for enhancing interfacial and bulk Li-ion conduction in HSEs. Furthermore, correlating the overall Li-ion conduction in the

HSEs system with the local, interfacial, and bulk aspects is indispensable for understanding the polymer-filler interactions and their impact on system performance. This demonstrates that optimizing phase compatibility within HSEs is key to improving their overall performance.

Samenvatting

Herlaadbare lithium (Li)-metaal batterijen (LMBs) onderscheiden zich als een van de voornaamste mededingers voor de oplossingen van de volgende generatie voor opslag met hoge energiedichtheid, dankzij de hoge theoretische soortelijke capaciteit en lage redox potentiaal van metallisch Li. Echter, de ontwikkeling van LMBs wordt gehinderd door veiligheidskwesties voortkomend zowel uit de groei van dendrietten als reacties waar het elektrolyt uiteenvalt tijdens het neerslaan van Li en weer in oplossing gaan. Deze dendrietten kunnen doorslagen veroorzaken die leiden tot een warmte-explosie, wat het brandgevaar sterk verhoogt. De snelle reactie tussen het elektrolyt en Li-metaal leidt tot de vorming van een grensfase tussen vaste-stof en elektrolyt (SEI), waarvan structuur- en Li-ionengeleidings-eigenschappen cruciaal zijn voor de uniformiteit van Li neerslag. Dit heeft gevolgen voor dendrietvorming en cycleerefficiëntie, wat op zijn beurt de levensduur van de batterij beïnvloedt. Toch is heel weinig bekend over de Li-ionenkinetiek door de SEI en hoe dit samenhangt met de structuur en samenstelling van de SEI.

Om LMBs verder te brengen is het essentieel een fundamenteel begrip te ontwikkelen over de kinetiek van Li uitwisseling over de SEI en praktische elektrolyt technische oplossingen te implementeren om de structuur en eigenschappen van SEI op maat te maken en ook de veiligheid van batterijen te verbeteren. Vergeleken met vloeibare elektrolyten hebben vastestofelektrolyten (SSEs) het unieke voordeel, dat zij de veiligheidszorgen verminderen of zelfs elimineren en de energiedichtheid verbeteren. Onder deze elektrolyten hebben hybride vaste stof elektrolyten (HSEs), die een organisch polymeer elektrolyt met een anorganische vaste-stof elektrolyt combineren, het potentieel de kracht van beide typen te benutten, terwijl hun individuele beperkingen worden aangepakt. Ondanks hun veelbelovende vooruitzichten bieden HSEs intrinsieke uitdagingen, zoals de wisselwerking

tussen de componenten, vulverhoudingen en grootten en laagvormende structuren en hoe deze op hun functionele eigenschappen uitwerken, wat nog niet volkomen begrepen is. Daarom is fundamenteel onderzoek essentieel om de ionentransportverschijnselen in HSEs op atomaire schaal beter te begrijpen.

Dit proefschrift streeft er naar om het fundamentele begrip van Li-ionendiffusie door de SEI chemie te verdiepen voor vloeibare electrolyten en alternatieve HSEs, om hiermee de ontwikkeling van veilige en efficiënte vaste-stof LMBs (SSLMBs) mogelijk te maken. De belangrijkste onderzoeksvragen die in dit proefschrift worden uitgediept omvatten twee hoofdaspecten, die verwijzen naar de studiedoelen:

(i) *Li-ionenkinetiek van de SEI*: Specifiek, hoe beïnvloedt het elektrochemische vormingsprotocol Li-ionenkinetiek op het Li/SEI grensvlak en wat zijn gevolgen voor de cycleerprestatie in daaropvolgende cycli?

(ii) *Li-ionendynamica in HSEs*: Li-ionengeleiding in HSEs is het resultaat van een complex diffusiepad dat verscheidene fasen en grensfasen omvat. Om meer inzicht te krijgen sonderen wij naar de Li-ionendynamica over verschillende lengteschalen in HSEs en brengen dit gedrag in verband met hun structurele kenmerken. Wanneer een anorganische Li-ionengeleider wordt ingebed in de polymeermatrix, in welke mate wijzigt dat de configuratie van de polymeren en de faseverdeling? Daarbij, zorgt dit voor een actieve bijdrage in de ionegeleiding? Wat is hiervoor verantwoordelijk en hoe kunnen wij dat verbeteren?

De vragen, die hierboven geschetst zijn, worden onderzocht en samengevat in vier hoofdstukken:

In **Hoofdstuk 3** zijn complementaire technieken gebruikt om een dynamisch-opgeloste en kwantitatieve inschatting te maken van de langdurige invloed van de vormingsstroomdichtheid op Li-metaal anodes. Door ssNMR te combineren met XPS, SEM en TEM worden de chemische samenstelling en microstructuur van de gevormde SEI ontsluitend. Kwantificatie van de spontane Li-ionendiffusie tussen elektrochemisch neergeslagen Li-metaal en de originele SEI wijst op een sterke afhankelijkheid van de vormingsstroomdichtheid. Gebruik van een gematigd hoge vormingsstroomdichtheid (2 mA cm^{-2}) verhoogt de Li-ionenmobiliteit tussen het Li-metaal en de corresponderende SEI. Deze verbetering wordt toegeschreven aan de compacte Li microstructuur en gunstige SEI samenstelling, welke leiden tot een uniformere Li neerslag en de opbouw van inactieve Li

reduceren. De durende invloed van deze optimale SEI verbetert de Li-ionendiffusie tussen verschillende vaste fasen, wat gunstige voorwaarden schept voor daaropvolgende cycli en leidt tot grote verbetering in de stabiliteit en efficiëntie van de Li-metaalanode. Deze studie verschaft diepgaand begrip over de invloed van vormingscycli op LMBs, wat onthult hoe de spontane Li-ionendiffusiedynamica tussen Li-metaal en de SEI informatie kan verstrekken voor diverse optimalisatiestrategieën waaronder elektrolyt ontwerp, stroomcollector techniek en de ontwikkeling van nieuwe elektrodematerialen.

Hoofdstuk 4 bespreekt hoe het inbouwen van $\text{Li}_6\text{PS}_5\text{Cl}$ anorganische vulstoffen in het PEO-LiTFSI polymeer elektrolyt (SPE) de ionengeleidbaarheid van het SPE aanzienlijk verhoogt, in het bijzonder wanneer een vloeistofondersteunde productiemethode wordt gebruikt. Onder benutting van NMR's vermogen om dynamisch en structureel inzicht te bieden, werden de lokale Li-ionenmobiliteit en de structuur van de polymeerfase bestudeerd om het Li-ionentransportmechanisme in de HSEs op te helderen. De lijnbreedte metingen suggereren dat het inbouwen van het $\text{Li}_6\text{PS}_5\text{Cl}$ vulmiddel kristallisatie remt in de polymeerfase wanneer de temperatuur daalt. De activatie energieën afgeleid uit de fits met het Hendrickson-Bray en Abragam model van data van de lijnbreedte wijzen op verbeterde lokale Li-ionenmobiliteit in de HSEs vergeleken met de SPE. De temperatuurafhankelijkheid van de correlatietijd, τ_c , laat de karakteristieke faseovergangen van de PEO fase zien, die typisch Vogel-Tamman-Flucher (VTF) gedrag op intermediaire temperaturen en Arrhenius gedrag in de volledig gekristalliseerde toestand vertoont. Bij lage temperatuur suggereert de tweede component in de T_1 relaxatie in de hybride systemen de verschijning van twee verschillende dynamische modes in de polymeermatrix, waarschijnlijk te danken aan het vulmateriaal. Fits van de 2D Richards spectrale dichtheidsfunctie impliceren dat het Li-ionentransport plaats vindt langs de zoutrijke polymeer-vulmiddel grensvlakken. Hoewel de inbouw van vulmiddel lokale Li-ionenmobiliteit verhoogt, kunnen morfologische inhomogeniteiten deze verbeteringen teniet doen, zoals weerspiegeld in de gereduceerde geleidbaarheid en Li-ionendynamica waargenomen in het oplosmiddelvrij geproduceerde elektrolyt vergeleken met zijn in oplossing geproduceerde tegenhanger. Hoewel de verhoging van de geleiding niet direct kan worden toegeschreven aan de actieve Li-ionengeleidende rol van $\text{Li}_6\text{PS}_5\text{Cl}$, verbetert het de lokale Li-ionendynamica die ook gekoppeld zijn aan: (i) toegenomen Li-zoutdissociatie; (ii) veranderingen in polymeer configuratie en; (iii)

verhoogde mobiliteit van de polymeerketens. Tevens wordt de vorming van een anorganisch-rijke SEI laag bij het Li/HSE grensvlak gunstig bevonden voor zijn toepassing in vastestof LMBs.

Bouwend op het HSE systeem (PEO-LiTFSI-Li₆PS₅Cl) bestudeerd in Hoofdstuk 4, gaat **Hoofdstuk 5** dieper in op het organisch/anorganisch grensvlak met het doel om te ontdekken of Li₆PS₅Cl actief bijdraagt in de HSE geleiding en, zoniet, te ontrafelen wat de oorzaken daarvan zijn. Hier identificeren wij de fasegrens tussen deze twee componenten als het hoofdknelpunt voor Li-ionentransport in de HSEs. De waargenomen slechte lokale Li-ionengeleidbaarheid op deze grensvlakken wordt geassocieerd met een gebrek aan zuurstof van het ethertype en onvoldoende lokale Li-ionenmobiliteit. Het gebruik van een ionische vloeistof als bevochtigingsmiddel is een effectieve aanpak om de grensvlak diffusiviteit te verbeteren. Een ionische vloeistof met lage mengbaarheid in PEO, b.v., PP13-TFSI, wordt gelokaliseerd bij de fasegrenzen en treedt op als een brug voor Li-ionentransport. In tegenstelling daarmee verhoogt een ionische vloeistof die mengbaar is met PEO, b.v., EMIM-TFSI, de geleidbaarheid door zich te verspreiden over de PEO fase, waardoor zowel keten- als Li-ionenmobiliteit verhoogd wordt, maar alleen in de polymeerfase. Ongelukkigerwijs blijft in dit geval het grensvlak tussen polymeer en vulmiddel het knelpunt voor Li-ionentransport. De ssNMR analyse lost de grensvlakstructuur tussen de organische en anorganische fasen in het HSE en zijn effect op Li-ionendiffusie op. Deze inzichten kunnen leiden tot de ontwikkeling van grensvlak strategieën, zoals het gebruik van niet-mengbare ionische vloeistoffen, die de geleidbaarheid en compatibiliteit met Li-metaalanodes sterk verbeteren. Deze studie benadrukt ook het potentieel van multinucleaire NMR voor detectie van grensvlakeigenschappen, in het bijzonder in HSEs.

Om het onderzoek te vervolgen verkent **Hoofdstuk 6** het verband tussen structuur en eigenschappen van HSEs door een functioneel LiI additief in het eerdergenoemde hybride systeem te introduceren met als doel om de Li-diffusiviteit tussen de PEO matrix en de Li₆PS₅Cl vulstof te verbeteren, en daarmee de algehele geleiding. De wisselwerking tussen LiI en het HSE verbetert de Li zout dissociatie in de bulk PEO matrix, terwijl het ook de grensvlakken tussen organisch en anorganisch materiaal stabiliseert, waardoor organische/anorganische Li-ionendiffusie langs het grensvlak wordt bevorderd. Multidimensionale NMR experimenten leggen bloot dat de toevoeging van LiI de degradatie

van de PEO fase en zijn wisselwerkingen met de $\text{Li}_6\text{PS}_5\text{Cl}$ fase reduceert, waardoor het een beter geleidende grensvlakomgeving creëert en zo de algehele ionengeleidbaarheid verbetert. Bovendien leidt de gewijzigde decompositie reeks van LiTFSI tot een SEI rijk aan anorganisch materiaal bij het Li/HSE-LiI grensvlak, wat het Li-ionentransport faciliteert en dendrietvorming belemmert. De toevoeging van het multifunctionele LiI additief verschaft waardevol inzicht in het ontwerp van grensvlakken tussen organisch en anorganisch materiaal in het HSE systeem en bij de Li/HSE/kathode grensvlakken, waardoor het de weg wijst naar de ontwikkeling van vastestof LMBs met hoge veiligheid en hoge energiedichtheid.

Concluderend, het fundamenteel begrip gepresenteerd in dit proefschrift zal de weg wijzen bij de bevordering van Li-metaal anodes in praktische LMBs. De cruciale rol van vormingscycli bij het vormgeven van de initiële SEI en haar geleidingseigenschappen is blootgelegd, met zijn durende effecten op cycleerprestatie over extra cycli. Om HSEs met Li-metaal anodes te aanvaarden voor SSLMBs, zijn drie aspecten van de polymeer-opvulmiddel wisselwerking verkend, de lokale Li-ionendynamica van de polymeerfase, het grensvlak tussen organisch en anorganisch en de polymeer bulk structuur, evenals de correlatie tussen deze aspecten. Het toevoegen van additieven wordt voorgesteld als veelbelovende strategie ter verhoging van de grensvlak- en bulkgeleidbaarheid in HSEs. Om de interacties tussen opvulmiddel en polymeer en de impact op de systeemprestaties te begrijpen is het noodzakelijk om de correlatie te maken tussen de Li-ion geleiding in het HSE-systeem en de lokale grensvlak- en bulkaspecten. Het laat zien dat de sleutel voor het verbeteren van de prestaties ligt in het optimaliseren van de comptabiliteit tussen de fasen in HSEs.

Acknowledgements

When I started my PhD, the Netherlands had just imposed its first curfew since World War II due to COVID-19. It hasn't been the easiest journey, but I made it here thanks to all the kind and wonderful people I have met along the way. I am deeply grateful to everyone who not only guided me through the twists and turns of science but also taught me how to live wisely and positively. Your support, encouragement, and warmth have truly been at the heart of this incredible adventure.

First and foremost, my deepest gratitude goes to my supervisors: my promotor Prof. Marnix Wagemaker; my co-promotor and daily supervisor, Dr. Swapna Ganapathy; and my daily supervisor during the first year of my PhD, Dr. Ming Liu.

I can still picture our first Skype meeting back in 2019, when Marnix wrapped up with those unforgettable words, “hope you enjoy the science!” Those words sparked a wave of excitement for the journey that lay ahead. Thank you for offering me the position and for being a supportive guide throughout this journey. I have learned a lot and also truly enjoyed it. I deeply admire your superpower to extract deep insights from the experimental data and distil complex information into clear, meaningful conclusions. I may have mentioned this before, you should start to think about Nobel prize. Over the past four years, I have gained invaluable insights from our discussions - the way to frame and polish a good and meaningful paper, the value of “learning by doing”, and how to cultivate scientific thinking and creativity. And I also liked the catch-up time we had when you were not as busy as now. I still remember when you showed me how to use a CD to watch the total solar eclipse, and the times you ran away and hid in the doorway when I called you. Beyond these lighter moments, I truly appreciate how you encouraged and supported me through times of frustration and stress.

I am incredibly thankful to Swapna, who has always been so supportive during my entire

PhD. Our countless discussions and NMR experiments have laid a solid foundation for this thesis. You always share the most genuine advice and insights with me without hesitation. I have benefited so much from your help in planning and supervising my projects, and you are the one who made me started to truly interested in NMR. On top of being an excellent supervisor, you are also a friend and a family that I cherish here in the Netherlands. I could easily share my feelings with you, whether they were about worries, happiness, or simply my vague visions about life and future. I can't imagine I would have made it without your patience, calmness, tolerance, and encouragement. I was also impressed by how sincere, generous, and kind you are to everyone. And it was through you that I saw the power of women in the scientific community. There were also many other beautiful moments, like when we followed you to do yoga on the grass after the boating group activity, and watched Kader grow from a little baby into a cheerful little boy who likes to smile so much. I feel really lucky to be your student.

My sincere appreciation also goes to Ming, who has been not only an incredibly supportive supervisor but also a great friend. Especially when I was starting my PhD during the toughest time, Ming was there to help me get my project off the ground. Even after you moved back to China, you never stopped being there for me, always stepping in with the support I needed. Every time I felt stuck, whether it was in experiments or making research choices, I always gained many fresh insights from our discussions. I am also truly grateful for the thoughtful advice you have given me on my career path. Beyond that, I also loved joining your family walks along the Delft Hout on the weekends and savoring those delicious dinners together. Those moments were always highlights. It was wonderful to catch up with you again, both in Shenzhen and in Delft. Thank you for being there through it all.

I would also heartily like to thank all the thesis committee members for their careful evaluation of this thesis.

Furthermore, I would like to express my gratitude to Lars Bannenberg, who helped me a lot with the XPS measurements, data analysis, paper revisions and coding. I also learnt a lot from you like how to supervise students and work more efficiently. I really appreciate how generous you have always been in helping me whenever I feel stuck or confused. I still remember when I was very hesitant about attending the Hercules school, you guided me to write down the pros and cons to make the decision easier. And when I felt anxious about how

to start writing my thesis, you shared your experiences and helped me organize my thoughts. And sometimes when I isolated myself too much with work, you always checked in to see how I was doing. I am especially grateful for your gentle nudges to step outside, enjoy the sunshine, and take a break now and then. And I hope that, under your influence, I have developed some “error bar” sensitivity as a materials scientist. Zhu Cheng, who felt like my brother for the first time we met. Thank you for being so kind and patient in answering all my either simple or difficult questions, and our discussions were always uplifting. Your constant support during tough times made me to believe what you said: “No matter how difficult it is now, we should always believe that our future is bright!” You are such a sincere friend, always thoughtful and ready to lend a hand. It is amazing that our hometowns are so close. I cherished our trips together to Frankfurt, Changsha, and Hong Kong, they brought me so much joy and relaxation. I would also like to extend my heartfelt thanks to Frans Ooms, a man with magical pockets like Doraemon! Thank you for your help with all my technical problems in the lab, especially when I was struggling to prepare the operando cell for the microbeam experiments. Even though I teasingly called you out for your “domme humor” (dumb humor), I truly appreciate the laughter and fun you brought to both the lab and the office. I enjoyed our discussions not only about work, but also about “irrelevant” movies, cooking and anecdotes. Your positive life attitude has influenced me not to be too negative about everything, and try to be flexible with the uncertainties in life. And thank you for encouraging me to be my true self and reminding me not overly influenced by others.

I would like to especially acknowledge to Yuhang Li, thank you for all of your help with the experiments and discussions. Your tireless work ethic has been an inspiration to me as well. It is no surprise Ming calls you “Xiaojuanwang” (the ultimate workaholic). And thank you for picking me up and showing me around the lab when I was in Shenzhen, which made me feel very welcomed. Laurence Macray and Leon Felix Mueller, it was an honor to supervise your master’s projects. The dry-processing method further explored by Laurence, and the local dynamics NMR study conducted by Felix, have deepened my understanding of hybrids solid electrolytes. I also genuinely enjoyed our conversations along the way. I am also profoundly thankful to the hybrid team members, Meera Mohan Kumer Sreelatha and Peter van den Berg, who helped me unravel the mysteries of polymer-LiI interactions and explain the NMR spectra. Jef Canals-Riclot, you have always been so warm-hearted and

willing to help. And thanks to Pranav Karanth and Xuehang Wang for your valuable suggestions too. Moreover, I am especially thankful to Martijn van Hulzen, thank you for all your efforts in the data analysis for the microbeam project. You were always so patient in explaining the methods and codes to me, even responding to my questions in the middle of the night. My gratitude also goes to Robert Dankelman for all your help with the XRD measurements, although many of them were for projects not included in this thesis. It was always nice to hear your jokes and have you test my Dutch once in a while. A special note of thanks to Juke Heringa for helping me translate the Summary into Dutch, and for your assistance with the ICT-related problems. I also enjoyed our conversations and hearing about your past experiences. Many thanks as well to our secretary team, Martine van Vliet, Ilse van der Kraaij, and Nicole Banga, for your invaluable assistance in organizing all kinds of registrations and travel arrangements. And a special thanks to Martine for going above and beyond to arrange my contracts, I deeply appreciate it.

I feel lucky to be part of a group as warm as SEE, and surrounded by such fascinating officemates, groupmates, and faculty mates. Violetta, Tammo, Remco, and Hanan, you made me feel so welcome when I barely knew anyone at the start, and always being generous with your time and help all the time. And Victor, thank you for being such a warm and friendly officemate. Eveline, you are so great at sharing and being such a cheerful, lovely officemate, without you, I never would have made it to Hercules. It was wonderful seeing you again after your graduation. Zhaolong, you saved the day by lending me one of your bikes when mine was broken, and I am grateful for your help with the in-situ XRD measurements and career advices. I also had enjoyable times for the nice dinners with you, Dan and little Kevin. Yueer and Ziyang, your warmly chatting with me at the beginning made me feel much less alone in the building, and I truly enjoyed playing badminton and exploring restaurants with you. Yifan and Huanhuan, you two are so warm-hearted and generous, I really enjoyed the lunch time together when you were still around. And Xuehang, I still remember that we had our first Chinese New Year Eve dinner here together, and the nice cake you shared with me when we were still living in the same building. Chenglong and Qidi, thank you for the very nice home-made dumplings and we had nice catch-ups both outside and in the office too. Anastasiia, you are such a sweet officemate too, thank you for all the treats you brought back after your travels. Theo, thank you for helping me solve the diffraction questions, and reviewing the

hybrid paper together was a great experience too. Ajay, it was nice to be at the beamline in Berlin together, and many thanks to your warm suggestions about PhD life. Xavier, thank you for encouraging me to participate in more activities and for organizing them as well. I had a great time during the board game. Biffo, thank you for helping me with the coding when it almost drove me crazy. Mark Weijers and Pranav, thank you for being such nice lab companions. And Mark Kwakernaak, I am grateful for your assistance with the organic chemistry questions, and it was so fun to fly power kites together! Rui, thank you for the super nice Chinese New Year Eve dinner and your lovely gift. And Hao, thank you for your guidance in wine tasting and making travel plans. Alexandros, thank you for even taught me some MD calculations at the beginning, even though I was not patient enough to continue. Wenxuan, it was nice to explore the delicious food in Hong Kong together, and thank you for teaching me how to synthesize halides, even though I didn't have the chance to continue that project further. Qi Shen, thank you for sharing your experience in learning Dutch and for the lovely dinner. And Fengqi, thank you for always giving me your sincere advices. My gratitude also goes to other PhD and postdoc fellows whom I had the opportunity to meet and chat with too: Albert de Kogel, Angie Rangel Cardenas, Anika Kiecana, Bowei Huang, Chao Ma, Chao Wang, Chun-Ting Cho, Hamutu, Hanggai, Hanting Ye, Ilse van Ogtrop, Jing Lin, Jingjing Zhao, Kaouther Toudjine, Luca Maran, Lucas Huet, Mengfu Tu, Pedro Braga Groszewicz, Pierfrancesco Ombrini, Qi Jia, Qinru Li, Rijk E. Hogenbirk, Ruize Wang, Shuaiqi Yuan, Tian Gu, Tianyu Li, Walter Legerstee, Xinming You, Xueqing Miao, Zamran Khan, Zichao Li, Ziqing Yuan.

I would also like to acknowledge the support and kindness of other colleagues at RID. Michel Steenvoorden, thank you for your help with the XRD measurements, and Michel Thijs, I appreciate your kindness in helping me oil my bike chain and lock, even though we only met at the shed. Bart Boshuizen, thank you for your assistance with the XPS experiments at ChemE. I am also grateful for the technical help from Esther Bijl, Katarina Rajic-Miskovic, Dan Luo, and Nirmal Ilavazhakan. Katarina, thank you for encouraging me to start swimming, I would really like to start it soon. And Tim, your cookies from Germany and Japan were a delight, and I really enjoyed our chats and it was fun to explore what behind the map too. Beyond these names, my gratitude extends to all my colleagues from FAME, NPM2, and DEMO: Anton J. E. Lefering, Astrid van der Meer, Baukje Terpstra, Ekkes Brück, Eline

Heuvelman, Erik Kelder, Henk Schut, Ingrid de Haer-Douma, Iulian Dugulan, Jeroen Plomp, Lambert van Eijck, Niels van Dijk, Stephan Eijt, Steven Parnell, Wim Bouwman.

I am also grateful for the people I met outside of the Reactor world. The five weeks at the Hercules school were truly unforgettable. I was so impressed by the passion for knowledge among my classmates from around the world. Outside the classroom, the numerous hiking tours, cable car rides, weekend travels, and fun evening talks and hotpot parties at the hotel have left me with many cherished memories. My sincere thanks go to Han Sun, Mingfeng Xu, Yuqing Ge, Wan-Ju Yu, Zexiang Hu, Zisheng Yao, Lipeng Yao, Hang Li, Vidha, Esra, Atreyee, Carmen, Albert, and Chiara. It was wonderful to share so many great moments with all of you. And Mingfeng, the unforgettable trip to PSI in Switzerland will always stand out, and it was so great to see you again in Hong Kong. In Berlin, it was wonderful to meet Zora and Elmar, and I had so much fun hearing the stories behind Zora's tattoos. I am also grateful for the warm hospitality from Yaolin. In Hong Kong, it was great to explore the city with Xiaozhi (Yu Li) and my college roommate, Lu Liu.

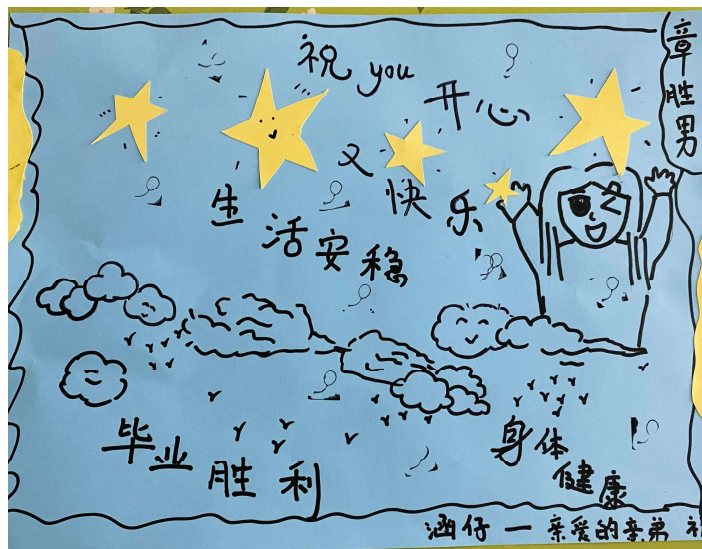
I would also like to express my deepest gratitude to my Master's supervisor, Shuanjin Wang. Thank you for teaching me so much, not only in battery research but also in how to approach research itself. Without your encouragement and support, I wouldn't have discovered my passion for research or considered pursuing a PhD abroad. I am also deeply grateful to my friends from my former group, Yilong Lin, Lei Zhong, Geng Cheng, and Zhibo Zhang, for always caring about me, even from so far away. I am glad I was finally able to visit you again in 2023 after three years.

My most heartfelt thanks go to my bestie, Yaru Zhang. Ever since high school, you have always given me so much understanding and care, although we were in different cities already during college. I know I can always count on you, no matter what I am going through in the "outside" world. I truly regret missing your wedding, but it was wonderful to see you again last Christmas.

With special appreciation, I would like to deeply thank two of my family-like and best friends in Delft, Chaofan Chen and Siyuan Wang. Chaofan, thank you for always being so generous with your help and support. Your kindness and willingness to help make every challenge feel manageable. As long as you are around, I feel I don't need to worry about anything. We have shared so many wonderful moments, both in the office and during our

adventures outside, and those experiences have created cherished memories that I will always treasure. Whether we were deep in discussion about our projects or exploring new places, your infectious enthusiasm and curiosity for life have truly inspired me to embrace new experiences. Siyuan, it was such a wonderful destiny to know you even since we were still applying for PhD positions. We have been though so many things together during these four years. I can't thank you enough for being my rock, especially during my darkest times. Your constant support has been incredibly meaningful to me. Your presence has had a profound impact on me, teaching me the value of sharing life, inspiring me to adopt a positive attitude, and encouraging me to face the future with courage and fearlessness. I will always cherish our unforgettable trip to Italy, filled with laughter and adventures, and I hope we get the chance to travel together again in the future!

Last but not least, my deepest gratitude goes to my family. Thanks to my mum and dad for your unwavering love and support. I am also grateful to my little brother for bringing joy into my life, and to my lovely aunt for your constant support!



(A drawing gift from my brother Zihan with the message: "Wishing you joy and happiness, a peaceful life, good health, and a triumphant graduation!")

Shengnan Zhang

October 2024, Delft, Netherlands

List of publications

Publications related to this thesis:

1. Liu M., **Zhang S.**, van Eck E. R., Wang C., Ganapathy S. & Wagemaker M. Improving Li-ion interfacial transport in hybrid solid electrolytes, *Nature Nanotechnology* 17, 959-967 (2022).
2. **Zhang, S.**, Li, Y., Bannenberg, L.J., Liu, M., Ganapathy, S. & Wagemaker, M. The lasting impact of formation cycling on the Li-ion kinetics between SEI and the Li-metal anode and its correlation with efficiency. *Science Advances* 10, eadj8889 (2024).
3. **Zhang, S.**, Li, Y., Bannenberg, L.J., Liu, M., Wagemaker, M. & Ganapathy, S. Elucidating the impact of functional additives on the structure and ion dynamics of hybrid solid electrolytes. *Advanced Energy Materials*, accepted (2025).
4. **Zhang, S.**, Mueller L. F., Macray L., Wagemaker M., Bannenberg L. J. & Ganapathy S. Revealing local diffusive dynamics in hybrid solid electrolytes. *In peer review*.

Other publications:

5. **Zhang, S.**, Ren, S., Han, D., Xiao, M., Wang, S., Sun, L. & Meng, Y. A highly immobilized organic anode material for high performance rechargeable lithium batteries. *ACS Applied Materials Interfaces* 12, 36237-36246 (2020).
6. **Zhang, S.**, Ren, S., Han, D., Xiao, M., Wang, S. & Meng, Y. Aqueous sodium alginate as binder: dramatically improving the performance of dilithium terephthalate-based organic lithium ion batteries. *Journal of Power Sources* 438, 227007 (2019).
7. **Zhang, S.**, Ren, S., Han, D., Xiao, M., Wang, S. & Meng, Y. Immobilization strategies of organic electrode materials. *Progress in Chemistry* 32, 103-118 (2020).
8. **Zhang, S.**, Yang K., Han, D., Xiao, M., Wang, S. & Meng, Y. Multifunctional lithium-sulfur battery separator. *Progress in Chemistry* 30, 1942-1959 (2018).

Curriculum vitae

Shengnan Zhang was born on December 16, 1995, in Hunan, China. She started her research in battery materials at Sun Yat-sen University under the supervision of Prof. Yuezhong Meng and Prof. Shuanjin Wang, where she focused on organic electrode materials derived from dilithium terephthalate. In June 2020, she graduated with a Master of Engineering degree in Materials Physics and Chemistry.

In November 2020, she began her PhD at Delft University of Technology in the Storage of Electrochemical Energy (SEE) group, under the supervision of Prof. Dr. Ir. Marnix Wagemaker, with financial support from the China Scholarship Council (CSC). Her doctoral research focused on using solid-state NMR to investigate Li-ion dynamics across Li-SEI interfaces and the structure-property relationships in hybrid solid electrolytes.

